Optimizing resource allocation for the Internet of Things with uncoordinated spectrum access and NOMA

Joseph Doumit

COLLEGES SCIENCES
BRETAGNE POUR L'INGENIEUR
LOIRE ET LE NUMERIQUE

IMT Atlantique
Bretagne-Pays de la Loire
École Mines-Télécom

THESE DE DOCTORAT DE

L'ÉCOLE NATIONALE SUPERIEURE
MINES-TELECOM ATLANTIQUE BRETAGNE PAYS DE LA LOIRE –
IMT ATLANTIQUE

ECOLE DOCTORALE N° 648
Sciences pour l'Ingénieur et le Numérique
Spécialité : *Télécommunications*

Par

Joseph DOUMIT

Optimisation de l'allocation de ressources pour l'internet des objets dans un contexte d'accès non coordonné au spectre et de NOMA

Optimizing resource allocation for the Internet of Things with uncoordinated spectrum access and NOMA (in English)

Thèse présentée et soutenue à IMT Atlantique, Brest, le 01 décembre 2023
Unité de recherche : Lab-STICC
Thèse N° : 2023IMTA0371

Rapporteurs avant soutenance :

Claire GOURSAUD	Maître de conférences HDR, INSA de Lyon
Eric SIMON	Maître de conférences HDR, Université de Lille

Composition du Jury :

Président :	Jean-Pierre CANCES	Professeur, Université de Limoges
Rapporteurs :	Claire GOURSAUD	Maître de conférences HDR, INSA de Lyon
	Eric SIMON	Maître de conférences HDR, Université de Lille
Dir. de thèse :	Charbel ABDEL NOUR	Professeur, IMT Atlantique
Co-dir. de thèse :	Joumana FARAH	Professeur, INSA de Rennes
Encadrante :	Catherine DOUILLARD	Professeur, IMT Atlantique

Invité(s)

Matthieu CRUSSIERE	Professeur, INSA de Rennes
Marie-Joséphа YOUSSEF	Docteur, Capital Fund Management

IMT Atlantique

École Doctorale SPIN

Resource Allocation in Mixed Traffic Uncoordinated Communication Systems with Non-Orthogonal Multiple Access

---

Thèse de Doctorat

Spécialité : Télécommunications

Présentée par **Joseph Doumit**

Département : Mathematical and Electrical Engineering

Laboratoire : Lab-STICC

Directeurs de thèse : **Charbel Abdel Nour, Joumana Farah**

Encadrants : **Catherine Douillard, Marie-Joséphа Youssef**

Acknowledgments

I would like to express my deepest gratitude to all those who have contributed to completing my Ph.D. journey. This academic milestone would not have been possible without numerous individuals' support, guidance, and encouragement.

First and foremost, I am indebted to my supervisors, Charbel ABDEL NOUR, Catherine DOUILLARD, Joumana FARAH and Marie-Josepha YOUSSEF, whose expertise, patience, and unwavering support have been invaluable throughout this research adventure. Your mentorship has been a beacon guiding me through the complexities of academia, and I am truly grateful for the knowledge and skills I have gained under your guidance.

I extend my appreciation to the members of my doctoral committee, Jean-Pierre CANCES, Claire GOURSAUD, Eric SIMON and Matthieu CRUSSIERE, for their insightful feedback and constructive criticism. Their expertise has significantly enriched the quality of my research.

I am grateful to the MEE department for providing the necessary resources and a conducive environment for academic exploration. IMT Atlantique community has been instrumental in shaping my scholarly pursuits.

My sincere thanks go to my colleagues and friends who have provided a supportive and collaborative atmosphere. Your presence has made the academic journey enjoyable and memorable.

Finally, my deepest gratitude goes to my family for their tireless support, love, and understanding. Your encouragement has been my source of strength and I am grateful for the sacrifices you made to see me succeed in my academic pursuits.

Thank you.
Joseph DOUMIT

Abstract

Resource Allocation in Mixed Traffic Uncoordinated Communication Systems with Non-Orthogonal Multiple Access

Joseph Doumit

Mathematical and Electrical Engineering Department, IMT Atlantique

The Internet of Things (IoT) has become a major driving use case in the evolution of wireless communication networks. Indeed, it is expected that IoT devices will constitute the major part of the fifth generation (5G) communication networks and beyond 5G (B5G) with billions of connected IoT devices projected to be used. This increase in connected IoT devices will not only lead to a significant increase in wireless capacity requirements, but also will introduce new wireless use cases that differ from conventional human user-oriented services. Thus, to ensure the integration of IoT devices into future communication networks while continuously supporting broadband users, it is necessary to devise new techniques that meet the quality of service (QoS) requirements of all connected equipment. Some of the key elements expected to be applied in B5G communication networks include novel spectrum access techniques, scalable and auto-configured networks, and the utilization of reconfigurable intelligent surfaces (RIS) to enhance the wireless communication link quality and system performance.

In this context, the main objective of this thesis is to study innovative solutions for resource allocation and network design that aim to optimize the utilization of available radio resources in future wireless communication networks. Specifically, our focus lies in the utilization of non-orthogonal multiple access (NOMA) for radio access. By exploiting the power domain, NOMA enables multiple users to share the same orthogonal resource block, thereby enhancing system performance in terms of spectral efficiency, achieved throughput, and fairness among users/devices.

First, we study the uplink uncoordinated spectrum and power allocation problems in a NOMA IoT network while minimizing the age of information (AoI). In such systems, power-limited IoT devices aim at auto-organizing their transmissions on available resources, i.e., the subband-power level pairs, without any coordination between them. To this aim, we propose resource allocation algorithms based on the multi-armed bandit (MAB) framework from reinforcement learning. In order to enhance spectral efficiency and support multiple data traffic types including latency sensitive and sporadic ones, we propose to introduce full-duplex relays with traffic priority management and queuing capabilities. To solve the problem of minimizing the AoI, specific modifications were introduced simultaneously to the aforementioned MAB framework and traffic priority management algorithms. The resulting uncoordinated spectrum access system was compared to coordinated systems applying matching theory from prior-art under similar simulation conditions. Results show that the proposed uncoordinated MAB-based solution achieves rate satisfaction for the users, even under demanding system conditions in

terms of target user-rates and channel quality. Moreover, it reveals to be efficient in minimizing AoI, transmit power and overhead compared to the coordinated solution.

Second, we shift our focus to investigate the integration of RIS in an uplink uncoordinated communication system. In fact, RIS has been hailed as a novel and promising technology thanks to its ability to alter the wireless propagation environment. We propose a new technique based on the MAB framework to design efficient NOMA for the system applying RISs. This is made possible by varying the characteristics of the reflective elements while guaranteeing a minimum requested rate for the communicating IoT devices with superimposed signals. In addition, using the branch and bound algorithm (BBA), we determine the optimal subset of surfaces to be activated from a pool of a wide set of available RISs in a way to maximize the system energy efficiency (EE). Simulation results demonstrate the efficiency and the robustness of the developed algorithm in terms of achieved rates and EE compared to other RIS configuration methods.

Third, we study the integration of aerial RIS (ARIS) where an unmanned aerial vehicle (UAV) carries the RIS throughout its trajectory. In this context, we investigate an ARIS-supported uplink NOMA cellular network, especially in environments where the direct channels between IoT devices and the base station (BS) are heavily shadowed. IoT devices simultaneously transmit their data to the BS using a unique power level. The NOMA power separation between device signals is then achieved through the configuration of RIS reflective elements, taking into account the resulting channel made up from a concatenation of two line-of-sight (LoS) links. The proposed allocation algorithm for such a system is designed to offer the possibility of sharing efficiently the spectrum among devices while satisfying target rates. This is made possible by the ability to estimate/predict the evolution of such a concatenated LoS channel largely facilitating the study of the UAV trajectory in order to maximize the spectral efficiency.

Keywords: Non-orthogonal multiple access, uncoordinated spectrum, reconfigurable intelligent surfaces, multi-armed bandits, mixed traffic, two-hop communication networks

Contents

List of Figures

List of Tables

List of Abbreviations

3G	Third generation of mobile communications networks
4G	Fourth generation of mobile communications networks
5G	Fifth generation of mobile communications networks
AoI	Age of information
ARIS	Aerial reconfigurable intelligent surfaces
AWGN	Additive white Gaussian noise
B5G	Beyond 5G
BBA	Branch and bound algorithm
bps	Bit-per-second
BS	Base station
CSI	Channel state information
dB	Decibel
DF	Decode-and-forward
EE	Energy efficiency
eMBB	Enhanced mobile broadband
FCFS	First-come-first-served
FD	Full duplex
GU	Ground user
IDMA	Interleave division multiple access
i.i.d	Independent and identically distributed
IoT	Internet of things
IRS	Intelligent reflecting surface

LCFS	Last-come-first-served
LoS	Line-of-sight
LTE	Long-term evolution
MAB	Multi-armed bandit
MBS	Macro base station
MIMO	Multiple-input multiple-output
mMTC	Massive machine-type communication
mmWave	Millimeter-wave
MP-MAB	Multi-player multi-armed bandit
MT	Matching theory
nLoS	Non-line-of-sight
NOMA	Non-orthogonal multiple access
OFDM	Orthogonal frequency division multiplexing
OMA	Orthogonal multiple access
PAPR	Peak-to-average power ratio
PDMA	Pattern division multiple access
PD-NOMA	Power-domain NOMA
PER	Packet error rate
PF	Proportional fair
PIN	Positive intrinsic negative
PS	Power splitting
QoS	Quality of service
RACH	Random access channel
RIS	Reconfigurable intelligent surface
RL	Reinforcement learning
RMS	Root mean square
SC	Superposition code
SCMA	Sparse code multiple access
SE	Spectral efficiency
SINR	Signal-to-interference-plus-noise ratio
SNR	Signal-to-noise ratio
SIC	Successive interference cancellation
SWIPT	Simultaneous wireless information and power transfer

UAV	Unmanned aerial vehicle
UCB	Upper confidence bound
URLLC	Ultra-reliable low-latency communication
UE	User equipment
WPT	Wireless power transfer

List of Notations

α	Weight for distance between the ARIS and the charging point
α_1	Path loss exponent
β	Weight for power budget
β_0	PL at a reference distance
$\beta_{s,i}$	Reflection amplitude of sub-surface s of RIS i
Γ_{d_k,a_b}	Achieved SINR for device d_k when playing an arm a_b
$\Gamma_{d_k,c}$	Achieved SINR for device d_k over subband c
$\Gamma_{l,req}$	Target SINR when using power level v_l
Δ_1	AoI measured for device-relay link
Δ_2	AoI measured for relay-BS link
ϵ_l	Relative error on power level v_l
η_{d_k,a_b}	Collision indicator
Φ_i	Configuration of RIS i
$\phi_{s,i}$	Phase shift of sub-surface s of RIS i
σ^2	AWGN power density
$\theta_{g_{d_k,s}}$	Angular phase of $g_{d_k,s}$
θ_{h_s}	Angular phase of h_s
$\theta_{h_{d_k}}$	Angular phase of h_{d_k}
$\mathcal{A}_{d_k}$	Set of actions d_k
$\mathcal{A}_{ARIS}$	Set of actions of the ARIS
a_b	Element of set of actions $\mathcal{A}_{d_k}$
a_n	Element of set of actions $\mathcal{A}_{ARIS}$
B	Total bandwidth
Bu_r	Buffer size
BP_{BS}	Base power consumed by the BS
C	Subbands
C_{SI}	Residual self-interference

$\mathcal{D}$	Set of IoT Devices
d_k	Device
d_{secu}	Safety distance for ARIS
$\text{dist}_{ARIS,CP}$	Distance between the ARIS and the charging point
$\text{dist}_{d_k,ARIS}$	Distance between device d_k and the ARIS
$\text{dist}_{BS,ARIS}$	Distance between the BS and the ARIS
e	Empty slots for the system
e_{v_l}	Empty slots for power level v_l
$\mathbf{g}_{d_k,i,c}$	Vector of channel gains between device d_k and each sub-surface of RIS i over subband c
$g^{LoS}_{d_k,i,c}$	LoS component of $\mathbf{g}_{d_k,i,c}$
$g^{nLoS}_{d_k,i,c}$	nLoS component of $\mathbf{g}_{d_k,i,c}$
$\mathfrak{g}_{d_k,s}$	Module of an element $g_{d_k,s}$ of $\mathbf{g}_{d_k,i,c}$
$\underline{\mathbf{g}}_{d_k}$	Concatenated channels between device d_k and the different RISs
$\hat{\underline{\mathbf{g}}}_{d_k,c}$	Estimated channels of $\underline{\mathbf{g}}_{d_k}$
$h_{d_k,r}$	Channel gain between device d_k and relay r
$h_{r,BS}$	Channel gain between relay r and the BS
$h_{d_k,c}$	Channel gain between device d_k and the BS over subband c
$\hat{h}_{d_k,c}$	Estimated channel of $h_{d_k,c}$
$\mathbf{h}_{i,c}$	Vector of channel gains between each sub-surface s of RIS i and the BS over subband c
$h^{LoS}_{i,c}$	LoS component of $\mathbf{h}_{i,c}$
$h^{nLoS}_{i,c}$	nLoS component of $\mathbf{h}_{i,c}$
$\mathfrak{h}_s$	Module of an element h_s of $\mathbf{h}_{i,c}$
$\underline{\mathbf{h}}$	Concatenated channels between the different RISs and the BS
$\hat{\underline{\mathbf{h}}}_c$	Estimated channels of $\underline{\mathbf{h}}$
I	Number of RISs
J	Number of active RISs
$\mathcal{K}$	Set of active IoT devices
K	Number of active IoT devices
K_c	Number of devices per subband c
K_r	Number of served devices by the ARIS
κ	Rician factor

L	Number of power levels
$\tilde{L}_{d_k}$	Highest possible value of L for a device d_k
M	Passive reflective elements
N	Number of IoT devices
n_1	Number of devices with continuous traffic type
n_2	Number of devices with periodic traffic type
n_3	Number of devices with sporadic traffic type
n_3^c	Number of non-collided devices with sporadic traffic type
$n_{d_k}(a_b, t)$	Number of times an action a_b is played, measured at t
P_{BS}	Power consumed by the BS
P_{RIS}	Power consumed by a RIS
$P^t_{d_k,b}$	Transmit power of device d_k when playing an arm a_b
$P^t_{r,c}$	Transmit power of relay r over subband c
$P^{max}_{d_k}$	Power budget of device d_k
$P^{max}_{r,c}$	Power budget of relay r over subband c
PL	Path loss
PP_{BS}	Processing power of the BS
$p^a_{d_k^{spo}}$	Spectrum access probability for device d_k
Q	Average reward
Q_l	Supported number of collisions on power level v_l
$\mathcal{R}$	Set of relays
R	Number of relays
$R_{cont,req}$	Rate required for devices with continuous traffic type
$R_{ncont,req}$	Rate required for devices with non-continuous traffic type
R_{d_k,a_b}	Achieved rate for device d_k when playing an arm a_b
$R_{d_k,c}$	Achieved rate for device d_k over subband c
$R_{d_k,req}$	Rate required for device d_k
$R_{r,c}$	Achieved rate for relay c over subband c
$R_{r,req}$	Rate required for relay r
Rad_l	Maximum distance between device d_k and the ARIS that allows the device to be assigned to v_l
r	Relay
S	Sub-surfaces of RIS
$Step_{LoS}$	Distance traveled by the ARIS when the ARIS is in LoS position

$Step_{nLoS}$	Distance traveled by the ARIS when the ARIS is in nLoS position
$Step_{threshold}$	Minimum distance that the ARIS can take
s_{d_k}	Total sum reward
T	Time horizon
$T^{on}_{d^{per}_K}$	Period between two consecutive transmissions for devices with periodic traffic type
T_{conv}	Convergence time for devices with continuous traffic type
t	Timeslot
U_{d_k,a_b}	Utility function for device d_k when playing action a_b
U_{ARIS,a_n}	Utility function for the ARIS when playing action a_n
v_l	Received power level
$v^*_{d_k}$	Power level attributed to d_k
W	Bandwidth per subband
ws	Window size for averaging the achieved rewards
$X_{0,r}$	Maximum number of received signals that a relay can forward to the BS without buffering
X^t_r	Number of signals successfully decoded ar relay r
$\left(x^{(t)}_{ARIS}, y^{(t)}_{ARIS}, z^{(t)}_{ARIS}\right)$	Position of the ARIS at timeslot t
$x_{d_k,c}$	Signal transmitted by device d_k over subband c
y_c	Received signal over subband c
z_{min}	Minimal altitude for the ARIS
z_{max}	Maximal altitude for the ARIS
$(.)^T$	Transpose vector/matrix
$\circ$	Hadamard product

Résumé étendu de la thèse en français

Chapitre 1: Introduction Générale

Les progrès rapides des technologies de communication sans fil ont fait de l'internet des objets (IoT) un concept qui a transformé le domaine des réseaux. L'IoT facilite la connectivité et l'interaction sans effort entre un large éventail de dispositifs, tels que des capteurs, des actionneurs et même des objets courants, formant ainsi un réseau d'objets connectés. Avec la transition prochaine vers les réseaux de communication de l'après-cinquième génération (B5G), l'intégration de l'IoT dans ces réseaux offre de nouvelles possibilités et pose en même temps de nouveaux défis [1, 2]. L'un des principaux défis pour les futurs réseaux consiste à adapter les paramètres du système aux caractéristiques spécifiques des dispositifs IoT et à leur déploiement. En effet, ces appareils sont appelés à être déployés à grande échelle, avec des besoins de communication exigeants et de fortes contraintes énergétiques. Les contraintes de déploiement nécessitent l'utilisation de stratégies efficaces de gestion et d'allocation des ressources conçues pour garantir le respect des contraintes de qualité de service (QoS) pour tous les appareils actifs, tout en offrant la possibilité d'une évolutivité en termes de connexion au réseau. Les contraintes de qualité de service comprennent la fiabilité des communications, la latence et l'efficacité énergétique (EE) [3–5]. Lorsque celles-ci sont satisfaites, ces systèmes peuvent permettre des scénarios d'application ou des cas d'utilisation dans divers domaines. Toutefois, pour exploiter le potentiel de l'IoT dans les réseaux B5G, il faut satisfaire les exigences spécifiques posées par les applications ciblées. Des communications ultra-fiables et à faible latence sont essentielles pour les applications IoT critiques telles que la surveillance dans le domaine de la santé et l'automatisation industrielle. L'efficacité énergétique est cruciale pour la durabilité des appareils IoT fonctionnant sur batterie, facilitant les déploiements durables et rentables. L'évolutivité est également essentielle pour faire face à la croissance exponentielle du nombre d'appareils IoT et à leur intégration dans les réseaux B5G. En outre, la sécurité et la confidentialité sont importantes pour protéger les données sensibles et favoriser une large diffusion des systèmes IoT.

Afin de répondre aux exigences des applications susmentionnées, les réseaux sans fil existants doivent évoluer et adopter des technologies innovantes. Plus précisément, les futurs réseaux de communication devront explorer des solutions permettant de mieux exploiter le spectre disponible grâce à des méthodes d'accès multiple avancées comme l'accès multiple non orthog-

onal (NOMA), au déploiement de cellules plus denses comprenant des relais dotés de capacités auto-configurables, aux communications par ondes millimétriques (mmWave), aux communications *grant free* et aux communications assistées par des surfaces intelligentes réfléchissantes (RIS). La question de savoir comment concevoir un système sans fil bien intégré qui intègre ces nouvelles techniques afin d'optimiser de manière dynamique l'utilisation des ressources sans fil et de répondre aux exigences de qualité de service a été au cœur de la littérature récente.

Cette thèse explore l'utilisation des stratégies d'optimisation et d'apprentissage par renforcement (RL) afin de concevoir des algorithmes efficaces d'allocation de ressources pour la prochaine génération de réseaux cellulaires sans fil. L'objectif est de servir les utilisateurs ayant des exigences variables en matière de qualité de service dans le cadre d'un accès multiple non coordonné et de réseaux auto-configurables. En outre, l'utilisation des RIS passifs dans les systèmes de communication sans fil est étudiée. Plus précisément, la thèse aborde le problème de la configuration du RIS pour un système NOMA efficace bien qu'utilisant des dispositifs avec un niveau de puissance d'émission unique. En outre, la thèse étudie l'utilisation de RIS aériens qui peuvent être utiles lorsque la mise en œuvre de RIS au sol devient physiquement compliquée en raison des effets d'ombrage (*shadowing).* En fait, le travail porte sur la détermination de la trajectoire du RIS aérien dans le but de répondre à des exigences de qualité de service.

Chapitre 2: Contexte et Outils

Dans ce chapitre, nous posons les bases des concepts clés qui sont essentiels à la recherche menée dans la thèse. La première partie du chapitre donne un bref aperçu de la prise en charge de l'IoT dans les futures générations de réseaux cellulaires, en mettant l'accent sur les méthodes d'accès multiple innovantes, en particulier le NOMA. En outre, nous insistons sur l'utilisation des RIS dans les systèmes de communication sans fil en discutant des avantages et des défis potentiels liés à l'incorporation des RIS et des RIS aériennes dans les systèmes sans fil. La dernière partie du chapitre présente les fondements des techniques analytiques utilisées pour les solutions proposées, telles que le RL et plus particulièrement le cadre du bandit à bras muliples (MAB), ainsi que la théorie de l'appariement (*matching theory*).

Les Futurs Réseaux de Communication

Le développement des systèmes sans fil a été largement motivé par la demande de débits de données plus élevés et de connectivité massive. Cependant, l'avènement d'applications IoT innovantes a rendu les exigences des réseaux 5G et B5G de plus en plus diverses comme le montre la figure 1. Par conséquent, les futurs réseaux de communication devront prendre en charge les services mobiles à haut débit améliorés (eMBB), les communications massives de type machine (mMTC) et les communications ultra-fiables à faible latence (URLLC).

Afin de répondre à ces diverses exigences, d'importants travaux de recherche ont été consacrés à l'exploration de nouvelles techniques et d'architectures de réseau susceptibles de suivre les progrès rapides des systèmes sans fil. Parmi les stratégies clés, on peut citer le déploiement dense

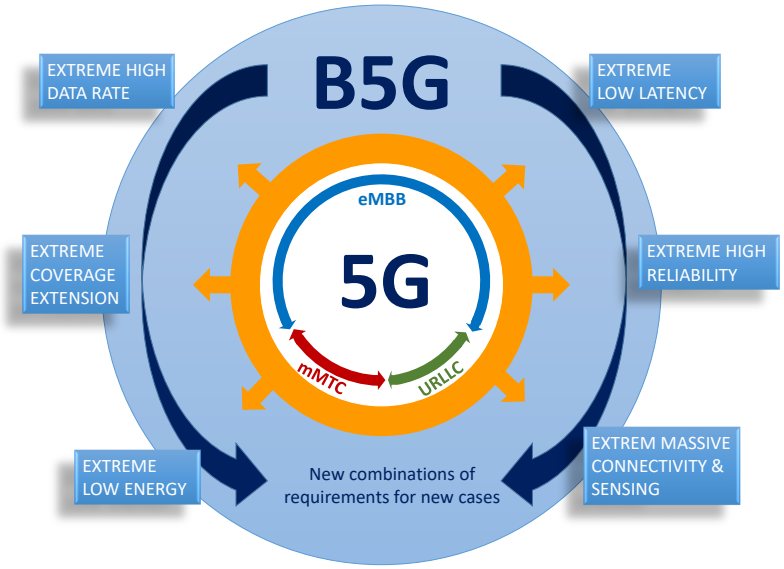

Figure 1: Cas d'utilisation et exigences de la 5G et de la B5G

des relais full-duplex (FD), l'utilisation des RIS et l'utilisation efficace du spectre disponible avec NOMA.

Accès Multiple Non-Orthogonal (NOMA)

Le principe de base du NOMA consiste à utiliser le domaine de puissance pour desservir plusieurs utilisateurs de manière non orthogonale sur le même bloc de ressources temps-fréquence. Du côté de l'émetteur, le NOMA repose sur le codage par superposition (SC) [6]. Par conséquent, du côté du récepteur, les interférences entre utilisateurs doivent être gérées, généralement en appliquant l'annulation successive des interférences (SIC) [7].

NOMA en voie montante

Dans les systèmes de communication en liaison montante, les utilisateurs/appareils doivent se mettre d'accord sur le contrôle de la puissance et l'attribution des fréquences avant toute transmission NOMA. Cet accord peut être coordonné de manière classique par des signaux de commande provenant de la station de base. Une fois l'accord obtenu, chaque utilisateur/appareil peut transmettre son message avec le niveau de puissance cible sur la fréquence attribuée. La station de base reçoit donc un signal combiné composé des transmissions qui se chevauchent de tous les utilisateurs actifs. Soit K le nombre total d'utilisateurs et C le nombre total de sous-bandes dans le système. B_c représente la largeur de bande pour chaque sous-bande c. Supposons en outre que $\mathcal{K}_c$ désigne l'ensemble des utilisateurs programmés sur la sous-bande c, où $k_c(n)$ est le n-ième utilisateur programmé sur la sous-bande c et $|\mathcal{K}_c| = K_c$ représente le nombre total d'utilisateurs sur cette sous-bande.

Dans l'hypothèse d'un décodage SIC réussi dans l'ordre décroissant des gains de canal, le débit maximal réalisable pour l'utilisateur $k_c(n)$ sur la sous-bande c est donné par la formule

de Shannon :

$$R_{k_c(n),c} = B_c \log_2 \left(1 + \frac{P_{k_c(n),c} h^2_{k_c(n),c}}{\sum_{j=n+1}^{K_c} P_{k_c(j),c} h^2_{k_c(j),c} + \sigma^2} \right), \tag{1}$$

où $P_{k_c(.)}$ est sa puissance d'émission dans la sous-bande c et $h_{k_c(.),c}$ le gain de canal dans la sous-bande c entre l'utilisateur $k_c(.)$ et la station de base. Le terme σ^2 représente la variance du bruit blanc additif gaussien (AWGN).

Considérons, à titre d'exemple, un scénario dans lequel deux utilisateurs $k_c(1)$ et $k_c(2)$ sont programmés sur la sous-bande c, comme le montre la figure (2a). Si $k_c(1)$ a le gain de canal le plus élevé, les débits atteints dans le système NOMA de liaison montante peuvent être exprimés comme suit :

$$\begin{aligned} R_{k_c(1),c} &= B_c \log_2 \left(1 + \frac{P_{k_c(1)} h^2_{k_c(1),c}}{P_{k_c(2)} h^2_{k_c(2),c} + \sigma^2} \right), \\ R_{k_c(2),c} &= B_c \log_2 \left(1 + \frac{P_{k_c(2)} h^2_{k_c(2),c}}{\sigma^2} \right). \end{aligned} \tag{2}$$

NOMA en voie descendante

Dans un scénario de liaison descendante, la station de base utilise SC pour envoyer un signal combiné de tous les messages destinés aux utilisateurs programmés. Au niveau de la réception, si possible, chaque utilisateur applique le SIC pour récupérer les signaux des autres utilisateurs avant de décoder son message individuel, comme le montre la figure (2b).

En supposant que le décodage SIC est réussi et qu'il n'y a pas de propagation d'erreur du côté du récepteur, le débit atteint par l'utilisateur $k_c(n)$ dans la sous-bande c est donné par la formule suivante :

$$R_{k_c(n),c} = B_c \log_2 \left(1 + \frac{P_{k_c(n),c} h^2_{k_c(n),c}}{\sum_{j=1}^{n-1} P_{k_c(j),c} h^2_{k_c(j),c} + \sigma^2} \right). \tag{3}$$

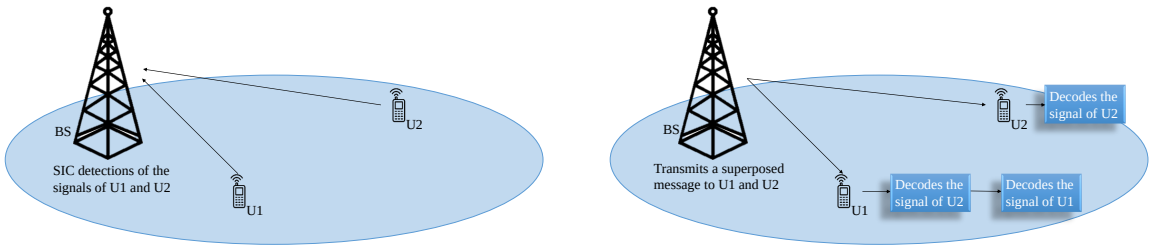

(a) NOMA en voie montante (b) NOMA en voie descendante

Figure 2: Décodage SIC

Surfaces Intelligentes et Réfléchissantes (RIS)

La RIS, également connue sous le nom de métasurface, est une structure bidimensionnelle principalement composée d'un grand nombre de particules diffusantes programmables ou méta-atomes. En ajustant leurs propriétés électriques de manière dynamique, ces méta-atomes peuvent contrôler les caractéristiques de propagation des ondes électromagnétiques en termes d'amplitude et de phase. Intégrées avec soin, les RIS peuvent améliorer les performances des communications sans fil en temps réel [8, 9] en modifiant les conditions de propagation.

Les RIS peuvent améliorer considérablement l'efficacité d'une communication sans fil en optimisant la propagation des ondes électromagnétiques. Il en résulte une amélioration de la qualité du signal, une réduction de l'évanouissement par trajets multiples et une diminution de la consommation d'énergie. En ajustant la phase des méta-éléments, la RIS peut concentrer l'énergie électromagnétique vers des directions spécifiques, maximisant la force du signal aux endroits souhaités tout en la minimisant à d'autres endroits. Cette capacité de formation de faisceau permet d'augmenter la portée de transmission et de réduire les interférences, améliorant ainsi les performances globales du réseau, en particulier pour les déploiements de grande envergure. En outre, sa faible consommation d'énergie, associée à sa nature passive - il n'émet pas de signaux mais manipule uniquement ceux qui lui parviennent - en fait une solution *verte* alignée sur les objectifs de développement durable.

RIS Aériennes (ARIS)

Les surfaces intelligentes et réfléchissantes aériennes (ARIS) sont apparues comme un concept révolutionnaire dans le domaine des communications sans fil (Figure 3) [10]. Déployées à l'état aéroporté, ces surfaces programmables modifient les caractéristiques des ondes électromagnétiques incidentes, ouvrant la voie à une nouvelle ère dans les paysages de communication. Comme le RIS terrestre décrit dans la section précédente, l'ARIS contrôle la propagation des ondes électromagnétiques pour créer un environnement sans fil optimal via des liaisons en visibilité directe (LoS) [11].

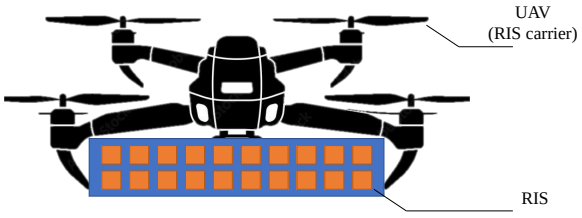

Figure 3: Surfaces intelligentes réfléchissantes aériennes (ARIS)

Bandits à Bras Multiples

Le cadre MAB [12] est un cas particulier de RL qui correspond à un scénario à état unique. Dans ce contexte, l'objectif de l'agent est de découvrir l'action qui fournit la récompense maximale dans un environnement à état unique. Le problème MAB a fait l'objet d'une étude approfondie dans la littérature. Récemment, le cadre des bandits multijoueurs à bras multiples (MP-MAB), qui implique plusieurs agents d'apprentissage s'efforçant de découvrir les actions produisant la récompense la plus élevée, a suscité une grande attention dans la communauté de recherche sur les communications sans fil. Plusieurs stratégies ont été proposées pour le problème MP-MAB dans la littérature, notamment la limite supérieure de confiance (UCB) [13], l'échantillonnage de Thompson [14], et les stratégies ϵ-greedy [15]. L'algorithme UCB atteint une convergence plus rapide que les autres stratégies tout en équilibrant efficacement l'exploration et l'exploitation. Ces techniques ont été utilisées pour résoudre de nombreux problèmes, notamment l'accès opportuniste au spectre dans les réseaux radio cognitifs [16–19], l'accès au spectre non coordonné [20, 21] et l'optimisation des trajectoires dans les réseaux cellulaires utilisant des drones [22].

La Théorie de l'Appariement

La théorie de l'appariement [23] est un outil mathématique robuste qui a été utilisé pour résoudre le problème d'allocation de ressources décrit au chapitre 3. La théorie de l'appariement, ancrée dans le domaine de l'économie, fournit un cadre pour la formation de relations mutuellement avantageuses et est particulièrement utile lorsqu'il s'agit de traiter des dilemmes d'affectation similaires à ceux auxquels est confronté une station de base centralisée. Quelques études ont proposé des algorithmes faisant appel à la théorie de l'appariement pour résoudre les problèmes d'allocation des ressources [24–28].

Chapitre 3: Allocation de Ressources pour les Types de Trafic Mixtes dans les Systèmes de Communication avec Relais en Full-Duplex

Dans ce chapitre, nous étudions un système de transmission NOMA non coordonné sur la liaison montante, dans lequel des relais full-duplex avec des files d'attente de type "dernier arrivé premier servi" sont déployés. Les dispositifs IoT visent à auto-organiser leurs communications avec les relais disponibles à l'aide du cadre MAB, sans communiquer entre eux. Les relais transmettent ensuite les signaux reçus à la station de base, ce qui donne un système de communication à deux sauts.

Les dispositifs IoT étant déployés pour des cas d'utilisation multiples avec des caractéristiques et des exigences de trafic variables, nous considérons le système de trafic mixte composé de transmissions continues, sporadiques et périodiques. En outre, chaque appareil IoT dispose d'un budget énergétique limité. Nous proposons un algorithme en plusieurs étapes basé sur

le cadre MAB dans lequel nous effectuons l'allocation de sous-bande et de puissance tout en garantissant les contraintes de puissance d'émission et en minimisant l'âge de l'information (AoI) pour les appareils de manière non coordonnée. La principale contribution de ce chapitre concerne la proposition d'une méthode efficace pour attribuer les ressources de spectre et de puissance disponibles aux dispositifs ayant des types de trafic mixtes dans un système non coordonné, minimiser la puissance d'émission au niveau des dispositifs et des relais tout en maximisant les débits atteints et minimiser l'AoI pour les appareils IoT en utilisant le cadre MAB.

La performance de la méthode non coordonnée basée sur le MAB proposée est comparée à celle d'une technique de référence consistant en une technique coordonnée d'allocation de spectre et de puissance basée sur la théorie de l'appariement qui minimise elle-aussi l'AoI.

Algorithme Basé sur le MAB

Dans un système où l'accès au spectre n'est pas coordonné, les appareils visent à auto-organiser leurs transmissions sans intervention extérieure. Pour résoudre le problème de l'attribution conjointe de sous-bandes et de puissance, un cadre MAB multi-joueurs avec récompense nulle en cas de collision est adopté [29]. L'ensemble des bras est l'ensemble des paires sous-bande-niveau de puissance disponibles. Disposant de différents types de trafic et d'un budget de puissance d'émission, chaque dispositif d_k construit son espace d'action $\mathcal{A}_{d_k}$, en tenant compte des paires sous-bande-niveau de puissance sur lesquelles il peut émettre sans enfreindre son budget de puissance. Lorsqu'il choisit une action, chaque dispositif d_k reçoit une récompense de la part du relais. Dans ce travail, la récompense est définie comme le taux atteint au niveau du relais, donné par la formule de Shannon [30], pour les dispositifs à trafic continu. Par contre, la récompense est inversement proportionnelle à l'AoI pour les dispositifs à trafic sporadique.

En raison de l'absence de communication entre les appareils IoT, chaque appareil n'observe que sa propre liste d'actions et la liste de récompenses correspondante. Comme les récompenses sont inconnues à l'avance au niveau de l'appareil, une phase d'exploration est nécessaire au cours de laquelle les appareils apprennent les récompenses.

Algorithme Basé sur la Théorie de l'Appariement

Le problème de l'attribution des sous-bandes est modélisé comme un jeu d'appariement un à un. Dans ce modèle, l'ensemble des bras et l'ensemble des appareils forment deux ensembles indépendants en fonction de leurs préférences. Dans ce scénario, chaque bras représente une paire puissance-sous-bande et ne peut être attribué qu'à un seul appareil, et chaque appareil ne peut émettre que sur un seul bras par créneau temporel.

Chaque appareil classe les canaux dans un ordre décroissant en fonction de leurs gains. Ainsi, lorsque tous les dispositifs sont associés à des bras différents, les exigences en matière de débit sont satisfaites tout en tendant à consommer le moins de puissance d'émission possible. La préférence d'appariement des bras dépend de l'état de la file d'attente de tous les relais, des conditions du canal, de la puissance de transmission et de l'activité des dispositifs.

Le problème est ensuite résolu à l'aide de l'algorithme de Gale-Shapley [31] au niveau de la

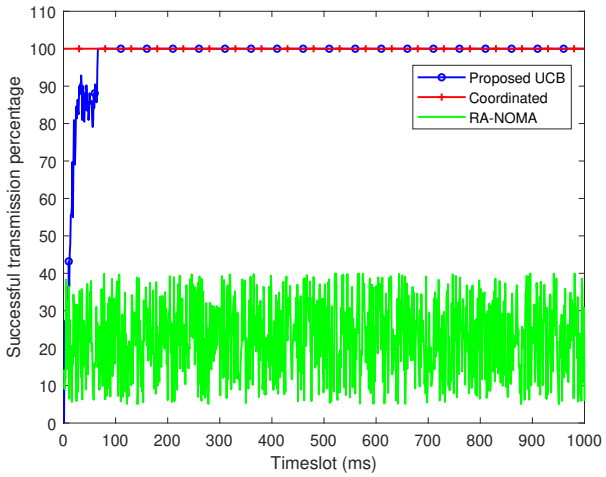

Figure 4: Pourcentage instantané de transmission réussie en fonction du temps.

station de base.

Exemples de Résultats

Les performances des algorithmes proposés avec et sans estimation de l'AoI sont évaluées pour $T = 1000$ créneaux temporels. La performance de la technique proposée est comparée à la référence basée sur une allocation coordonnée qui applique un cadre centralisé supposant que la station de base connaît parfaitement les gains de canal entre les dispositifs et les relais, et ceux entre les relais et la station de base, ainsi que l'état de la file d'attente des relais. L'allocation des ressources est alors optimisée en conséquence. Cette méthode est appelée "Coordinated". En plus de la "Coordinated", des comparaisons sont faites avec une autre méthode non coordonnée : NOMA à accès aléatoire (appelée "RA-NOMA" dans la légende de la figure), dans laquelle les appareils choisissent leurs bras de manière aléatoire. L'affectation des bras est évaluée dans la figure 4, où le pourcentage instantané de transmission réussie est représenté en fonction du temps. La figure 4 montre que la technique UCB proposée atteint la convergence avec un taux de satisfaction de 100 %, ce qui signifie que la fin de la phase d'exploration pour tous les appareils se produit dans un délai de 80 créneaux temporels pour tous les appareils IoT. Pendant les 80 premiers intervalles de temps en moyenne, les appareils explorent les différents bras pour connaître leurs récompenses. Ensuite, chaque appareil sélectionne le bras qui maximise sa fonction de décision. Étant donné que la technique d'appariement est entièrement coordonnée par la station de base, la convergence vers l'état de satisfaction totale est atteinte dans les tout premiers intervalles de temps. Cependant, RA-NOMA ne peut atteindre un taux de réussite supérieur à 40 % avec une moyenne de 28 %.

Chapitre 4: Configuration de Surfaces Intelligentes et Réfléchissantes pour NOMA

Dans ce chapitre, nous considérons un système de communication non coordonné sur la liaison montante comprenant plusieurs RIS et appliquant le cadre MAB proposé dans le chapitre précédent. Des appareils IoT ayant différents types de trafic transmettent leurs messages à la station de base. Une ou plusieurs RIS sont introduites pour améliorer la qualité des transmissions entre les appareils et la station de base en offrant la possibilité de créer un canal complémentaire. Ce dernier est constitué de deux ensembles de deux liaisons LoS. Le premier ensemble de liens LoS se situe entre les appareils IoT et le(s) RIS et le second ensemble de liens LoS se situe entre le(s) RIS et la station de base. L'approche proposée vise à créer des systèmes NOMA avec une efficacité spectrale et énergétique améliorée en modifiant la configuration des RIS. Cela peut même s'appliquer à des dispositifs ne disposant que d'une seule valeur de puissance d'émission.

Algorithme Proposé

L'objectif principal de cette étude est d'optimiser la sélection des RIS et la configuration de ses éléments réfléchissants de manière à maximiser l'efficacité énergétique du système. Nous recourons à l'algorithme *branch and bound* (BBA) [32] pour la sélection des RIS. À chaque étape de l'algorithme, la configuration d'un ou plusieurs RIS simultanés est effectuée en fonction du nombre de RIS testés. Il convient de noter que les éléments RIS sont configurés de manière à atteindre les valeurs des niveaux de puissance prédéfinis tout en répartissant les dispositifs dans leurs sous-bandes de manière non coordonnée.

Dans notre cas, chaque nœud est défini par l'ensemble des variables binaires δ_i représentant la sélection du RIS (c'est-à-dire l'activation ou la désactivation du RIS) qui définissent un sous-ensemble de la région réalisable. Les nœuds sont classés par ordre croissant du nombre de RIS actives. La première RIS activée est celle qui présente le meilleur gain de canal agrégé moyen sur la liaison appareil-RIS-BS (moyenne de tous les appareils connectés). Ensuite, l'activation de RIS supplémentaires est testée dans chaque nœud suivant jusqu'à ce que l'activation de toutes les RIS ait été testée. Les limites inférieure et supérieure sont alors calculées pour chaque nœud : la limite inférieure est la meilleure solution trouvée pour ses nœuds parents, tandis que la limite supérieure est la meilleure solution possible pour ce nœud sur la base du nouveau système d'équations du nœud exploité. Ensuite, le nœud représentant le choix de RIS avec le plus grand potentiel d'amélioration, c'est-à-dire la plus grande différence entre la borne supérieure et la borne inférieure, est ramifié. Ceci signifie qu'il est divisé en nœuds plus petits, appelés nœuds enfants, qui représentent l'activation de nouvelles RIS en plus de celles du nœud parent. Le cycle est réitéré jusqu'à ce que l'activation de nouveaux RIS n'entraîne plus d'augmentation de l'efficacité énergétique du système.

Exemples de Résultats

Les performances des algorithmes proposés sont comparées à celles de quatre autres solutions :

- un système à accès multiple orthogonal (OMA) comportant des RIS (appelé RIS-OMA), c'est-à-dire qu'un appareil est associé à chaque sous-bande à l'aide d'un niveau de puissance unique,
- un système sans RIS (appelé NOMA-no-RIS) qui s'appuie sur le cadre MAB développé dans [33] tout en considérant uniquement les liens dispositif-BS sans visibilité directe (nLoS),
- un système sans OMA RIS (appelé no-NOMA-no-RIS), dans lequel les appareils transmettent à la station de base en utilisant leur liaison nLoS appareil-BS,
- un système qui utilise NOMA tout en configurant les RIS de manière à maximiser les gains de canal (appelé RIS-NOMA-maxCG), comme dans [34], c'est-à-dire sans tenir compte des contraintes de puissance reçue ou des exigences en matière de débit.

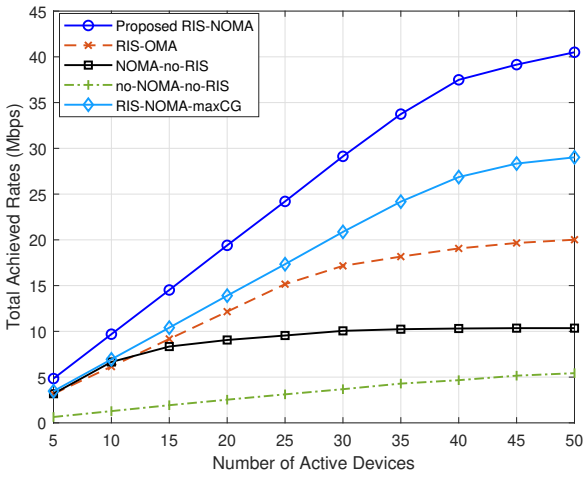

Figure 5: Débit total atteint en fonction du nombre de dispositifs.

La figure 5 présente les performances de la méthode RIS-NOMA proposée et des méthodes concurrentes en termes de somme des débits obtenus pour les dispositifs actifs après convergence. On constate qu'en configurant les RIS, il est possible d'obtenir des gains significatifs en termes de débit total par rapport à toutes les autres méthodes, en particulier lorsqu'un grand nombre d'appareils sont actifs. En fait, l'utilisation de RIS améliore les liaisons agrégées entre les appareils et la station de base, tandis que la méthode NOMA permet de maximiser les débits atteints. Dans le cas d'une configuration NOMA sans RIS, certains appareils n'ont pas accès à des niveaux de puissance reçus élevés en raison de la limitation de leur budget de puissance d'émission et/ou de mauvaises conditions de canal. Les débits atteints sont donc faibles pour ces dispositifs, ce qui pénalise les performances de ce type de système. Dans le cadre de l'OMA,

une largeur de bande plus large serait nécessaire pour obtenir des débits supérieurs, étant donné qu'une sous-bande ne peut accueillir qu'un seul appareil. Pour RIS-NOMA-maxCG, tous les signaux sont reçus avec un gain de canal maximisé. Par conséquent, la puissance de l'interférence NOMA est beaucoup plus importante que pour les autres méthodes, ce qui se traduit par des débits atteints plus faibles.

Chapitre 5: Surfaces Intelligentes Réfléchissantes Aériennes dans les Systèmes d'Accès au Spectre Non-coordonnés en Liaison Montante avec NOMA

Dans ce chapitre, les travaux réalisés se concentrent sur l'étude d'un réseau NOMA en liaison montante assisté par une ARIS, où les liaisons entre les dispositifs IoT et la station de base sont soumises à des phénomènes d'ombrage profond (*deep shadowing*). En fait, les appareils IoT transmettent des données simultanément à la station de base en utilisant le cadre NOMA MAB décrit dans le chapitre précédent avec l'aide de l'ARIS pour améliorer la qualité des liens LoS concaténés grâce à l'exploration/définition de la trajectoire du drone. Le cadre considéré exploite la souplesse d'un partage efficace du spectre entre les dispositifs, en tirant parti de l'effet conjoint de la mobilité du drone, de la modification de l'environnement sans fil fournie par la reconfiguration des RIS et d'algorithmes d'accès multi-utilisateurs distribués efficaces. Les principaux objectifs de ce travail sont d'optimiser la trajectoire de l'ARIS, de déterminer sa position finale optimale, de configurer les éléments RIS en conséquence et de maximiser l'efficacité spectrale du système. Le problème de la maximisation de l'efficacité spectrale est ensuite divisé en deux sous-problèmes. Le premier sous-problème vise à optimiser les trajectoires des ARIS pour qu'ils atteignent leurs destinations finales, tandis que le second sous-problème vise à attribuer les sous-bandes et les niveaux de puissance aux appareils et à configurer l'ARIS en conséquence.

Algorithme Proposé

L'objectif de l'étude est de déterminer la meilleure approche pour résoudre les sous-problèmes discutés précédemment. Lorsque l'ARIS est en mouvement, les gains de canal entre l'ARIS et les appareils ainsi que ceux entre l'ARIS et la station de base varient dans le temps. Par conséquent, les canaux concaténés varient lors de la résolution du problème de la configuration de la RIS. Par conséquent, le choix de la trajectoire de l'ARIS a un impact important sur la configuration RIS. Cependant, nous proposons une stratégie dans laquelle le problème de la définition de la trajectoire de l'ARIS n'est pas affecté par la configuration de la ARIS. En fait, l'identification d'une position adéquate de l'ARIS offre à la configuration des RIS un plus large éventail de solutions potentielles que n'importe quelle autre position. Ainsi, la détermination d'une position adéquate de l'ARIS est cruciale pour établir une configuration RIS efficace. Une position est considérée comme optimale dans une région (optimum local) lorsque le gain moyen du canal à cette position est le plus élevé possible dans cette région. Une fois que l'ARIS est

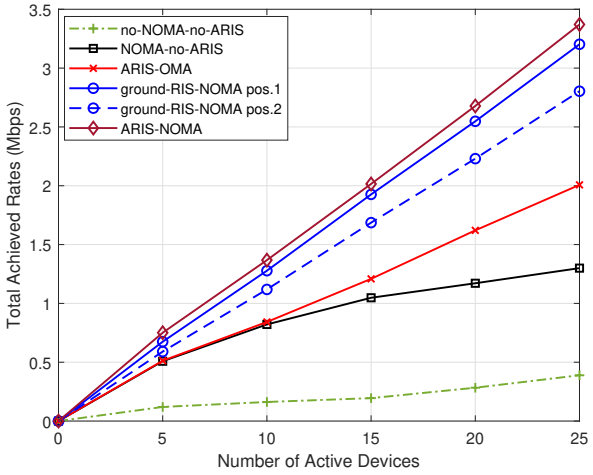

Figure 6: Débit total atteint en fonction du nombre de dispositifs.

placée à une position localement optimale, l'efficacité spectrale réalisable est également maximisé dans cette région. En outre, étant donné que l'ARIS est limité en puissance, une trajectoire de charge doit également être envisagée. Pour résoudre ces sous-problèmes, un algorithme en plusieurs étapes est donc proposé. Il commence par résoudre le problème de l'optimisation de la trajectoire de l'ARIS. Ensuite, les sous-problèmes de l'attribution des niveaux de puissance et de la configuration de l'ARIS sont traités. L'algorithme d'attribution des sous-bandes s'exécute en parallèle et le processus de détermination de la trajectoire de charge est activé lorsque le niveau de la batterie de l'ARIS est faible. Il convient de noter que cette stratégie peut être appliquée dans le cas de plusieurs ARIS qui ne coopèrent pas.

Exemples de Résultats

Les performances des algorithmes proposés sont comparées à celles de quatre stratégies différentes:

- un système OMA qui inclut des ARIS (appelé ARIS-OMA), c'est-à-dire qu'un dispositif est attribué à chaque sous-bande en utilisant un niveau de puissance unique,
- un système NOMA qui n'utilise pas d'ARIS (appelé NOMA-no-ARIS), mais qui s'appuie sur le cadre MAB développé au chapitre 3 tout en considérant uniquement les liens nLoS dispositif-BS,
- un système sans ARIS ni NOMA (appelé no-NOMA-no-ARIS), dans lequel les appareils transmettent à la station de base en utilisant leur liaison nLoS appareil-BS,
- un système qui utilise NOMA tout en configurant une RIS au sol de manière à satisfaire les exigences de qualité de service des appareils (appelé ground-RIS-NOMA), comme au chapitre 4, c'est-à-dire sans aucun avantage lié à la mobilité de l'ARIS. Deux positions différentes de la RIS au sol ont été envisagées pour ce scénario.

La performance de l'ARIS-NOMA proposée en termes de débit total est évaluée sur la figure 6. Celle-ci montre la somme des débits atteints en fonction du nombre de dispositifs actifs après convergence tout en maximisant l'efficacité spectrale du système. En configurant l'ARIS, on obtient des gains significatifs en termes de somme des débits atteints par rapport à toutes les autres méthodes. En fait, l'utilisation d'ARIS, comme l'utilisation de RIS au sol, améliore les liens agrégés entre les dispositifs et la station de base, tandis que la NOMA contribue à maximiser les débits atteints. En outre, les ARIS ont l'avantage d'améliorer encore les gains de canal grâce à leur mobilité, ce qui n'est pas le cas des RIS au sol. En d'autres termes, la performance d'un système avec RIS au sol dépend largement de la position choisie pour sa RIS. L'ARIS pourrait être utilisé dans ce cas soit pour déterminer la meilleure position pour déployer une RIS au sol, soit pour couvrir temporairement une région en cas d'événement rare. Si l'on considère le contexte NOMA-no-ARIS, peu de signaux provenant des dispositifs peuvent atteindre la station de base avec des niveaux de puissance reçus élevés en raison de la limitation de leur budget de puissance et des mauvaises conditions de canal. Il en résulte des taux de réussite médiocres pour ces dispositifs. Dans le cadre de l'OMA, une largeur de bande plus large serait nécessaire pour atteindre des débits plus élevés, étant donné qu'une sous-bande ne peut accueillir qu'un seul appareil.

Conclusions et Perspectives

Dans cette thèse, nous avons abordé plusieurs problèmes complexes d'allocation de ressources pour les futures générations de réseaux sans fil.

Tout d'abord, nous avons relevé le défi de l'optimisation autonome de l'allocation du canal et de la puissance dans un contexte de liaison montante NOMA avec relais FD. La mise en mémoire tampon a été introduite pour permettre la prise en charge d'un type de trafic mixte pour les algorithmes d'allocation adaptative proposés. L'accent a été mis sur la minimisation de l'age de l'information afin de prendre en charge les applications sensibles à la latence. En utilisant le cadre MAB, l'algorithme proposé assigne efficacement différents types de trafic à des combinaisons de sous-bandes et de niveaux de puissance afin de satisfaire les contraintes de débit pour tous les dispositifs tout en donnant la priorité à la réduction de l'age de l'information pour ceux qui ont des contraintes de temps.

Ensuite, nous avons présenté une solution innovante au défi que représente la configuration des RIS dans un système de liaison montante amélioré par la NOMA. Notre approche vise spécifiquement à atteindre des niveaux de puissance reçue prédéfinis, en veillant à ce que tous les dispositifs, qui émettent à une puissance constante, atteignent le débit de données demandé. La caractéristique distinctive de notre système réside dans sa capacité à différencier les signaux en fonction des niveaux de puissance reçus, en ajustant la configuration des éléments réfléchissants passifs RIS. En outre, nous avons proposé un algorithme qui détermine la séquence d'activation des RIS afin d'optimiser l'efficacité énergétique du système. Des analyses comparatives ont révélé la supériorité de la méthode proposée par rapport aux techniques de configuration RIS

antérieures et aux systèmes sans RIS ou utilisant l'OMA.

Enfin, nous avons approfondi les détails de la mise en place du système ARIS dans un environnement de liaison montante NOMA. Notre principal objectif est d'identifier la position ARIS la plus appropriée qui réponde aux exigences de qualité de service tout en adoptant la meilleure trajectoire pour la recharge de la batterie. Un autre objectif de notre approche est de fixer des niveaux de puissance reçus spécifiques et de garantir un débit de données minimum requis pour les dispositifs transmettant à un niveau de puissance unique. En configurant efficacement les réflecteurs passifs de l'ARIS, nous pouvons distinguer les signaux en fonction de leurs niveaux de puissance reçus. Nous avons également introduit un nouvel algorithme pour réduire la largeur de bande utilisée et augmenter les débits atteignables, ce qui, à son tour, augmente l'efficacité spectrale du système. Comparée à d'autres configurations de système, notre approche s'avère supérieure du point de vue du débit, de l'efficacité spectrale ou de l'occupation de la bande passante.

De nombreuses perspectives peuvent être envisagées pour compléter ce travail. En effet, une extension de cette étude consisterait à faire en sorte que l'ARIS serve les appareils en mouvement. Cependant, les contraintes liées à la recherche d'une trajectoire ARIS appropriée qui tienne compte des gains de canal avec les effets Doppler doivent être soigneusement prises en compte. De plus, la généralisation de la solution à des sauts multiples peut être particulièrement intéressante pour les applications IoT dans un scénario d'accès massif. En fait, dans un réseau à sauts multiples, chaque relais peut être considéré comme un nœud avec un débit de données cible plus important et une marge d'erreur variable pour ses messages. Son débit dépend du nombre de messages de l'appareil qu'il doit transmettre. Avec de telles définitions, nous pouvons déjà prévoir des contraintes supplémentaires qui doivent être prises en compte pour ces systèmes. Elles concernent le dimensionnement adéquat de la taille de la mémoire tampon des relais et la minimisation de l'indice d'intégrité agrégé. En effet, ces relais servent maintenant leurs utilisateurs et potentiellement les relais du ou des sauts précédents.

Chapter 1

Introduction

1.1 Motivations

The rapid progress of wireless communication technologies has resulted in the Internet of things (IoT) becoming a game-changing concept in networking. IoT facilitates effortless connectivity and interaction among a wide array of devices, such as sensors, actuators, and even common objects forming a web of connected things. With the forthcoming transition to post-fifth-generation (B5G) communication networks, incorporating IoT into these networks brings forth novel possibilities and challenges at the same time [1,2]. A key challenge for future networks resides in adapting system parameters for the unique characteristics of IoT devices and their deployment. Indeed, such devices are expected to be deployed on a massive scale with demanding communication needs and energy constraints. The deployment constraints call for the use of efficient resource management and allocation strategies designed to guarantee that quality of service (QoS) constraints are met for all active devices while offering the possibility for scalability in terms of network connections. QoS constraints include communications reliability, latency and energy efficiency (EE) [3–5]. When met, such systems can enable application scenarios or use cases across diverse domains/fields. In healthcare, such systems can facilitate remote patient monitoring, real-time health tracking and customized healthcare services. Smart cities can gain from IoT-powered infrastructure, including smart transportation systems, energy management and environmental surveillance. Industrial automation can be transformed by IoT-enabled smart factories, predictive maintenance and supply chain enhancements. The agricultural sector can benefit from IoT in precision farming, crop monitoring and livestock management. However, capitalizing on the IoT potential within B5G networks necessitates recognizing and meeting the specific demands posed by targeted applications. Ultra-reliable and low-latency communications are pivotal for mission-critical IoT applications such as health monitoring and industrial automation. Energy efficiency is crucial for the sustainability of battery-operated IoT devices, facilitating long-lasting and cost-effective deployments. Scalability is also vital to cope with the exponential growth of IoT devices and their integration into B5G networks. Additionally, security and privacy are important to safeguard sensitive data and encourage a wide reach of IoT systems.

In order to meet the demands of the aforementioned applications, existing wireless networks must evolve and adopt innovative technologies. Specifically, the future communication networks are expected to explore solutions to better exploit available spectrum through advanced multiple access methods, through denser cell deployment including relays with self-configurable capabilities, through millimeter wave (mmWave) communications, grant-free communications and communications aided by reconfigurable intelligent surfaces (RIS). The question of how to craft a well-integrated wireless system that brings these new techniques in order to dynamically optimize wireless resource usage and provide necessary QoS requirements has been a key focus in the recent literature.

1.1.1 Radio Access Techniques

Radio access can be split into two categories: grant-based and grant-free access [35, 36]. In grant-based radio access, devices compete over random access channels (RACH) to secure radio resources before transmitting data using the reserved resources. Knowing that most of IoT applications call for short-packet transmissions, using grant-based connectivity in this context results in significant signaling overheads. Furthermore, the potential high number of active IoT devices could lead to increased radio access congestion, causing communication delays and unnecessary energy consumption.

Also, the concept of grant-free communications for short-packet transmissions has been proposed [37, 38]. This approach allows each device to transmit as soon as it has new data, without needing to reserve a radio resource first. Nevertheless, the issue of transmission collisions must be addressed. With careful design, grant-free access methods have the potential to improve system performance by reducing both communication delays and signaling overhead.

1.1.2 Multiple Access Techniques

Upcoming communication network systems will leverage innovative multiple access schemes to boost performance, enhance spectral efficiency, amplify network capacity, and increase the number of served users. One way to achieve these goals is by resorting to non-orthogonal multiple access (NOMA) [39–44]. As its name suggests, the goal of NOMA is to serve multiple users simultaneously on the same resource block. Depending on the considered NOMA category, non-orthogonal multiplexing can be achieved by utilizing either the power domain or the code domain. In fact, by facilitating non-orthogonal user scheduling, NOMA allows for a higher number of served users within the same bandwidth. In addition, NOMA boosts system capacity, fairness, and spectral efficiency.

1.1.3 Relays with Self-Configurable Capabilities

In the third (3G) and fourth-generation (4G) of wireless communication systems, cellular networks relied on macro base stations (MBS) to cover large geographic areas. However, this base station (BS) deployment approach may not yield the best results in terms of capacity

and coverage [45]. Furthermore, to reach cell-edge users, MBSs would need to resort to large amounts of transmit power, thereby increasing inter-cell interference. A viable solution to these challenges is to decrease cell size by deploying half-duplex relays or full-duplex relays [46–49]. These relays reduce the average distance between the users and the serving BS, which allows for improved coverage, capacity, and lower power consumption.

When it comes to allocating resources among distributed relays, there are two primary strategies. The first one involves a central controller that optimizes network resource allocation among the distributed antennas [48, 49]. The second strategy consists of outfitting the distributed relays with self-configurable capabilities [50, 51]. This enables them to optimize their resource usage in a decentralized way and minimizes human intervention which is critical in networks with dense deployments of relays.

1.1.4 Reconfigurable Intelligent Surfaces

The use of RIS has emerged as a promising technique that can bring several advantages to wireless communications [52,53]. Indeed, they enable a significant improvement in signal quality by manipulating the propagation environment, leading to enhanced coverage and capacity. In this way, passive RISs can achieve low system energy consumption since they are limited to reflecting signals, making RIS a viable option for wireless networks. Finally, their ability to be reconfigured to modify propagation conditions allows for great flexibility and adaptability to changing network conditions, ensuring improved performance at all times and leading to self-adaptation for the network.

1.2 Thesis Contributions

This thesis explores means to employ optimization and reinforcement learning (RL) strategies in order to devise efficient resource allocation algorithms for the next generation of wireless cellular networks. The goal is to serve users with variable QoS requirements under uncoordinated multiple access and self-configurable networks. Moreover, the utilization of passive RISs in wireless communication systems is explored. More specifically, the thesis tackles the configuration of the RIS in order to lead to an efficient NOMA system while using devices with a unique transmit power level. In addition to that, the thesis investigates the use of aerial RISs which can be useful when implementing ground RISs becomes physically complicated due to shadowing. In fact, the work delves into determining the trajectory of the aerial RIS with the objective of meeting the QoS requirements. The main contributions of this thesis can be summarized as follows:

- First, we study the subject of uncoordinated spectrum access in wireless communication networks with distributed full-duplex (FD) relays, allowing them to transmit and receive data at the same time. Grant-free communications are studied where the devices schedule their transmissions with no communication or coordination between them, aiming to optimize performance and minimize transmission collisions. To accommodate different IoT use

cases, the system includes a mixture of traffic types, including continuous, sporadic, and periodic transmissions. However, this induces the use of queuing at the relays level in order to reduce data loss and latency which can be measured with the age of information (AoI). A solution is proposed grounded in the multi-armed bandits (MAB) framework, which is related to RL. The key contributions to this problem can be summarized as follows:

  - An algorithm based on the MAB is proposed to allocate the available spectrum and power resources to the devices with multiple traffic types in a way to achieve an efficient uncoordinated uplink NOMA. The algorithm aims to maximize the achieved rates, minimize the transmit power and minimize the AoI.
  - The algorithm aims to achieve stability of the uncoordinated system with the devices having mixed traffic and without overflow-induced data loss.
  - A coordinated allocation technique based on matching theory is introduced to benchmark the performance of the proposed MAB-based algorithm in order to assess its efficiency.

- Second, we extend the uncoordinated spectrum access system with terrestrial RIS. Specifically, the RIS is deployed to create line-of-sight (LoS) links between the active nodes, i.e. the devices and the BS, in order to ensure better radio conditions. The configuration of the RIS under system constraints is then studied in order to achieve an efficient NOMA. The main contributions of this problem can be summarized as follows:

  - An algorithm to configure the reflective elements of the RIS in order to achieve multiple predefined received power levels at the decoding BS through the aggregated channel gains. Indeed, each device transmits using the same transmit power level and the separation of the signals is guaranteed through the configuration of the RIS.
  - An algorithm based on the MAB framework to allocate the available spectrum to the devices in an uncoordinated manner while maximizing their energy efficiency.
  - A method based on the branch and bound algorithm (BBA) in order to identify the minimum subset of RISs to be activated out of a set of available ones, in such a way to maximize the system EE while satisfying the QoS requirements.

- Third, we extend the previous study to an aerial RIS, i.e. carried by an unmanned aerial vehicle (UAV). In fact, aerial RISs are recommended in scenarios where the implementation of the terrestrial RIS is challenging or not feasible (for reasons like difficult terrain or for temporary event-based coverage). The purpose of this work is to find the optimal aerial RIS position while meeting rate requirements of connected devices. Here also, NOMA is used to enhance system performance. The contributions in this third problem can be summarized as follows:

  - An algorithm based on the MAB framework in order to optimize the trajectory and find the optimal position of the aerial RIS while maximizing the achieved rates.

Moreover, the algorithm aims to find strategies for setting the trajectory to follow by the UAV for battery charging.

- An algorithm for NOMA user pairing to maximize the spectral efficiency of the system by maximizing the achieved rates and minimizing the used spectrum.
- The algorithm based on the MAB to allocate the available spectrum to the devices in an uncoordinated manner is maintained.

1.3 List of Publications

This work has led to the following patent filing and publications:

1.3.1 Patent Filing

- **J. Doumit**, C. Abdel Nour, J. Farah and M. -J. Youssef, “System and Method Implementing NOMA Uplink via Reconfigurable Intelligent Surfaces”, filed in October 2023.

1.3.2 Magazine Publication

- **J. Doumit**, M. -J. Youssef, C. Abdel Nour, J. Farah and C. Douillard, "Uncoordinated Spectrum Access for Massive Connectivity in IoT Applications," accepted for publication in the IEEE Internet of Things Magazine.

1.3.3 Journal Publication and Submissions

- **J. Doumit**, M. -J. Youssef, C. Abdel Nour, J. Farah and C. Douillard, "AoI Minimization in Mixed Traffic Full-Duplex Uncoordinated Communication Systems with NOMA," in IEEE Internet of Things Journal, doi: 10.1109/JIOT.2023.3296437.

Two other journal publications, targeting RIS and ARIS augmented networks, are ready for submission and were delayed due to patent filing.

1.3.4 Conference Publication

- **J. Doumit**, M. -J. Youssef, C. Abdel Nour, J. Farah and C. Douillard, "Resource Allocation in Full-Duplex Uncoordinated Communication Systems with NOMA," 2021 IEEE 32nd Annual International Symposium on Personal, Indoor and Mobile Radio Communications (PIMRC), Helsinki, Finland, 2021, pp. 1104-1110, doi: 10.1109/PIMRC50174.2021.9569356.

1.4 Thesis Structure

The rest of the manuscript is organized as follows:

- **Chapter 2** provides a comprehensive review of the topics related to the PhD work. The first section offers an overview of next-generation communication networks. The chapter

then presents the concepts of NOMA and RIS. The remaining part of this chapter is reserved for introducing the analytical frameworks that underpin some of the proposed solutions in this thesis, specifically matching theory and the MAB framework.

- **Chapter 3** presents the proposed resource allocation solutions in coordinated and uncoordinated communication systems with mixed traffic and having NOMA scheduling. The solutions aim at maximizing the achieved rates of the devices and minimizing their transmit power and their AoI.

- **Chapter 4** introduces RISs into uplink communication systems. The goal of this work is to optimize system performance and achieve NOMA scheduling through RIS configuration while solving the spectrum allocation in uncoordinated settings. Also, the number of needed RISs is determined in order to satisfy the QoS requirements of the devices.

- **Chapter 5** explores a communication network using aerial RISs. The goal of this work is to optimize the trajectory of the aerial RISs as well as efficiently allocate the spectrum in order to maximize system spectral efficiency in a distributed system.

- **Chapter 6** wraps up the research conducted and outlined in this thesis and suggests prospects for future studies that may extend and enrich this work.

Chapter 2

Background

In this chapter, we lay the grounds for the key concepts that are essential to the research conducted in the thesis. The initial part of the chapter provides a brief background on IoT support for future-generation cellular networks with an emphasis on the innovative multiple access methods, specifically NOMA. Additionally, we highlight the use of RIS in wireless communication systems discussing the potential advantages and challenges related to incorporating RIS and aerial RIS into the wireless systems. The last part of the chapter presents the foundations of the analytical techniques that are used for the proposed solutions, such as RL and more specifically the MAB framework and matching theory.

2.1 Future-Generation Cellular Networks

The development of wireless systems has largely been driven by the demand for higher data rates and massive connectivity. However, the advent of innovative IoT applications has made the requirements for 5G and B5G networks increasingly diverse as shown in Figure 2.1. Hence, future communication networks are expected to support enhanced mobile broadband (eMBB) services, massive machine-type communications (mMTC), and ultra-reliable low-latency communications (URLLC). The key elements of B5G can be summarized as follows:

- **Higher data rates and improved coverage:** Future networks should provide an area capacity that is extremely higher than what 4G and 5G mobile networks offer.
- **High reliability:** The packet error rate (PER) should typically be lower than 10^{-6}.
- **Low latency:** Some applications with extremely low latency requirements will demand a round-trip air latency of less than 1 millisecond.
- **Support for machine-type devices:** Future networks should be capable of supporting devices like autonomous vehicles, virtual reality headsets, and connected sensors.
- **Energy efficiency:** Communications for energy-constrained IoT devices (like sensors) need to be designed to extend the device's lifespan. Moreover, future communication systems should increase system capacity while keeping the energy consumption at the

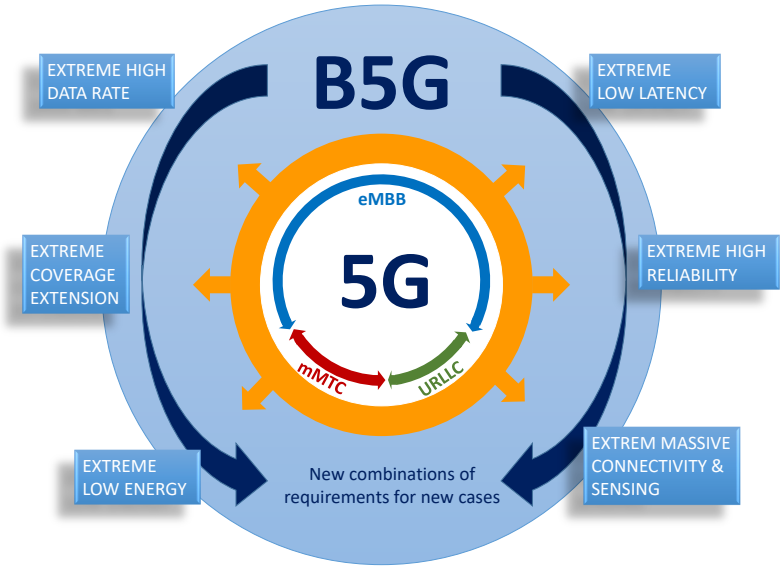

Figure 2.1: 5G and B5G use cases and requirements

active nodes as low as possible, in line with green communications principles. They are also expected to limit the use of active nodes by using passive ones such as RIS.

In order to meet these diverse requirements, significant research has been invested into exploring new techniques and network architectures that could keep up with the rapid advancements in wireless systems. Some key strategies include:

- **Dense deployment of FD relays:** Future communication networks are expected to feature a dense deployment of FD relays. This approach will enhance area capacity and coverage as well as reduce overall power consumption.
- **Utilization of RIS:** There has been a growing interest in the use of RIS within cellular networks. The key advantage lies in the ability to enhance channel conditions between active nodes and hence increase the total capacity.
- **Efficient use of the available spectrum:** To increase spectrum efficiency, data rates, and the number of served users, it is necessary to leverage novel multiple access techniques like NOMA.

In the following, we provide an overview of NOMA, a promising multiple access technique for future communication networks.

2.2 Non-Orthogonal Multiple Access

The fundamental principles of NOMA are introduced in this section. NOMA is a multi-access technique that allows multiple users to be served simultaneously on the same orthogonal time/frequency resource. Several types of NOMA have been studied in the literature including:

- power-domain NOMA (PD-NOMA) [54–57],

- sparse code multiple access (SCMA) [58],
- pattern division multiple access (PDMA) [59],
- interleave division multiple access (IDMA) [60].

This thesis focuses on PD-NOMA denoted by NOMA in the rest of the manuscript for brevity.

The basic principle of NOMA involves using the power domain to serve multiple users non-orthogonally on the same time-frequency resource block. At the transmitter side, NOMA relies on superposition coding (SC) [6]. Consequently, at the receiver side, inter-user interference has to be managed, typically by applying successive interference cancellation (SIC) [7]. Figure 2.2 illustrates an example of NOMA pairing of devices/users on the subbands.

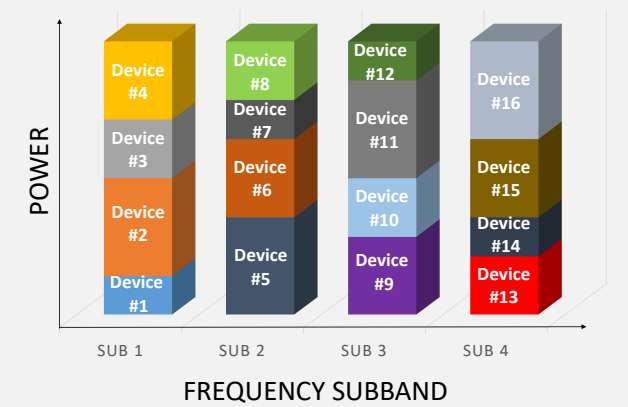

Figure 2.2: NOMA pairing of users/devices on subbands

2.2.1 Basics of Uplink NOMA

In uplink communication systems, power control and frequency allocation should be agreed upon by the users/devices prior to any NOMA transmission. This can be classically coordinated through control signals from the BS. Once agreed upon, each user/device can transmit its message with the target power level on the allocated frequency. Hence, the BS receives a combined signal that consists of the overlapping transmissions from all active users.

In order to decode individual user messages from the combined signal, the BS usually resorts to SIC. The corresponding procedure begins by decoding the message of the user with the highest channel gain while treating the signals from the other users as interference. The decoded signal of the user with the highest channel gain is then re-encoded and subtracted from the total received signal, thereby reducing the interference for decoding the remaining user signals. The signal of the user with the lowest channel gain is decoded last regardless of interference from other users.

Consider K as the total number of users and C as the total number of subbands within the system. B_c denotes the bandwidth for each subband c. Furthermore, suppose that $\mathcal{K}_c$ denotes the set of users scheduled on subband c, where $k_c(n)$ is the n-th user scheduled over subband c and $|\mathcal{K}_c| = K_c$ represents the total number of users on that subband.

Assuming successful SIC decoding in the decreasing order of channel gains, the maximum achievable rate for user $k_c(n)$ on subband c is given by the Shannon formula:

$$R_{k_c(n),c} = B_c \log_2\left(1 + \frac{P_{k_c(n),c} h^2_{k_c(n),c}}{\sum_{j=n+1}^{K_c} P_{k_c(j),c} h^2_{k_c(j),c} + \sigma^2}\right), \tag{2.1}$$

where $P_{k_c(.)}$ its transmit power on subband c and $h_{k_c(.),c}$ the channel gain on subband c between user $k_c(.)$ and the BS. σ^2 is the variance of the additive white Gaussian noise (AWGN). For simplicity's sake, in the rest of this document, we'll refer to the "maximum achievable rate" as the "achieved rate".

For example, consider a scenario where two users $k_c(1)$ and $k_c(2)$ are scheduled on subband c as shown in Fig. (2.3a). If $k_c(1)$ has the higher channel gain, the achieved rates in the uplink NOMA system can be expressed as follows:

$$\begin{aligned} R_{k_c(1),c} &= B_c \log_2\left(1 + \frac{P_{k_c(1)} h^2_{k_c(1),c}}{P_{k_c(2)} h^2_{k_c(2),c} + \sigma^2}\right), \\ R_{k_c(2),c} &= B_c \log_2\left(1 + \frac{P_{k_c(2)} h^2_{k_c(2),c}}{\sigma^2}\right). \end{aligned} \tag{2.2}$$

For successful SIC decoding at the BS level in uplink NOMA with two scheduled users on subband c, the following condition needs to be met:

$$P_{k_c(1),c} h^2_{k_c(1),c} > P_{k_c(2),c} h^2_{k_c(2),c}. \tag{2.3}$$

While most of the research on NOMA is concentrated on a downlink setting, some work has explored its use in uplink scenarios. One study used the Karush-Kuhn-Tucker (KKT) conditions to derive power allocation factors for maximizing sum throughput [61]. Another proposed an algorithm for subband and power allocation to maximize system throughput [62]. However, these studies commonly assume that subband assignment and power allocation are conducted in a centralized manner with the BS efficiently distributing power and users across multiple channels based on full channel state information (CSI). As a result, these studies cannot be directly suited for uncoordinated spectrum access.

In contrast, a different work proposed a power allocation algorithm for random access using NOMA where the BS does not coordinate uplink transmissions [63]. It suggested that if all users have a target signal-to-interference-plus-noise ratio (SINR) requirement Γ, a set of predefined received power levels can be established, allowing up to L users to simultaneously access each subband. This paper demonstrated that if the L users coordinate their transmissions in such a way that each user chooses a unique received power level, all L users achieve the same SINR requirement Γ with respect to the formula:

$$v_l = \sigma^2 \Gamma \left(\Gamma + 1\right)^{L-l}. \tag{2.4}$$

The transmit power value for user k who selects power level v_l on subband c can be calculated as follows:

$$P_{k,c,l} = \frac{v_l}{h_{k,c}^2}. \tag{2.5}$$

However, this power allocation scheme does not accommodate distinct SINR requirements while supporting multiple collisions on lower levels.

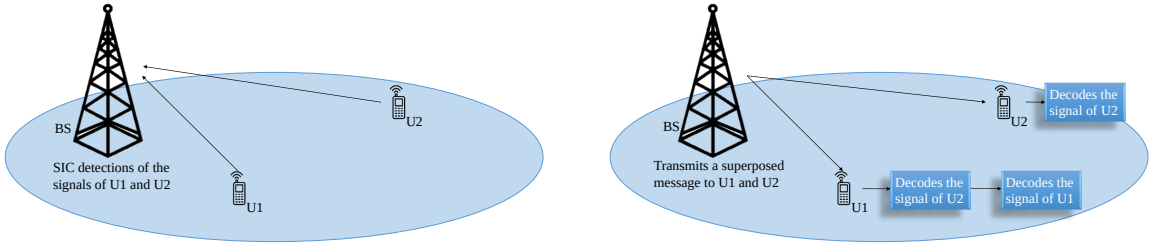

(a) Uplink NOMA (b) Downlink NOMA

Figure 2.3: SIC decoding

2.2.2 Basics of Downlink NOMA

In a downlink scenario, the BS employs SC to send a combined signal of all the messages destined to the scheduled users. At the receiving end, when possible, each user applies SIC to retrieve other users' signals before decoding its individual message.

In this context, if $x_{k,c}$ represents the modulated signal for user k on subband c, then the signal x_c transmitted by the BS over the subband c is essentially the superimposed signal of all users in $\mathcal{K}_c$. This superposed signal can be mathematically represented as follows:

$$x_c = \sum_{k \in \mathcal{K}_c} x_{k_c}. \tag{2.6}$$

The signal received by user k is represented by:

$$y_{k,c} = h_{k,c} x_c + w_{k,c}, \tag{2.7}$$

where $w_{k,c}$ represents the noise experienced by user k on subband c.

The users in $\mathcal{K}_c$ are arranged in decreasing order of channel gain. Signal separation at the receiver side is done using SIC decoding in the increasing order of channel gains. The user with the lowest channel gain does not perform SIC and decodes its message directly, treating signals from all other users as noise. Each one of the remaining users decodes the signals of users with lower channel gains before decoding its own.

Assuming successful SIC decoding and no error propagation at the receiver side, the rate

achieved by user $k_c(n)$ on subband c is given by:

$$R_{k_c(n),c} = B_c \log_2 \left(1 + \frac{P_{k_c(n),c} h^2_{k_c(n),c}}{\sum_{j=1}^{n-1} P_{k_c(j),c} h^2_{k_c(j),c} + \sigma^2} \right). \tag{2.8}$$

Note that the user with the lower channel gain, also called the weak user with respect to the others, suffers from co-channel interference. Considering the case of two users assigned to subband c, in order to ensure SIC stability, the power allocated to the weak user must be larger than that allocated to the strong user, as shown in the constraint [64]:

$$P_{k_c(2),c} > P_{k_c(1),c}, \forall c \in C, \tag{2.9}$$

with (2) being the weak user and (1) the strong user.

The choice of users multiplexed over a subband and the amount of power allocated to each user significantly affect system performance. Therefore, in order to maximize NOMA system performance, the allocation of frequency resources, scheduling, user pairing, and power allocation must all be carefully considered and designed.

The current manuscript only deals with uplink NOMA. Therefore, our proposals in this context will be detailed in the upcoming chapters.

2.3 Reconfigurable Intelligent Surfaces

RIS, also known as intelligent reflecting surface (IRS) or metasurface, is a two-dimensional structure primarily composed of a large array of programmable scattering particles or meta-atoms. By adjusting their electrical properties dynamically, these meta-atoms can control the propagation characteristics of electromagnetic waves in terms of amplitude and phase. When integrated carefully, RIS can improve the performance of wireless communications in real-time [8, 9] through modifying the propagation conditions.

2.3.1 Fundamentals and Construction of Reconfigurable Intelligent Surfaces

Understanding the functionality of a RIS goes through understanding its core components and the principles guiding its construction [65, 66]. At the heart of the RIS are meta-atoms, artificially constructed materials designed to exhibit desired electromagnetic properties. These are typically made from various materials such as metal, dielectric, or semiconductor and can take various shapes and sizes. Indeed, positive intrinsic negative (PIN) diodes and varactors are fundamental components in the design of meta-atoms:

- **PIN diodes** function as switching elements within the meta-atoms. Moreover, they allow high-frequency operation and rapid switching times. This ability to toggle each meta-atom between different states enables effective control over the overall electromagnetic response of the surface.

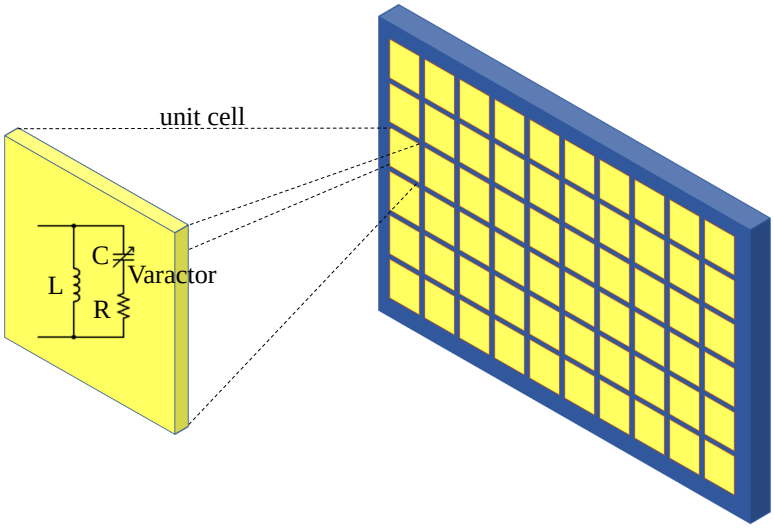

Figure 2.4: Schematic diagram of the varactor RIS

- **Varactors** provide dynamic adjustments to the resonant frequency of each meta-atom (Figure 2.4). By varying the reverse bias voltage across a varactor, the capacitance and resonant frequency of the meta-atom can be controlled, enabling dynamic control of the phase shifts of the electromagnetic waves interacting with the surface.

The configuration of these meta-atoms into a two-dimensional array forms the RIS. The specific layout of this array, including the distance between meta-atoms and their alignment, significantly influences the RIS's electromagnetic properties. A network interface card facilitates the interface between the RIS and a controlling computer, providing the necessary control signals to adjust the properties of the meta-atoms. The ability to actively shape and steer electromagnetic waves in a desirable direction makes up the *intelligence* of such devices.

2.3.2 Advantages and Applications

RIS can significantly enhance the efficiency of a wireless communication by optimizing the propagation of electromagnetic waves. This results in improved signal quality, reduced multi-path fading and lower energy consumption. By adjusting the phase of the meta-elements, RIS can focus electromagnetic energy towards specific directions, maximizing signal strength at desired locations while minimizing it at others. This beamforming capability allows for increased transmission range and reduced interference, enhancing overall network performance, especially for large deployments. Moreover, RIS can be integrated into existing wireless infrastructure with relative ease, providing a cost-effective solution for improving network performance without requiring extensive hardware upgrades. Its low power consumption, coupled with its passive nature, where it does not emit signals but only manipulates those incident on it, makes it a *green* solution aligned with sustainable development goals.

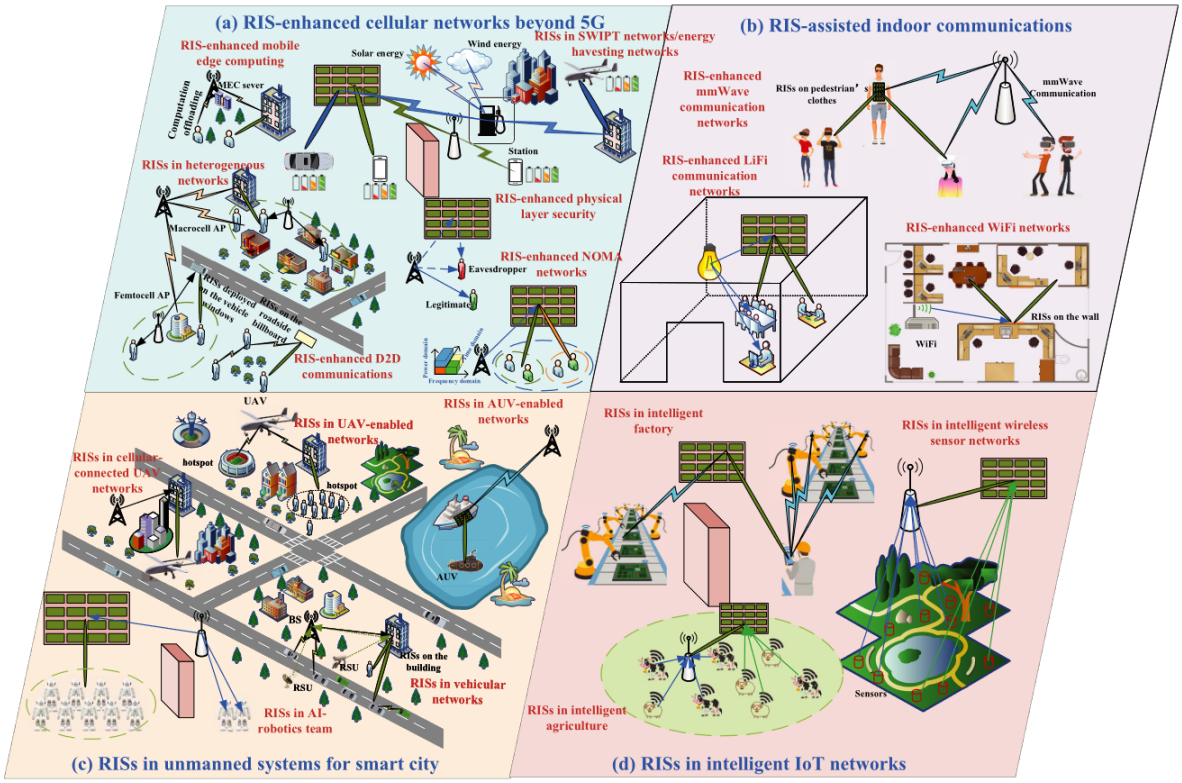

Figure 2.5: RIS applications in wireless communication networks from [66] ©[2021] IEEE.

The applications of RIS are vast and still being explored. In the domain of 5G and beyond, RIS can play a vital role in addressing challenges related to high-frequency millimeter-wave propagation such as path loss and signal attenuation. By intelligently manipulating the signal's propagation characteristics, RIS can ensure reliable and high-speed connectivity. The introduction of RIS is also gaining attention in the IoT domain. With its ability to enhance signal quality and transmission range, RIS can help build robust IoT networks. Other applications include wireless power transfer where RIS can focus energy towards specific receivers, and physical layer security where RIS can direct signals away from potential eavesdroppers. Figure 2.5 illustrates some of the applications of RISs in wireless communication networks.

2.3.3 Challenges in Wireless Communication Systems

While the use of RIS promises a significant transformation in the field of wireless communications, it is crucial to acknowledge that the pathway to its implementation is riddled with numerous challenges. These obstacles cover various dimensions of this technology, including hardware complexity, channel models, and security issues. While the concept of RIS has presented researchers and technologists with a promising potential, the successful incorporation of RIS into real-world wireless communication systems hinges on overcoming these challenges.

2.3.3.1 Hardware and Implementation Challenges

The physical realization of RIS poses significant challenges, primarily due to the hardware complexities and the associated costs. First and foremost, designing a RIS requires the precise arrangement of numerous meta-atoms that should be individually controllable. This requires complicated circuit designs and manufacturing complexity can be high. Moreover, achieving optimal performance mandates that each meta-atom is accurately calibrated, which is a complex process considering the large number of meta-atoms in an RIS. Furthermore, the development of RIS technology demands durable, reliable, and cost-effective components. The varactors and PIN diodes, essential for the functionality of RIS, should be able to operate at high frequencies and handle significant amounts of electromagnetic power. These requirements pose substantial challenges to the material science and electronics fields to develop components that can fulfill these requirements while maintaining economical feasibility.

2.3.3.2 Channel Models

The integration of RIS introduces some complexities into the communication channels of wireless systems. The propagation environment becomes dynamic due to the adaptive nature of RIS, i.e. the different configurations of the RIS elements, leading to significant variations in the CSI. Selecting and maintaining accurate CSI in real-time becomes a substantial challenge. Furthermore, the multi-path propagation caused by RIS considerably complicates channel modeling. Traditional modeling methods often fall short of accurately capturing these complexities, demanding novel modeling techniques to ensure efficient communication. Additionally, the existence of multiple RISs in a single environment may result in overlapping coverage and inter-RIS interference. These issues necessitate sophisticated interference management strategies to guarantee optimal communication performance.

2.3.3.3 Security

RIS-aided wireless systems can also present unique security challenges. As RISs can direct signals away from potential eavesdroppers, they can also potentially be exploited to direct signals towards them. Robust security measures need to be implemented to prevent this and ensure that the use of RIS does not introduce new vulnerabilities into the wireless system.

2.4 Aerial Reconfigurable Intelligent Surfaces

Aerial reconfigurable intelligent surfaces (ARIS) have emerged as a groundbreaking concept in the domain of wireless communications (Figure 2.6) [10]. Deployed in an airborne state, these programmable surfaces alter the characteristics of incident electromagnetic waves, paving the way for a new era in communication landscapes. As ground RIS described in the previous section, the ARIS controls the propagation of electromagnetic waves to create an optimal wireless environment via LoS links [11]. However, the ARIS advantages and challenges may differ from those of ground RIS.

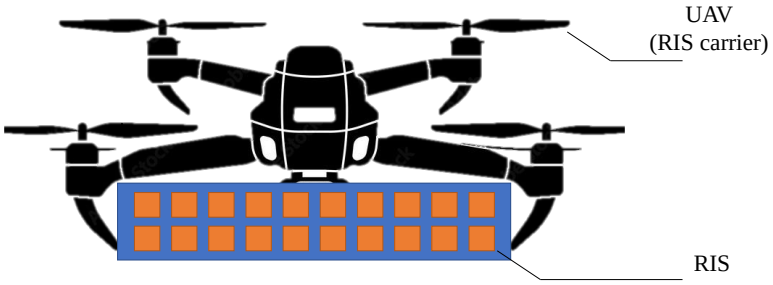

Figure 2.6: Aerial reconfigurable intelligent surfaces (ARIS)

2.4.1 Advantages of Aerial RIS

The advantages of ARIS compared with terrestrial communication system can be summarized as follows:

- **Unprecedented Coverage:** Being deployed aerially, ARISs significantly boost signal coverage. They can provide connectivity to distant and/or difficult-to-reach areas, overcoming obstacles that are challenging in ground-based systems. This ability to extend the reach of wireless services is a considerable advantage of aerial RIS.
- **Dynamic Adaptability:** The ARISs offer the flexibility of movement. They can be repositioned based on changing communication needs, offering dynamic adaptability to variations in user distribution or density, thereby optimally shaping the wireless environment.
- **Superior Signal Quality:** ARISs have the power to mitigate the adversities of wireless communication, such as multipath fading and shadowing effects, which often degrade signal quality. By creating favorable propagation conditions, they ensure improved signal quality and reliability.

2.4.2 Challenges of Aerial RIS

- **System Integration:** Integrating ARIS with host platforms such as UAVs, drones, or blimps can be a challenging task. The process must ensure seamless operation of the RIS without compromising the flight performance of the host platform.
- **Energy Efficiency:** The reconfiguration and operation of ARIS can be energy-intensive. This can be attributed to the energy required for the drone to effectively position and transport the RIS, thereby contributing significantly to the overall energy burden of the

system. Ensuring energy efficiency while meeting the operational demands of RIS is a significant challenge that researchers need to address.

- **Stability and Resilience:** The stability of the ARIS is crucial given the impact of weather variations and flight maneuvers. Maintaining performance under such conditions is a critical consideration. Hence, the ARIS are used to either establish a fixed location for a ground RIS if possible or for temporarily serving the users/devices during an event scenario.

2.5 Multi-Armed Bandits

RL is a methodological structure in which one or more learning agents engage with an environment to achieve a specific goal [67]. This goal usually involves the maximization of a numerical reward. Given the interactions with an environment, the central aspect of RL is to learn how to select the most beneficial actions to accomplish the learning agent's goal. The RL process is illustrated in Figure 2.7. Following this process and after surveying the environmental state, the learning agent decides on an action based on its established policy or strategy. The environment, in turn, responds to this selected action by altering its state according to a probability distribution, which is influenced by the action taken by the agent. Additionally, the environment generates a numerical reward, which is then relayed back to the learning agent. Upon witnessing the new state and receiving the reward, the agent picks a new action. However, the agent is not pre-informed about which actions will yield the most significant reward, so it needs to figure out which actions are optimal through trial and error. The primary aim of the agent in RL is to maximize the perceived total reward over time. Since the agent does not know in advance which actions will produce the highest rewards, a strategy should be devised for the selection of the actions to be taken. Indeed, to enhance the received reward, the learning agent needs to lean more towards actions proven to be effective in the past. However, in order to discover such actions, the agent has to attempt actions that have not been chosen previously. This means the learning agent must both exploit actions that have been tested before and have produced satisfactory rewards and explore actions that are new or rarely chosen to make more informed choices in the future and increase its long-term reward. Consequently, the strategy employed by the learning agent for action selection must be carefully balanced between exploration and exploitation, which represents the main challenge for the application of RL.

The MAB framework [12] is a particular case of RL that corresponds to a single state scenario. In this context, the agent's goal is to discover the action that provides the maximum reward in a single-state environment. The MAB problem has been thoroughly explored in the literature. Recently, the multi-player multi-armed bandits (MP-MAB) framework, which involves multiple learning agents striving to discover actions yielding the highest reward, has been drawing significant attention in the wireless communication research community. It has been applied to solve multiple problems, including:

- opportunistic spectrum access in cognitive radio networks [16–19],

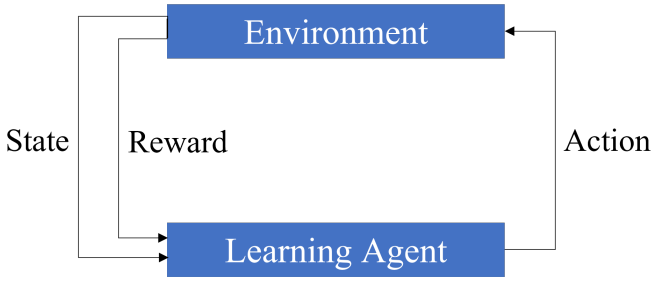

Figure 2.7: Reinforcement learning process

- uncoordinated spectrum access [20, 21],
- trajectory optimization in UAV-enabled cellular networks [22],
- beam alignment in millimeter wave communications [68].

There are two primary frameworks for the MAB problem, and these depend on the reward feedback model: stochastic MAB, where the reward of an arm is derived from an unknown probability distribution and assumed to be independent and identically distributed (i.i.d.) variables and adversarial MAB, more general problem where the reward of the arm is determined by an adversary and does not necessarily adhere to a probability distribution. Both MP-MAB frameworks include:

- a set of K players, $\mathcal{K} = \{1, ..., K\}$,
- a set of M arms, $\mathcal{M} = \{1, ..., M\}$,
- the mean achieved reward $\mu(k, m)$ when a player $k \in \mathcal{K}$ is pulling an arm $m \in \mathcal{M}$,
- the unknown probability distribution of an arm m with respect to a player k, $v(k, m)$,
- the set of actions for a player k, $\mathcal{A}_k$,
- the set of actions for all players, $\mathcal{A} = \prod_{k \in \mathcal{K}} \mathcal{A}_k$,
- the action $a_k^{(t)}$ played by a player k at a timeslot t, where $a_k^{(t)}(m) \in \{0, 1\}^{1 \times M}$ represents the non-selection or selection of the arm m by the player k respectively,
- the strategy profile of all players at timeslot t, $a^{(t)} = \{a_1^{(t)}, a_2^{(t)}, ..., a_K^{(t)}\}$,
- the collision indicator under $a^{(t)}$, $\eta_m(a^{(t)})$ which is equal to 0 in the case of multiple players pulling the same arm m simultaneously and 1 otherwise.

The players do not know beforehand the average reward associated with each arm. When player k chooses an arm m, k receives a reward for playing arm m. In most prior work on MP-MAB in wireless systems, the assumption is that if two or more players select the same channel, they will all receive a zero reward. Therefore, the problem in an MP-MAB context is determining

how the players should choose arms to maximize their collective rewards. Here, learning agents also encounter the balance between exploration and exploitation.

Indeed, if the players primarily exploit arms that have proven effective in the past, they will not gather information about other arms that may potentially provide superior rewards. As a result, the players could become trapped in a local optimum. Conversely, if the players consistently choose to explore new arms, they will acquire information about all arms. However, they will not maximize their collective rewards since they are not taking advantage of the arms that offer the highest average rewards. Therefore, the players' strategies must achieve a balance between exploration and exploitation.

To assess the effectiveness of the strategy pursued by the learning agent, the concept of accumulated regret is introduced. Generally, the accumulated regret is measured as the difference between the total reward that would be gained by consistently playing the optimal arm at each time instance, and the actual reward received by the player. The goal of the learning player's strategy is to adapt and refine its approach in a manner that minimizes its accumulated regret.

Within the MP-MAB framework, a common assumption is that the number of arms M is greater than or equal to the number of players K. Consequently, in this case, an optimal distribution of the arms among the users, without any collision, is feasible. Let's denote the optimal arm selection for all players as a^* as follows:

$$a^* = \underset{a \in \mathcal{A}}{\operatorname{argmax}} \sum_{k \in \mathcal{K}} \sum_{m \in \mathcal{M}} a_k(m)\mu(k,m)\eta_m(a). \tag{2.10}$$

In the MP-MAB framework, the accumulated regret over a time horizon T is described by [12] as:

$$R = T \sum_{k \in \mathcal{K}} \sum_{m \in \mathcal{M}} a_k^*(m)\mu(k,m) - \mathbb{E}\left[\sum_{t=1}^{T} \sum_{k \in \mathcal{K}} \sum_{m \in \mathcal{M}} a_k^{(t)}(m)\mu(k,m)\eta_m(a^{(t)})\right]. \tag{2.11}$$

The challenge within the MP-MAB framework is to develop a strategy for all players that minimizes the regret provided by (2.11). There are several proposed strategies for the MAB problem in the literature, including the upper confidence bound (UCB) [13], Thompson Sampling [14], and ϵ-greedy strategies [15]. The UCB algorithm achieves faster convergence compared to other strategies. Hence, in the following section, we briefly discuss the UCB algorithm as it is used in the next chapters for the trade-off between the exploration and exploitation phases.

UCB Algorithm

The UCB algorithm operates on the principle of "optimism in the face of uncertainty" [12]. This principle employs the observed rewards so far to provide each arm with an upper confidence bound. In fact, this serves as an overestimation of the unknown arm's mean reward with a high probability. At time t, let $N_{k,m}^{(t-1)}$ be the number of observations learning agent k has of arm m. Additionally, let $\hat{\mu}(k,m)$ represent the estimated mean of arm m by player k. The UCB index

attributed by player k to arm m, $UCB^{(t)}(k,m)$, is given by:

$$UCB^{(t)}(k,m) = \begin{cases} \infty, & \text{if } N_{k,m}^{(t-1)} = 0, \\ \hat{\mu}(k,m) + \sqrt{\frac{\phi \log(t)}{N_{k,m}^{(t-1)}}}, & \text{otherwise.} \end{cases} \tag{2.12}$$

In (2.12), ϕ represents a parameter providing the trade-off between the exploration and the exploitation phases. Then, every learning agent follows Algorithm 1 to determine its action at timeslot t. The index of each arm m for each player k, $UCB^{(t)}(k,m)$, is the summation of

Algorithm 1: UCB Algorithm

```
Input: φ, M.
for t=1:T do
    Choose the arm having m_k^* = argmax_{m∈M} UCB^(t)(k,m).
    Observe the achieved reward and update the decision value of the confidence bound
     m_k^*.
end
```

the empirical average of rewards previously encountered on m and an exploration bonus, often referred to as the confidence width. According to Eq. (2.12), a learning agent k is more likely to explore an arm m if m appears promising due to a high estimated mean $\hat{\mu}(k,m)$ or if it has not been well explored, in other words if $N_{k,m}^{(t-1)}$ is small. As time passes, the learning agent tends to exploit arms that have high estimated means. Therefore, the UCB algorithm efficiently balances between exploration and exploitation.

2.6 Matching Theory

In this paragraph, we will cover the basics of matching theory [23], a robust mathematical tool that was used for solving the resource allocation challenge outlined in Chapter 3. Matching theory, rooted in the field of economics, provides a framework for forming mutually advantageous relationships and is especially useful when dealing with assignment dilemmas similar to the ones faced by a centralized MBS. A few studies have suggested algorithms rooted in the matching theory framework to address resource allocation problems [24–28]. We will now define some critical elements and terms of a matching problem in the context of wireless resource allocation:

- **Two separate sets of players:** You can picture a matching problem Ψ as a bipartite graph, where the resources and users, termed as players in game theory, form two separate sets. The matching problem Ψ involves assigning resources from one set ($r \in \mathcal{R}$) to the players of the other set ($k \in \mathcal{K}$). Let $\Psi(k) \in \mathcal{R}$ represent the resources allocated to user k and $\Psi(r) \in \mathcal{K}$ be the users assigned to resource r. In wireless communication networks, examples of resources can be the timeslots, frequency channels, and serving antennas.

- **Quota:** The quota for each player p defines the maximum number of players from the other set with which it can be matched. Assume q_k and q_r are the quotas for user k and

resource r respectively. A matching outcome Ψ must ensure: $|\Psi(k)| \leq q_k$ and $|\Psi(r)| \leq q_r$.

- **Utility function:** Each player assigns a utility function to the players from the other set. This utility function is the objective function of user k. By maximizing its utility, each user aims to maximize its objective function.

- **Preference relation and strategy:** A player uses a preference relation $\succeq$ to rank players from the other set based on a metric they aim to maximize. This ranking forms the player's strategy. Player p quantifies the preference relation by assigning a utility U to each player from the other set. Let $\succeq_k$ and $U_K(k,r)$ represent the preference relation of user k and the utility assigned by user k to resource r respectively. If $U_K(k,r_1) \geq U_K(k,r_2)$, it means that user k prefers resource r_1 over resource r_2, i.e. $r_1 \succeq_k r_2$. Also, let $\succeq_r$ and $U_R(r,k)$ signify the preference relation of resource r and the utility assigned by resource r to user k respectively. If $U_R(r,k_1) \geq U_R(r,k_2)$, it means resource r prefers user k_1 over user k_2, i.e. $k_1 \succeq_r k_2$.

- **Solution of the matching problem:** The solution is a function $\Psi : \mathcal{K} \longrightarrow \mathcal{R}$ that satisfies specific criteria, ensuring that each user k and each resource r are matched together under certain conditions. The criteria include conditions for mutual inclusivity, i.e. $r \in \Psi(k) \iff k \in \Psi(r)$ and a quota limitation, i.e. $|\Psi(k)| \leq q_k$, $\forall k \in \mathcal{K}$ and $|\Psi(r)| \leq q_r$, $\forall r \in \mathcal{R}$.

- **Two-sided stable matching:** This refers to a matching where there is no pair that could benefit from deviating from the current match. If such a pair exists, they form a blocking pair which would make the matching unstable.

Depending on the quota of the players, matching problems can be classified as one-to-one, many-to-one, or many-to-many:

1. **One-to-one matching:** This occurs when each user is matched with exactly one resource and each resource is matched with exactly one user ($q_k = q_r = 1, \forall k \in \mathcal{K}, \forall r \in \mathcal{R}$).

2. **Many-to-one matching:** This happens when each user is matched with exactly one resource, but a resource can be matched with more than one user or vice versa, i.e. $q_k = 1, \forall k \in \mathcal{K}$ and $q_r > 1, \forall r \in \mathcal{R}$ or $q_k > 1, \forall k \in \mathcal{K}$ and $q_r = 1, \forall r \in \mathcal{R}$.

3. **Many-to-many matching:** This situation arises when a user can be matched with multiple resources and a resource can be matched with multiple users, i.e. $q_k > 1$ and $q_r > 1, \forall k \in \mathcal{K}, \forall r \in \mathcal{R}$.

Wireless communication-centric classifications of matching problems, as presented in [69], include:

- **Canonical matching:** This encompasses standard matching problems where the preferences of the players do not change during the resource allocation process, like allocation of orthogonal frequency bands.

- **Matching with externalities** This involves scenarios where player preferences are interdependent, causing changes in preferences and strategies during resource allocation. This is seen in non-orthogonal frequency bands allocation, cell association, and load balancing.
- **Matching with dynamics:** This third class encompasses matching problems where current strategies of the players depend on past resource allocations. This can occur in resource allocation problems under changing environment conditions.

2.7 Conclusion

This thesis focuses on how we can leverage new resource allocation strategies to meet the needs of emerging applications in future wireless communication networks. Specifically, these strategies include new radio access techniques like NOMA, introducing full-duplex relays with self-organizing capabilities and using RIS and aerial RIS. In particular,

- The MP-MAB framework is used to address the issues of uncoordinated spectrum access and power control in wireless communication networks with NOMA in Chapters 3, 4 and 5.
- The matching theory is used to address the issues for the coordinated spectrum access and power control in wireless communication networks with relays in Chapter 3.
- RIS-aided networks and ARIS-aided networks with NOMA are investigated in chapter 4 and 5 respectively.
- The MAB framework is used to optimize the ARIS trajectory while considering an uncoordinated spectrum access in Chapter 5.

Chapter 3

Resource Allocation for Mixed Traffic Types in Communication Systems with Full-Duplex Relays

3.1 Introduction

IoT has become a major driving use case in the evolution of wireless communication networks. In fact, IoT devices are expected to make up most of the mobile traffic exchanged in 5G and B5G networks. They are being deployed to enable different applications spanning various sectors such as e-health, smart agriculture and autonomous cars. With the large diversity of target IoT applications, the characteristics and requirements of the generated mobile traffic are becoming increasingly heterogeneous. Indeed, depending on the application, the traffic can be continuous, periodic or sporadic. In addition, with massive device deployment scenarios, the number of transmitted IoT packets may suffer from unacceptable latency. Therefore, the network should adopt topologies and resource allocation strategies designed to meet the low-latency and low-complexity requirements of target applications and pave the way for scalable and self-configurable massive IoT systems [70,71]. These constraints necessitate the design of appropriate novel frameworks to optimize the performance of modern wireless communication systems, since classical centralized optimization techniques fail to address the scalability requirement and the continuous evolution of IoT networks.

To enhance the capacity of the system, NOMA has been introduced as a promising multiple access technique to accommodate a larger number of devices as discussed in Chapter 2. Specifically, PD-NOMA consists of scheduling multiple users on the same resource block by multiplexing them in the power domain [33,72–74]. Therefore, NOMA can achieve a higher spectral efficiency and higher data rates when compared to OMA schemes [75].

Added to NOMA, relaying can be quite useful in massive communication settings to reduce network congestion at the central BS level, extend cellular coverage and increase achieved rates. Mobile relays that can be deployed in a quick manner, such as unmanned aerial vehicles, can also

restore communication in damaged networks infrastructure [76,77]. In order to achieve high data rates, reduce latency and enhance spectral efficiency, full-duplex relays can be considered. By allowing the simultaneous transmission and reception of messages on the same frequency resource, full-duplex relays achieve a lower communication latency but suffer from self interference [77]. The joint use of NOMA and full-duplex relay techniques allows for enhanced spectrum efficiency and massive connectivity through multiple transmissions on the same resource block [78].

In this chapter, we investigate an uplink uncoordinated NOMA transmission system with the deployment of multiple full-duplex relays. The focus is on enabling IoT devices to autonomously organize their communications with available relays in an uncoordinated spectrum access environment. To accomodate different IoT use cases, the system includes a mixture of traffic types, including continuous, sporadic, and periodic transmissions. Furthermore, each IoT device operates under a limited power budget. We propose a multi-step algorithm based on the MAB framework. The approach is designed to adaptively and efficiently allocate power and subbands to IoT devices, thus optimizing their communication performance without centralized coordination. The work of this chapter was presented at the IEEE 32$^{\text{nd}}$ Annual International Symposium on Personal, Indoor and Mobile Radio Communications (PIMRC 2021) [33], an extended journal version was published in the IEEE Internet of Things Journal in July 2023 [79], and an extended magazine version in the IEEE Internet of Things Magazine was accepted for publication in October 2023. Next, we give an overview of the related literature before presenting our problem statement and contributions.

3.1.1 Related Work

Most of the early works studying NOMA focused on downlink scenarios. Some work studied the maximization of the average achieved throughput [72], others focused on minimizing the average downlink transmission power while satisfying user rate requirements [33,73]. In [74], the authors showed an enhancement of the spectral efficiency using novel mutual SIC techniques. To ensure successful decoding at the receiver side in a NOMA system, power allocation is key. Hence, a variety of power allocation schemes were proposed in the literature. Focusing on the uplink scenario, while some works are based on a back-off step between power levels [80] to safely decode signals, others focus on an allocation scheme that aims at guaranteeing the minimum user rate requirements [81]. The authors in [82] addressed the challenge of maximizing the minimum user rate by jointly optimizing the transmit powers and decoding order. Others showed that adding a new precoding block before the subcarrier mapping may help in reducing peak to average power ratio (PAPR) [83]. Moreover, many studies showed that NOMA applied whether in uplink or downlink communication systems ensures low latency communication and massive connectivity [84], rendering it a promising technique to support IoT network communications [71].

On a different note, in the case of NOMA coordinated communication systems, matching theory has been commonly applied to solve optimization problems [85]. It is employed to address assignment problems between two distinct sets of players. The fundamental challenge of the matching problem is to assign resources from players of one set to those of another set in an

optimal manner. To achieve this, each player builds a preference list based on a utility function, in order to rank players of the opposing set as described in Chapter 2.

Furthermore, to prevent data loss in case of system congestion, relays can be equipped with queuing capabilities. Queuing was mostly considered in the literature in coordinated spectrum access settings, where users receive, in addition to their messages, information about the relay buffer size [86]. That said, few works have considered queuing in an uncoordinated manner, where no information about the relay buffer state is communicated to users. Nonetheless, whether applied in a coordinated or uncoordinated setting, queuing has the drawback of increasing the AoI [87]. AoI is a metric referring to the degree of freshness of the information that quantifies the time elapsed from the source generation of the message till its reception [88]. AoI can vary depending on network congestion, transmission delays, and the efficiency of information processing and delivery mechanisms. It is usually measured at the receiver end, but can also be measured at the transmitter if the latter receives acknowledgments from the former. The higher the AoI, the older the information and the less useful it is [89].

Several works studied the optimization of AoI in downlink systems [90], others studied the optimization of a queue depending on its size and packet replacement [91]. Moreover, many studies have compared the AoI for different types of queues, e.g., for first-come first-served (FCFS), last-come first-served (LCFS) with or without preemption, or proportional fair (PF) queues [92]. This analysis sparked further research on both peak and average AoI in various queuing systems [93–98]. Many of these studies focused on optimizing peak and average AoI by adjusting the update service rates. Additionally, researchers investigated queue scheduling disciplines and packet management strategies to minimize AoI. The benefits of employing parallel servers to improve AoI were demonstrated in [99]. Furthermore, improvements in AoI were observed by reducing buffer sizes and introducing packet deadlines, where a packet deletes itself after exceeding its deadline, as shown in [93], [94] and [95], respectively. While having a packet deleted reduces the measured AoI, it does lead to a loss of information that needs to be managed. The consideration of AoI in updates traversing a network of queues was addressed in [100]. It was found that the LCFS queue scheduling discipline, with preemptive service, is age-optimal when the service times follow an exponential distribution. In this chapter, we use AoI as a design criterion, especially for latency-sensitive applications.

On another note, enabling scalable networks that can accommodate a variable number of devices and traffic types is crucial for unleashing the full potential of IoT. Uncoordinated or grant-free spectrum access strategies can be well-suited to this context. Indeed, uncoordinated strategies gained great interest in recent literature [101,102] motivated by their ability to reduce signaling overhead and latency in communication networks. However, most of the available literature on uplink NOMA considered fully coordinated spectrum access. Only few works considered either partially or fully uncoordinated spectrum access [103, 104]. Dealing with uncoordinated spectrum access requires novel techniques such as reinforcement learning or game theory to allocate available resources, since information sharing is restricted. A few studies adopted reinforcement learning [105–107], and more specifically the MAB framework, to allow

users to auto-organize their transmissions on the available channels [105]. In the MAB framework, the users, referred to as players, compete to find the actions, i.e., resources called arms, that maximize their expected reward or welfare, usually their rate [29], as shown in Chapter 2. These algorithms have already been used to solve the allocation problem in cognitive radio systems [108] for an uncoordinated spectrum access [105]. In our work, we use the MAB framework to optimize the allocation of resources.

3.1.2 Problem Statement and Contributions

To the best of our knowledge, no previous work has considered the use of full-duplex relays in an uncoordinated uplink NOMA system with transmit power limits and AoI constraints for devices with mixed traffic types. Hence, in this chapter, we study an uplink uncoordinated NOMA transmission system, where full-duplex relays with LCFS queues are deployed. IoT devices aim at auto-organizing their communications with the available relays using the MAB framework, without communicating with each other. Relays then forward the received signals to the BS, resulting in a two-hop communication system. IoT devices being deployed for multiple use cases with varying traffic characteristics and requirements, we consider the mixed traffic system consisting of continuous, sporadic and periodic transmissions. Moreover, each IoT device has a limited power budget. We propose a multi-step algorithm based on the MAB framework where we conduct the power-subband allocation while guaranteeing the transmit power constraints and minimizing the AoI for the devices in an uncoordinated manner. The main contribution of this chapter concerns the proposal of an efficient method to:

- allocate the available spectrum and power resources to devices with mixed traffic types in an uncoordinated system,
- minimize the transmit power at the devices and relays while maximizing the achieved rates,
- minimize the AoI for the IoT devices using the MAB framework.

The performance of the proposed MAB-based uncoordinated method is compared to that of a benchmark technique consisting of a coordinated spectrum and power allocation technique based on matching theory that minimizes AoI.

The rest of the chapter is organized as follows. In section 3.2, the system model is described while the considered optimization problem is formulated in section 3.3. Section 3.4 provides the foundations of the proposed MAB-based uncoordinated framework for mixed traffic systems. Section 3.5 elaborates on the concept of a stable system and the constraints related to continuous traffic, while the constraints of non-continuous traffic are discussed in section 3.6. The coordinated system based on matching theory for efficient resource allocation and taken as reference for performance analysis is developed in section 3.7. The proposed algorithms are evaluated using numerical simulations for which results are provided in section 3.8. Lastly, conclusions are drawn in section 3.9.

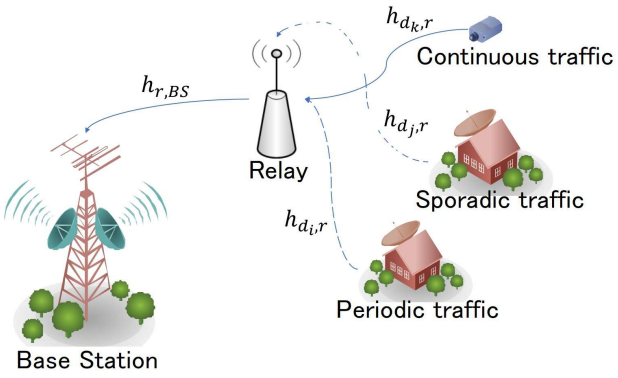

Figure 3.1: System model with one BS, one relay and devices with different traffic types.

3.2 System Model

Consider a hexagonal cell with one BS located at the cell center, R relays and N IoT devices. Grouped in a set $\mathcal{R} = \{r_1, r_2, \ldots, r_R\}$, the relays are distributed on a circle at mid-distance between the BS and the cell edges. Let $\mathcal{D}^{\text{cont}} = \{d_1^{cont}, d_2^{cont}, \ldots, d_{n_1}^{cont}\}$, $\mathcal{D}^{\text{per}} = \{d_1^{per}, d_2^{per}, \ldots, d_{n_2}^{per}\}$ and $\mathcal{D}^{\text{spo}} = \{d_1^{spo}, d_2^{spo}, \ldots, d_{n_3}^{spo}\}$, where $n_1 + n_2 + n_3 = N$, denote the sets of devices having continuous, periodic and sporadic traffic types, respectively. The set of all IoT devices is denoted by $\mathcal{D} = \{\mathcal{D}^{\text{per}}, \mathcal{D}^{\text{spo}}, \mathcal{D}^{\text{cont}}\}$. For devices with a sporadic traffic, also referred to as *sporadic devices* below, the probability of successful spectrum access is represented by $p^a_{d_k^{spo}}$. For devices with a periodic traffic, also referred to as *periodic devices*, for example sensors used in medical applications, the period between two consecutive transmissions is $T^{on}_{d_k^{per}}$.

Due to possible large distances between the BS and the power-limited IoT devices, we assume that the latter can not transmit their signals directly to the BS. Hence, a two-hop communication network is considered where the devices transmit their signals to relays that forward them to the BS, as shown in Figure 3.1. A grant-free or uncoordinated uplink communication system is studied where IoT devices aim at organizing their transmissions without any communication between them. During each time slot, every IoT device is allowed to communicate only with one relay over one subband. The relays operate in a full-duplex mode, i.e., simultaneously receive the signals from IoT devices and forward them to the BS on the same frequency resource. Therefore, relays suffer from self-interference, possibly impeding the successful decoding of the received signals. Each relay is assigned a frequency subband and conventional OMA is implemented between the relays and the BS. Thereby, relays do not suffer from inter-relay interference. Moreover, by selecting a subband, a device automatically selects the corresponding relay. For the communication link between devices and the relays, NOMA is considered for multiple access. That means that multiple power levels are available per subband and that devices need to select different power levels to avoid collisions.

3.2.1 Power Allocation Scheme

In this chapter, the uplink NOMA power allocation scheme proposed in [81] is generalized to the case of full-duplex transmissions and the consideration of multiple collisions.

Consider L available received power levels per subband at the relay. Let $\Gamma_{l,req}$ be the minimum SINR required to correctly decode the signal of each IoT device. Inspired by [81], it is shown in Appendix A that the l^{th} received power level at the relay, $v_l, l = \{1, ..., L\}$, such that $v_1 > v_2 > ... > v_L$, guarantees the target SINR when facing Q_l supported collisions at each power level lower than l if and only if:

$$v_l = \left(\sigma^2 + C_{SI} \times P_{r,c}^{max}\right) \times \Gamma_{l,req} \prod_{i=l+1}^{L} (Q_i \Gamma_{i,req} + 1). \tag{3.1}$$

In (3.1), σ^2 is the additive Gaussian noise power, C_{SI} the residual self-interference factor, and $P_{r,c}^{max}$ the maximum transmit power of relay r on each of its subband c. Hence, $C_{SI} \times P_{r,c}^{max}$ is the maximum self-interference power experienced at the relay. Note that $v_l > \sum_{i=l+1}^{L} v_i$.

For successful SIC decoding at the relays, the signals of devices transmitting on the same subband should be received with different power levels. In other words, if two or more users have chosen the same power level v_l on the same subband of a certain relay, a collision occurs, rendering their signals non-decodable. In uplink NOMA, SIC is performed in the decreasing order of channel gains. Therefore, when a collision occurs at level l, the signals of devices having chosen lower received power levels are also non-decodable. Nevertheless, upper-level signals remain decodable as long as the number of colliding signals at each lower level is less than or equal to Q_l.

In the considered system, IoT devices with periodic and sporadic traffic are allowed to transmit only at the lowest power level. The reason for this choice is to ensure that the signals of the top $L-1$ levels are not lost, in the case where multiple, but less than $Q_L + 1$, devices with non-continuous transmissions collide on level L. This means that devices with continuous transmission, also referred to as *continuous devices*, are given a higher priority than the others. Perfect channel estimation is considered in this chapter. Also, channel gains account for large-scale fading, i.e., path loss and shadowing. In order to guarantee the received power level v_l at the r^{th} relay, each device d_k sets its transmit power according to:

$$P_{d_k,l}^{t} = \frac{v_l}{h_{d_k,r}^2}, \tag{3.2}$$

where $h_{d_k,r}$ is the channel gain between device d_k and relay r.

3.2.2 Uncoordinated Joint subband and Power Allocation

In a system with uncoordinated spectrum access, the devices aim at auto-organizing their transmissions without any external intervention. To solve the problem of joint subband and power allocation, a multi-player MAB framework with zero-reward on collision is adopted [29].

Let $\mathcal{D}_{\text{active}} = \{\mathcal{D}^{\text{cont}}, \mathcal{D}^{\text{spo}}_{\text{active}}, \mathcal{D}^{\text{per}}_{\text{active}}\}$ be the combined set of active IoT devices, where $\mathcal{D}^{\text{spo}}_{\text{active}}$ and $\mathcal{D}^{\text{per}}_{\text{active}}$ are the active devices with sporadic and periodic traffic respectively. Note that $\mathcal{D}_{\text{active}} \subset \mathcal{D}$. The set of arms is the set of available subband-power level pairs. Having different traffic types and a transmit power budget $P^{max}_{d_k}$, each device d_k builds its action space $\mathcal{A}_{d_k}$, accounting for the subband-power level pairs on which it can transmit without violating its power budget. Let $\mathcal{A}_{d_k}=\{a_1, a_2, \dots, a_{A_{d_k}}\}$, where A_{d_k} represents the available number of arms for user d_k.

When choosing an action, each device d_k receives a reward from the relay. In this work, the reward is set as the achieved rate at the relay level, given by the Shannon formula [30]:

$$R_{d_k,a_b} = W \log_2(1 + \Gamma_{d_k,a_b}), \tag{3.3}$$

with W being the channel bandwidth and Γ_{d_k,a_b} the achieved SINR of device d_k, given by:

$$\Gamma_{d_k,a_b} = \frac{v_l(a_b)}{\sum_{j=l+1}^{L} v_j + C_{SI} P^t_r + \sigma^2}. \tag{3.4}$$

In (3.4), $v_l(a_b)$ is the power level chosen by device d_k in action a_b. $\sum_{j=l+1}^{L} v_j$ is the residual NOMA interference not canceled by SIC, and P^t_r the transmit power of relay r per subband at timeslot t. Hence, $C_{SI} P^t_r$ represents the instantaneous self-interference experienced by the relay.

If two or more devices select the same subband-power level pair, a collision occurs, causing the decoding of the involved users' signals to fail. Hence, the reward achieved by the concerned users is equal to 0. Let η_{d_k,a_b} represent the collision indicator for device d_k on arm a_b, i.e.:

$$\eta_{d_k,a_b} = \begin{cases} 0, & \text{in case of a collision,} \\ 1, & \text{otherwise.} \end{cases} \tag{3.5}$$

Hence, the reward or utility received by device d_k when selecting arm a_b, U_{d_k,a_b}, can be expressed as:

$$U_{d_k,a_b} = \eta_{d_k,a_b} \times R_{d_k,a_b}. \tag{3.6}$$

Due to the absence of communication between IoT devices, each device only observes its own list of actions and its corresponding list of rewards. Since the rewards are unknown beforehand at the device level, there is a need for an exploration phase during which the devices learn the rewards. To enhance system performance, the objective of this work is to maximize the welfare of all IoT devices, given by:

$$w = \sum_{k=1}^{n_1} U_{d_k^{cont},a_b} + \sum_{k=1}^{n_2} U_{d_k^{per},a_b} + \sum_{i=k}^{n_3} U_{d_k^{spo},a_b}, \tag{3.7}$$

where the sums represents the welfare of the devices having continuous, periodic and sporadic traffic, respectively.

3.2.3 Relay-BS Communication

As previously stated, relays are equipped with full-duplex communication capabilities. To satisfy the QoS requirements of devices when forwarding their messages to the BS, the transmit power of each relay must be optimized.

Let $X^t_{r,cont}$ and $X^t_{r,ncont}$ be the number of continuous and non-continuous signals correctly decoded by relay r at timeslot t. The minimum rate required for the relay to be able to transmit all successfully decoded signals to the BS is equal to:

$$R_{r,req} = X^t_{r,cont} \times R_{cont,req} + X^t_{r,ncont} \times R_{ncont,req}, \tag{3.8}$$

where $R_{cont,req}$ and $R_{ncont,req}$ are the required rates for devices with continuous and non-continuous transmission, respectively.

Each relay transmits its data over C subbands. Moreover, as already mentioned, we assume orthogonal channel allocation between different relays, i.e., different relays do not share the same subbands. Thus, the rate achieved by relay r on subband c is given by:

$$R_{r,c} = W \times \log_2\left(1 + \frac{h^2_{r,BS} P^t_r}{\sigma^2}\right), \tag{3.9}$$

where $h_{r,BS}$ is the channel gain between relay r and the BS. Assuming an equal rate repartition among the C subbands, to meet the rate requirement in (3.8), the transmit power of the relay r on a subband c should satisfy:

$$P^t_{r,c} = min\left\{\frac{\sigma^2}{h^2_{r,BS}}\left(2^{\frac{R_{r,req}}{C \times W}} - 1\right), P^{max}_{r,c}\right\}. \tag{3.10}$$

When the transmit power needed by the relay exceeds its budget, an overflow scenario is expected. In case of an overflow due to continuous traffic, the system becomes unstable. To avoid this, a solution based on the application of a timeout period can be considered, in which the devices having continuous traffic are invited, through the value of their received rewards, to connect to another relay following a *timeout* mechanism that is described in section 3.5. This solution guarantees that continuous traffic is transmitted to the BS during the first timeslot after the timeout period. It is motivated by the sensitivity to latency of the underlying application for continuous devices. Therefore, the devices having continuous traffic would not suffer from high values of AoI.

3.2.4 Sources of AoI

The overall instantaneous AoI of an IoT device is computed as the summation of the AoIs for the relay uplinks and backhaul links that carry the data sent by the device. Let $\Delta_1(d_k, t)$ denote the AoI related to the uplink, i.e., device-to-relay communication, and $\Delta_2(d_k, t)$ denote the AoI related to the backhaul link, i.e., relay-to-BS communication, measured at timeslot t. Both $\Delta_1(d_k, t)$ and $\Delta_2(d_k, t)$ are measured at the relay level since the latter is able to identify

the timeslot of each message transmitted by users as well as the timeslot it can retransmit the signal to the BS. The total AoI for a device d_k is equal to:

$$\Delta(d_k, t) = \Delta_1(d_k, t) + \Delta_2(d_k, t). \tag{3.11}$$

$\Delta_1(d_k, t)$ depends on the number of collisions the signal undergoes before being successfully received at the relay. Hence, optimizing the subband-power level allocation can reduce the AoI of the first link, $\Delta_1(d_k, t)$, by minimizing the number of signal collisions.

On the other hand, $\Delta_2(d_k, t)$ depends on the state of the data buffer at the relay. This state represents the number of timeslots that a packet has to wait in the buffer of the relay before being forwarded to the BS. Considering the variable throughput at the relay level due to the nature of the traffic, a buffer is introduced for the cases where the capacity of the relay-to-BS link is lower than the aggregated throughput of the device-to-relay links. Equivalently, this corresponds to situations where the power required to forward the received device signals exceeds the relay power budget i.e.:

$$P^t_{r,c} \geq P^{max}_{r,c}. \tag{3.12}$$

While being beneficial to avoid data loss, buffering at the relay level increases AoI for the devices. Eq. (3.10) and (3.12) are now modified to include a new parameter $X_{0,r}$ that represents the maximum number of received signals that a relay can forward per timeslot to the BS without the need for buffering. Using Shannon's formula, parameter $X_{0,r}$ can be formulated as:

$$X_{0,r} = \frac{C \times W}{R_{d_k,req}} \log_2 \left(1 + \frac{P^{max}_{r,c} h^2_{r,BS}}{\sigma^2}\right). \tag{3.13}$$

$R_{d_k,req}$ is the rate required by user d_k and is either equal to $R_{cont,req}$ or $R_{ncont,req}$ depending on the traffic type of the device. Note that when the number of correctly decoded signals at the relay, X^t_r, exceeds $X_{0,r}$, $\Delta_2(d_k, t)$ increases, leading to an increase of the total AoI $\Delta(d_k, t)$.

3.2.5 AoI Computation

We consider that IoT devices submit new messages at timeslots $t_1, t_2, \ldots$ and that these messages are successfully received at the relay at timeslots $t'_1, t'_2, \ldots$, respectively. The instantaneous AoI for device d_k transmitting a message m, $\Delta_1(d_k, t)$ is given by:

$$\Delta_1(d_k, t) = t'_m - t_m, \ m = 1, 2, \ldots \tag{3.14}$$

As for $\Delta_2(d_k, t)$, it is given by:

$$\Delta_2(d_k, t) = t''_m - t'_m, \tag{3.15}$$

where t''_m is the timeslot where the signal is correctly received at the BS. The average AoI is given by:

$$\Delta_{d_k} = \frac{1}{T} \int_0^T \Delta(d_k, t)\, dt, \tag{3.16}$$

where T is the time horizon of the allocation.

3.3 Problem Formulation

The main purpose of this study is to minimize the AoI of IoT devices and relays while satisfying their rate requirements and minimizing their transmit power. The optimization problem is formulated as:

$$\max_{P^t_{d_k}, P^t_{r,c}, \Omega_{d_k,c}} -\left(\sum_{k=1}^{n_2} \Delta_{d_k^{per}} + \sum_{k=1}^{n_3} \Delta_{d_k^{spo}}\right), \tag{3.17}$$

such that:

$$\sum_{c} \Omega_{d_k,c} R_{d_k,c} \geq R_{d_k,req}, \forall d_k \in \mathcal{D} \tag{3.17a}$$

$$\sum_{k=1}^{n_1} \sum_{c} \Omega_{d_k^{cont},c} R_{d_k^{cont},c} \leq \sum_{c} R_{r,c}, \tag{3.17b}$$

$$\sum_{c} \Omega_{d_k,c} P^t_{d_k,l} \leq P^{max}_{d_k}, \tag{3.17c}$$

$$P^t_{r,c} \leq P^{max}_{r,c}. \tag{3.17d}$$

In (3.17), $\Delta_{d_k^{per}}$ and $\Delta_{d_k^{spo}}$ represent the average AoI for periodic and sporadic traffic devices respectively. (3.17a) is the rate requirement constraint per IoT device where $\Omega_{d_k,c} = 1$ if device d_k transmits using subband c, and 0 otherwise. Constraint (3.17b) is the rate constraint for avoiding overflow scenarios while serving continuous traffic devices. (3.17c) and (3.17d) are the transmit power constraints for devices and relays, respectively.

Problem (3.17) consists in minimizing the AoI by optimizing the power and subband allocations. To solve this problem, a multi-step algorithm is proposed. For each device, it starts by assigning a subband-power level pair while satisfying their rate requirements. Then, it checks for overloaded relays where the non-continuous traffic devices suffer from AoI and proceeds to address the latency issue.

3.4 Subband Power-Level Assignment

We first propose a solution for the subband-power level assignment problem. As previously mentioned, IoT devices are energy-limited and need to minimize their transmit power. To satisfy this goal, the UCB algorithm is used to find the allocation of subband-power level pairs while accounting for the power budget of communicating devices.

3.4.1 Continuous Traffic

Each IoT device having continuous traffic type aims at achieving a rate larger than or equal to its requested rate, while consuming the least amount of transmit power. Thus, two parameters should be taken into consideration in the design: the transmit power of device d_k, $P^t_{d_k,l}$, and its

achieved rate, $R_{d_k,c}$. As shown in (3.2), $P^t_{d_k,l}$ depends on both the received power level chosen by d_k and the channel gain between the relay and d_k. Any increase in the channel gain reduces the amount of required transmit power. Hence, the minimum transmit power value is reached when the device chooses its best radio channel, i.e., the one with the largest gain. However, having each device choose its best arm in terms of channel gain might not always lead to system convergence. Constrained by its power budget, the device d_k might not be able to transmit on all arms associated with subband c. In such a case, the choice of all users must be adapted in a way that system welfare is maximized.

IoT devices should choose their subbands and corresponding received power levels in a way to strike a trade-off between the achieved rate and the consumed transmit power. Therefore, instead of choosing the arm that maximizes the achieved rate, each device d_k chooses arm $a^{cont,*}_{d_k} \in \mathcal{A}_{d_k}$ that satisfies:

$$a^{cont,*}_{d_k} = \underset{a^{cont}_b \in \mathcal{A}_{d_k}}{\operatorname{argmax}} \left((1-\beta)\, \frac{R_{d_k,c}}{R_{max}} - \beta \frac{P^t_{d_k,b}}{P^{max}_{d_k}} \right). \tag{3.18}$$

In (3.18), β is a positive weight parameter less than 1 relative to the transmit power. $R_{max} = W \log_2(1 + \frac{v_1}{\sigma^2})$ is the maximum achievable rate by all users. The proposed technique to solve the uncoordinated joint subband and power allocation problem is summarized in Algorithm 2, where T is the time horizon and $n_{d_k}(a_b, t)$ the number of times arm a_b is played by device d_k until timeslot t.

Algorithm 2: UCB Power Minimization for Continuous traffic

Initialization: Each device d^{cont}_k generates a random permutation of $\mathcal{A}_{d^{cont}_k}$. During the first $|\mathcal{A}_{d^{cont}_k}|$ iterations, d^{cont}_k plays the arms iteratively and updates the utilities accordingly.

for $k=1{:}n_1$ **do**

  // Best arm identification:

  $$a^{cont,*}_{d_k} = \underset{a_b \in \mathcal{A}^{cont}_{d_k}}{\operatorname{argmax}} \left((1-\beta)\, \frac{Q(d_k,a_b) + \sqrt{\frac{2\log(t)}{n_{d_k}(a_b,t)}}}{R_{max}} - \beta \frac{P^t_{d_k,b}}{P^{max}_{d_k}} \right)$$

  // Parameters update:

  $$s_{d_k}(a^{cont,*}_{d_k}, t+1) = s_{d_k}(a^{cont,*}_{d_k}, t) + U_{d_k, a^{cont,*}_{d_k}}$$

  $$n_{d_k}(a^{cont,*}_{d_k}, t+1) = n_{d_k}(a^{cont,*}_{d_k}, t) + 1$$

  $$Q(d_k, a^{cont,*}_{d_k}) = \frac{s_{d_k}(a^{cont,*}_{d_k}, t+1)}{n_{d_k}(a^{cont,*}_{d_k}, t+1)}$$

end

3.4.2 Non-Continuous Traffic

For devices with sporadic traffic, a different approach is considered. Depending on its access probability, a device may not be active for all available timeslots. Hence, we define T_{on} as the total number of timeslots where a device is transmitting. Note that this type of device may

successfully transmit on an arm at a timeslot t_{on} and fail to do so at a timeslot t'_{on} using the same arm because of a potential collision with another device. Note that $t_{on}, t'_{on} \in \{1, \ldots, T_{on}\}$. A weight function $f(\tau, ws, t_{on})$ of window size ws representing the weight of the last ws rewards at the device level is introduced. We define $f(\tau, ws, t_{on})$ as an increasing linear function based on the last ws active timeslots each represented by τ in $[t_{on} - ws, t_{on}]$, $t_{on} \in \{1, \ldots, T_{on}\}$ such that:

$$f(\tau, ws, t_{on}) = \begin{cases} 0, & \text{for } \tau = t_{on} - ws, \\ \frac{\tau}{ws}, & \text{for } t_{on} - ws < \tau < t_{on}, \\ 1, & \text{for } \tau = t_{on}. \end{cases} \tag{3.19}$$

The device with sporadic traffic calculates the achieved rewards in the last ws active timeslots by multiplying the rewards with $f(ws, t_{on})$. Consequently, the choice of the sporadic devices only depends on the achieved rewards in the last ws active allocation choices. In this way, the sporadic device tends to explore different arms than the one previously selected following a collision rather than persisting with a single arm for an extended period without reaching its desired target rate. For such devices, there is always a need to minimize the transmit power while meeting the rate requirements. Therefore, sporadic IoT devices also choose the arms that maximize their decision function:

$$a^*_{d_k} = \underset{a_b \in \mathcal{A}_{d_k}}{\operatorname{argmax}} \left((1 - \beta) \frac{R_{d_k, a_b}}{R_{ncont,max}} - \beta \frac{P^t_{d_k, b}}{P^{max}_{d_k}} \right), \tag{3.20}$$

where $R_{ncont,max} = W \log_2(1 + \frac{v_L}{\sigma^2})$ is the maximum rate achievable by a device with sporadic traffic. Inspired by [33], the proposed technique to solve the subband and power allocation problem for sporadic devices is summarized in Algorithm 3 where $n_{d_k}(a_b, t_{on})$ is the number of times arm a_b is played by device d_k during the t_{on} active timeslots. Note that in case of collision between two sporadic devices, they retransmit their signals in the next timeslot.

For each IoT device d_k with periodic transmission, the solution for devices having continuous traffic is applied in its active period $T^{on}_{d^{per}_k}$. However, since sporadic and periodic devices share the same power levels on the subbands, collisions may occur. In this case, the IoT device with periodic transmission goes into a pseudo-sporadic mode with an increasing access probability value in order to prioritize the sporadic traffic device competing for the same arm. In other words, the corresponding periodic traffic device retransmits its message at a later stage in order to free the arm it occupies. When the pseudo-sporadic device retransmits successfully its signal, it returns to the initial state, i.e., to the periodic mode.

The complexity of this assignment technique is given by the complexity of the UCB algorithm. Hence, it amounts to $O(log(n))$, n being the time horizon.

3.5 System Stability

When the relay successfully decodes the signals received from the IoT devices, it forwards them to the BS. Occasionally, in the case of congestion or bad channel states between the relay

Algorithm 3: UCB subband-power level assignment for devices with sporadic traffic

Initialization: Each device d_k^{spo} generates its action profile set $\mathcal{A}_{d_k}$ depending on its power budget and channel gains. These devices only transmit on the lowest power level of each subband.

for $k=1{:}n_3$ **do**

// If t is an active timeslot:

$t_{on} = t_{on} + 1$

// Utility function sent by the relay:

$U_{d_k,a_{d_k}^*}(t) = \eta_{d_k,a_{d_k}^*} \times R_{d_k,a_{d_k}^*}$

// Best arm identification:

$$a_{d_k}^* = \underset{a_b \in \mathcal{A}_{d_k}}{\operatorname{argmax}} \left((1-\beta) \frac{Q(d_k,a_b) + \sqrt{\frac{2\log(t_{on})}{n_{d_k}(a_b,t_{on})}}}{R_{d_k,req}} - \beta \frac{P_{d_k,b}^t}{P_{d_k}^{max}} \right)$$

// Parameters update:

$s_{d_k}(a_{d_k}^*, t_{on}-ws : t_{on}) = U_{d_k,a_{d_k}^*}(t_{on}-ws : t_{on})$

$n_{d_k}(a_{d_k}^*, t_{on}+1) = n_{d_k}(a_{d_k}^*, t_{on}) + 1$

$Q(d_k, a_{d_k}^*) = f(ws, t_{on}) .* s_{d_k}(a_{d_k}^*, t_{on}-ws : t_{on})$

end

and the BS, the relay may not be able to transmit all the received data to the BS within a unique timeslot. To avoid data loss in such a case, buffering the unsent signals at the relay can be used. In fact, this is necessary when the required power to transmit the received signals from the devices, P_r^t, exceeds the relay power budget per channel, i.e., when:

$$P_r^t \geq P_r^{max}. \tag{3.21}$$

This can be translated as the number of correctly decoded signals at the relay level at timeslot t, X_r^t, being greater than some threshold value $X_{0,r}$ (eq. 3.13). However, to set up a stable system, the relay buffers must not suffer from persistent overflows. To do so, the rate requirements of devices generating continuous traffic should not exceed the capacity of the backhaul link.

When buffering occurs, a certain number of IoT devices generating continuous traffic should be incited to connect to another, less congested, relay. This is necessary to enable each relay to forward all received messages generated by these devices to the BS during one timeslot, thereby satisfying the QoS requirements of the corresponding devices. However, the system being uncoordinated, very little information is shared between the relay and the connected devices. Thus, IoT devices must learn on their own the need to connect to another relay. To do so, the relay having reached its overflow threshold, i.e., a full buffer possibly entailing information loss, returns a zero reward to all its connected devices for a certain period. This period is referred to as a *timeout* period which is determined in practice depending on the system parameters.

During the timeout period of relay r, devices with continuous traffic associated with r are encouraged to perform a new exploration phase. In other words, those devices may try to access arms associated with another relay, if their power budgets allow so. By exploring new arms associated with less congested relays, these devices aim at reaching a new stable state leading

to system convergence. Note that this solution could lead to some devices remaining silent, i.e., refraining from transmitting for multiple timeslots, if they are not able to connect to another relay.

To represent the zero utility in the case of a buffering overflow, the collision indicator is modified as follows: $\eta_{d_k,a_b} = 0$ in case of collision or buffer overflow, and 1 otherwise.

To avoid returning a zero reward for a long period by the congested relay, i.e., to help devices react faster in the timeout period, they may take into consideration the total transmit power that has been spent on each specific arm a_b, reflected by $P^t_{d_k,b} \times n_{d_k}(a_b,t)$. Since the congested relay is replying with zero rewards, the decision function on this relay depends mostly on the consumed power, leading to free some arms and to try new ones. Therefore, to choose their actions, instead of using (3.18), IoT devices adopt the following metric:

$$a^{cont,**}_{d_k} = \underset{a_b \in \mathcal{A}_{d_k}}{\operatorname{argmax}} \left((1-\beta) \frac{R_{d_k,a_b}}{R_{max}} - \beta \frac{P^t_{d_k,b}}{P^{max}_{d_k}} \times \frac{n_{d_k}(a_b,t)}{t} \right). \tag{3.22}$$

To summarize, Algorithm 4 is proposed to account for buffering needs at the relays.

Algorithm 4: UCB Power Minimization and Queuing in an Uncoordinated System

```
while X_r^t ≤ X_{0,r} do
    Run Algorithm 2
end
while X_r^t ≥ X_{0,r} and t ≤ Timeout do
    for devices connecting to r do
        U_{d_k,a_b} = 0 ∀d_k
        Rerun Algorithm 2 with the decision function in (3.22) to change arms if possible
    end
end
```

3.6 Proposed Solution for AoI Minimization

Being in an uncoordinated spectrum access setting, the problem of AoI minimization is solved using the MAB framework with zero-reward for unsent messages, once the system is guaranteed to be stable, i.e. at T_{conv}. In fact, when the messages from IoT devices successfully reach a relay with queuing capabilities, the relay transmits all the traffic from the continuous devices and schedules the messages of the sporadic ones with respect to the following priority:

$$P_r(d_k,t) = \frac{number_{arr}(d_k)}{number_{sent}(d_k)} \times \frac{t}{t - \Delta_1(d_k,t)}. \tag{3.23}$$

In (3.23), $number_{arr}$ and $number_{sent}$ stand for the number of messages arriving at the relay and the number of messages sent by the relay for a given device d_k, respectively. This priority metric ensures that the less the sporadic device is served by the relay, the higher its priority. Eq. (3.23) also avoids the dominance of the first type of AoI $\Delta_1(d_k)$. Indeed, in the case where

$\Delta_1(d_k,t)$ is large, $t-\Delta_1(d_k,t)$ is small, hence the sporadic device d_k is prioritized.

In order to minimize the overall AoI, we consider a new reward $U_{d_k,a_b{}^+}$ received by all the devices from the relay. It accounts not only for the rate achieved by the devices but also for the AoI induced by link 2. This new reward, $U_{d_k,a_b{}^+}$, is given by:

$$U_{d_k,a_b{}^+} = \frac{R_{d_k,a_b}}{R_{ncont,max}} \times \frac{1}{\Delta_2(d_k,t)}. \tag{3.24}$$

In (3.24), $R_{ncont,max}$ stands for the maximum rate a device with non-continuous traffic can achieve. It is given by $R_{ncont,max} = W\log_2\left(1+\frac{v_L}{\sigma^2}\right)$ and is equal to the rate required by the device, i.e. $R_{ncont,max} = R_{ncont,req}$. Thus, the first fraction is a binary function equal to either 0 in case of collision or 1 otherwise. Hence the reward function can be expressed as:

$$U_{d_k,a_b{}^+} = \eta_{d_k,a_b} \times \frac{1}{\Delta_2(d_k,t)}. \tag{3.25}$$

In case of a collision, a zero-reward is sent back to the user. As a result, the first type of AoI, $\Delta_1(d_k,t)$, is the dominant part in the AoI expression, which can be directly determined by the device itself. Moreover, the utility function is inversely proportional to the second AoI type. Therefore, if the information reaches the relay successfully but its forwarding to the BS is delayed, the utility function of the arms belonging to the given relay becomes smaller. In that case, device d_k is encouraged to perform a new exploration phase until it finds a temporary gateway to transmit its messages to the BS. The same approach is applied for devices with periodic traffic. The technique is summarized in Algorithm 5.

Algorithm 5: UCB AoI minimization for devices with non-continuous traffic

Initialization: Run Algorithm 3 to adapt for every device its subband-power level pair while minimizing its transmit power for T timeslots.
for t=T_{conv}:end **do**
  for k=1:n_2+n_3 **do**
    // If t is an active timeslot:
    $t_{on} = t_{on} + 1$
    // Utility function sent by the relay:
    $U_{d_k,a_b{}^+} = \eta_{d_k,a_b} \times \frac{1}{\Delta_2(d_k,t)}$
    // Best arm identification:
    $a^+_{d_k} = \underset{a_b\in\mathcal{A}_{d_k}}{\text{argmax}}\left((1-\beta)\,\frac{Q(d_k,a_b^+)+\sqrt{\frac{2\log(t)}{n_{d_k}(a_b,t)}}}{R_{d_k,req}} - \beta\frac{P^t_{d_k,b}}{P^{max}_{d_k}}\right)$
    // Parameters update:
    $s_{d_k}(a_i^+, t_{on}-ws:t_{on}) = U_{d_k,a^+_{d_k}}(t_{on}-ws:t_{on})$
    $n_{d_k}(a^+_{d_k}, t_{on}+1) = n_{d_k}(a^+_{d_k}, t_{on}) + 1$
    $Q(d_k,a_i^+) = f(ws,t_{on}).*s_{d_k}(a^+_{d_k}, t_{on}-ws:t_{on})$
  end
end

The complexity of the proposed technique is also dominated by the complexity of the UCB

algorithm, i.e., in the order of $O(log(N))$. Note that in case of overflow due to continuous traffic, it is recommended to use the timeout period method previously described. By doing so, the continuous traffic is guaranteed to be forwarded to the BS in the same timeslot.

Further improvements in AoI can be achieved by predicting the corresponding impact of the number of active devices with sporadic traffic in upcoming timeslots. In fact, in Algorithm 5, the relay replies with the current AoI, $\Delta_2(d_k, t)$, depending on the current state of its queue whatever the value of the next state is. In other words, a congested relay may be able to clear its queue in the next timeslot if the number of received messages allows for it. Consequently, it will be able to accept new messages from the IoT devices instead of encouraging them to go through another relay by sending them low rewards. In such a case, the predicted AoI for the next timeslot, $\Delta_2(d_k, t+1)^*$, may be low, but the current one $\Delta_2(d_k, t)$ is high.

The predicted number of active sporadic IoT devices follows a simple probabilistic calculation. Let Y be a discrete random variable representing the number of potential active sporadic devices at timeslot t and taking values in $\{0, ..., n_3^c\}$ with n_3^c being the non-collided devices with sporadic traffic at timeslot $t-1$. Note that we do not consider the collided sporadic traffic devices at $t-1$ since they surely retransmit their signals at timeslot t. The probability of having k active sporadic devices among the uncertain ones is given by:

$$pr(Y = k) = \left(1 - p^a_{d_k^{spo}}\right)^{n_3^c - k} \times \left(p^a_{d_k^{spo}}\right)^k \times \binom{n_3^c}{k}. \tag{3.26}$$

Let:

$$k^* = \underset{k}{\operatorname{argmax}}\, pr(Y = k) \tag{3.27}$$

be the number of messages having the largest probability. Hence, the number of estimated sporadic messages will be equal to: $k^* + n_3 - n_3^c$. By relying on the estimated number of messages, the relay performs the scheduling of the next timeslot and estimates the corresponding AoI by assuming the worst case scenario where all expected active users transmit to the relay in question. Then, it replies with the estimated AoI $\Delta_2^*(d_k, t+1)$. The reward is then expressed as:

$$U_{d_k, a_{i^+}} = \eta_{d_k, a_k} \times \frac{1}{\Delta_2^*(d_k, t+1)}. \tag{3.28}$$

The approach then follows the algorithm described earlier by just modifying the utility function.

3.7 Resource Allocation using Coordinated Matching

This section describes the coordinated allocation alternative based on the matching framework [85] introduced to benchmark the proposed uncoordinated MAB-based method.

Starting from a fully coordinated system, the BS is assumed to have full knowledge of the power budget and traffic types of all users, as well as the power budget, the buffer size and the current state of the queues at the relays.

The subband allocation problem is modeled as a one-to-one matching game. In this model,

the set of arms and the set of devices form two independent sets depending on their preferences. In this scenario, each arm represents a power-subband pair and can be allocated to just one device and each device can transmit on just one arm per timeslot. Each device sorts channels in a descending order with respect to their gains. By doing so, when all devices are matched with different arms, the rate requirements are satisfied while tending to consume the least amount of transmit power possible. Since only large-scale fading is considered in this chapter, the channel preference of a device is equivalent to a relay preference (i.e. choosing a channel results in choosing a particular relay). Consider the preference relation of device d_k to be given by:

$$f_1 = h^2_{d_k,r}(r, d_k). \tag{3.29}$$

The matching preference of the arms depends on the queue state of all the relays, the channel conditions and the transmission power and activity of the devices. Thus, the arms preference function is modeled as follows:

$$f_2 = \frac{\frac{h_{r,BS}}{\max_r h_{r,BS}}}{\frac{Queue_r(t)}{Bu_r} \times \psi(d_k)}. \tag{3.30}$$

In (3.30), $Queue_r(t)$ stands for the number of packets currently in the queue of the relay r, Bu_r is its buffer size and $\psi(d_k)$ is a function defined according to the traffic type of each user:

$$\psi(d_k) = \begin{cases} 1 & \text{if the traffic is continuous or periodic,} \\ 1 - p^a_{d_k^{spo}} & \text{otherwise.} \end{cases} \tag{3.31}$$

The arms preference function is designed to be an inversely proportional function of the occupancy of the relay queue. In other words, a congested relay is less likely to admit devices. Also, this preference relation ensures that a higher access probability of a non-continuous traffic device results in a lower $\psi(d_k)$. Hence, the sporadic traffic devices having high access probability are mostly matched with non-congested relays. The problem is then solved using the Gale-Shapley algorithm [31] at the BS level.

The algorithms developed throughout this Chapter are summarized in Fig. 3.2.

3.8 Simulation Results

Extensive simulations were performed to validate the performance of the proposed algorithms. We first consider an uplink communication system with one BS at the cell center, one relay and $N = 60$ IoT devices divided among $n_1 = 36$ continuous traffic devices, $n_2 = 12$ periodic traffic devices and $n_3 = 12$ sporadic traffic devices with an access probability equal to 0.3. The periodic traffic devices are further divided into 4 groups of 3 devices each, transmitting in subsequent periods so that they do not interfere with each other. The cell radius is equal to 250 m. The number of available subbands and power levels are given respectively by $C = 9$ and $L = 5$. Hence, the maximum number of available resources is $C \times L = 45$. IoT devices are distributed around the relay according to a Poisson distribution [109]. Signals undergo a distance-dependent

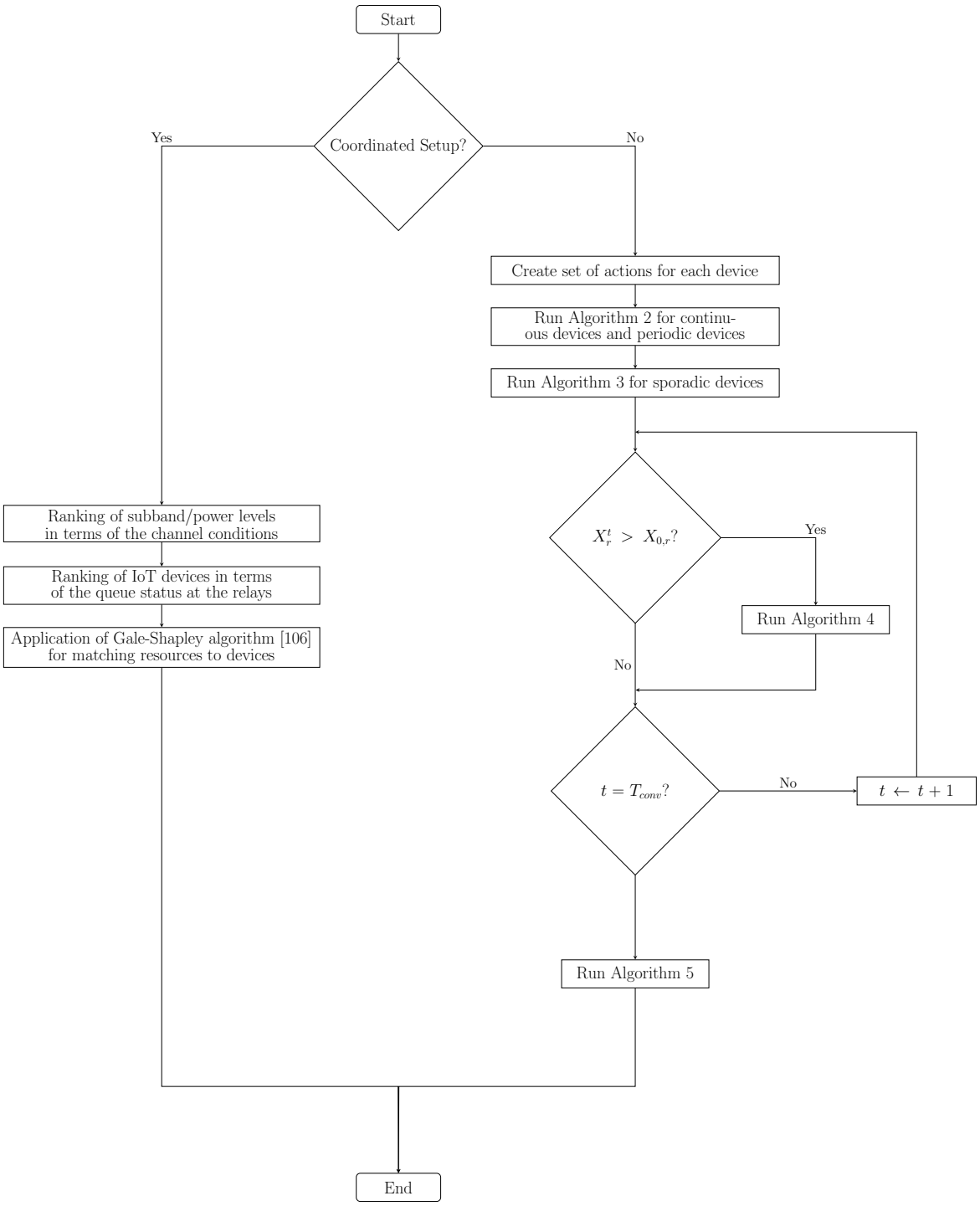

Figure 3.2: Flowchart of the applied algorithms in coordinated and uncoordinated settings.

path loss with a decay factor of 3.76, and a zero-mean log-normal shadowing with an 8 dB variance. The noise power spectral density is equal to $N_0 = 4 \times 10^{-21}$ W/Hz. In a subsequent step, the system is evaluated with two relays. Other system parameters are summarized in Table 3.1.

Table 3.1: Design parameters values

$R_{cont,req}$	0.75 Mbps	$P_{d_k}^{max}$	23 dBm
$R_{periodic,req}$	0.3 Mbps	$R_{sporadic,req}$	0.3 Mbps
$C \times P_r^{max}$	5W	C_{SI}	-120 dB
W	156 kHz	ws	10
$p_{d_k^{spo}}^a$	0.3	β	0.5

The performance of the proposed algorithms with and without AoI estimation, as described in Algorithm 5, is evaluated for $T = 1,000$ timeslots. The performance of the proposed technique is compared to the benchmark based on a coordinated allocation using matching theory, presented in Section 3.7. This coordinated method applies a centralized setting which assumes that the BS has full knowledge of the channel gains between devices and relays, and those between relays and BS, as well as the queue status of the relays. The resource allocation is then optimized accordingly. This method is referred to as "Coordinated MT". In addition to "Coordinated MT", comparisons are made against two uncoordinated methods:

- a random access NOMA method (called RA-NOMA in the figure captions), where devices choose their arms randomly,
- an allocation technique where the devices solely allocate their arms using Algorithm 3, without taking AoI into consideration (Algorithm 3 - no AoI).

3.8.1 Performance of the Arm Assignment Technique

The assignment of arms is evaluated in Figure 3.3, where the instantaneous successful transmission percentage is plotted as a function of time. Figure 3.3 shows that the proposed UCB technique based on Algorithms 2 and 3 reaches convergence with 100% satisfaction, hence termination of the exploration phase for all devices succeeds within 80 timeslots for all IoT devices. During in average the first 80 timeslots, the devices explore the different arms to learn their rewards. Then, each device selects the arm that maximizes its decision function. Since the matching technique is fully coordinated by the BS, convergence to the full satisfaction state is reached within the very first timeslots. However, RA-NOMA cannot reach a successful rate better than 40% with an average of 28%.

The average transmission power per device as a function of the requested rate is evaluated in Figure 3.4. By varying weight β, we observe that $\beta = 0.5$ is the best choice for minimizing the power consumption as it strikes the best balance between decreasing transmit power and

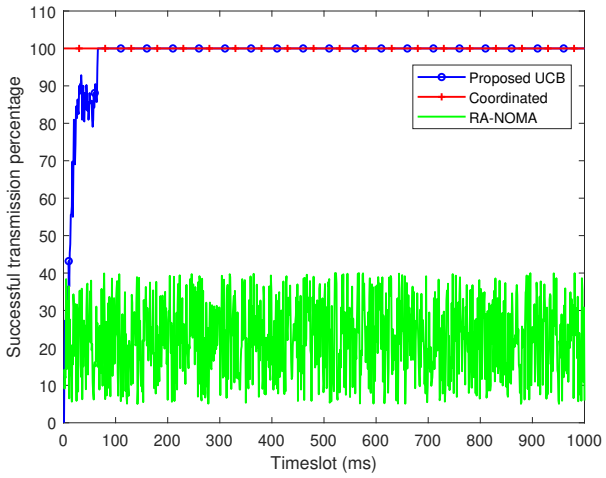

Figure 3.3: Instantaneous successful transmission percentage as a function of time.

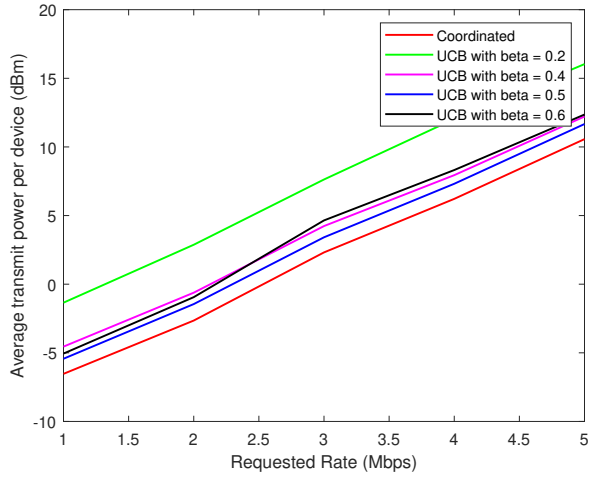

Figure 3.4: Average transmit power for a varying requested rate.

increasing the achieved rate. Moreover, for the same average transmit power, the proposed UCB-based method with $\beta = 0.5$ is within 0.2 Mbps from the coordinated solution.

3.8.2 Performance Assessment with Queuing Needs at the Relays

In this paragraph, we consider a system with $R = 4$ relays and $n_1 = 160$ uniformly distributed IoT devices having continuous traffic. We are interested in studying the case of continuous devices only because they determine whether a system is stable or not. A total of $C = 10$ subbands and $L = 5$ available power levels for continuous traffic are considered per relay, leading to a maximum of $R \times C \times L = 200$ arms per IoT device. The purpose of this setting is to validate the role of queuing at the relays. As explained in Section 3.5, to avoid the need for queuing, relay r can support a maximum of $X_{0,r}$ connected devices of continuous traffic type. The value of $X_{0,r}$, estimated using (3.13), for one realization of the channel gains of the considered illustration, is shown in Table 3.2.

Table 3.2: Maximum number of supported IoT users per relay, $X_{0,r}$.

Relay	1	2	3	4
Arms	50	50	50	50
$X_{0,r}$	43	87	36	75

Table 3.2 shows that there is no need for queuing at the level of relays 2 and 4. In fact, the number of users that can connect to relays 2 and 4 per timeslot, i.e., the number of users able to choose unique arms, is lower than the maximum number of supported users. This is not the case for relays 1 and 3 where a queue may be needed if the number of connected devices exceeds the maximum supported number $X_{0,r}$.

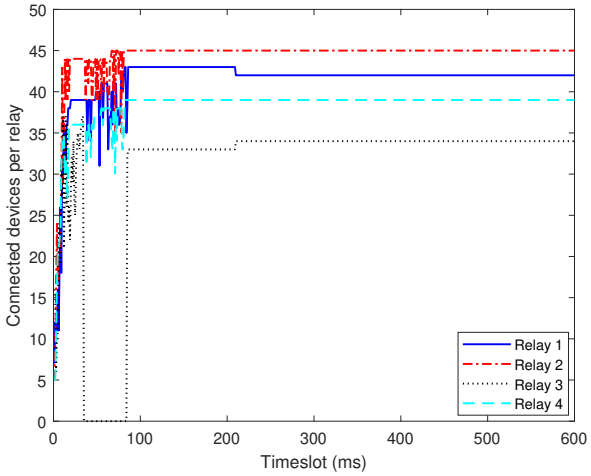

Figure 3.5: Number of connected devices per relay.

In Figure 3.5, the instantaneous number of successfully connected devices per relay is shown for this setup. The devices start by exploring the available arms until reaching convergence. Relay 3 reaches its overflow conditions since the number of connected devices to this relay when reaching the first convergence state is larger than its maximum supported number $X_{0,r}$. Hence, relay 3 enters a timeout period between timeslots 40 and 90, in which a zero reward is returned to all devices trying to connect to it. During this period, users previously associated with relay 3 attempt to connect to other less congested relays. Having succeeded to do so, a first convergence is reached within 100 timeslots and then full convergence is reached within 200 timeslots, as shown in Figure 3.5. Upon reaching convergence, the rate requirements of all relays and IoT users are satisfied.

3.8.3 Performance Assessment of the Proposed Solution

We consider now a system having two relays and we assume that one of the relays is congested and cannot transmit the signals of all sporadic, periodic and continuous devices to the BS. In Figure 3.6, we show that application of Algorithm 3 alone, with no AoI consideration, leads to a large achieved AoI value, especially due to the increase in $\Delta_2(d_k, t)$, since it does not account for the measured AoI. Thus, the devices always transmit to the same relay without taking into

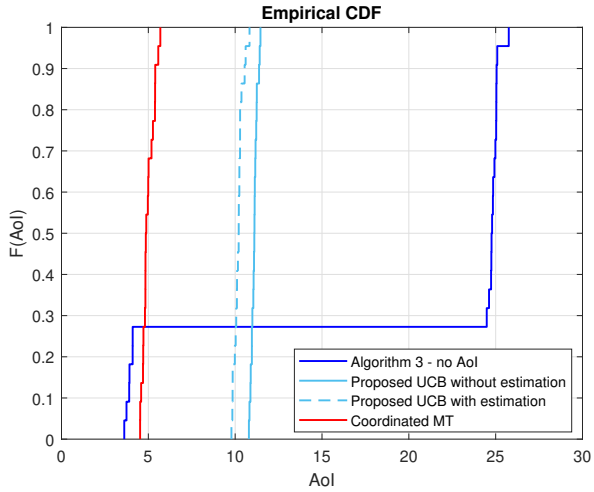

Figure 3.6: Cumulative distribution function of AoI.

account the state and occupation of the relay. Consequently, they do not consider switching to another less congested relay. By using the proposed UCB-based technique for AoI minimization, we see a considerable decrease in the achieved AoI. Moreover, predicting the future number of active devices brings an additional non-negligible benefit. The choice of the adopted method depends on the complexity the relay can afford. Also, note that the performance of both UCB-based techniques is close to the centralized technique based on matching theory.

In Figure 3.7, we evaluate the method proposed to estimate the number of active devices in the next timeslot. We observe that the proposed probabilistic approach provides estimates close to the actual numbers of active devices, leading to a slightly better performance when

estimating the AoI, $\Delta_2(d_k, t)$, for a device d_k, as it will be shown in the subsequent results in Figures 3.8, 3.9 and 3.10 and as it was seen in Figure 3.6.

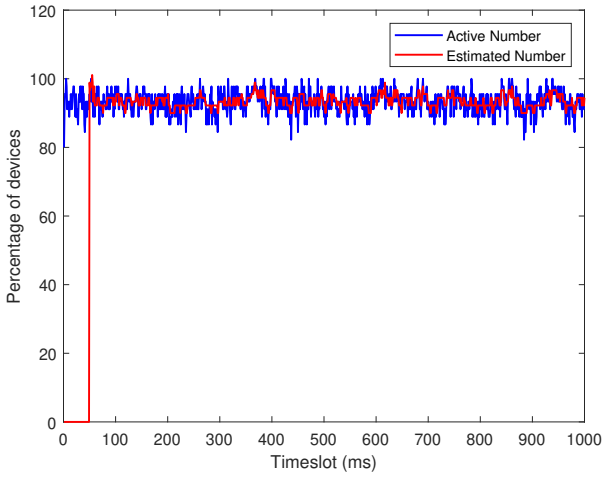

Figure 3.7: Estimation of active IoT devices.

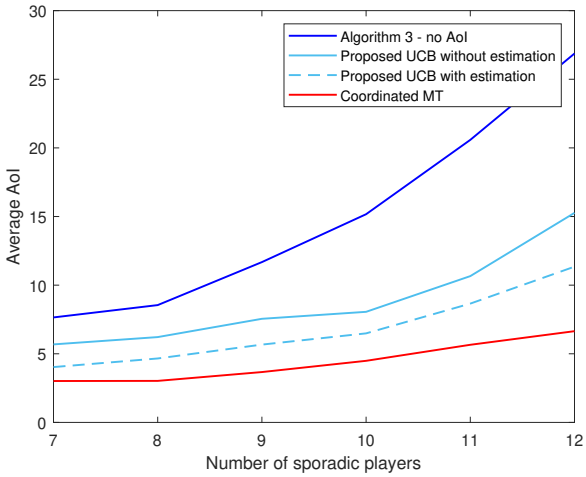

Figure 3.8: Average AoI for a varying number of devices with sporadic traffic.

In Figures 3.8 and 3.9, we show the average AoI while varying the total number of sporadic players and the access probability, respectively. The different variants of the proposed approach significantly decrease the average AoI compared to the method based on Algorithm 3.

In Figure 3.10, the average peak AoI is plotted while keeping the product of access probability and total number of sporadic devices constant and equal to 6. It is observed that the proposed UCB algorithm presents an inflection point around an access probability of 0.2 after which it becomes more efficient in decreasing the AoI. This means that when the number of active devices in the system increases, the method becomes increasingly challenging due to the situation where there are more active devices than available resources to distribute them efficiently.

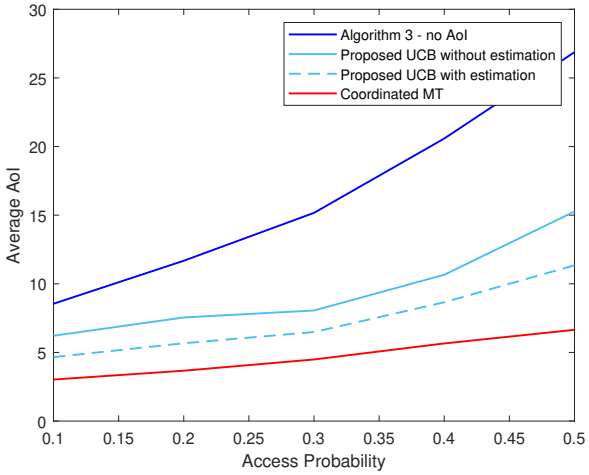

Figure 3.9: Average AoI for a varying access probability for 9 sporadic devices.

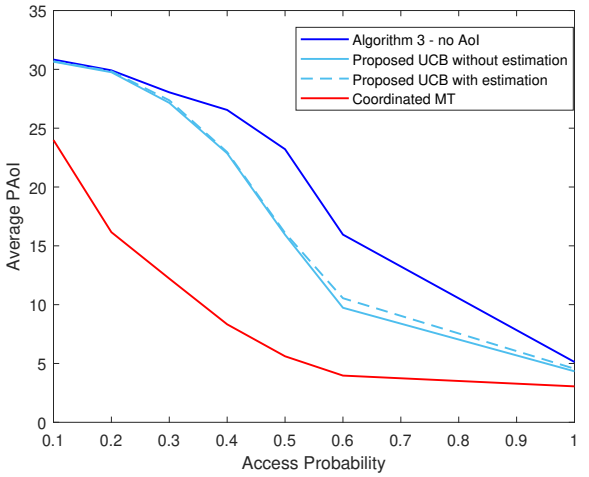

Figure 3.10: Average AoI in the particular case where $p^{a}_{d_i^{spo}} \times n_3 = 6$.

3.9 Summary

In this chapter, the uncoordinated joint subband and power allocation problem was studied in a mixed-traffic NOMA uplink system, with the aim of minimizing the AoI. The problem was formulated using the MAB framework with zero-reward on collisions. An algorithm based on the UCB was proposed to assign devices with different traffic types to the available subband-power level pairs, and to minimize the AoI of non-prioritized users, i.e., users with a non-continuous traffic. The efficiency of this technique in terms AoI minimization and device transmit power, as well as achieved rates maximization, was shown to outperform competing techniques and to closely approach a centralized approach with a perfect knowledge of system and channel state parameters.

Chapter 4

Configuration of Reconfigurable Intelligent Surfaces for NOMA

4.1 Introduction

The use of RISs is being explored as a potential means to improve spectrum and energy efficiencies in wireless networks. By using a vast array of affordable and passive reflecting elements and a control link to the BS, RISs can modify some characteristics of the wireless propagation environment in order to improve the quality of the wireless link. In fact, each reflective element of the RIS can adjust the reflection coefficients of the incident signal, such as the phase shift and the amplitude, in order to increase the signal power at the receiver side. Unlike traditional amplify-and-forward relays, the considered RIS type lacks signal processing capabilities and only passively reflects signals as described in [110, 111]. Added to that, unlike active intelligent surface-based massive multiple-input multiple-output (MIMO) [112], RISs do not suffer from high hardware costs and power consumption. As shown in [113, 114], increasing the number of elements allows RISs to provide superior performance at a reasonable hardware cost and with a manageable power consumption.

In this chapter, we consider an uplink uncoordinated communication system featuring multiple implemented RISs and applying the MAB framework proposed in the previous chapter. IoT devices having various traffic types transmit their messages to the BS. One or more RISs are introduced to improve the quality of the device-to-BS transmissions by offering the possibility of creating a complementary channel. This latter is made-up from two sets of two LoS links. The first LoS link set lies between the IoT devices and the RIS(s) and the second LoS link set lies between the RIS(s) and the BS. The proposed approach targets the creation of NOMA systems with improved spectral and energy efficiencies through the modification of the configuration of the RISs. This can even apply for devices with a single transmitting power value. The work of this chapter constitutes the content of a patent filing and a journal publication ready for submission.

4.1.1 Related Work

As stated in chapter 2, NOMA can achieve massive connectivity and enhance spectral efficiency. In addition to that, NOMA can optimize the system EE, defined as the ratio of total rate to total power consumption. Several research studies have proposed techniques to maximize the system EE in wireless networks using various transmission schemes such as OMA and NOMA. In [115], the authors focus on maximizing both EE and throughput in decoupled 5G heterogeneous networks by optimizing cell association. In [116], the authors propose a downlink NOMA network and maximized EE by optimal sub-channels and power allocation. In [117], EE is maximized through optimal resource allocation and cell selection. In [118], the authors study a simultaneous wireless information and power transfer (SWIPT) scheme to maximize EE while considering limited energy supply constraints. In [119], the authors consider perfect and imperfect channel state information in 5G heterogeneous networks for EE-based user equipment (UE) scheduling and power allocation. Finally, in [120] and [121], heuristic algorithms are proposed to maximize EE by jointly considering UE clustering, subband assignment, and power allocation. Overall, these studies demonstrate the importance of optimizing EE in wireless networks to improve performance and reduce energy consumption.

On a different note, the ability to control channel conditions through adjusting the amplitude and the phase shift of RIS elements compels one to explore the potential benefits of RIS assisted NOMA systems, as demonstrated by recent literature. There have been many works on RIS-assisted NOMA systems in the literature. In [122], the joint optimization of power allocation and phase shifts is studied by using an alternating optimization algorithm and semi-definite relaxation. The authors propose a novel decoding order searching algorithm based on maximizing the combined channel gain of each user. In [123], a multiple-input single-output (MISO) RIS-NOMA transmission model with a fixed decoding order is considered. The phase shift is optimized using zero-forcing beamforming to maximize the SINR under ideal beamforming assumptions, and a low-cost implementation structure is proposed by applying on-off control under finite resolution beamforming. In [124], an algorithm based on effective second-order cone programming alternating direction method of multipliers is proposed for MISO RIS-NOMA systems, assuming perfect SIC decoding order. To reduce complexity, a zero-forcing based sub-optimal algorithm is introduced.

4.1.2 Problem Statement and Contributions

The optimization problems arising from the introduction of a RIS can be complex to solve since the reflection coefficients of the RIS need to be optimized along with other variables, such as transmit power and beamforming vectors. Therefore, it is crucial to design efficient algorithms for RIS-assisted wireless communication systems. In this chapter, we consider an uplink uncoordinated communication system with multiple deployed RISs. Using the MAB framework, IoT devices having different traffic types aim at transmitting their messages to the BS using LoS links with the RIS without any coordination from the BS. To our knowledge, there is no existing work in uplink RIS-assisted NOMA systems on optimizing the subband

assignment, configuration of the RIS elements and power allocation while guaranteeing a target rate for the IoT devices in an uncoordinated manner.

The main contribution of this part of the work is the proposal of a new technique that

- configures the reflective elements of the RIS with the objective of achieving multiple predefined power levels at the decoding BS via the cumulative channel gains. This means that each device transmits using the same power level, and the signal separation is guaranteed via the configuration of the RIS,
- assigns the available spectrum to devices with mixed traffic types in an uncoordinated manner, while maximizing their EE using the MAB framework,
- relies on the BBA algorithm to determine the required number of RISs while guaranteeing the QoS requirements.

The rest of the chapter is organized as follows. In section 4.2, the system model is described, while the considered optimization problem is formulated in section 4.3. Section 4.4 provides the methods to configure the RIS elements and section 4.5 presents the algorithm to solve the EE maximization problem. The proposed algorithms are then evaluated using numerical simulations whose results are provided in section 4.6. Finally, conclusions are drawn in section 4.7.

4.2 System Model

We consider an uplink communication system that includes one BS, I RISs uniformly distributed over the coverage area and comprising M passive reflective elements each, and N IoT devices, as shown in fig. 4.1. Each device has an access probability p_k. Let K be the number of active IoT devices, i.e., transmitting devices. Let $\mathcal{I} = \{1, 2, \ldots, I\}$ be the set of RISs and $\mathcal{K} = \{d_1, d_2, \ldots, d_K\}$ be the set of actives devices. The total system bandwidth B is equally divided into C subbands, each with a bandwidth of $W = B/C$. Denote $\mathcal{K}_c \subset \mathcal{K}$ the subset of devices assigned to the c-th subband. Suppose that one subband can be assigned to K_c devices but each device can be assigned to only one subband per timeslot. In the case where only one device transmits on a subband, the system is operating in an OMA setup.

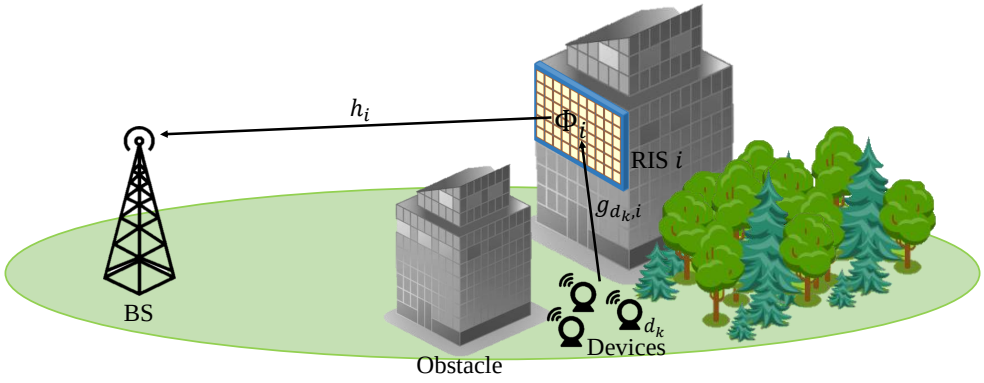

Figure 4.1: System Model

The M passive reflecting elements of a RIS constitute the set $\mathcal{M} = \{1, 2, \ldots, M\}$. The reflecting elements are grouped into S sub-surfaces depending on environment conditions and having almost the same channel conditions with respect to the BS and to each user. Therefore, the reflection coefficients of the i-th RIS can be represented with a matrix $\mathbf{\Phi}_i$ given by:

$$\mathbf{\Phi}_i = \begin{pmatrix} \beta_{1,i} e^{j\phi_{1,i}} & 0 & \cdots & 0 \\ 0 & \beta_{2,i} e^{j\phi_{2,i}} & \cdots & 0 \\ \vdots & \vdots & \ddots & \vdots \\ 0 & 0 & \cdots & \beta_{S,i} e^{j\phi_{S,i}} \end{pmatrix}. \tag{4.1}$$

$\beta_{s,i} \in [0, 1]$ and $\phi_{s,i} \in]-\pi, \pi]$ represent respectively the amplitude and phase shift of the s-th sub-surface in the i-th RIS.

The signal y_c received by the BS over the c-th subband is given by:

$$y_c = \left(\sum_{i=1}^{I} \delta_i \times \mathbf{g}_{d_k,i,c}^T \mathbf{\Phi}_i \mathbf{h}_{i,c} + h_{d_k,c} \right) x_{d_k,c} + n_c. \tag{4.2}$$

In (4.2), $\delta_i \in \{0, 1\}$ is a binary indicator that reflects the non-selection or selection of the RIS i, $\mathbf{g}_{d_k,i,c} \in \mathbb{C}^{S\times 1}$ is a vector comprising the channel gains between the device d_k and each one of the S sub-surfaces of the i-th RIS, over the c-th subband. $(.)^T$ represents the vector transpose. The channel gain vector of size $S \times 1$ between RIS i and the BS is denoted by $\mathbf{h}_{i,c}$, and the channel gain on subband c between device d_k and the BS by $h_{d_k,c}$. $x_{d_k,c}$ is the transmitted signal from device d_k over subband c, while n_c represents the additive Gaussian noise.

In this work, we consider the case where the LoS paths are blocked between the BS and the devices. Thus, the devices-BS channels follow a Rayleigh-distributed fading. We also assume that the RISs are deployed in a way to allow LoS links between the BS and the RIS and also between the RIS and the devices. Hence, the Rician fading channel model is assumed for the device-RIS links and RIS-BS links, leading to the channel gain vector between user d_k and RIS i being given as in [125] by:

$$\mathbf{g}_{d_k,i,c} = PL \left(\sqrt{\frac{\kappa}{1+\kappa}} \mathbf{g}_{d_k,i,c}^{LoS} + \sqrt{\frac{1}{1+\kappa}} \mathbf{g}_{d_k,i,c}^{nLoS} \right), \tag{4.3}$$

where PL denotes the distance-dependent path loss between device d_k and RIS i, κ represents the Rician factor, $\mathbf{g}_{d_k,i,c}^{LoS}$ and $\mathbf{g}_{d_k,i,c}^{nLoS}$ corresponds to the vectors of LoS and nLoS small-scale fading components. Note that when $\kappa = 0$, the channel is considered to follow a Rayleigh fading because of the sole existence of the nLoS components. Similarly, the channel gain vector between

the BS and RIS i over subband c, $\mathbf{h}_{i,c}$, is defined as:

$$\mathbf{h}_{i,c} = PL\left(\sqrt{\frac{\kappa}{1+\kappa}}\mathbf{h}_{i,c}^{LoS} + \sqrt{\frac{1}{1+\kappa}}\mathbf{h}_{i,c}^{nLoS}\right), \tag{4.4}$$

with $\mathbf{h}_{i,c}^{LoS}$ and $\mathbf{h}_{i,c}^{nLoS}$ being the small scale LoS and nLoS components respectively.

We assume that channel state information is available at the BS level simply through estimation. The known information relates to that of the aggregated channel, i.e. $\mathbf{g}_{d_k,i,c} \circ \mathbf{h}_{i,c}$, with $\circ$ the Hadamard product. However, the BS has no knowledge regarding of either device-RIS or RIS-BS channels separately.

4.2.1 NOMA Model

The uplink NOMA power allocation scheme is inspired from [81] and [33] and designed in a way to guarantee a minimum requested rate for each device. Let L be the available received power levels per subband, i.e., $v_1, v_2, \ldots, v_L$ such that $v_1 > \ldots > v_L$. Let $\Gamma_{l,req}$ be the minimum required SINR to correctly decode the signal of each IoT device. It is shown in Appendix A that the l-th received power level guarantees $\Gamma_{l,req}$, while facing Q_k collisions on each power level k lower than l, if and only if:

$$v_l = \sigma^2 \Gamma_{l,req} \prod_{k=l+1}^{L} (Q_k \Gamma_{k,req} + 1), \tag{4.5}$$

where σ^2 is the additive Gaussian noise power.

For successful SIC decoding, devices transmitting on the same subband must have unique received power levels v_l. In the case where the same power level is used by multiple users, a collision occurs, rendering all signals received with the same power level, as well as with lower power levels, non-decodable. However, upper-level signals remain decodable as long as the number of colliding signals on each lower level l is less than or equal to Q_l. In order to prevent a collision, the maximum number of devices per subband, K_c, must satisfy:

$$K_c \leq L. \tag{4.6}$$

In our system, each device transmits with a constant transmit power:

$$P_{d_k}^t = P, \tag{4.7}$$

where t is the timeslot index. The separation of the signals at the receiver is done by the different power levels of the considered NOMA model and guaranteed through the configuration of the reflecting elements of the RIS. This type of configuration can be particularly appealing for sensors with a low-cost radio-frequency front-end.

4.2.2 Uncoordinated Resource Allocation

In a system where spectrum access is uncoordinated, devices strive to organize their transmissions autonomously, without relying on any external intervention. In order to solve the problem of subband allocation, a multi-player MAB framework with zero reward in case of collision is adopted [29]. The set of players consists of the set of devices $\mathcal{K}$, and the set of actions available to each player d_k is the set of available subbands $\mathcal{A}_{d_k}$.

When playing an action, assuming no collision, the device receives a reward equivalent to its achieved rate given by Shannon's formula [30]:

$$R_{d_k,c} = W \log_2(1 + \Gamma_{d_k,c}), \tag{4.8}$$

where $\Gamma_{d_k,c}$ is the achieved SINR of device d_k on the c-th subband, given by:

$$\Gamma_{d_k,c} = \frac{v_l}{\sum_{j=l+1}^{L} v_j + \sigma^2}. \tag{4.9}$$

In (4.9), $v_l = P^t_{d_k} \times \left| \sum_{i=1}^{I} \delta_i \times \mathbf{g}^T_{d_k,i,c} \mathbf{\Phi}_i \mathbf{h}_{i,c} + h_{d_k,c} \right|^2$ is the received power level configured by the RIS for detecting the signal of device d_k. In the denominator, each v_j corresponds to a received power level configured for a user whose signal has not been retrieved yet (i.e. whose decoding order comes after that of d_k's signal). Hence, $\sum_{j=l+1}^{L} v_j$ is the residual NOMA interference not canceled by SIC. Note that (4.9) is expressed here for the particular case where each one of the levels $l+1$ to L is attributed by the BS to one device on subband c. In general, some levels may not be attributed in some timeslots (*e.g.* if less than L users access the subband c), and more than one device may be attributed to the same power level (*e.g.* if more than L devices access the subband c).

If the number of devices that have selected the same subband c at a timeslot t is larger than the total number of power levels, i.e., if $K_c > L$, a collision occurs leading to a failure in decoding the involved signals of the devices. Let η_{d_k} be the collision indicator for device d_k on subband c:

$$\eta_{d_k,c} = \begin{cases} 0, & \text{in case of a collision,} \\ 1, & \text{otherwise.} \end{cases} \tag{4.10}$$

The reward that a device obtains when selecting a subband c is therefore given by:

$$U_{d_k,c} = \eta_{d_k,c} \times R_{d_k,c}. \tag{4.11}$$

Since the system is uncoordinated, no communication occurs between the devices. In fact, each device has only access to its own list of played actions and their corresponding rewards. Since the rewards are unknown beforehand, an exploration phase is needed to learn them.

4.3 Problem Formulation

The main purpose of this study is to optimize the RIS selection and the configuration of the reflecting elements in a way to maximize the EE of the system given by:

$$EE = \frac{\sum_{c=1}^{C} \sum_{k=1}^{K_c} R_{d_k,c}}{\sum_{k=1}^{K} P^t_{d_k} + P_{BS} + \sum_{i=1}^{I} \delta_i \times P_{RIS}}. \tag{4.12}$$

In (4.12), the numerator represents the total achieved rate while the denominator represents the total consumed power. $\sum_{i=1}^{K} P^t_{d_k}$ is the total transmit power of the devices, while P_{BS} is the power consumed by the BS. It is expressed by:

$$P_{BS} = BP_{BS} + PP_{BS}, \tag{4.13}$$

where BP_{BS} represents the base power consumed by the BS when it is turned on, PP_{BS} is the power consumed by the base station to process the incoming signals and data, and depends on the traffic load and the control power needed to configure the RIS elements. Finally, P_{RIS} represents the circuit power of a RIS to control its reflecting elements.

The optimization problem can be formulated as follows:

$$\max_{\delta_j, \Phi_j} EE, \tag{4.14}$$

such that:

$$P^t_{d_k} \times \left| \sum_{i=1}^{I} \delta_i \times \mathbf{g}^T_{d_k,i,c} \mathbf{\Phi}_i \mathbf{h}_{i,c} + h_{d_k,c} \right|^2 \in \{v_1, v_2, \ldots, v_L\}, \tag{4.14a}$$

$$\sum_{c} \mathbf{\Omega}_{d_k,c} R_{d_k,c} \geq R_{d_k,req}, \forall d_k \in \mathcal{K}, \tag{4.14b}$$

$$\delta_i \in \{0,1\}, \forall i \in \mathcal{I}, \tag{4.14c}$$

$$\phi_{s,i} \in]-\pi, \pi], s = 1, 2, \ldots, S, \forall i \in \mathcal{I}, \tag{4.14d}$$

$$\beta_{s,i} \in [0,1], s = 1, 2, \ldots, S, \forall i \in \mathcal{I}. \tag{4.14e}$$

Constraint (4.14a) guarantees that the received power level is equivalent to one of the predefined power levels by the SIC decoder. (4.14b) represents the rate constraints for the devices, where $R_{d_k,req}$ is the minimum required rate by device d_k. In (4.14b), $\mathbf{\Omega}_{d_k,c} = 1$ if device d_k transmits using subband c, and 0 otherwise. In (4.14c), $\delta_i = 1$ if the i-th RIS is turned on. (4.14d) and (4.14e) are respectively the phase shift and amplitude constraints for the configuration of the RIS elements.

Problem (4.14) is a mixed-integer and non-convex optimization problem. In order to solve it, we refer to the BBA algorithm [32] for the RIS selection. At each step of the algorithm, the configuration of one or several simultaneous RISs is done depending on the tested number of RISs. Note that the RIS elements are configured in a way to achieve the values of the predefined

power levels while allocating the devices to their subbands in an uncoordinated manner.

4.4 Subband Allocation and RIS Configuration Algorithm

We start by describing the uncoordinated allocation technique where users are assigned subbands through the UCB algorithm [106]. This algorithm consists of two phases: exploration and exploitation. In the exploration phase, the devices learn the performance of the arms, which are the subbands, by identifying their rewards before the exploitation phase where they select the arm having the best reward. In this work, each IoT device chooses its arm in a way to maximize its achieved rate. However, the achieved rates depend on the number of users transmitting on the same subband, K_c, and on the configuration of the RIS reflective elements, i.e., Φ_i. Therefore, we first proceed to the description of the configuration technique by which the coefficients of each RIS are determined in a way to allow the successful decoding of the non-orthogonally multiplexed signals. The problem is first formulated using one RIS (with different numbers of sub-surfaces), then it is generalized for the joint configuration of multiple RISs. In the sequel, the RIS index is first dropped to simplify the notations and calculations for the case of one RIS, and will be used for the case of configuring multiple RISs. The subband index c is omitted when the description focuses on a single subband.

4.4.1 Configuration of the Reflecting Elements of a RIS

To formulate the configuration of a RIS, we first consider the special cases of a RIS having 2 or 3 sub-surfaces, then generalize the study to S sub-surfaces.

4.4.1.1 RIS with two sub-surfaces

We first consider the case of a RIS with two sub-surfaces serving two devices over a single subband with two available receive power levels v_1 and v_2 formulated as in equation (4.5). We assume that the BS associates the device presenting the highest channel gain of the aggregated channel to the highest power level v_1, while the other device is associated to v_2. The reasoning of this assumption is also extended to the case of more than two devices/users in the rest of the work. To guarantee the reception of the signals with power levels v_1 and v_2, Φ must satisfy the following equations:

$$\begin{cases} v_1 = P^t_{d_1} \left| \mathbf{g}^T_{d_1} \Phi \mathbf{h} + h_{d_1} \right|^2, \\ v_2 = P^t_{d_2} \left| \mathbf{g}^T_{d_2} \Phi \mathbf{h} + h_{d_2} \right|^2. \end{cases} \tag{4.15}$$

By inspecting (4.15), it can be noted that, in the general setup with an arbitrary number of sub-sufaces, the number of available power levels L should not exceed the total number of sub-surfaces.

Let $g_{d_k,s} = \mathfrak{g}_{d_k,s} e^{j\theta_{g_{d_k,s}}}, s = 1, 2$, denote the sth element of $\mathbf{g}_{d_k}$ where $\mathfrak{g}_{d_k,s}$ is the amplitude of $g_{d_k,s}$ and $\theta_{g_{d_k,s}}$ its angular phase. Moreover, $h_s = \mathfrak{h}_s e^{j\theta_{h_s}}, s = 1, 2$, represents the sth element of $\mathbf{h}$ where $\mathfrak{h}_s$ is the amplitude of h_s and θ_{h_s} its angular phase. After some manipulations, (4.15)

can be re-written as:

$$\begin{cases} \frac{v_1}{P^t_{d_1}} = |\mathcal{X}_1 + j\mathcal{Y}_1|^2, \\ \frac{v_2}{P^t_{d_2}} = |\mathcal{X}_2 + j\mathcal{Y}_2|^2, \end{cases} \tag{4.16}$$

with:

$$\mathcal{X}_k = \mathfrak{g}_{d_k,1}\mathfrak{h}_1\beta_1 \cos\left(\phi_1 + \theta_{g_{d_k,1}} + \theta_{h_1}\right) + \mathfrak{g}_{d_k,2}\mathfrak{h}_2\beta_2 \cos\left(\phi_2 + \theta_{g_{d_k,2}} + \theta_{h_2}\right) + \mathfrak{h}_{d_1} \cos\left(\theta_{h_{d_k}}\right), \tag{4.17}$$

and

$$\mathcal{Y}_k = \mathfrak{g}_{d_k,1}\mathfrak{h}_1\beta_1 \sin\left(\phi_1 + \theta_{g_{d_k,1}} + \theta_{h_1}\right) + \mathfrak{g}_{d_k,2}\mathfrak{h}_2\beta_2 \sin\left(\phi_2 + \theta_{g_{d_k,2}} + \theta_{h_2}\right) + \mathfrak{h}_{d_1} \sin\left(\theta_{h_{d_k}}\right), \tag{4.18}$$

with $h_{d_k} = \mathfrak{h}_{d_k} e^{j\theta_{h_{d_k}}}$ the polar form of h_{d_k}.

Let $\psi_{d_k,s} = \phi_s + \theta_{g_{d_k,s}} + \theta_{h_s}$. By developing and simplifying the expressions, (4.16) can be expressed as:

$$\begin{cases} \frac{v_1}{P^t_{d_1}} = \left(\mathfrak{g}_{d_1,1}\mathfrak{h}_1\beta_1\right)^2 + \left(\mathfrak{g}_{d_1,2}\mathfrak{h}_2\beta_2\right)^2 + \left(\mathfrak{h}_{d_1}\right)^2 + 2\mathfrak{g}_{d_1,1}\mathfrak{g}_{d_1,2}\mathfrak{h}_1\mathfrak{h}_2\beta_1\beta_2 \cos\left(\psi_{d_1,1} - \psi_{d_1,2}\right) \\ \qquad +2\mathfrak{g}_{d_1,1}\mathfrak{h}_1\mathfrak{h}_{d_1}\beta_1 \cos\left(\psi_{d_1,1} - \theta_{h_{d_1}}\right) + 2\mathfrak{g}_{d_1,2}\mathfrak{h}_2\mathfrak{h}_{d_1}\beta_2 \cos\left(\psi_{d_1,2} - \theta_{h_{d_1}}\right), \\ \frac{v_2}{P^t_{d_2}} = \left(\mathfrak{g}_{d_2,1}\mathfrak{h}_1\beta_1\right)^2 + \left(\mathfrak{g}_{d_2,2}\mathfrak{h}_2\beta_2\right)^2 + \left(\mathfrak{h}_{d_2}\right)^2 + 2\mathfrak{g}_{d_2,1}\mathfrak{g}_{d_2,2}\mathfrak{h}_1\mathfrak{h}_2\beta_1\beta_2 \cos\left(\psi_{d_2,1} - \psi_{d_2,2}\right) \\ \qquad +2\mathfrak{g}_{d_2,1}\mathfrak{h}_1\mathfrak{h}_{d_2}\beta_1 \cos\left(\psi_{d_2,1} - \theta_{h_{d_2}}\right) + 2\mathfrak{g}_{d_2,2}\mathfrak{h}_2\mathfrak{h}_{d_2}\beta_2 \cos\left(\psi_{d_2,2} - \theta_{h_{d_2}}\right). \end{cases} \tag{4.19}$$

Assume that the totality of the signal is reflected by the RIS, hence $\beta_s = 1, s = 1, 2$. By replacing $\psi_{d_k,s}$ by its value and expanding, one can show that (4.19) can be expressed as:

$$\begin{cases} f_1(x_1x_2 + y_1y_2)\cos(F_1) - f_1(x_1y_2 - x_2y_1)\sin(F_1) + f_2x_1\cos(F_2) \\ \qquad -y_1f_2\sin(F_2) + x_2f_3\cos(F_3) - y_2f_3\sin(F_3) = J_1, \\ f_4(x_1x_2 + y_1y_2)\cos(F_4) - f_4(x_1y_2 - x_2y_1)\sin(F_4) + f_5x_1\cos(F_5) \\ \qquad -y_1f_5\sin(F_5) + x_2f_6\cos(F_6) - y_2f_6\sin(F_6) = J_2, \\ x_1^2 + y_1^2 = 1, \\ x_2^2 + y_2^2 = 1. \end{cases} \tag{4.20}$$

In (4.20):

$$\begin{cases} J_i = \frac{v_i}{P^t_{d_k}} - \left(\mathfrak{g}_{d_k,1}\mathfrak{h}_1\right)^2 - \left(\mathfrak{g}_{d_k,2}\mathfrak{h}_2\right)^2 - \left(\mathfrak{h}_{d_1}\right)^2, \forall i \in \{1,2\}, \\ f_1 = 2\mathfrak{g}_{d_1,1}\mathfrak{g}_{d_1,2}\mathfrak{h}_1\mathfrak{h}_2, \\ f_2 = 2\mathfrak{g}_{d_1,1}\mathfrak{h}_1\mathfrak{h}_{d_1}, \\ f_3 = 2\mathfrak{g}_{d_1,2}\mathfrak{h}_2\mathfrak{h}_{d_1}, \\ f_4 = 2\mathfrak{g}_{d_2,1}\mathfrak{g}_{d_2,2}\mathfrak{h}_1\mathfrak{h}_2, \\ f_5 = 2\mathfrak{g}_{d_2,1}\mathfrak{h}_1\mathfrak{h}_{d_2}, \\ f_3 = 2\mathfrak{g}_{d_2,2}\mathfrak{h}_2\mathfrak{h}_{d_2}, \\ F_1 = \theta_{g_{d_1,1}} + \theta_{h_1} - \theta_{g_{d_1,2}} - \theta_{h_2}, \\ F_2 = \theta_{g_{d_1,1}} + \theta_{h_1} - \theta_{h_{d_1}}, \\ F_3 = \theta_{g_{d_1,2}} + \theta_{h_2} - \theta_{h_{d_1}}, \\ F_4 = \theta_{g_{d_2,1}} + \theta_{h_1} - \theta_{g_{d_2,2}} - \theta_{h_2}, \\ F_5 = \theta_{g_{d_2,1}} + \theta_{h_1} - \theta_{h_{d_2}}, \\ F_6 = \theta_{g_{d_2,2}} + \theta_{h_2} - \theta_{h_{d_2}}, \\ x_s = \cos(\phi_s), \forall s \in \{1,2\}, \\ y_s = \sin(\phi_s), \forall s \in \{1,2\}. \end{cases} \tag{4.21}$$

The resulting system (4.21) is non-linear. Hence, it is solved iteratively using the Levenberg-Marquardt algorithm [126], with properly chosen initial values of x_0 and y_0 to find the optimal values of x_s and y_s, $s \in \{1,2\}$.

4.4.1.2 RIS with three sub-surfaces

A similar development can be conducted for the case of a RIS with 3 sub-surfaces, 3 devices, one subband, and 3 available received power levels. The system can be expressed as follows:

$$\begin{cases} \frac{v_1}{P^t_{d_1}} = \left(\mathfrak{g}_{d_1,1}\mathfrak{h}_1\beta_1\right)^2 + \left(\mathfrak{g}_{d_1,2}\mathfrak{h}_2\beta_2\right)^2 + \left(\mathfrak{g}_{d_1,3}\mathfrak{h}_3\beta_3\right)^2 + \left(\mathfrak{h}_{d_1}\right)^2 + 2\mathfrak{g}_{d_1,1}\mathfrak{g}_{d_1,2}\mathfrak{h}_1\mathfrak{h}_2\beta_1\beta_2\cos\left(\psi_{d_1,1}-\psi_{d_1,2}\right) \\ +2\mathfrak{g}_{d_1,1}\mathfrak{g}_{d_1,3}\mathfrak{h}_1\mathfrak{h}_3\beta_1\beta_3\cos\left(\psi_{d_1,1}-\psi_{d_1,3}\right) + 2\mathfrak{g}_{d_1,2}\mathfrak{g}_{d_1,3}\mathfrak{h}_2\mathfrak{h}_3\beta_2\beta_3\cos\left(\psi_{d_1,2}-\psi_{d_1,3}\right) \\ +2\mathfrak{g}_{d_1,1}\mathfrak{h}_1\mathfrak{h}_{d_1}\beta_1\cos\left(\psi_{d_1,1}-\theta_{h_{d_1}}\right) + 2\mathfrak{g}_{d_1,2}\mathfrak{h}_2\mathfrak{h}_{d_1}\beta_2\cos\left(\psi_{d_1,2}-\theta_{h_{d_1}}\right) \\ +2\mathfrak{g}_{d_1,3}\mathfrak{h}_3\mathfrak{h}_{d_1}\beta_3\cos\left(\psi_{d_1,3}-\theta_{h_{d_1}}\right), \\ \\ \frac{v_2}{P^t_{d_2}} = \left(\mathfrak{g}_{d_2,1}\mathfrak{h}_1\beta_1\right)^2 + \left(\mathfrak{g}_{d_2,2}\mathfrak{h}_2\beta_2\right)^2 + \left(\mathfrak{g}_{d_2,3}\mathfrak{h}_3\beta_3\right)^2 + \left(\mathfrak{h}_{d_2}\right)^2 + 2\mathfrak{g}_{d_2,1}\mathfrak{g}_{d_2,2}\mathfrak{h}_1\mathfrak{h}_2\beta_1\beta_2\cos\left(\psi_{d_2,1}-\psi_{d_2,2}\right) \\ +2\mathfrak{g}_{d_2,1}\mathfrak{g}_{d_2,3}\mathfrak{h}_1\mathfrak{h}_3\beta_1\beta_3\cos\left(\psi_{d_2,1}-\psi_{d_2,3}\right) + 2\mathfrak{g}_{d_2,2}\mathfrak{g}_{d_2,3}\mathfrak{h}_2\mathfrak{h}_3\beta_2\beta_3\cos\left(\psi_{d_2,2}-\psi_{d_2,3}\right) \\ +2\mathfrak{g}_{d_2,1}\mathfrak{h}_1\mathfrak{h}_{d_2}\beta_1\cos\left(\psi_{d_2,1}-\theta_{h_{d_2}}\right) + 2\mathfrak{g}_{d_2,2}\mathfrak{h}_2\mathfrak{h}_{d_2}\beta_2\cos\left(\psi_{d_2,2}-\theta_{h_{d_2}}\right) \\ +2\mathfrak{g}_{d_2,3}\mathfrak{h}_3\mathfrak{h}_{d_2}\beta_3\cos\left(\psi_{d_2,3}-\theta_{h_{d_2}}\right), \\ \\ \frac{v_3}{P^t_{d_3}} = \left(\mathfrak{g}_{d_3,1}\mathfrak{h}_1\beta_1\right)^2 + \left(\mathfrak{g}_{d_3,2}\mathfrak{h}_2\beta_2\right)^2 + \left(\mathfrak{g}_{d_3,3}\mathfrak{h}_3\beta_3\right)^2 + \left(\mathfrak{h}_{d_3}\right)^2 + 2\mathfrak{g}_{d_3,1}\mathfrak{g}_{d_3,2}\mathfrak{h}_1\mathfrak{h}_2\beta_1\beta_2\cos\left(\psi_{d_3,1}-\psi_{d_3,2}\right) \\ +2\mathfrak{g}_{d_3,1}\mathfrak{g}_{d_3,3}\mathfrak{h}_1\mathfrak{h}_3\beta_1\beta_3\cos\left(\psi_{d_3,1}-\psi_{d_3,3}\right) + 2\mathfrak{g}_{d_3,2}\mathfrak{g}_{d_3,3}\mathfrak{h}_2\mathfrak{h}_3\beta_2\beta_3\cos\left(\psi_{d_3,2}-\psi_{d_3,3}\right) \\ +2\mathfrak{g}_{d_3,1}\mathfrak{h}_1\mathfrak{h}_{d_3}\beta_1\cos\left(\psi_{d_3,1}-\theta_{h_{d_3}}\right) + 2\mathfrak{g}_{d_3,2}\mathfrak{h}_2\mathfrak{h}_{d_3}\beta_2\cos\left(\psi_{d_3,2}-\theta_{h_{d_3}}\right) \\ +2\mathfrak{g}_{d_3,3}\mathfrak{h}_3\mathfrak{h}_{d_3}\beta_3\cos\left(\psi_{d_3,3}-\theta_{h_{d_3}}\right). \end{cases} \tag{4.22}$$

and then solved iteratively as in the case of two sub-surfaces.

4.4.1.3 RIS with S sub-surfaces

In order to generalize the proposed approach, we consider the case of a RIS having S sub-surfaces, with K devices transmitting over one subband using L received power levels. To simplify the derivations and without loss of generality, we consider in the following that $\beta_s = 1, \forall s$. Indeed, several combinations of β_s and ϕ_s can jointly lead to the same solution for a configuration. Hence, considering $\beta_s = 1$ does not restrict the pool of potential configuration solutions.

The general constraint to satisfy in order to guarantee the discrete received power levels v_l is expressed by:

$$v_{d_k} = P^t_{d_k}\left|\mathbf{g}^T_{d_k}\mathbf{\Phi}\mathbf{h} + h_{d_k}\right|^2, \tag{4.23}$$

where v_{d_k} is the power level chosen by d_k.

By developing and expanding (4.23), as was done in the cases of two and three sub-surfaces,

the system of equations can be written as:

$$\frac{v_{d_k}}{P^t_{d_k}} = \sum_{s=1}^{S} \left(\mathfrak{g}_{d_k,s}\mathfrak{h}_s\right)^2 + \mathfrak{h}^2_{d_k} + 2\sum_{s=1}^{S-1}\sum_{s'=s+1}^{S} \mathfrak{g}_{d_k,s}\mathfrak{h}_s\mathfrak{g}_{d_k,s'}\mathfrak{h}_{s'}\cos\left(\psi_{d_k,s} - \psi_{d_k,s'}\right) + 2\sum_{s=1}^{S} \mathfrak{g}_{d_k,s}\mathfrak{h}_s\mathfrak{h}_{d_k}\cos\left(\psi_{d_k,s} - \theta_{h_{d_k}}\right), \tag{4.24}$$

with $\psi_{d_k,s} = \phi_s + \theta_{g_{d_k,s}} + \theta_{h_s}$.

By further developing the expression of $\psi_{d_k,s}$, we get:

$$\begin{aligned}\frac{v_{d_k}}{P^t_{d_k}} = \sum_{s=1}^{S} \left(\mathfrak{g}_{d_k,s}\mathfrak{h}_s\right)^2 + \mathfrak{h}^2_{d_k} &+ 2\sum_{s=1}^{S-1} \mathfrak{g}_{d_k,s}\mathfrak{h}_s\cos\phi_s \sum_{s'=s+1}^{S} \mathfrak{g}_{d_k,s'}\mathfrak{h}_{s'}\cos F_{d_k,s,s'}\cos\phi_{s'} \\ &+2\sum_{s=1}^{S-1} \mathfrak{g}_{d_k,s}\mathfrak{h}_s\sin\phi_s \sum_{s'=s+1}^{S} \mathfrak{g}_{d_k,s'}\mathfrak{h}_{s'}\cos F_{d_k,s,s'}\sin\phi_{s'} \\ &-2\sum_{s=1}^{S-1} \mathfrak{g}_{d_k,s}\mathfrak{h}_s\sin\phi_s \sum_{s'=s+1}^{S} \mathfrak{g}_{d_k,s'}\mathfrak{h}_{s'}\sin F_{d_k,s,s'}\cos\phi_{s'} \\ &+2\sum_{s=1}^{S-1} \mathfrak{g}_{d_k,s}\mathfrak{h}_s\cos\phi_s \sum_{s'=s+1}^{S} \mathfrak{g}_{d_k,s'}\mathfrak{h}_{s'}\sin F_{d_k,s,s'}\sin\phi_{s'} \\ &+2\mathfrak{h}_{d_k}\sum_{s=1}^{S} \mathfrak{g}_{d_k,s}\mathfrak{h}_s\cos G_{d_k,s}\cos\phi_s \\ &-2\mathfrak{h}_{d_k}\sum_{s=1}^{S} \mathfrak{g}_{d_k,s}\mathfrak{h}_s\sin G_{d_k,s}\sin\phi_s,\end{aligned} \tag{4.25}$$

with:

$$\begin{cases} F_{d_k,s,s'} = \theta_{g_{d_k,s}} - \theta_{g_{d_k,s'}} + \theta_{h_s} - \theta_{h_{s'}}, \\ G_{d_k,s} = \theta_{g_{d_k,s}} + \theta_{h_s} - \theta_{h_{d_k}}. \end{cases} \tag{4.26}$$

Since $\cos^2\phi_s + \sin^2\phi_s = 1$, the system is a non-linear system of n equations with n unknowns. To solve it, the values of $\cos(\phi_s)$ and $\sin(\phi_s)$, $s = 1, \ldots, S$, that satisfy all n equations need to be found simultaneously. This can be done using various methods such as substitution or matrix inversion. Appendix B contains the details of the mathematical proof. Then, the angles are obtained at the BS. Their configuration is sent to the RIS through the control link between the BS and the RIS.

As for the power level configuration, it should be noted that the order in which devices are assigned to power levels by the BS affects the RIS configuration. In other words, the values of the RIS coefficients are dependent on which user d_k is attributed by the BS to a particular power level v_l, generally speaking the ordered matching of devices to power levels. In the following, the device having the highest aggregated channel gain is allocated to the highest power level v_1, the device with the second highest aggregated channel gain is allocated to the second highest power level and so on until each device is allocated to a specific power level. In the case where the number of transmitting devices on a subband c exceeds the total number of available power levels

L, the BS performs the RIS configuration in a way that all the collisions are considered to have taken place on the lowest power level. This way, these collisions do not cause decoding failures on the higher power level signals, as long as the number of collisions is lower than Q_L. In the case where the number of devices on the lowest power level exceeds Q_L, all devices transmitting on the corresponding subband receive a zero reward from the BS.

The studied problem so far aims to configure the RIS over one subband. For a multiple-subband system, the same problem is formulated for each subband separately. Then, each sub-problem is solved independently and the solutions with the common values of the angles are found, knowing that each sub-problem usually yields several possible solutions by the proposed iterative method. In the case where common values cannot be found, we propose two approaches as a way forward: Either the BS swaps randomly the attribution of users to power levels to find a common solution, or the BS chooses the subband having the highest number of available solutions as a reference with which the BS configures the RIS. The BS then sends to the devices that use this reference subband their achieved rates as rewards. Moreover, it sends zero rewards to the other users in order to encourage them to change their played actions, i.e., transmit data on different subbands in the aim of exploring alternative subband allocations to find a common solution for the whole system. If such a solution is not found, the allocation that satisfies the largest number of users/devices is retained.

4.4.2 Case of Multiple RISs with S Sub-Surfaces

In this section, we consider the case where multiple RISs are simultaneously used for signal communication. Dealing with multiple RISs is a bit similar to dealing with one RIS with multiple sub-surfaces. In fact, considering I RISs with S sub-surfaces each is equivalent to formulating the problem for one RIS with $S \times I$ sub-surfaces. However, the vector of channel gains denoted by $\mathbf{g}_{d_k,i,c}$ linking a RIS i with a device d_k, and the vector of channel gains denoted by $\mathbf{h}_{i,c}$ linking the RIS i and the BS are generally different from those corresponding to another RIS j. Indeed, this depends on the geographical positions of the different RISs.

Let J be the number of active RISs with $J \leq I$. All J RISs are to be jointly configured in order to guarantee the reception of the signals of all devices, each with a different power level. The general constraint to satisfy with one subband is given by:

$$v_{d_k} = P^t_{d_k} \left| \sum_{j=1}^{J} \mathbf{g}^T_{d_k,j} \mathbf{\Phi}_j \mathbf{h}_j + h_{d_k} \right|^2 . \tag{4.27}$$

The problem is then formulated as if having one RIS with $S \times J$ sub-surfaces as follows:

$$v_{d_k} = P^t_{d_k} \left| \underline{\mathbf{g}}^T_{d_k} \mathbf{\Phi} \underline{\mathbf{h}} + h_{d_k} \right|^2 , \tag{4.28}$$

where $\underline{\mathbf{g}}^T_{d_k} = \left[\mathbf{g}^T_{d_k,1} \mathbf{g}^T_{d_k,2} ... \mathbf{g}^T_{d_k,J} \right]$ represent the concatenated channels between the device d_k and all the J RISs and $\underline{\mathbf{h}} = [\mathbf{h}_1; \mathbf{h}_2; ...; \mathbf{h}_J]$ denotes the concatenated channels between the J RISs and the BS. Similar mathematical developments and expansions to the case of S sub-surfaces

are made. Hence, this leads to:

$$\begin{aligned}\frac{v_{d_k}}{P^t_{d_k}} = \sum_{s=1}^{S\times J}\left(\underline{\mathfrak{g}}_{d_k,s}\underline{\mathfrak{h}}_s\right)^2 + \mathfrak{h}_{d_k}^2 + 2\sum_{s=1}^{S\times J-1}\underline{\mathfrak{g}}_{d_k,s}\underline{\mathfrak{h}}_s\cos\phi_s\sum_{s'=s+1}^{S\times J}\underline{\mathfrak{g}}_{d_k,s'}\underline{\mathfrak{h}}_{s'}\cos F_{d_k,s,s'}\cos\phi_{s'}\\ +2\sum_{s=1}^{S\times J-1}\underline{\mathfrak{g}}_{d_k,s}\underline{\mathfrak{h}}_s\sin\phi_s\sum_{s'=s+1}^{S\times J}\underline{\mathfrak{g}}_{d_k,s'}\underline{\mathfrak{h}}_{s'}\cos F_{d_k,s,s'}\sin\phi_{s'}\\ -2\sum_{s=1}^{S\times J-1}\underline{\mathfrak{g}}_{d_k,s}\underline{\mathfrak{h}}_s\sin\phi_s\sum_{s'=s+1}^{S\times J}\underline{\mathfrak{g}}_{d_k,s'}\underline{\mathfrak{h}}_{s'}\sin F_{d_k,s,s'}\cos\phi_{s'}\\ +2\sum_{s=1}^{S\times J-1}\underline{\mathfrak{g}}_{d_k,s}\underline{\mathfrak{h}}_s\cos\phi_s\sum_{s'=s+1}^{S\times J}\underline{\mathfrak{g}}_{d_k,s'}\underline{\mathfrak{h}}_{s'}\sin F_{d_k,s,s'}\sin\phi_{s'}\\ +2\mathfrak{h}_{d_k}\sum_{s=1}^{S\times J}\underline{\mathfrak{g}}_{d_k,s}\underline{\mathfrak{h}}_s\cos G_{d_k,s}\cos\phi_s\\ -2\mathfrak{h}_{d_k}\sum_{s=1}^{S\times J}\underline{\mathfrak{g}}_{d_k,s}\underline{\mathfrak{h}}_s\sin G_{d_k,s}\sin\phi_s.\end{aligned} \tag{4.29}$$

The corresponding proposed solutions for subband allocation and RIS elements configuration are summarized in Algorithm 6.

4.4.3 Robustness to Channel Gain Estimation Errors

Since the proposed RIS configuration algorithms depend upon the knowledge of the aggregated channel, the aim of this section is to propose a simple assessment method for their robustness against channel estimation errors.

Consider that

- $\hat{\underline{\mathbf{g}}}_{d_k,c}$ are the estimated channels of $\underline{\mathbf{g}}_{d_k,c}$ between device d_k and the sub-surfaces of the different RISs,
- $\hat{\underline{\mathbf{h}}}_c$ are the estimated channels of $\underline{\mathbf{h}}_c$ between the sub-surfaces and the BS,
- $\hat{h}_{d_k,c}$ are the estimated channels of $h_{d_k,c}$ between device d_k and the BS,

with:

- $\hat{\underline{\mathbf{g}}}_{d_k,c} = \underline{\mathbf{g}}_{d_k,c} + \epsilon_{est,\underline{\mathbf{g}}}$,
- $\hat{\underline{\mathbf{h}}}_c = \underline{\mathbf{h}}_c + \epsilon_{est,\underline{\mathbf{h}}}$,
- $\hat{h}_{d_k,c} = h_{d_k,c} + \epsilon_{est,h_d}$,

where $\epsilon_{est,\underline{\mathbf{g}}}$, $\epsilon_{est,\underline{\mathbf{h}}}$ and ϵ_{est,h_d} represent the channel estimation error of $\hat{\underline{\mathbf{g}}}_{d_k,c}$, $\hat{\underline{\mathbf{h}}}_c$ and $\hat{h}_{d_k,c}$, respectively. ϵ_{est} being the additive channel estimation error [127]. It follows a normal distribution of zero mean and a variance ϵ_0 equal to a percentage of the amplitude of each of the estimated channels.

Algorithm 6: Proposed RIS-NOMA
Subband Allocation and Configuration of the RIS Elements

Initialization: Each device d_k builds its action profile set $\mathcal{A}_{d_k}$ containing all the available subbands. All devices transmit data using a constant power $P^t_{d_k}$.
for *t=1:T* **do**
  1- On each subband c, the received power levels are allocated by the BS to the devices. For a single RIS i, the allocation is done based on the decreasing order of the aggregated channel gains, i.e. $\mathbf{g}_{d_k,i,c} \circ \mathbf{h}_{i,c}$. For the case of J RISs, the sorting is done using the concatenated aggregated channel gains, i.e. $\underline{\mathbf{g}}_{d_k,c} \circ \underline{\mathbf{h}}_c$.
  When $K_c > L$, all the collisions are assigned to the L-th power level.
  2- Solve the system of equations formulated in (4.29) on each subband independently.
  3- Check for common solutions of the reflection angles for the different subbands.
  In case of a common solution:
  Configure the RIS with the common solution found. Devices transmitting on the subbands receive their achieved rates as rewards.
  4- **In case of no common solution found:**
  Choose the subband with the highest number of solutions as reference. Devices transmitting on this reference receive their achieved rates as rewards, while others receive a zero reward.
  // Subband Allocation at the devices level:
  for *k=1:K* **do**
    // Utility function received from the BS:
    $U_{d_k,a_{j^*}} = \eta_{d_k,c} \times R_{d_k,c}$
    // Best arm identification:
    $a^*_j = \underset{a_j \in \mathcal{A}_{d_k}}{\operatorname{argmax}}\, Q(d_k, a_j) + \sqrt{\frac{2\log(t)}{n_{d_k}(a_j,t)}}$
    // Parameters update:
    $s_k(a^*_j, t+1) = s_i(a^*_j, t) + U_{d_k,a^*_j}$
    $n_k(a^*_j, t+1) = n_i(a^*_j, t) + 1$
    $Q(d_k, a^*_j) = \frac{s_i(a^*_j,t+1)}{n_i(a^*_j,t+1)}$
  end
end

In the case where channel estimation errors are taken into account when running Algorithm 6 following the proposed model, the estimated values of the channel gains are used instead of the perfect ones for the configuration of the RIS elements. Found solutions lead to approximated $\hat{\mathbf{\Phi}}$ configuration angles. Consequently, the received power at the BS level could be different than the one computed through (4.25) with the accurate channel values. Let $v^{reached}_{d_k}$ be the reached power level by the BS given by:

$$v^{reached}_{d_k} = P^t_{d_k} \left| \underline{\mathbf{g}}^T_{d_k,c} \hat{\mathbf{\Phi}} \underline{\mathbf{h}}_c + h_{d_k,c} \right|^2 . \tag{4.30}$$

The relative error ϵ_l on each power level is defined by:

$$\epsilon_l = \frac{\left| v_l - v_{d_k}^{reached} \right|}{v_l}. \tag{4.31}$$

When ϵ_l is not zero, a different received power is measured at the BS, leading to an actual SINR value different from the targeted or requested one. This could have implications on the SIC decoding success rate. Indeed, the success of the SIC decoding process is directly related to the comparison between the actual SINR value and the targeted one. In other words, if the actual SINR is still larger than the requested one, i.e., if $\Gamma_{d_k,c} \geq \Gamma_{k,req}$, the SIC decoding still succeeds. Thus, the robustness of the methods for RIS configuration to channel estimation errors can be evaluated by setting a target threshold for an acceptable SIC process decoding error rate. Corresponding evaluations are provided in section 4.6.

4.5 Algorithm for Energy Efficiency Maximization through Selection of Active RISs

The EE maximization problem formulated in (4.14e) is a non-convex mixed-integer problem. It depends on the number of active RISs and their configuration. Algorithm 6 provides a solution for the configuration part. However, the problem related to the selection of active RISs is yet to be addressed. To do so, we propose to use the BBA to solve this non-linear binary problem.

The BBA [128], [129] is a widely used technique for solving optimization problems that involve discrete variables, such as binary problems. In this method, the feasible region of the problem is partitioned into smaller sub-regions called nodes, and a bound is computed for each sub-region. The sub-regions are then systematically searched, and those that cannot contain a better solution than the current best solution are discarded. This process is repeated until the optimal solution is found.

In our setting, each node is defined by the set of binary variables δ_i representing the selection of the RIS (i.e. turning on or off the RIS) that define a subset of the feasible region. The nodes are ordered by the increasing number of active RISs. The first RIS to be activated is the one that has the best average aggregated channel gain on the device-RIS-BS link (averaged over all connected devices). Then, activating additional RISs is tested in each subsequent node until activating all RISs has been tested. Lower and upper bounds are then computed for each node: the lower bound is the best solution found for its parent nodes, while the upper bound is the best possible solution for that node based on the new system of equations of the exploited node. Then, the node representing the choice of RIS with the highest potential for improvement, i.e., the largest difference between the upper and lower bound, is branched. This way, the node is split into smaller nodes, known as child nodes, representing turning on new RISs in addition to the ones from the parent node. The cycle then restarts until turning on new RISs fails to increase the system EE.

The BBA is summarized in Algorithm 7 and an example is given in Fig. 4.2.

Algorithm 7: Proposed RIS-NOMA-EE
Branch and Bound Algorithm for EE maximization

1 **Initialization:** Start with only the RIS with the highest average aggregated channel gain turned on.
2 Step 1- Partition the feasible region:
3 Divide the feasible region into smaller nodes that are sequentially explored. Each node is defined by turning on an additional RIS. The number of child nodes from each node is equal to the number of turned-off RISs and not investigated yet.
4 Step 2- Bound computation:
5 Compute a lower and upper bound for each node in the tree. The lower bound is the solution found so far for its parent nodes. The upper bound is the best possible solution for that node.
6 Step 3- Branching:
7 Choose the node with the largest difference between its upper and lower bounds. Split it into a number of child nodes equal to the number of remaining RISs.
8 Step 4- Repeat steps 2 to 3 for each child node until no gain in EE is achieved by activating additional RISs.
9 Step 5- Return the best solution found among all the explored nodes.

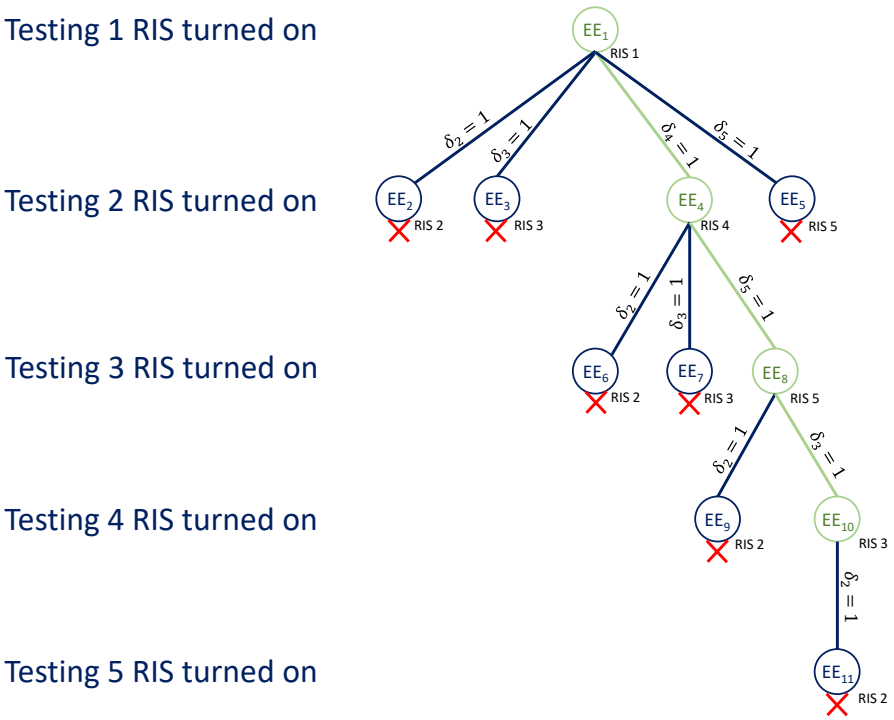

Figure 4.2: Example of BBA application for a system with 5 RISs. The green nodes represent the RISs having the largest positive difference between its upper and lower bounds. The set of RISs to be turned on is $\{RIS_1, RIS_3, RIS_4, RIS_5\}$.

4.6 Simulation Results

The simulation setup consists of an uplink communication system having one BS at the cell center, one RIS with $S = 6$ sub-surfaces and $N = 54$ IoT devices with an access probability equal

to $p_k = 0.5$. The cell radius is equal to 250 m. The maximum number of available power levels is $L = 6$ and the number of available subbands C is equal to 9, with a bandwidth of $W =$ 156 kHz each. The maximum number of available power/spectral resources is hence $C \times L = 54$. IoT devices are distributed in the proximity of the RIS following a Poisson distribution [109]. We assume LoS links between the RIS sub-surfaces and the BS on one hand, and between the RIS sub-surfaces and the devices on the other hand. All signals undergo Rayleigh multipath fading with a root mean square (RMS) delay spread of 500 ns and distance-dependent path loss with a decay factor of 3.76. Additionally, the nLoS links are subject to zero-mean log-normal shadowing with an 8 dB variance. The additive noise power spectral density is equal to $N_0 = 4 \times 10^{-21}$ W/Hz. The system is also evaluated with multiple RISs of up tp 6 sub-surfaces each. The remaining system parameters are summarized in Table 4.1.

The performance of the proposed algorithms is compared against four alternative solutions:

- an OMA system featuring RISs (called RIS-OMA), i.e., one device is attributed to each subband using a unique power level,
- a RIS-free system(called NOMA-no-RIS) that relies on the MAB framework developed in [33] while considering only the nLoS device-BS links,
- an OMA RIS-free system (called no-NOMA-no-RIS), where the devices transmit using their nLoS device-BS link to the BS,
- a system that uses NOMA while configuring the RISs in a way to maximize channel gains (called RIS-NOMA-maxCG), as done in [34], i.e., without any consideration for received power constraints or rate requirements.

Table 4.1: Design parameters values

Parameter	**Value**	**Parameter**	**Value**
$R_{d_k,req}$	0.75 Mbps	$P^t_{d_k}$	20 dBm
$Q_{1,\ldots,L-1}$	1	Q_L	5
κ	10	P_{RIS}	8.5 mW
BP_{BS}	300 mW	PP_{BS}	$K \times 250$ W

The performance of the proposed RIS-NOMA is provided in Fig. 4.3 in terms of the sum of achieved rates for active devices after convergence. It can be seen that, by configuring the RISs through solving (4.29), significant gains in sum rate can be achieved with respect to all other methods, especially for a large number of active devices. In fact, the use of RISs improves the aggregated links between the devices and the BS, while NOMA helps in maximizing the achieved rates. Considering the NOMA-no-RIS setting, some devices do not have access to high received power levels due to their transmit power budget limitation and/or bad channel conditions. This

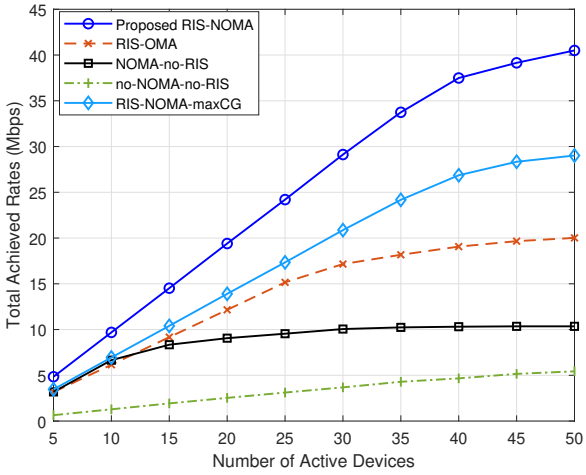

Figure 4.3: Achieved sum rate as a function of the number of devices.

leads to poor achieved rates for such devices which penalizes the performance of this type of system. For the OMA setting, a wider bandwidth would be necessary to achieve better rates, since one subband can only accomodate a single device. For RIS-NOMA-maxCG, all signals are received over a maximized channel gain. Hence, the resulting NOMA interference power in the denominator of (4.9) is much more significant than for the other methods, leading to lower achieved rates.

The performance of the proposed technique is then assessed with respect to its robustness against channel estimation errors in Figure 4.4. When the BS relies on the estimated channel values using (4.25) to determine the configuration of the RIS, a bias is incurred on the resulting received powers with respect to the specified ones denoted by v_{d_k} in (4.23). As can be seen from the obtained results, as long as the variance of the channel estimation error that we denote by ϵ_0 is less than 0.08, the success rate that shows the number of devices satisfying their target rates remains larger than 80%. Beyond this value, the performance of the system rapidly decays. This shows a relative robustness of the system to such error types since the RIS can still be configured in the presence of channel estimation errors without leading to collisions when decoding the signals. For the case of RIS-OMA, the success rate remains robust against the channel estimation error. This can be explained by the absence of multi-device interference (thanks to OMA) and the resulting channel quality improvement (thanks to the introduction of the RIS). However, the price to pay is the reduction in number of connected devices since each subband can handle one device per timeslot. For RIS-NOMA-maxCG, the objective function that was optimized targets the improvement of the channel gain. Since the error would affect directly this metric, the impact on the success rate is larger as we can see in Figure 4.4 down to a success rate of around 20%. The observed improvement below 20% is not interesting in practice. Indeed, such success rates are well below acceptable levels.

In order to evaluate the performance of the active RIS selection algorithm, we consider a system with $K = 40$ active devices and five RISs with $S = 5$ sub-surfaces each. The maximum number of available power levels is $L = 5$ and the number of available subbands is 10. Thus, the

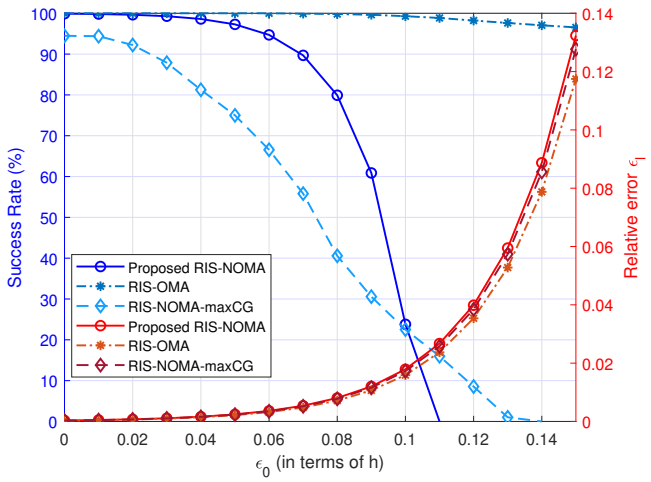

Figure 4.4: Average relative error ϵ_l on the received power levels and success rate as a function of the variance ϵ_0.

maximum number of available resources is $C \times L = 50$.

First, we assess the performance in terms of the number of used RISs J. For this purpose, Figures 4.5 and 4.6 show the achieved sum rate and EE respectively obtained when multiple RISs are turned on according to Algorithm 7. In other words, Algorithm 7 is modified in a way to enforce a specific number of used RISs.

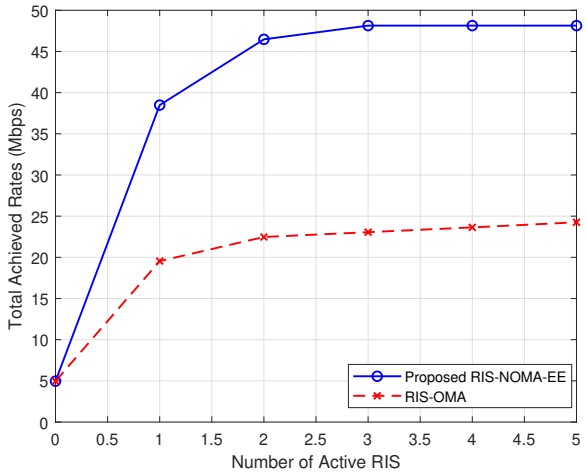

Figure 4.5: Achieved sum rate as a function of the number of activated RISs.

It can be observed that the achieved sum rate increases with the number of active RISs until 3 RISs are turned on. This increase is due to the fact that the additional RISs create a higher granularity in the equation system (4.29), which enhances the chances of obtaining valid solutions while using higher power levels, thus yielding better SINRs. In fact, the activation of a larger number of RISs tends to enhance the resulting aggregated channels. However, since the number of the received power levels is kept constant following (4.5), the achieved sum rate saturates starting from $J = 3$ active RISs. Note that the method outperforms a system that

optimizes EE by RIS selection while using OMA.

Figure 4.6 shows that the EE peaks at the same number of active RISs as the one that maximizes the achieved rates, i.e., 3. In fact, the numerator of (4.12) saturates starting from $J = 3$, while the total RIS power consumption in the denominator increases with J. Thus, the EE decreases starting from $J = 3$.

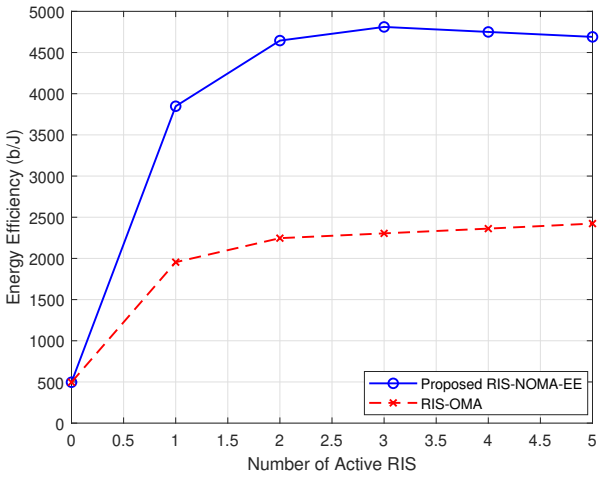

Figure 4.6: Energy Efficiency as a function of the number of activated RISs.

Figure 4.7 shows the EE for a fixed number of active RISs. It can be seen for the case of 1 active RIS that the EE starts to decrease when the total number of active devices is equal to 30. This behavior is due to the non-satisfaction of all the devices leading to a smaller sum rate. This cannot be compensated without having a second active RIS. By turning on the second RIS, the sum rate is guaranteed to be at least the requested rate for all devices. The same scenario happens for a total number of active devices equal to 45 and 55.

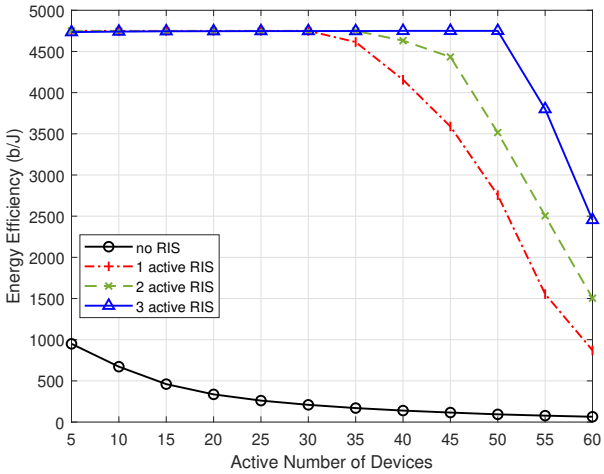

Figure 4.7: The evolution of EE when varying the number of active devices and the number of active RISs.

Finally, Figure 4.8 shows the needed number of active RISs according to Algorithm 7. In

fact, the EE is maintained at a constant level since the devices achieve the requested rates. In order to maintain the target requested rates, i.e. a target EE, the needed number of active RISs increases when the system has more active devices.

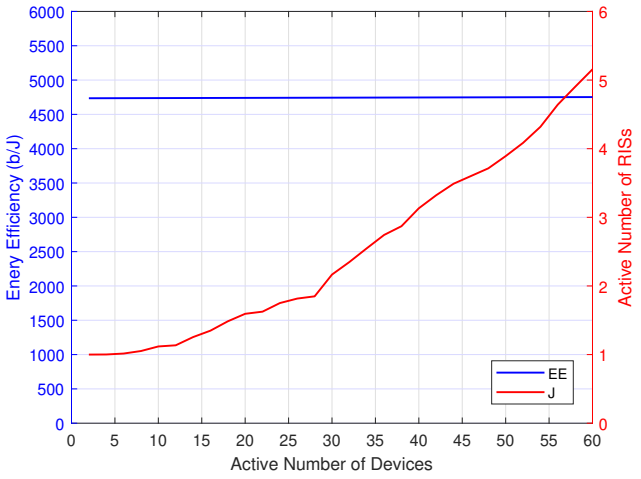

Figure 4.8: The evolution of EE and needed number of active RISs as a function of the number of active devices.

4.7 Summary

In this chapter, we proposed a solution for the RIS configuration problem in a RIS-assisted NOMA uplink system. The solution aims at reaching a specific set of received power levels, while guaranteeing a minimum target rate for the devices transmitting with a predetermined single power level. The separation of the signals through received power levels is done by a proper configuration of the passive reflecting elements of the introduced RISs. Then, the selection of the active RISs out of a set of available ones is achieved in a way to maximize the EE of the system under target rate constraints. The superiority of the proposed method with respect to similar systems with/without RISs and NOMA was shown through simulations. The robustness of the proposed algorithm was also evaluated under channel estimation errors.

Chapter 5

Aerial Reconfigurable Intelligent Surfaces in Uplink Uncoordinated Spectrum Access Systems with NOMA

5.1 Introduction

To fulfill the increasing demand for data rates, spectral efficiency and broader coverage, various technologies such as RISs, UAVs, and NOMA have become under extensive joint investigation [130]. UAVs can be of great use in wireless communication systems due to their cost effectiveness, rapid deployment, controllable mobility and ease of implementation [131–133]. They find diverse applications as aerial base stations, relays, mobile users and for sensor data collection for IoT applications.

By associating RIS and UAV-aided transmissions with NOMA in uncoordinated spectrum access, we expect to enhance the performance of wireless networks through optimized resource utilization. In this chapter, we focus on the implementation of a RIS mounted on a UAV in an uplink uncoordinated communication system where we study the optimization of the UAV trajectory and the configuration of the RIS, in addition to the uncoordinated spectrum access allocation. The results of this work constitute partially the contents of a patent filing on one side and a journal publication ready for submission on the other.

5.1.1 Related Work

In recent literature, researchers have extensively investigated the application of RIS in wireless communication networks [134–137]. For instance, in [134], the performance of a RIS-assisted point-to-point communication was explored, where the BS transmits information symbols to ground users (GU) using a RIS when a direct link was unavailable. In [135], a concept of relaying-assisted communication was introduced, where the controller of the RIS acted as a

decode-and-forward (DF) relay to facilitate information exchange between the BS and a GU. The achievable rate was maximized by jointly optimizing the passive beamforming phase of the RIS elements and time allocation for the controller-based DF relay. Furthermore, [136] studied the impact of resource allocation optimization on the achievable capacity in a RIS-aided multi-user communication system.

Lately, researchers have been inspired by the idea of an aerial relay and proposed the concept of an aerial RIS (ARIS) for wireless communication networks, where a RIS is mounted over an aerial platform like an air balloon or a UAV. This approach offers additional advantages including an easy and rapid deployment, and providing the RIS with the ability to modify its location. This latter advantage is used to modify the propagation environment to create LoS channels with ground devices (BS or GUs) in order to enhance network performance [138–140]. In [138], the performance of an ARIS was studied to maximize the worst-case SNR at a single GU compared to a conventional/fixed RIS. The improvements were attributed to a better deployment capability, a more appropriate height for LoS paths, and a wider signal-view reflection. In [139], the use of multiple ARISs, each mounted on a UAV, and a fixed RIS for SWIPT was investigated. The achievable throughput was maximized by jointly optimizing the power-splitting (PS) ratio and the phase shifts of all the RIS elements. These previous works focused solely on using UAVs as RIS carriers and did not explore their other capabilities, such as relaying as done in [141, 142]. In other words, the UAVs do not carry a transceiver system (like a flying BS), but only the RIS.

In a recent study [143], a novel approach of utilizing UAV-RIS relaying in a single-user downlink network was explored. The study optimized the height of the UAV and the number of RIS reflecting elements separately to maximize the EE of the network. This relaying strategy can be highly effective in scenarios where a reliable link is essential and where physical structures hinder direct communication, especially for disaster management and emergency services. Moreover, when the RIS cannot provide the desired QoS due to various factors like excessive fading, insufficient elements, or circuit failure, employing a full-duplex UAV to assist in information transfer becomes extremely valuable. Nevertheless, the study in [143] focused on a single-user scenario with perfect CSI, which simplifies the considerations but may not accurately reflect real-world conditions. In practical multi-user scenarios, imperfect CSI introduces challenges, especially concerning inter-user interference, leading to performance degradation. To combat this interference and optimize resource utilization efficiently, advanced multiple access techniques are essential for these networks. One such popular technique is NOMA.

Researchers have examined the performance of NOMA in both RIS and UAV-aided relay communication networks separately [144–147]. For example, studies investigated the impact of NOMA in RIS-aided wireless relay networks, achieving maximum performance by optimizing the passive beamforming vector [144, 145]. Similarly, [146] and [147] highlighted the significance of employing NOMA over conventional techniques like OMA to achieve better energy and spectral efficiency in UAV-aided relay networks.

5.1.2 Problem Statement and Contributions

The existing literature has explored the benefits of applying NOMA and ARIS in wireless communications. However, whether the NOMA-ARIS scheme can provide significant performance gains in uplink communications is still an open question that requires further investigation. This largely depends on proposing efficient algorithms to explore and evaluate the most suitable position/trajectory of the UAV on the fly, in order to improve the quality of LoS links. Moreover, previous works often overlook the crucial flight safety constraints on UAV trajectory design in different directions which is essential in practical ARIS-based communication systems.

Addressing these challenges involves many aspects. Firstly, the introduction of NOMA creates a more complex interference-prone environment and requires a careful design of the decoding order based on channel conditions. This results in a highly coupled problem involving the UAV trajectory, the RIS configuration and the subband allocation, largely complexifying suitable solutions. Secondly, due to the obstacles present in the cell, making decisions about the UAV trajectory becomes crucial in order to find LoS positions. Finding efficient methods to enhance the robustness of decision-making in the presence of these obstacles is another key challenge.

This chapter aims to partly address the aforementioned challenges. More precisely, the performed work focuses on studying the ARIS-aided uplink NOMA network where the links between the IoT devices and the BS experience deep shadowing. In fact, the IoT devices transmit data simultaneously to the BS using the NOMA MAB framework described in the previous chapter with the assistance of the ARIS to improve the quality of the concatenated LoS links through UAV trajectory exploration/definition. The considered framework leverages the flexibility in efficient spectrum sharing between the devices, by leveraging the joint effect of the mobility of the UAV, of the modification of the wireless environment provided by the reconfiguration of the RISs, and of efficient distributed power-domain multi-user access algorithms. The main contributions of this chapter can be summarized as follows:

- We propose an algorithm based on the MAB framework in order to find a suitable position of the ARIS while aiming to maximize the achieved rates. Moreover, the algorithm for trajectory optimization accounts for the UAV battery charging via wireless power transfer (WPT).
- We propose a method to define the number of received power levels in order to increase the achieved rates of the devices.
- We introduce a technique to minimize the used spectrum for target minimum achieved user rates.
- We modify the algorithm based on the MAB to allocate the available spectrum to the devices in an uncoordinated manner in order to take into consideration the constraints of ARIS-aided networks.

The rest of the chapter is organized as follows. The system model is described in section 5.2, while the considered optimization problem is formulated in section 5.3. Section 5.4 provides the

methods to optimize the ARIS trajectory. Section 5.5 describes the clustering of devices while section 5.6 presents the configuration of the RIS in order to maximize the SE. The proposed algorithms are then evaluated using numerical simulations whose results are provided in section 5.7. Finally, conclusions are drawn in section 5.8.

5.2 System Model

Consider an uplink communication system that comprises one BS and one ARIS. The ARIS uses a UAV as a RIS carrier and does not act as a mobile relay. The system also includes K active IoT devices that constitute a set $\mathcal{K}$. We assume that each IoT device has a continuous traffic type. The total system bandwidth B is divided equally into C subbands, each having a bandwidth of $W = B/C$. Let $\mathcal{K}_c \subset \mathcal{K}$ be the subset of devices assigned to the c-th subband. A subband can be assigned to K_c devices, but each device can be assigned to only one subband per timeslot. When only one device transmits on a subband, the system operates in an OMA setup. A first use case for such a system is to identify the deployment location of a ground RIS. Indeed, the movement of the ARIS can be used to explore several potential locations for ground RIS installation. Another use case could be to serve the devices in a predetermined deployment region to complement a classical network, in the event of ground equipment failure or exceptionally high congestion due to an emergency situation for example. The RIS carried by a UAV consists of M passive reflecting elements grouped into S sub-surfaces. We denote the reflection coefficients matrix of the ARIS by $\Phi = \text{diag}\{\beta_1 e^{j\phi_1}, \beta_2 e^{j\phi_2}, \ldots, \beta_S e^{j\phi_S}\}$. Here, $\beta_s \in [0,1]$ and $\phi_s \in]-\pi, \pi]$ represent the amplitude and phase shift, respectively, of the s-th sub-surface in the ARIS. In addition, the ARIS can charge its battery via WPT [148] when reaching a charging point. Note that the studied system can be scaled to the case of multiple ARISs, as shown in Figure 5.1, with no overlapping between the regions served by the different ARISs. In this case, the signal of each device is considered to reach a single ARIS and the ARISs elements can be configured independently.

The received signal y_c at the BS over the c-th subband is given by the following equation:

$$y_c = \left(\mathbf{g}_{d_k,c}^T \Phi \mathbf{h}_c + h_{d_k,c}\right) x_{d_k,c} + n_c. \tag{5.1}$$

In (5.1), vector $\mathbf{g}_{d_k,c} \in \mathbb{C}^{S\times 1}$ comprises the channel gains between the IoT device d_k and each of the S sub-surfaces of the ARIS over subband c. $(.)^T$ represents the vector transpose. The channel gain vector $\mathbf{h}_c$ of size $S \times 1$ represents the channel gains between the ARIS and the BS over subband c. $h_{d_k,c}$ represents the channel gain between IoT device d_k and the BS over subband c. $x_{d_k,c}$ is the transmitted signal from IoT device d_k over subband c, and n_c represents an additive Gaussian noise. In this study, the LoS paths between the BS and the IoT devices are blocked, resulting in Rayleigh fading for the device-BS channels. However, the ARISs need to find the positions for which LoS links between the BS and the ARIS and also between the ARIS and the devices do exist. Hence, the Rician fading channel model is used for the device-ARIS and ARIS-BS links as it was done in Chapter 4. The channel gain vector $\mathbf{g}_{d_k,c}$ between IoT

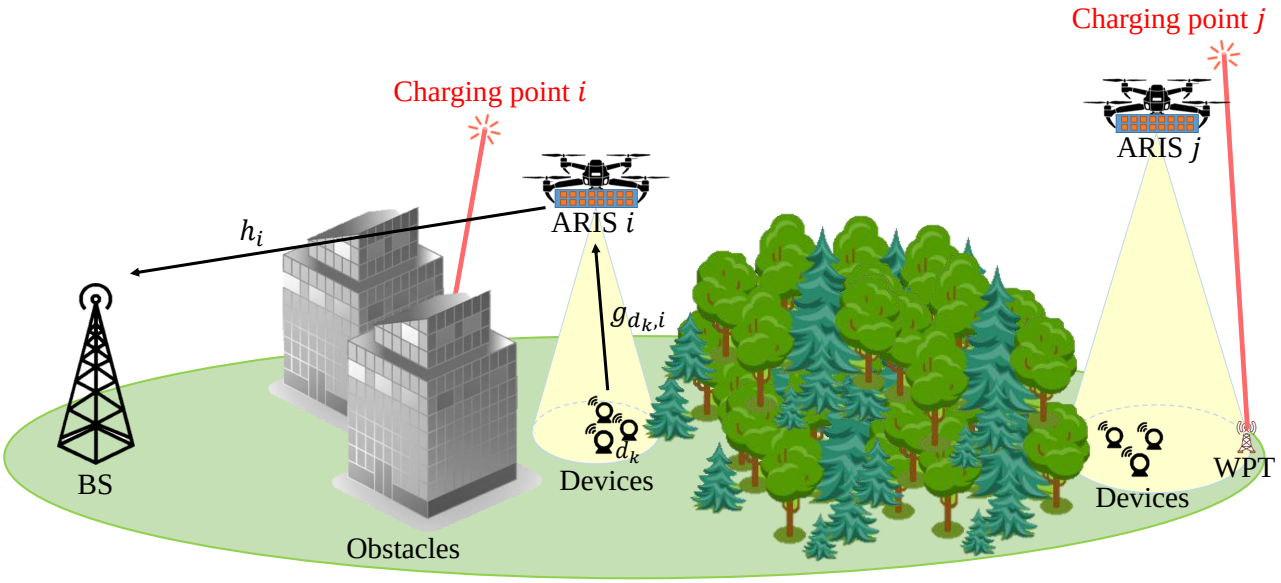

Figure 5.1: System Model

device d_k and the ARIS is expressed as follows:

$$\mathbf{g}_{d_k,c} = PL\left(\sqrt{\frac{\kappa}{1+\kappa}}\mathbf{g}_{d_k,c}^{LoS} + \sqrt{\frac{1}{1+\kappa}}\mathbf{g}_{d_k,c}^{nLoS}\right), \tag{5.2}$$

where PL is the distance-dependent path loss between IoT device d_k and the ARIS, κ is the Rician factor, $\mathbf{g}_{d_k,c}^{LoS}$ and $\mathbf{g}_{d_k,c}^{nLoS}$ are the vectors of LoS and nLoS small-scale fading components, respectively. When $\kappa = 0$, the channel is considered to follow Rayleigh fading due to the nLoS components. Similarly, the channel gain vector $\mathbf{h}_c$ between the BS and the ARIS over subband c is expressed as follows:

$$\mathbf{h}_c = PL\left(\sqrt{\frac{\kappa}{1+\kappa}}\mathbf{h}_c^{LoS} + \sqrt{\frac{1}{1+\kappa}}\mathbf{h}_c^{nLoS}\right), \tag{5.3}$$

where $\mathbf{h}_c^{LoS}$ and $\mathbf{h}_c^{nLoS}$ represent the small-scale LoS and nLoS components, respectively.

The BS has some channel state information available, specifically the aggregated channel information $\mathbf{g}_{d_k,c} \circ \mathbf{h}_c$, where $\circ$ denotes the Hadamard product. However, the BS has no information about the condition of either the device-ARIS or ARIS-BS channels.

5.2.1 NOMA Model

The uplink NOMA power allocation scheme is designed to ensure a minimum requested rate for each IoT device as it was done in Chapter 4. We recall the formula of the l-th received power level v_l, guaranteeing a SINR $\Gamma_{l,req}$ and tolerating Q_i collisions on each power level i lower than

l, given by:

$$v_l = \sigma^2 \Gamma_{l,req} \prod_{i=l+1}^{L} (Q_i \Gamma_{i,req} + 1), \tag{5.4}$$

where σ^2 represents the additive Gaussian noise power.

To avoid collisions, the maximum number of devices per subband, denoted as K_c, must satisfy:

$$K_c \leq L. \tag{5.5}$$

In our system, each device transmits with a constant power denoted by $P^t_{d_k} = P$ for all timeslot indices t. The separation of the signals at the receiver is achieved thanks to the different power levels in the NOMA model, and this separation is ensured through the configuration of the reflecting elements of the ARIS.

5.2.2 Uncoordinated Resource Allocation

Similarly to Chapter 4, the devices autonomously organize their transmissions without relying on external intervention. To address the subband allocation problem, a multi-player MAB framework with zero reward is adopted in the case of a collision. The set of players consists of the devices $\mathcal{K}$, and each device d_k has the set of available subbands $\mathcal{A}_{d_k}$ as its set of actions. The reward received by the device for playing an action is equivalent to its achieved rate calculated using Shannon's formula:

$$R_{d_k,c} = W \log_2(1 + \Gamma_{d_k,c}), \tag{5.6}$$

where $\Gamma_{d_k,c}$ is the SINR achieved by device d_k over subband c, given by:

$$\Gamma_{d_k,c} = \frac{v_l}{\sum_{j=l+1}^{L} v_j + \sigma^2}. \tag{5.7}$$

At timeslot t, if $K_c > L$, a collision occurs resulting in a failure to decode the involved signals of the devices. The collision indicator $\eta_{d_k,c}$ for device d_k over subband c is defined as follows:

$$\eta_{d_k,c} = \begin{cases} 0, & \text{in case of a collision,} \\ 1, & \text{otherwise.} \end{cases} \tag{5.8}$$

The reward that a device obtains when selecting the subband c is then given by:

$$U_{d_k,c} = \eta_{d_k,c} \times R_{d_k,c}. \tag{5.9}$$

As the system is uncoordinated, there is no communication between the devices. Each device has access only to its own list of played actions and the corresponding rewards. Since the rewards are not known beforehand, an exploration phase is necessary to learn them.

5.3 Problem Description

The main objectives of this work are to optimize the ARIS trajectory, determine its optimal final position (destination), configure the RIS elements accordingly and maximize the SE of the system given by:

$$SE = \frac{\sum_{c=1}^{C} \sum_{k=1}^{K_c} R_{d_k,c}}{\sum_{c=1}^{C} \omega_c W}. \tag{5.10}$$

In (5.10), the numerator represents the total achieved rate, while the denominator represents the total bandwidth used, which depends on the subbands selection: ω_c is a binary indicator such that $\omega_c = 1$ if subband c is used and 0 otherwise.

The optimization problem can be formalized as follows:

$$\max_{\Phi,\Omega,\omega_c,X_{ARIS}} SE, \tag{5.11}$$

such that:

$$P \times \left| \mathbf{g}_{d_k,c}^T \Phi \mathbf{h}_c + h_{d_k,c} \right|^2 \in \{v_1, v_2, \ldots, v_L\}, \tag{5.11a}$$

$$\sum_c \Omega_{d_k,c} R_{d_k,c} \geq R_{d_k,req}, \forall d_k \in \mathcal{K}, \tag{5.11b}$$

$$\phi_s \in]-\pi, \pi], s = \{1, 2, \ldots, S\}, \tag{5.11c}$$

$$\beta_s \in [0, 1], s = \{1, 2, \ldots, S\}, \tag{5.11d}$$

$$\omega_c \in \{0, 1\}, \forall c, \tag{5.11e}$$

$$z_{min} \leq z_{ARIS} \leq z_{max}. \tag{5.11f}$$

Constraint (5.11a) guarantees that the received power level is equivalent to one of the predefined power levels. (5.11b) represents the rate constraints for the devices, where $R_{d_k,req}$ is the minimum rate required by device d_k. In (5.11b), $\Omega_{d_k,c} = 1$ if device d_k transmits using subband c, and 0 otherwise. (5.11c) and (5.11d) are respectively the phase shift and amplitude constraints for the configuration of the RIS elements. (5.11f) is the altitude constraint of the ARIS. $X_{ARIS} = \left(x_{ARIS}^{(t)}, y_{ARIS}^{(t)}, z_{ARIS}^{(t)}\right)$ represents the position taken by the ARIS at time t during its trajectory.

Note that problem (5.11) is a mixed-integer and non-convex optimization problem. In order to solve it, the problem is divided into two sub-problems. The first sub-problem aims to optimize the ARISs trajectories to reach their final destinations, while the second sub-problem aims to allocate the subbands, attribute the power levels to the devices, and configure the RIS accordingly.

5.3.1 Problem-Solving Strategy

The objective of the study is to determine the best approach for solving the previously discussed sub-problems. When the ARIS is in motion, the channel gains between the ARIS

and the devices as well as those between the ARIS and the BS are variant over time. Hence, the concatenated channels vary when solving the problem of the RIS configuration. Therefore, the choice of the trajectory of the ARIS highly impacts the RIS configuration. However, we propose a strategy where the ARIS trajectory definition problem remains unaffected by the RIS configuration. In fact, identifying a suitable position of the ARIS provides the RIS configuration with a broader range of potential solutions compared to any other position. Thus, determining a suitable ARIS position is crucial for establishing an efficient RIS configuration. A position is considered optimal in a region (local optimum) when the average channel gain at this position is the highest possible in this region. Once the ARIS is located at a locally optimum position, the achievable SE is also maximized within that region. Besides, since the ARIS is power-limited, a *charging* trajectory must be considered as well. Hence, to solve these sub-problems, a multi-step algorithm is proposed. It starts by solving the ARIS trajectory optimization problem first. Then, the sub-problems consisting of the attribution of power levels and the configuration of the RIS are addressed. The subband allocation algorithm runs in parallel and the charging trajectory determination process is activated when the ARIS battery level is low. Note that, this strategy can be applied for the case of multiple non-cooperating ARISs. The procedure is summarized in Flowcharts 5.2 and 5.3 and described further in the following sections.

5.4 ARIS Trajectory

The very first objective is to find the best position of the ARIS, i.e. the position presenting the best radio conditions between the ARIS and devices as well as the ARIS and the BS. To do so, reinforcement learning is used once again and the MAB framework is invoked for solving the ARIS trajectory problem. More specifically, each potential direction of the RIS motion is considered as an arm in the MAB framework, i.e. the set of actions of the ARIS is:

$$\mathcal{A}_{ARIS} = \{(1,0,0),(-1,0,0),(0,1,0),(0,-1,0),(0,0,1),(0,0,-1)\} \times Step, \tag{5.12}$$

where $Step$ represents the distance traveled by the ARIS in one epoch. These arms represent the different displacements that the ARIS might choose. Note that, for security constraints, some actions may not be available to play if they violate the safety conditions of the ARIS:

- the altitude of the flying ARIS, z_{ARIS}, has to satisfy (5.11f),
- the distance separating the obstacles and the ARIS has to be at least d_{secu}.

The reward associated with each arm or direction is considered to be the amplitude of the average LoS component (if it exists) for the aggregate channels of all devices. It can be estimated depending on the path loss. Then, we propose to use the UCB algorithm to balance between exploration and exploitation phases. It operates by choosing the direction which has the highest

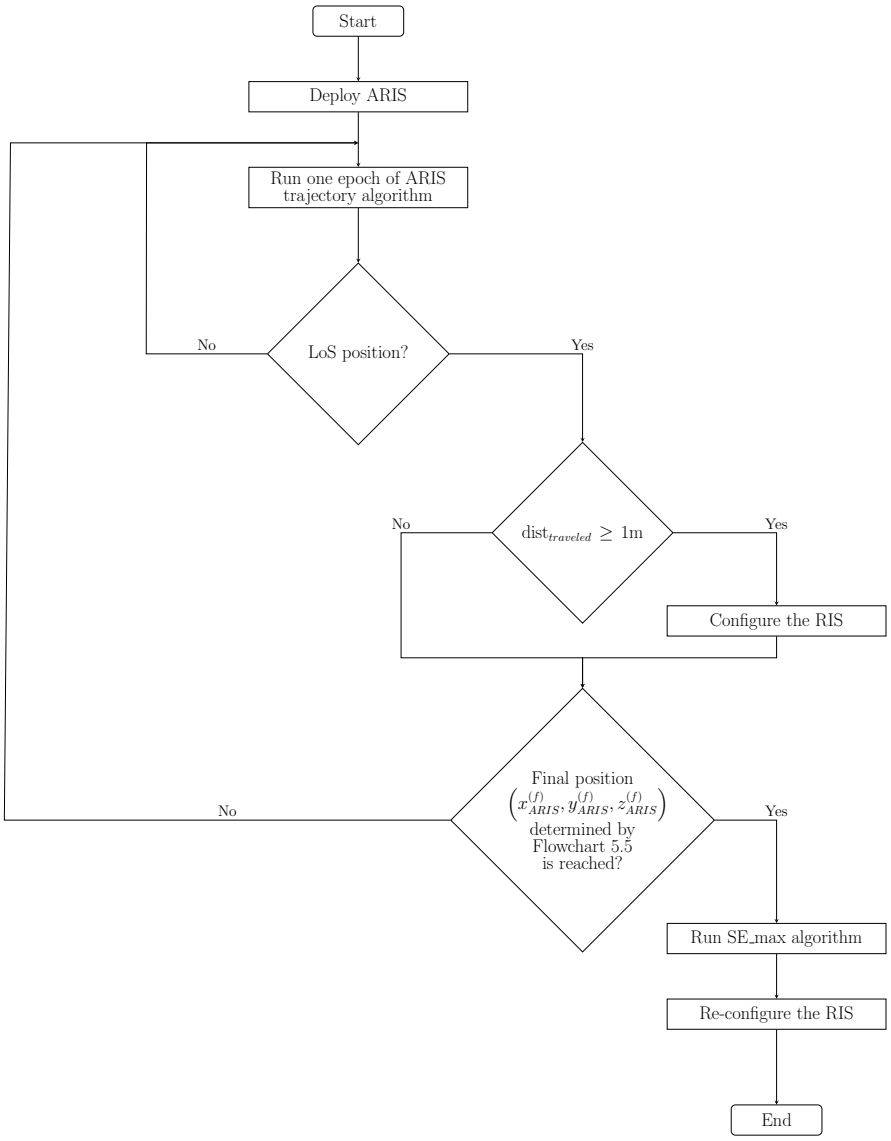

Figure 5.2: Flowchart of the strategy for solving the global problem

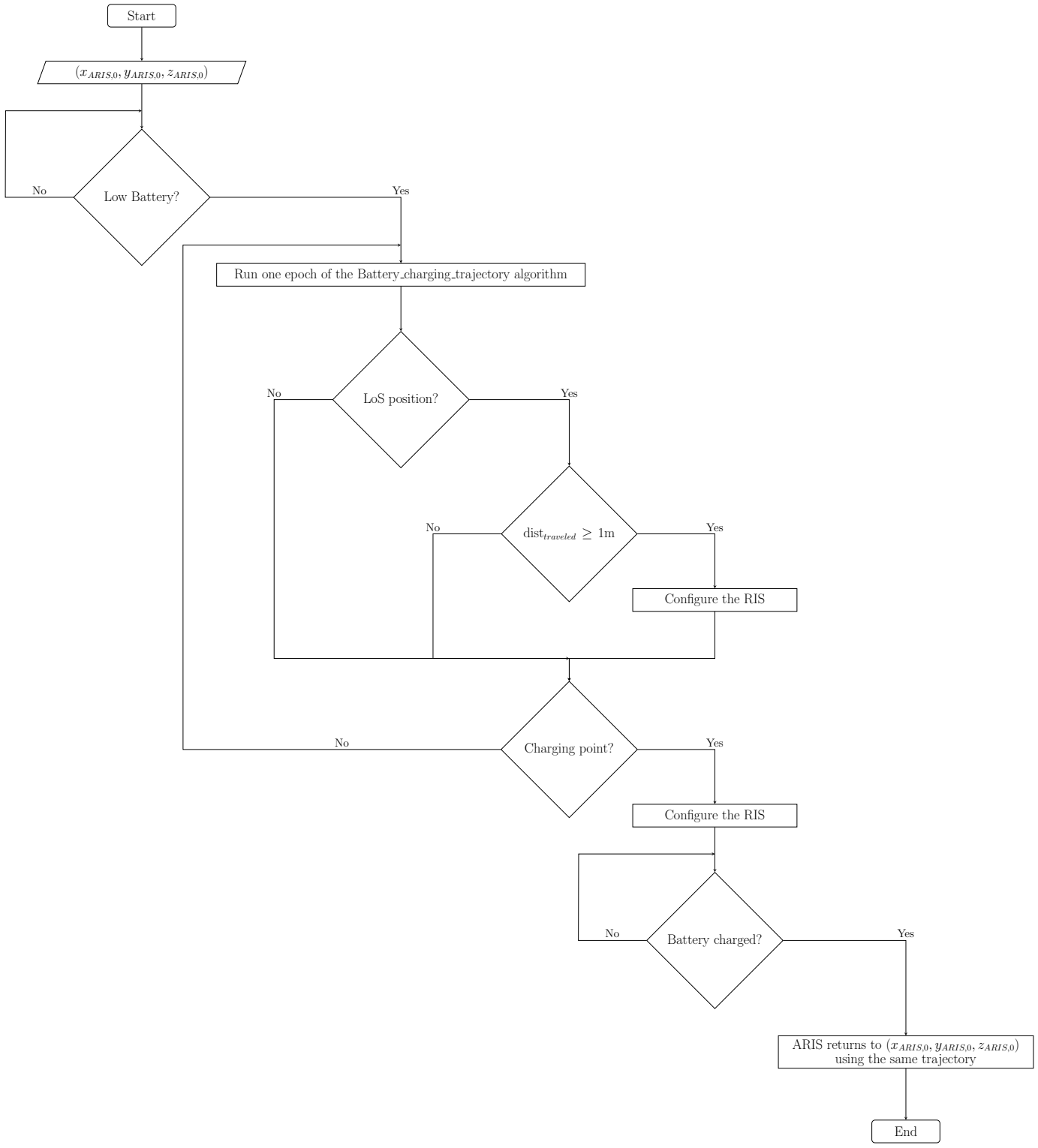

Figure 5.3: Flowchart of the optimization of the charging trajectory

upper confidence bound on the LoS reward given by equation (5.13):

$$U_{ARIS,a_n} = \frac{\sum_{k=1}^{K_r} \left| \mathbf{g}_{d_k,c}^{LoS} \circ \mathbf{h}_c^{LoS} \right|}{K_r}, \tag{5.13}$$

where a_n is the action chosen by the ARIS at a certain time and K_r is the number of devices belonging to the serving region of the ARIS. This strategy ensures that, when exploiting directions with high estimated LoS rewards, the directions less frequently chosen are still explored, given that their true rewards are uncertain. In order to save energy, the individual actions (minimum movement steps) of the ARIS need to consume the least amount of power while exploring the surrounding volume. Hence, the set of MAB actions for the ARIS should be defined to reduce the traveled distance for exploring a unit volume. To do so, the problem is formulated using the traveling salesman problem (TSP) in order to find the shortest possible route as shown in figure 5.4.

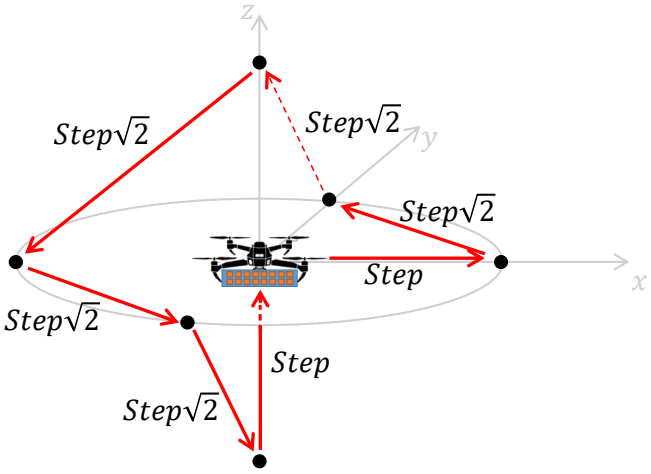

Figure 5.4: Example of TSP for 6 visiting points

Once the ARIS learns the actions, it selects the direction having the largest reward. Note that the ARIS performs the exploration of the six positions (or less, depending on the actual set of actions) before choosing the best action that it takes after returning to the initial position where it was before this exploration. Moreover, in our system, the $Step$ parameter is taken to be larger in nLoS positions than in LoS positions, because there is less utility in exploring nLoS regions compared to LoS. Note that, in order to determine whether the ARIS is in LoS position or not, the aggregate channel gain is compared to a threshold. In other words, if $\sum_{k=1}^{K_r} \left| \mathbf{g}_{d_k,c}^{LoS} \circ \mathbf{h}_c^{LoS} \right| \leq |\mathbf{g}_{th} \circ \mathbf{h}_{th}|$, the position is considered as nLoS. Otherwise, it is considered as LoS. If the rewards of the different explored actions for the current ARIS position are all smaller than the largest reward so far, then a dichotomy branching is applied for $Step$ and new actions are explored with $Step = Step/2$. This learning phase is iterated until having $Step \leq Step_{threshold}$. When $Step \leq Step_{threshold}$, the position reached by the ARIS, $\left(x_{ARIS}^{(f)}, y_{ARIS}^{(f)}, z_{ARIS}^{(f)}\right)$, is considered as the final destination and the traveled trajectory as the optimal one in its operational region.

The proposed solution for ARIS trajectory optimization is summarized in Figure 5.5.

Battery Charging

Since the ARIS operates with power limitations, a further constraint is set to effectively manage its trajectory in terms of the ability to reach a charging point before its power is exhausted. Hence, the decision function for defining the reward for a played arm or direction is augmented by the charging constraint, in addition to the considered effect regarding the quality of the associated LoS component. To this aim, it is assumed that the ARIS generates a beacon signal for low battery level signaling at a certain position $(x_{ARIS,0}, y_{ARIS,0}, z_{ARIS,0})$ at a certain time t.

During the low battery phase, the ARIS selects the direction with the highest upper confidence bound on the net reward, which is the LoS reward added to a term representing the potential of reaching a charging point. In other words, the decision function is updated as follows:

$$a^*_{ARIS} = (1-\alpha)\frac{\sum_{k=1}^{K_r}\left|\mathbf{g}^{LoS}_{d_k,c} \circ \mathbf{h}^{LoS}_{c}\right|}{\max\sum_{k=1}^{K_r}\left|\mathbf{g}^{LoS}_{d_k,c} \circ \mathbf{h}^{LoS}_{c}\right|} + \alpha\frac{RegR}{\text{dist}_{ARIS,CP}}. \tag{5.14}$$

In (5.14), $RegR$ is the radius of the ARIS serving region and $\text{dist}_{ARIS,CP}$ is the distance separating the ARIS from the closest charging point. α is a coefficient that weights the ARIS distance to the charging point. It is taken as a linearly increasing function with time in order to give more emphasis to a potential displacement towards a charging point when time elapses. Therefore, this strategy ensures a dynamic balance between achieving high communication quality and strategically reaching charging points. The ARIS stays at the charging point until its battery is fully charged. Once the battery level is full, the ARIS returns to the initial position $(x_{ARIS,0}, y_{ARIS,0}, z_{ARIS,0})$.

5.5 Grouping of Devices

In ARIS-assisted networks, we need to identify the subsets of devices that can be attributed, through the configuration of the ARIS, to each received power level $v_l, l = \{1, \ldots, L\}$, given by (5.4). In fact, it was observed that the devices having the same reachable values of v_l usually have very similar channel conditions (i.e. path loss values) with respect to the ARIS. Therefore, such a subset of devices with common values of v_l can be considered as being nearly positioned inside a ring around the ARIS. It was noticed that when multiple devices in the same subset transmit on the same subband, obtaining a solution for configuring the RIS through (5.31) is very challenging and occasionally impossible. Hence, it is preferred to have the devices belonging to the same ring transmitting on different subbands. Therefore, each ring allows us to identify a set of constraints for the power levels in order to find an efficient solution for the received power attribution problem. Note that the outer limit of the furthest ring from the ARIS determines its coverage area. The received power levels are influenced by the ARIS configuration and the overall channel gains. These channel gains are primarily dependent on the distances between

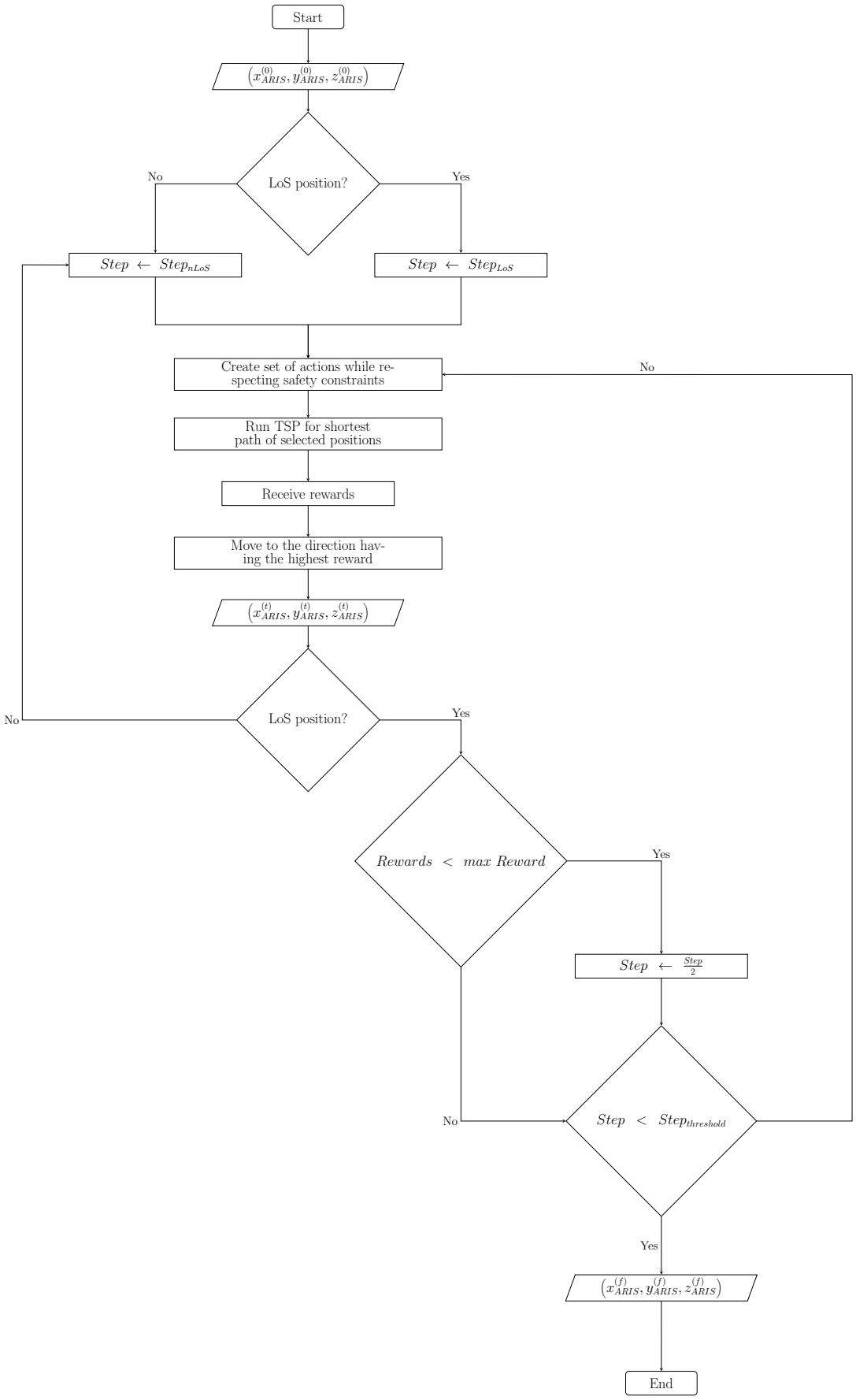

Figure 5.5: Flowchart of the ARIS trajectory algorithm

the IoT devices and the ARIS, as well as on the distance between the ARIS and the BS. Because of the ARIS mobility, its distance with the active devices varies. As a result, IoT devices may not consistently maintain the same received power levels throughout the entire trajectory of the ARIS. Consequently, determining the attributed received power levels requires a careful design, taking into consideration the positions of the IoT devices, the ARIS, and the BS. To do so, we start by determining the coverage area of the ARIS. This coverage area is then divided into multiple rings such that each ring corresponds to a subset of devices having common reachable power levels.

Assuming that, when configuring the RIS, the UAV is in LoS position with the IoT device and the BS, the nLoS component of the channel gains is neglected with respect to the LoS one. Thus, the aggregate channel gain $g_{d_k,c} \circ h_c$ can be approximated as follows:

$$\left|\mathbf{g}_{d_k,c} \circ \mathbf{h}_c\right| \approx \frac{\kappa}{\kappa+1} S\beta_0 \sqrt{\left(\text{dist}_{d_k,ARIS}.\text{dist}_{BS,ARIS}\right)^{-\alpha_1}}, \tag{5.15}$$

where β_0 is the path loss at the reference distance (1 m) [125], α_1 is the corresponding path loss exponent, $\text{dist}_{d_k,ARIS}$ is the distance between the device d_k and the ARIS, and $\text{dist}_{BS,ARIS}$ is the distance between the BS and the ARIS.

In uplink NOMA applying SIC, the grouping of devices and the optimization of their assignment to received power levels determine the improvement in SE of the system. These levels depend on the transmit power of devices and their channel gains. The ARIS is introduced to create two LoS links that would largely improve SE compared to the nLoS ground links. However, the considered RIS being passive, its configuration can only modify the experienced channel gains in a way to create the necessary separation between the values of the received power levels according to (5.4). The aim of this separation is to provide a large set of possible solutions for the RIS configuration that satisfy the earlier stated constraint of avoiding having devices with the same power constraints on the same subband. Moreover, RIS configuration is performed in compliance with a NOMA pairing strategy for resource allocation. For example, such a strategy can aim for maximizing sum-rate regardless of fairness (i.e. maximize the power levels at the receiver), or to ensure rate fairness between devices (i.e. balance power levels at the receiver with respect to past achieved device rates). The applied strategy in our case aims first to satisfy target device rates. When this target is at least met for all devices, their rates are maximized. This is clearly the way to go, especially for our system model where the devices transmit with a unique power level. Indeed, the reduction in transmit power consumption is not a possibility to explore in this case.

The use of a passive RIS can pose a strong limitation with regards to devices having a low channel gain (and, in the general case, also a low transmit power). This limitation can only be addressed through the ARIS mobility and the choice of a more suitable position. With the constraints on the transmit power (including the fact that it has a unique value in this study), the highest power levels at the receiver may not be available for the devices with the poorest channel conditions. Since channel gains predominantly depend on distances, the device furthest from the ARIS should be assigned the lowest power level. This implies that the corresponding

received power for this device must satisfy the following expression:

$$P^r_{d_k,c} = \nu_L = \sigma^2 \Gamma_{d_k,req}. \tag{5.16}$$

Knowing that $P^r_{d_k,c} = P\left|g_{d_k,i,c} \circ h_{i,c}\right|^2$, one can infer:

$$\text{dist}_{d_k,ARIS} = \frac{\sqrt[\alpha_1]{\frac{P\left(\frac{\kappa}{\kappa+1}\right)^2 S^2 \beta_0^2}{\sigma^2 \Gamma_{d_k,req}}}}{\text{dist}_{BS,ARIS}} = Rad_L. \tag{5.17}$$

Hence, for a position of the ARIS corresponding to $\text{dist}_{BS,ARIS}$, each IoT device whose distance towards the ARIS is bigger than Rad_L cannot be served by the ARIS.

The same approach is considered for the different power levels. In other words, in order to find the largest ARIS-device distance for which the IoT device can be assigned to power level ν_l, we write:

$$P^r_{d_k,c} = \nu_l = \sigma^2 \Gamma_{l,req} \prod_{i=l+1}^{L} (Q_i \Gamma_{i,req} + 1). \tag{5.18}$$

Then, one can determine the distance Rad_l between the IoT device and the ARIS that allows the devices to be assigned to ν_l as follows:

$$Rad_l = \frac{\sqrt[\alpha_1]{\frac{P\left(\frac{\kappa}{\kappa+1}\right)^2 S^2 \beta_0^2}{\sigma^2 \Gamma_{l,req} \prod_{i=l+1}^{L} (Q_i \Gamma_{i,req}+1)}}}{\text{dist}_{BS,ARIS}}. \tag{5.19}$$

Assuming all the IoT devices have the same target rate $\Gamma_{l,req} = \Gamma$ and $Q_l = 1 \forall l \neq L$, (5.19) can be re-written as follows:

$$Rad_l = \frac{\sqrt[\alpha_1]{\frac{P\left(\frac{\kappa}{\kappa+1}\right)^2 S^2 \beta_0^2}{\sigma^2 \Gamma (Q_L \Gamma+1)(\Gamma+1)^{l-2}}}}{\text{dist}_{BS,ARIS}}. \tag{5.20}$$

Therefore, the devices having the same received power level constraints (i.e. that can be served using the received power levels $\{\nu_{l+1}, \ldots, \nu_L\}$) are the devices belonging to the ring between Rad_l and Rad_{l+1}, i.e.

$$Rad_l \leq \text{dist}_{d_k,ARIS} \leq Rad_{l+1}. \tag{5.21}$$

As mentioned earlier, devices verifying (5.21) are invited to transmit their signals using different subbands for system convergence. The invitation is done by having the BS reply with zero-rewards in the subband allocation algorithm based on the MAB framework.

5.6 Optimization of Power Levels, Power Attribution, RIS Configuration and Subband Allocation

In the proposed system, we also leverage the MAB framework and particularly the UCB algorithm for the uncoordinated allocation of devices to subbands, as in Chapter 4. In this context, every IoT device elects its arm (subband) to optimize its achieved rate. Nevertheless,

it is imperative to note that these achieved rates depend on two factors: the number of devices sharing a subband, denoted by K_c, and the configuration of the ARIS reflective elements, defined by $\mathbf{\Phi}$. The latter depends on the current ARIS position which determines the channel conditions of the ARIS-BS and ARIS-devices links. For ensuring a successful decoding of signals under NOMA, the configuration of the ARIS should respect the constraints of the desired uplink NOMA model.

5.6.1 Optimization of the Number of Power Levels L and RIS Configuration

For the case of L levels, the general constraint to satisfy in order to guarantee the discrete received power levels $v_l, l = \{1, \ldots, L\}$, is expressed by:

$$v_{d_k} = P \left| \mathbf{g}_{d_k,c}^T \mathbf{\Phi} \mathbf{h}_c + h_{d_k,c} \right|^2, \tag{5.22}$$

where $v_{d_k} \in \{v_1, v_2, \ldots, v_L\}$ is the power level chosen by the BS for device d_k.

As for the power level-device correspondence, it clearly influences the optimization of the RIS coefficients, since the latter are dependent on which user d_k is chosen by the BS to be attributed a particular power level v_l. In contrast with Chapter 4 where the number of power levels L is fixed, the system of equations in this chapter is formed in a way that each device d_k is allocated to the highest available power level in its ring. This allows the device to maximize its achieved rate while using its available power. To reach these purposes, we start by determining the highest needed number of power levels L. Its value depends on the number of devices as well as their channel conditions and the ARIS position. To do so, the highest available power level for d_k is given by:

$$P_{d_k,c}^r = \sigma^2 \Gamma_{\tilde{L}_{d_k},req} \prod_{i=2}^{\tilde{L}_{d_k}} (Q_i \Gamma_{i,req} + 1), \tag{5.23}$$

where $\tilde{L}_{d_k}$ is a variable ranging from 1 to L and representing the highest possible value of L for d_k. (5.23) was obtained by setting $l = 1$ and $L = \tilde{L}_{d_k}$ in (5.4). For example, when $\tilde{L}_{d_k} = 1$, the highest possible associated power level for d_k is v_L. This corresponds to d_k being located in the furthest ring, i.e. $Rad_{L-1} \leq \text{dist}_{d_k,ARIS} \leq Rad_L$. When $\tilde{L}_{d_k} = L$, the highest possible associated power level for d_k is v_1. This corresponds to d_k being located in the closest ring to the ARIS, i.e. $0 \leq \text{dist}_{d_k,ARIS} \leq Rad_1$.

In order to find the value of $\tilde{L}_{d_k}$ for each device, the exact value, denoted by $\tilde{L}_{d_k,exact}$, that jointly considers LoS and nLoS links was derived in Appendix C and found to be:

$$\tilde{L}_{d_k,exact} = \left\lfloor \frac{\log\left(P\,|h^*|^2\right) - \log\left(\sigma^2 \Gamma \left(Q_{\tilde{L}_{d_k}} \Gamma + 1\right)\right)}{\log(\Gamma + 1)} + 2 \right\rfloor, \tag{5.24}$$

where h^* represents the highest possible aggregated channel gain as defined in Appendix C. Note that the complexity of finding $\tilde{L}_{d_k,exact}$ is determined by the complexity of finding the maximum value for h^*. The larger the number of sub-surfaces, the more complex the process of

computing $\tilde{L}_{d_k,exact}$ is.

In order to reduce the complexity, we assume in this work that the two aggregated LoS links through the RIS are largely dominant with respect to the nLoS links between the device and the BS. From (5.15) and by considering the same $\Gamma_{req} = \Gamma$ and $Q_i = 1 \forall i \neq \tilde{L}_{d_k}$, (5.23) can be written as:

$$P\left(\frac{\kappa}{\kappa+1}\right)^2 S^2 \beta_0^2 \left(\text{dist}_{d_k,ARIS}.\text{dist}_{BS,ARIS}\right)^{-\alpha_1} = \sigma^2 \Gamma_{req} \left(Q_{\tilde{L}_{d_k}} \Gamma_{req} + 1\right) \left(\Gamma_{req} + 1\right)^{\tilde{L}_{d_k}-2}. \quad (5.25)$$

In order to find $\tilde{L}_{d_k}$, (5.25) can be re-written as:

$$\left(\Gamma_{req} + 1\right)^{\tilde{L}_{d_k}-2} = \frac{P\left(\frac{\kappa}{\kappa+1}\right)^2 S^2 \beta_0^2 \left(\text{dist}_{d_k,ARIS}.\text{dist}_{BS,ARIS}\right)^{-\alpha_1}}{\sigma^2 \Gamma_{req} \left(Q_{\tilde{L}_{d_k}} \Gamma_{req} + 1\right)} \quad (5.26)$$

Therefore, $\tilde{L}_{d_k}$ can be expressed as:

$$\tilde{L}_{d_k} = \left\lfloor \frac{\log\left[P\left(\frac{\kappa}{\kappa+1}\right)^2 S^2 \beta_0^2\right] - \log\left[\left(\text{dist}_{d_k,ARIS}.\text{dist}_{BS,ARIS}\right)^{\alpha_1} \sigma^2 \Gamma \left(Q_{\tilde{L}_{d_k}} \Gamma + 1\right)\right]}{\log\left(\Gamma + 1\right)} + 2 \right\rfloor. \quad (5.27)$$

In order to assess the accuracy of the approximation in (5.27) on a validation example, we considered the case of a system with one ARIS of 2 sub-surfaces. We obtained an average percentage of times over 2000 simulations where the exact calculation leads to $\tilde{L}_{d_k,exact} = \tilde{L}_{d_k}$ equal to 97% of the cases. Hence, we consider in the following only the calculation based on $\tilde{L}_{d_k}$. On a side note, for the cases when $\tilde{L}_{d_k,exact} \neq \tilde{L}_{d_k}$, $\tilde{L}_{d_k} = \tilde{L}_{d_k,exact} - 1$ because of the truncation of the channel to its LoS component in addition to the floor operation. In such situations, it is nearly impossible to find a solution for the convergence of the whole system with $\tilde{L}_{d_k,exact}$ which tends to give d_k a maximum power level higher than the one with $\tilde{L}_{d_k}$. Therefore, achieving $\tilde{L}_{d_k,exact}$ requires specific configuration values of Φ which favor only the device d_k and can render the solution of the configuration impossible. In these cases, the number of power levels should be equal to $L = \tilde{L}_{d_k,exact} - 1$ which is the same value as $\tilde{L}_{d_k}$.

Once $\tilde{L}_{d_k}$ is found for all devices, the number of power levels L is chosen to be:

$$L = \max_k \tilde{L}_{d_k}. \quad (5.28)$$

This means that all devices having $\tilde{L}_{d_k} = L$ could be attributed any one of the power levels $\{v_1, \ldots, v_L\}$, while others can have access only to the power levels $\{v_{L-\tilde{L}_{d_k}+1}, \ldots, v_L\}$. Therefore, in the aim of attributing the highest possible received power to each device, the power level allocated to device d_k, $v^*_{d_k}$, should be taken as:

$$v^*_{d_k} = v_{L-\tilde{L}_{d_k}+1}. \quad (5.29)$$

However, if more than one device choose to transmit on the same subband while having the same value of $v^*_{d_k}$, the IoT device with the smallest channel gain is attributed to the next available

power level (smaller than $v^*_{d_k}$) and so on.

Moving to the RIS configuration, let $g_{d_k,s} = \mathfrak{g}_{d_k,s} e^{j\theta_{g_{d_k,s}}}, s = 1, 2$, be the s^{th} element of $\mathbf{g}_{d_k}$ with $\mathfrak{g}_{d_k,s}$ the amplitude of $g_{d_k,s}$ and $\theta_{g_{d_k,s}}$ its angular phase, and $h_s = \mathfrak{h}_s e^{j\theta_{h_s}}, s = 1, 2$, the sth element of $\mathbf{h}$ with $\mathfrak{h}_s$ the amplitude of h_s and θ_{h_s} its angular phase.

By developing and expanding (5.22), as in section 4.4.1.3 of Chapter 4, the system of equations can be written as:

$$\begin{aligned}\frac{v^*_{d_k}}{P} = \sum_{s=1}^{S} \left(\beta_s \mathfrak{g}_{d_k,s} \mathfrak{h}_s\right)^2 + \mathfrak{h}^2_{d_k} + 2\sum_{s=1}^{S-1}\sum_{s'=s+1}^{S} \beta_s \beta_{s'} \mathfrak{g}_{d_k,s} \mathfrak{h}_s \mathfrak{g}_{d_k,s'} \mathfrak{h}_{s'} \cos\left(\psi_{d_k,s} - \psi_{d_k,s'}\right) \\ +2\sum_{s=1}^{S} \beta_s \mathfrak{g}_{d_k,s} \mathfrak{h}_s \mathfrak{h}_{d_k} \cos\left(\psi_{d_k,s} - \theta_{h_{d_k}}\right),\end{aligned} \tag{5.30}$$

with $\psi_{d_k,s} = \phi_s + \theta_{g_{d_k,s}} + \theta_{h_s}$.

By further developing the expression of $\psi_{d_k,s}$, we get:

$$\begin{aligned}\frac{v^*_{d_k}}{P} = \sum_{s=1}^{S} \left(\beta_s \mathfrak{g}_{d_k,s} \mathfrak{h}_s\right)^2 + \mathfrak{h}^2_{d_k} + 2\sum_{s=1}^{S-1} \beta_s \mathfrak{g}_{d_k,s} \mathfrak{h}_s \cos\phi_s \sum_{s'=s+1}^{S} \beta_{s'} \mathfrak{g}_{d_k,s'} \mathfrak{h}_{s'} \cos F_{d_k,s,s'} \cos\phi_{s'} \\ +2\sum_{s=1}^{S-1} \beta_s \mathfrak{g}_{d_k,s} \mathfrak{h}_s \sin\phi_s \sum_{s'=s+1}^{S} \beta_{s'} \mathfrak{g}_{d_k,s'} \mathfrak{h}_{s'} \cos F_{d_k,s,s'} \sin\phi_{s'} \\ -2\sum_{s=1}^{S-1} \beta_s \mathfrak{g}_{d_k,s} \mathfrak{h}_s \sin\phi_s \sum_{s'=s+1}^{S} \beta_{s'} \mathfrak{g}_{d_k,s'} \mathfrak{h}_{s'} \sin F_{d_k,s,s'} \cos\phi_{s'} \\ +2\sum_{s=1}^{S-1} \beta_s \mathfrak{g}_{d_k,s} \mathfrak{h}_s \cos\phi_s \sum_{s'=s+1}^{S} \beta_{s'} \mathfrak{g}_{d_k,s'} \mathfrak{h}_{s'} \sin F_{d_k,s,s'} \sin\phi_{s'} \\ +2\mathfrak{h}_{d_k} \sum_{s=1}^{S} \beta_s \mathfrak{g}_{d_k,s} \mathfrak{h}_s \cos G_{d_k,s} \cos\phi_s \\ -2\mathfrak{h}_{d_k} \sum_{s=1}^{S} \beta_s \mathfrak{g}_{d_k,s} \mathfrak{h}_s \sin G_{d_k,s} \sin\phi_s,\end{aligned} \tag{5.31}$$

with:

$$\begin{cases} F_{d_k,s,s'} = \theta_{g_{d_k,s}} - \theta_{g_{d_k,s'}} + \theta_{h_s} - \theta_{h_{s'}}, \\ G_{d_k,s} = \theta_{g_{d_k,s}} + \theta_{h_s} - \theta_{h_{d_k}}. \end{cases} \tag{5.32}$$

The set of equations is formed for all devices d_k. To solve it, the values of β_s, $\cos(\phi_s)$ and $\sin(\phi_s), s = \{1, \ldots, S\}$, that satisfy all the equations need to be found simultaneously. This can be done using iterative methods such as the Levenberg-Marquardt algorithm. Then, the amplitudes and angles are obtained at the BS. Their configuration is sent to the ARIS through the control link between the BS and the ARIS. Note for the case of multiple subbands, the procedure proposed at the end of section 4.4.1.3 is applied.

5.6.2 Subband Allocation for SE Maximization

In order to solve the problem described in (5.11), the SE needs to be maximized. As defined in (5.10), SE is proportional to the achieved rates and inversely proportional to the occupied bandwidth. In fact, the rates are maximized by potentially attributing the highest possible power levels to the devices without causing any collision. Also, the bandwidth occupancy is minimized when the devices transmit on fewer subbands. In the following, we aim to minimize the number of subbands used by the IoT devices while at least satisfying their target device rates.

In the given transmission scenario, the channel gains of active devices are fairly consistent across different subbands because of LoS links. This implies that assigning a device d_k to a specific power level does not hinge on the particular subband c it utilizes for signal transmission. This understanding sets the stage for the initial operation of the algorithm: examining the feasibility of reducing the number of needed subbands. The algorithm kicks off this process by organizing the IoT devices according to an ascending order of their $\tilde{L}_{d_k}$ values determined as shown in (5.27). These devices are then positioned within an array with a number of columns corresponding to the available subbands and a number of rows corresponding to the total number of power levels L. The pivotal point here is the identification of the number of empty slots for each power level in the system, denoted by e_{v_l}, representing the unoccupied subbands. For example, if we consider a case where two devices occupy v_L on two different subbands out of five subbands, the system has three vacant slots on power level v_L. If the number of the unoccupied slots within each level v_l $e_{v_l} \neq 0$, the system can effectively reduce the number of occupied subbands by excluding a number of subbands e equal to the smallest value e_{v_l}. For example, in case of $e_{v_L} = 2$ and $e_{v_{L-1}} = 1$, there is a possibility to free only one subband, i.e. $e = 1$. Note that empty slots on lower levels can be used, if needed, to attribute devices with a value of $\tilde{L}_{d_k}$ larger or equal to 2. For example, in the case where $e_{v_L} = 2$ and $e_{v_{L-1}} = 0$, and since the devices with $\tilde{L}_{d_k} = 2$ can be attributed to either v_L or v_{L-1}, there is a potential of freeing one subband by attributing one of the devices, previously attributed to v_{L-1}, to v_L. The price to be paid is the decrease in the achieved rate for the device attributed to the lower level, knowing that the achieved rate would still be higher than the rate required. Thus, we can get $e_{v_L} = 1$ and $e_{v_{L-1}} = 1$ leading to $e = 1$. This can be fruitful if, at a certain stage of the allocation algorithm, only one device is using one subband and empty spots are available on the lower power levels on other subbands.

Once the number of empty spots e is determined, the system can operate efficiently using $C-e$ subbands instead of C subbands while guaranteeing target rate constraints. Then, a penalizing reward is sent from the BS to the devices transmitting on the e subbands, even if their signals are successfully decoded, in order to encourage them to change their chosen subband. If $e = 0$, the system cannot reduce the number of used subbands.

Having evaluated the feasibility of reducing the number of subbands, the subsequent challenge lies in assigning the power levels in a manner that maximizes the achieved rates. The algorithm adopts a structured approach, proceeding in an ascending order based on $\tilde{L}_{d_k}$ since the rates of

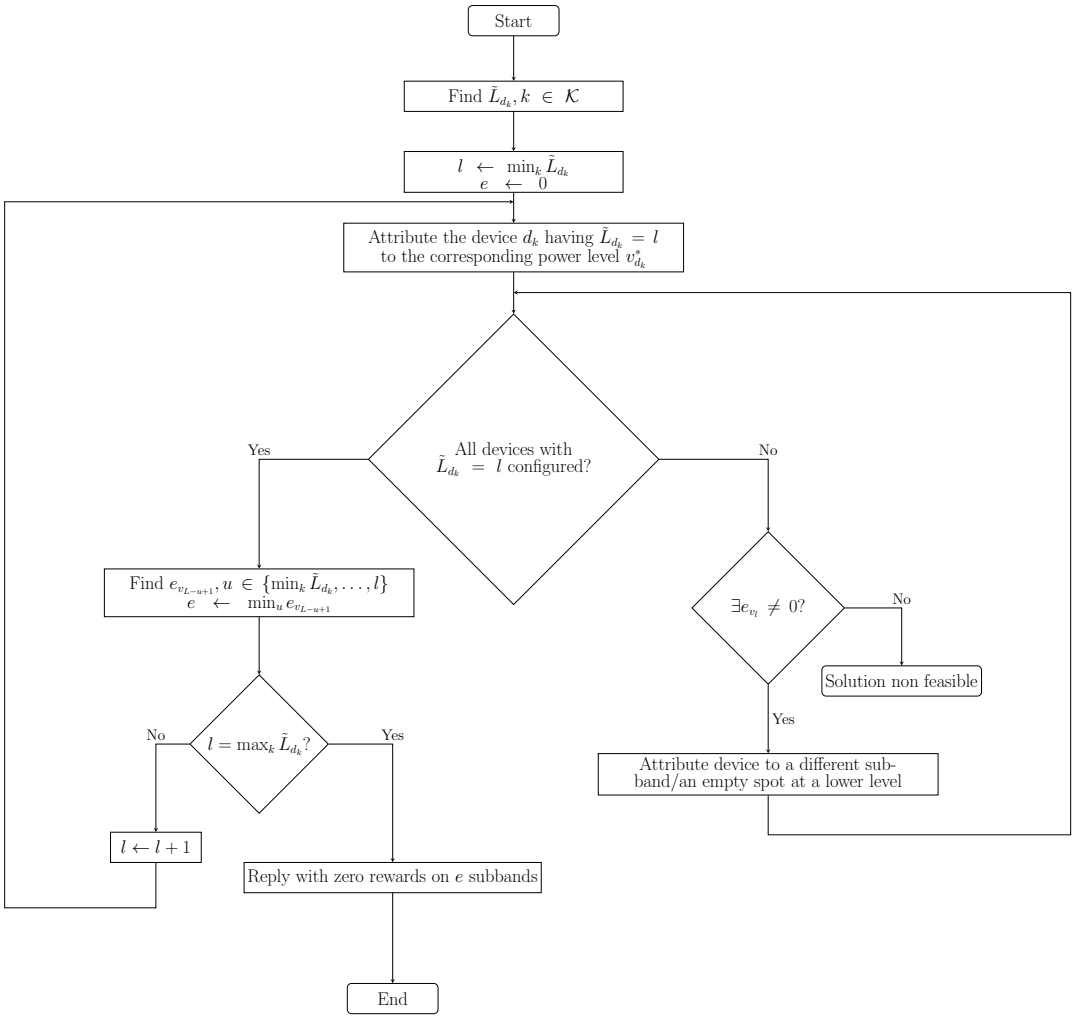

Figure 5.6: Proposed max-SE Algorithm

the devices attributed to lower power levels affect those with higher power levels as shown in eq. (5.7). The objective is to assign the highest possible power level $v_{L-\tilde{L}_{d_k}+1}$ to each device as in (5.29). When attributing a device d_k to a power level v_l, in the case where multiple possible subbands can be chosen, the algorithm prioritizes the subbands having empty allocation spots on the lower levels in order to maximize the achievable rates. Indeed, a device grouping with vacant lower power-level-spots improves the SINR compared to a grouping with fully occupied lower levels.

However, this sequential allocation can potentially hit a roadblock. As the allocation progresses, it is possible that the available slots on power level v_l get fully occupied. When this situation happens, the algorithm is designed to adapt the allocation. Instead of rigidly adhering to the original allocation sequence, it opts for a more pragmatic approach, i.e. device d_k is allocated to the nearest available slot among the lower power levels. Note that the algorithm can always reach a solution for the allocation process as long as the ARIS is appropriately positioned and the number of devices is less or equal to the number of available resources.

When reducing the number of subbands, the number of devices using the same subband increases. Hence, the total number of SIC operations slightly increases. Given that the number of SIC operations is given by $O = K - \sum_{c=1}^{C} \omega_c + 1$, only e operations are added by the SE optimization algorithm.

Due to the channels being almost frequency-non selective, the choice for a device to transmit either on a subband or on a different one leads to the same outcome. Therefore, to ensure a fast convergence, the algorithm aims to minimize the number of devices that need to change their allocated subbands. In fact, once the algorithm attributes the power levels for each device on a subband c, the devices already transmitting on c have priority to keep transmitting on the same one. In this way, the number of needed transitions can be highly reduced.

This approach ensures a dynamic and flexible allocation, capitalizing on available resources while consistently striving to reduce the active number of subbands and enhancing the achieved data rates across devices. It is summarized in the flowchart of Figure 5.6. In the following subsection, we further clarify the algorithm through an application example.

5.6.3 Application Example

Consider that 8 devices are transmitting on 3 subbands in the ARIS-aided wireless communication system. First, the number of power levels required in the considered system needs to be determined. Table 5.1 provides the values of $\tilde{L}_{d_k}$ computed for every device.

Table 5.1: $\tilde{L}_{d_k}$ for all devices.

	d_1	d_2	d_3	d_4	d_5	d_6	d_7	d_8
$\tilde{L}_{d_k}$	3	7	2	1	1	3	4	6

Since the maximum value of $\tilde{L}_{d_k}$ is 7, then let the number of power levels be $L = 7$. Therefore, the devices are distributed into an array of 3 columns (representing the subbands) and 7 rows

(representing the power levels) as shown in Tables 5.2, 5.3, 5.4 and 5.5.

We start first by attributing the devices with the smallest $\tilde{L}_{d_k}$, (i.e. d_4 and d_5) because these two devices are located in the furthest ring. Therefore, they come in the latest SIC stages and their interfering powers appear in the SINR expressions of all other devices. Hence, it is better to fix their interference contributions before the others to allow the determination of the expected rate of succeeding devices like d_3. d_4 and d_5 need to transmit on different subbands since they have a $\tilde{L}_{d_k} = 1$ which corresponds to v_7 (the lowest power level) according to (5.29). Thus, they are assigned to subbands 1 and 2 over v_7 in Table 5.2. As a result, there is one empty slot at v_7, i.e. $e_{v_7} = 1$.

Table 5.2: Attribution of d_4 and d_5.

	Subband #1	**Subband #2**	**Subband #3**
v_1			
v_2			
v_3			
v_4			
v_5			
v_6			
v_7	d_4	d_5	

Then, d_3 is processed since it has the second smallest $\tilde{L}_{d_k}$. d_3 has two possible power levels, v_6 and v_7. In order to maximize its rate, d_3 needs to be attributed to v_6. On a different side, to minimize the number of used subbands, two choices of subbands (Subband 1 or Subband 2) with v_6 are available for d_3 with no difference between them since the lower levels on both subbands are occupied. This leads to the configuration in Table 5.3. Note that $e_{v_6} = 2$, but the system e remains equal to 1.

Table 5.3: Attribution of d_3.

	Subband #1	**Subband #2**	**Subband #3**
v_1			
v_2			
v_3			
v_4			
v_5			
v_6	d_3		
v_7	d_4	d_5	

Next, devices d_1 and d_6 are considered and have the common value of $\tilde{L}_{d_k} = 3$. Their possible power levels are $\{v_5, v_6, v_7\}$. These devices need to be attributed to v_5 on subbands 1 and 2 since the objective is to free subband 3. Now, for d_7 with $\tilde{L}_{d_k} = 4$, the available powers are

$\{v_4, v_5, v_6, v_7\}$ and there are two possibilities for v_4. Since subband 2 has an empty spot on v_2 whereas subband 1 does not (and therefore allows a higher SINR), d_7 is attributed to subband 2 over v_4. This leads to Table 5.4.

Table 5.4: Attribution of d_1, d_6 and d_7.

	Subband #1	**Subband #2**	**Subband #3**
v_1			
v_2			
v_3			
v_4		d_7	
v_5	d_1	d_6	
v_6	d_3		
v_7	d_4	d_5	

There is no device with $\tilde{L}_{d_k} = 5$, hence v_3 remains unoccupied. For $\tilde{L}_{d_k} = 6$, d_8 is attributed to subband 1 since the two empty spots at subband 1 corresponding to two power levels are higher than those corresponding to the two empty spots on subband 2. This leads to a larger achieved rate for device d_8 on subband 1 compared to subband 2. Similarly, d_2 with $\tilde{L}_{d_k} = 7$ is attributed to subband 2 since the latter has an empty spot on v_2 whereas subband 1 does not. Table 5.5 presents the final attribution of the different devices following the proposed approach.

Table 5.5: Attribution of d_8 and d_2.

	Subband #1	**Subband #2**	**Subband #3**
v_1		d_2	
v_2	d_8		
v_3			
v_4		d_7	
v_5	d_1	d_6	
v_6	d_3		
v_7	d_4	d_5	

5.7 Numerical Results

We consider first an uplink communication system having one BS at the cell center, one ARIS with $S = 6$ sub-surfaces that will be deployed from different initial points in a region, and $N = 5$ to 25 IoT devices transmitting continuously their messages on $C = 5$ available subbands with a bandwidth of $W = 312$ kHz each. The IoT devices are distributed in a nLoS region with respect to the BS so that they cannot use their links with the BS to transmit their messages

without the use of the ARIS. All signals undergo Rayleigh multipath fading with a RMS delay spread of 500 ns and distance-dependent path loss with a decay factor of 3.76. Additionally, the nLoS links are subject to zero-mean log-normal shadowing with an 8 dB variance. The additive noise power spectral density is $N_0 = 4 \times 10^{-21}$ W/Hz. The remaining system parameters are summarized in Table 5.6.

Table 5.6: Design parameters values

Parameter	**Value**	**Parameter**	**Value**
$R_{d_k,req}$	0.1 Mbps	$P^t_{d_k}$	20 dBm
$Q_{1,\ldots,L-1}$	1	Q_L	1
κ	10	σ^2	$N_0 \times W$
z_{min}	30m	z_{max}	80m
$Step_{LoS}$	5m	$Step_{nLoS}$	15m
d_{secu}	20m	$Step_{threshold}$	15cm

The performance of the proposed algorithms is compared against four different strategies:

- an OMA system that includes ARISs (called ARIS-OMA), i.e., one device is attributed to each subband using a unique power level,
- a NOMA system that does not use ARISs (called NOMA-no-ARIS), but relies on the MAB framework developed in chapter 3 while considering only the nLoS device-BS links,
- a system with neither ARIS nor NOMA (called no-NOMA-no-ARIS), where the devices transmit using their nLoS device-BS link to the BS,
- a system that uses NOMA while configuring one ground RIS in a way to satisfy the QoS requirements of the devices (called ground-RIS-NOMA), as in Chapter 4, i.e., without any advantages of the mobility of the ARIS. Two different positions of the ground RIS were considered for this scenario.

The performance of the proposed ARIS-NOMA in terms of sum-rate is evaluated in Fig. 5.7. It shows the sum of achieved rates as a function of the number of active devices after convergence while maximizing the SE of the system. By configuring the ARIS through solving (5.31), significant gains in the achieved sum rate are reaped with respect to all other methods. In fact, the use of ARISs, as the use of ground RISs, improves the aggregated links between the devices and the BS, while NOMA helps in maximizing the achieved rates. Added to that, ARISs gain the advantage of further improving the channel gains due to their mobility which is not available for the ground RISs. In other words, the performance of a system with ground RIS largely depends on the chosen position of its RIS. The ARIS could be used in this case

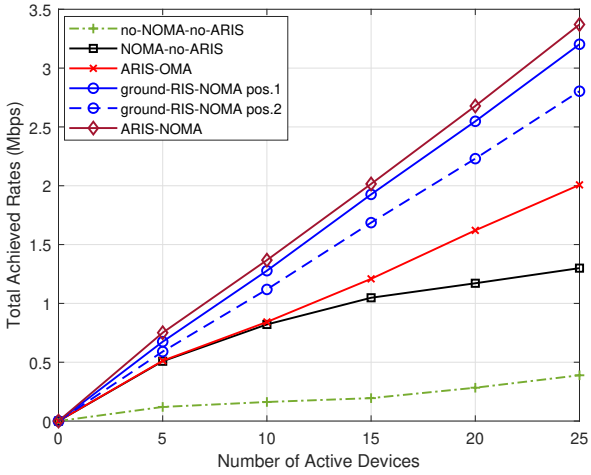

Figure 5.7: Achieved sum rate as a function of the number of devices.

either to determine the best position to deploy a ground RIS or to cover a region temporarily in case of a rare event. Considering the NOMA-no-ARIS setting, almost all the signals of the devices cannot reach the BS with high received power levels due to their power budget limitation and bad channel conditions. This leads to poor achieved rates for such devices. For the OMA setting, a wider bandwidth would be necessary to achieve higher rates, since a subband can only accommodate a single device.

The proposed algorithm is then evaluated with respect to the trajectory taken by the ARIS in Fig. 5.8 for 20 active devices. To do so, we consider that the ARIS is deployed from two different initial points. It can be seen that the final destinations of the ARIS are closer to the devices than to the BS. In fact, achieving LoS links with all the devices is more challenging than achieving LoS link with the BS, due to emulated shadowing. This is due to the distribution of the obstacles in-between. One can also notice that the initial points did not lead to the same final destination. In fact, due to the distribution of the obstacles in between, the ARIS is stuck in two different local optimums. Although the system converges in both final points, the decision of the best local optimum is determined based on the SE which will be shown in the following results. The red graph shows the charging trajectory traveled by the ARIS in low battery mode.

In order to find the optimum final position, we refer to the algorithm developed in section 5.6. First, we determine whether there is a possibility to free any subbands, and then we maximize the rates of the devices. Afterwards, we calculate the SE accordingly. The final point presenting the highest SE corresponds to the optimum final position. Table 5.7 and Table 5.8 show the subband allocation for the different devices, their achieved rates as well as the resulting system SE. As shown in Table 5.8, the system can converge while using four subbands. However, at the final position for the trajectory starting from initial point 1, d_{11} and d_{16} cannot transmit simultaneously their messages because they cannot be configured on different power levels. Also, there is a need to use the five subbands since we have six devices with $\tilde{L}_{d_k} = 1$. At the final point 2, there is a possibility to free one of the subbands since the SE maximization technique

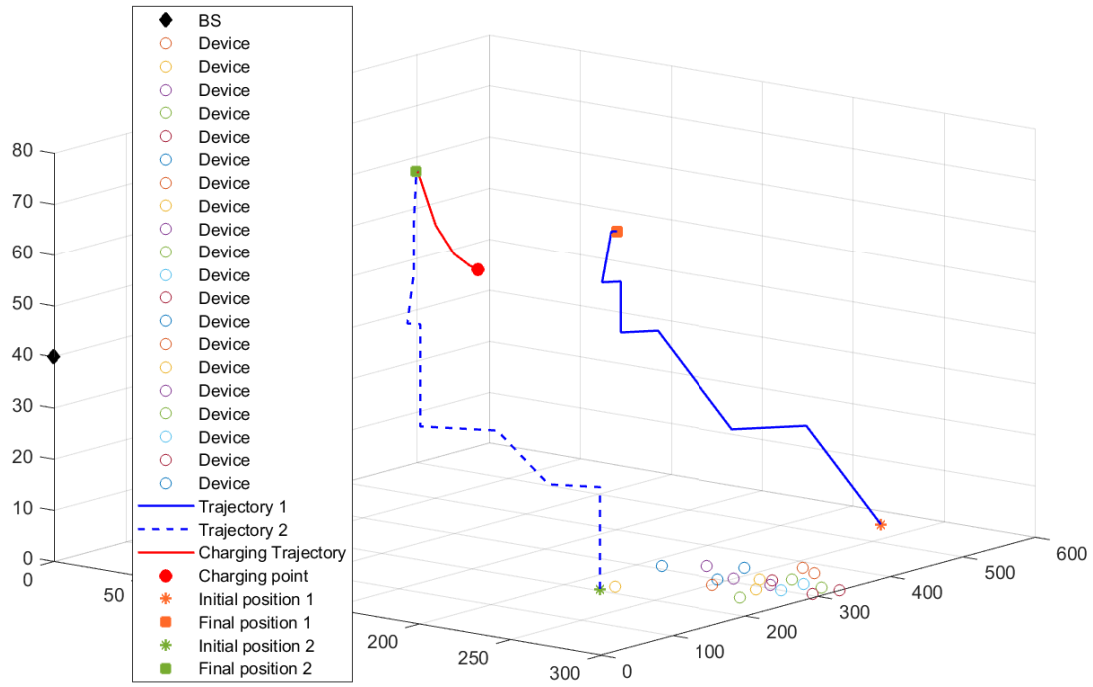

Figure 5.8: ARIS trajectory for two different initial positions.

presented in section 5.6.2 leads to a value of $e = 1$. As seen in Tables 5.7 and 5.8, the SE is larger with the max-SE algorithm than it was at final position 1 or at final position 2 before SE maximization. The colors represent the devices encouraged to change their subbands. Therefore, final position 2 is the optimum position in terms of system convergence and maximum SE.

Table 5.7: Subband Allocation for ARIS final position 1 with $L = 4$

RIS position	**Subband #1**	**Subband #2**	**Subband #3**	**Subband #4**	**Subband #5**	**System**
Final position 1	$L^*_{d_1} = 4 \rightarrow v_1$	$L^*_{d_2} = 4 \rightarrow v_1$	$L^*_{d_3} = 4 \rightarrow v_1$	$L^*_{d_4} = 4 \rightarrow v_1$	$L^*_{d_5} = 4 \rightarrow v_1$	$SE = 1.16$ b/s/Hz
	$L^*_{d_6} = 3 \rightarrow v_2$	$L^*_{d_7} = 3 \rightarrow v_2$	$L^*_{d_8} = 3 \rightarrow v_2$	$L^*_{d_9} = 3 \rightarrow v_2$	$L^*_{d_{10}} = 3 \rightarrow v_2$	
	$L^*_{d_{11}} = 1 \rightarrow v_4$	$L^*_{d_{12}} = 2 \rightarrow v_3$	$L^*_{d_{13}} = 2 \rightarrow v_3$	$L^*_{d_{14}} = 2 \rightarrow v_3$	$L^*_{d_{15}} = 2 \rightarrow v_3$	$Rate = 1.8$ Mbps
	$L^*_{d_{16}} = 1 \rightarrow v_4$	$L^*_{d_{17}} = 1 \rightarrow v_4$	$L^*_{d_{18}} = 1 \rightarrow v_4$	$L^*_{d_{19}} = 1 \rightarrow v_4$	$L^*_{d_{20}} = 1 \rightarrow v_4$	

Figure 5.9 shows the serving region of the ARIS at its optimal final position. One can see that the closer the device is to the ARIS, the larger $\tilde{L}_{d_k}$ is. Then, the device can be configured to a higher power level.

Figure 5.10 illustrates the obtained system SE as a function of the number of devices. The required number of subbands is also displayed, to ensure that the SINR of all the devices

Table 5.8: Subband Allocation for ARIS final position 2 with $L = 8$.

RIS position	**Subband #1**	**Subband #2**	**Subband #3**	**Subband #4**	**Subband #5**	**System**
Final position 2 without max-SE Algorithm	$L^*_{d_1} = 7 \rightarrow v_2$	$L^*_{d_2} = 6 \rightarrow v_3$	$L^*_{d_3} = 8 \rightarrow v_1$	$L^*_{d_4} = 5 \rightarrow v_4$	$L^*_{d_5} = 6 \rightarrow v_3$	$SE = 1.57$ b/s/Hz
	$L^*_{d_6} = 4 \rightarrow v_5$	$L^*_{d_7} = 5 \rightarrow v_4$	$L^*_{d_8} = 4 \rightarrow v_5$	$L^*_{d_9} = 4 \rightarrow v_5$	$L^*_{d_{10}} = 4 \rightarrow v_5$	
	$L^*_{d_{11}} = 3 \rightarrow v_6$	$L^*_{d_{12}} = 2 \rightarrow v_7$	$L^*_{d_{13}} = 2 \rightarrow v_7$	$L^*_{d_{14}} = 3 \rightarrow v_6$	$L^*_{d_{15}} = 3 \rightarrow v_6$	$Rate = 2.45$ Mbps
	$L^*_{d_{16}} = 1 \rightarrow v_8$	$L^*_{d_{17}} = 1 \rightarrow v_8$	$L^*_{d_{18}} = 1 \rightarrow v_8$	$L^*_{d_{19}} = 1 \rightarrow v_8$	$L^*_{d_{20}} = 2 \rightarrow v_7$	
Final position 2 with max-SE Algorithm			$L^*_{d_3} = 8 \rightarrow v_1$			$SE = 1.8$ b/s/Hz
				$L^*_{d_1} = 7 \rightarrow v_2$		
	$L^*_{d_5} = 6 \rightarrow v_3$	$L^*_{d_2} = 6 \rightarrow v_3$				
			$L^*_{d_7} = 5 \rightarrow v_4$	$L^*_{d_4} = 5 \rightarrow v_4$		
	$L^*_{d_6} = 4 \rightarrow v_5$	$L^*_{d_{10}} = 4 \rightarrow v_5$	$L^*_{d_8} = 4 \rightarrow v_5$	$L^*_{d_9} = 4 \rightarrow v_5$		$Rate = 2.23$ Mbps
	$L^*_{d_{11}} = 3 \rightarrow v_6$	$L^*_{d_{15}} = 3 \rightarrow v_6$		$L^*_{d_{14}} = 3 \rightarrow v_6$		
	$L^*_{d_{20}} = 2 \rightarrow v_7$	$L^*_{d_{12}} = 2 \rightarrow v_7$	$L^*_{d_{13}} = 2 \rightarrow v_7$			
	$L^*_{d_{16}} = 1 \rightarrow v_8$	$L^*_{d_{17}} = 1 \rightarrow v_8$	$L^*_{d_{18}} = 1 \rightarrow v_8$	$L^*_{d_{19}} = 1 \rightarrow v_8$		

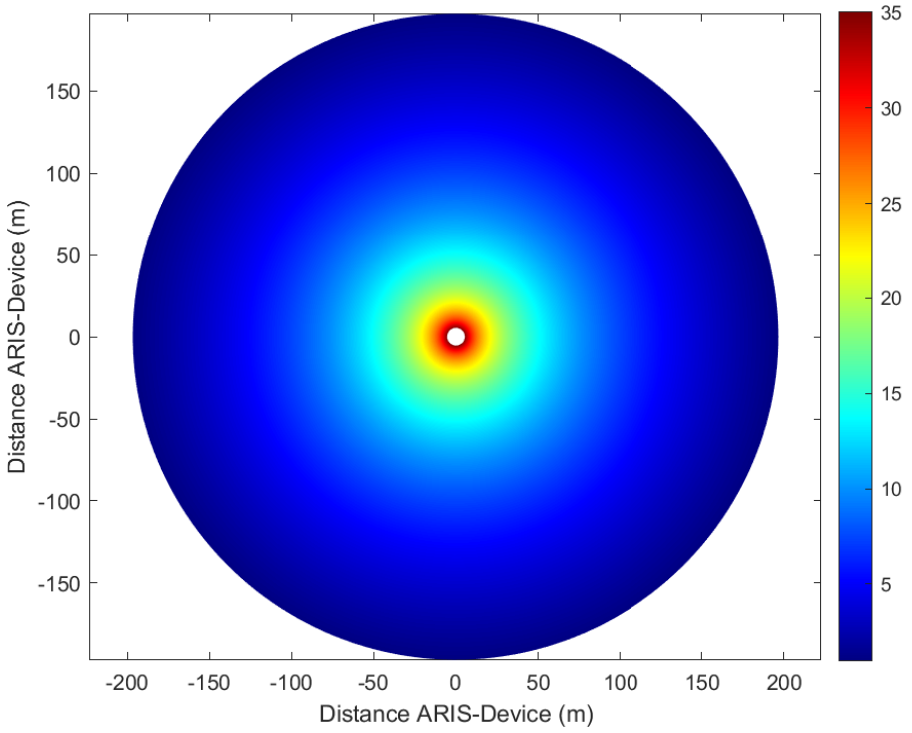

Figure 5.9: Variation of $\tilde{L}_{d_k}$ based on the distance between ARIS and devices

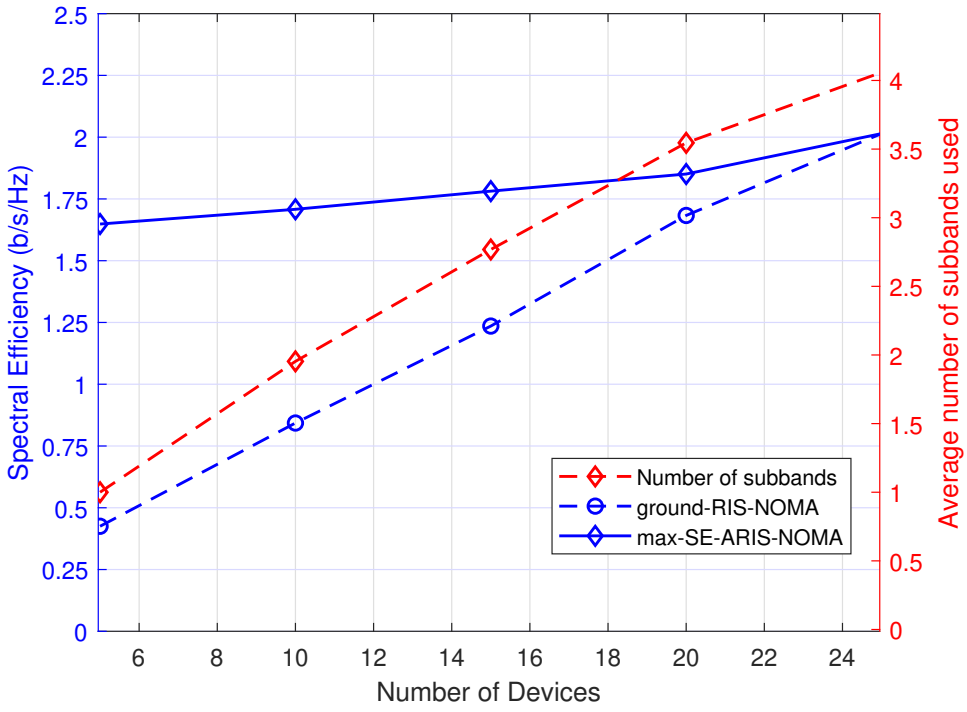

Figure 5.10: System SE with a varying number of devices.

reaches at least Γ_{req}. Compared to ground-RIS-NOMA where the number of available subbands is predefined and kept constant, i.e. $C = 4$, our proposed algorithm effectively increases the SE since it aims to better use the spectrum.

5.8 Summary

In this chapter, we introduced a strategy to address the challenges consisting of ARIS configuration and positioning in the context of an ARIS-assisted NOMA uplink communication system. Our approach is able to efficiently determine a suitable ARIS position that meets QoS requirements with a high success rate, depending on the starting position. During its exploration phase for finding the position, the algorithm also considers the need for modifying the trajectory for enabling wireless charging of the ARIS battery. Furthermore, the proposed algorithm efficiently configures the RIS reflective elements to jointly enable high user satisfaction rates and a SIC decodable NOMA through achieving designated power levels at the receiver side. The optimal number of needed power levels was also determined. A special effort was put to reduce the required bandwidth when meeting target user/device rates, thereby enhancing system SE. When compared with other system configurations, such as the ground RIS, and other systems without ARIS or without NOMA, the proposal showcased its distinct advantages in terms of achieved rates and SE.

Chapter 6

Conclusions and Future Work

In this thesis, we addressed several challenging resource allocation problems for future generations of wireless networks. These problems can be summarized as:

1. resource allocation for grant-free NOMA systems with mixed-traffic support applying distributed FD relays, uncoordinated channel access and power control,

2. resource allocation in RIS-aided grant-free communication networks benefiting from NOMA,

3. resource allocation and positioning for ARIS-aided grant-free communication networks benefiting from NOMA.

Next, we present a summary of the research that was carried out in the course of our work and our future research directions.

6.1 Thesis Summary

6.1.1 Resource Allocation for Mixed Traffic Type in Full-Duplex Relays Communication Systems

In Chapter 3, we tackled the challenge of autonomously optimizing both channel and power allocation in a NOMA uplink setting with FD relaying. Buffering was introduced to enable support of a mixed traffic type for the proposed adaptive allocation algorithms. A keen focus was put on minimizing the AoI in order to support latency-sensitive applications. By employing the MAB framework, the proposed algorithm efficiently assigns different traffic-type devices to subband-power level combinations to satisfy rate constraints for all devices while prioritizing the reduction of AoI for the ones with timing constraints. When assessed in terms of its ability to reduce AoI, minimize device transmit power and bolster achieved rates, the proposal, made-up from the algorithm and system components, distinctly outperforms rival methods. Furthermore, it is able to compete with centralized strategies that assume full access to system parameters and channel conditions.

6.1.2 Configuration of Reconfigurable Intelligent Surfaces for NOMA purposes

In Chapter 4, we presented an innovative solution to the challenge of configuring RISs in a NOMA-enhanced uplink system. Our approach specifically targets achieving predefined received power levels, ensuring that all devices, which are transmitting at a constant power, attain a requested data rate. The distinguishing feature lies in our system's ability to differentiate signals based on received power levels, through adjusting the configuration of the RIS passive reflective elements. Moreover, we proposed an algorithm that determines the RIS activation sequencing in order to optimize the EE of the system. Comparative analyses revealed the proposed method superiority over prior RIS configuration techniques and systems without RIS or using OMA. Furthermore, we demonstrated the resilience of the method against channel estimation inaccuracies.

6.1.3 Aerial Reconfigurable Intelligent Surfaces in Wireless Communication Networks

In Chapter 5, we delved into the details of setting up ARIS within a NOMA uplink environment. Our main goal is to identify the most suitable ARIS position that meets the QoS requirements while taking the best trajectory for battery recharging. Another target in our approach is setting specific received power levels and ensuring a minimum requested data rates for devices transmitting at a unique power level. By efficiently configuring the passive reflectors of the ARIS, we can distinguish signals based on their received power levels. We also introduced a new algorithm to reduce the used bandwidth and to improve the achieved rates, which in turn boosts system SE. Compared to other system configurations, as the ground RIS system in chapter 4, or setups without ARIS or NOMA, our approach proves to be superior from the throughput, SE or bandwidth occupancy perspectives.

6.2 Future Work

As a direct extension, future works include

- **Applying discrete RIS:** In chapter 4, we proposed a solution based on a continuous control of the RIS reflective elements. This study can be evolved by studying the same problem while considering discrete values of the RIS coefficients. In fact, the study has to address the power control in order to guarantee the same NOMA model. Reinforcement learning algorithms may be applied to the RIS in order to find the best configuration of the reflective elements.

- **ARIS serving while moving:** In chapter 5, the problems of optimizing the ARIS trajectory as well as configuring the RIS were studied in a sequential manner. An extension of this study would be having the ARIS serving the devices while moving. However, the

constraints of finding a suitable ARIS trajectory that considers channel gains with Doppler effects should be carefully addressed.

On a longer term, planned studies include

- **Extension to multi-hop communications:** Chapter 3 proposed an algorithm for a two-hop communication system. The generalization of the solution to multiple hops can be particularly interesting for IoT applications in a massive access scenario. In fact, when having a multiple-hop network, each relay can be considered as a node with a larger target data rate and a variable AoI for its messages. Its rate depends on the number of device messages it needs to convey. Message AoI depends on the proposed applied scheduling for each traffic type at the level of the relay. Under such definitions, we can already foresee additional constraints that need to be addressed for such systems. They concern adequate dimensioning of the buffer size of relays and the minimization of the aggregated AoI, especially for relays of later hops. Indeed, such relays now serve their users and potentially relays from the previous hop or hops.

- **Study of cell-free-like relaying [149]:** Under this scenario, each device transmits to two or more relays simultaneously on the same subband. One interesting use-case concerns the scenario where relays are considered as devices in a multi-hop network. While this is expected to increase the sum rate and improve the ability to convey information, the challenges of adapting the formulation of the reward function that should now consider all serving relays and of conveying them are to be efficiently tackled. Moreover, the assessment of AoI becomes extremely constraining.

- **Cooperative Multi-ARIS system:** Another extension of chapter 5 can be incorporating multiple cooperating ARISs to cover the desired areas. Designing a system with several ARISs is largely more complex compared to a system centered around a single one. In fact, the trajectory of an ARIS may affect the trajectories of the others in order to find the best positions to serve the active nodes.

- **Extension to grant-free/grant-based coexistence:** The considered future work aims to find novel resource allocation techniques using ML/DL that are suitable for systems integrating and switching between grant-free and grant-based applications. For grant-free applications, the focus will be on energy-efficient communications where transmission collisions are minimized and the number of successful transmissions is maximized. For grant-based applications, the devised ML/DL methods should prioritize their transmissions to meet their stringent QoS constraints, all the while guaranteeing a satisfactory performance for grant-free applications.

Appendix A

In this appendix, we demonstrate by induction the constraints on the power levels of the considered NOMA model, as stated in sections 3.2.1 and 4.2.1. These constraints are required to guarantee a target SINR Γ_l after SIC and when facing M_l supported collisions at each power level lower than l. For these purposes, let $v_l, l \in \{1, ..., L\}$, denote the power level l such that $v_1 > v_2 > ... > v_L$.

We start first by deriving successive instances v_L, v_{L-1}, v_{L-2} and v_{L-3} (for power levels $L, L-1, L-2$ and $L-3$ respectively) of the constraints in order to find the recursive equation of v_l:

$$\Gamma_L = \frac{v_L}{\sigma^2} \Rightarrow \boxed{v_l = \sigma^2 \Gamma_L}. \tag{A.1}$$

$$\begin{aligned} \Gamma_{L-1} &= \frac{v_{L-1}}{M_L \sigma^2 \Gamma_L + \sigma^2} = \frac{v_{L-1}}{\sigma^2 (M_L \Gamma_L + 1)} \\ &\Rightarrow \boxed{v_{L-1} = \sigma^2 \Gamma_{L-1} (M_L \Gamma_L + 1)}. \end{aligned} \tag{A.2}$$

$$\begin{aligned} \Gamma_{L-2} &= \frac{v_{L-2}}{M_{L-1} v_{L-1} + M_L v_L + \sigma^2} = \frac{v_{L-2}}{M_{L-1} \sigma^2 \Gamma_{L-1} (M_L \Gamma_L + 1) + M_L \sigma^2 \Gamma_L + \sigma^2} \\ \Gamma_{L-2} &= \frac{v_{L-2}}{M_{L-1} \sigma^2 \Gamma_{L-1} (M_L \Gamma_L + 1) + \sigma^2 (M_L \Gamma_L + 1)} = \frac{v_{L-2}}{\sigma^2 (M_L \Gamma_L + 1) (M_{L-1} \Gamma_{L-1} + 1)} \\ &\Rightarrow \boxed{v_{L-2} = \sigma^2 \Gamma_{L-2} (M_L \Gamma_L + 1) (M_{L-1} \Gamma_{L-1} + 1)}. \end{aligned} \tag{A.3}$$

$$\begin{aligned} \Gamma_{L-3} &= \frac{v_{L-3}}{M_{L-2} v_{L-2} + M_{L-1} v_{L-1} + M_L v_L + \sigma^2} \\ \Gamma_{L-3} &= \frac{v_{L-3}}{M_{L-2} \sigma^2 \Gamma_{L-2} (M_L \Gamma_L + 1) (M_{L-1} \Gamma_{L-1} + 1) + M_{L-1} \sigma^2 \Gamma_{L-1} (M_L \Gamma_L + 1) + M_L \sigma^2 \Gamma_L + \sigma^2} \\ \Gamma_{L-3} &= \frac{v_{L-3}}{\sigma^2 (M_L \Gamma_L + 1) [M_{L-2} \Gamma_{L-2} (M_{L-1} \Gamma_{L-1} + 1) + M_{L-1} \Gamma_{L-1} + 1]} \\ &\Rightarrow \boxed{v_{L-3} = \sigma^2 \Gamma_{L-3} (M_L \Gamma_L + 1) (M_{L-1} \Gamma_{L-1} + 1) (M_{L-2} \Gamma_{L-2} + 1)}. \end{aligned} \tag{A.4}$$

Let the initial assumption be:

$$v_{L-n} = \sigma^2 \Gamma_{L-n} \prod_{i=L-n+1}^{L} (M_i \Gamma_i + 1). \tag{A.5}$$

We calculate $v_{L-(n+1)}$ for the order $(n+1)$:

$$\Gamma_{L-n-1} = \frac{v_{L-n-1}}{M_{L-n}v_{L-n} + M_{L-n+1}v_{L-n+1} + \ldots + M_L v_L + \sigma^2}$$

$$\Gamma_{L-n-1} = \frac{v_{L-n-1}}{M_{L-n}\sigma^2\Gamma_{L-n}\prod_{i=L-n+1}^{L}(M_i\Gamma_i+1) + M_{L-n+1}\sigma^2\Gamma_{L-n+1}\prod_{i=L-n+2}^{L}(M_i\Gamma_i+1) + \ldots + M_L\sigma^2\Gamma_L + \sigma^2}$$

$$\Gamma_{L-n-1} = \frac{v_{L-n-1}}{\sigma^2\left(M_L\Gamma_L+1\right)[A]},$$

with:

$$A = M_{L-n}\Gamma_{L-n}\prod_{i=L-n+1}^{L-1}(M_i\Gamma_i+1) + M_{L-n+1}\Gamma_{L-n+1}\prod_{i=L-n+2}^{L-1}(M_i\Gamma_i+1) + \ldots + M_{L-1}\Gamma_{L-1} + 1$$

$$\Gamma_{L-n-1} = \frac{v_{L-n-1}}{\sigma^2\left(M_L\Gamma_L+1\right)\left(M_{L-1}\Gamma_{L-1}+1\right)[B]},$$

with:

$$B = M_{L-n}\Gamma_{L-n}\prod_{i=L-n+1}^{L-2}(M_i\Gamma_i+1) + M_{L-n+1}\Gamma_{L-n+1}\prod_{i=L-n+2}^{L-2}(M_i\Gamma_i+1) + \ldots + M_{L-2}\Gamma_{L-2} + 1$$

$$\vdots$$

$$\Gamma_{L-n-1} = \frac{v_{L-n-1}}{\sigma^2\left(M_L\Gamma_L+1\right)\left(M_{L-1}\Gamma_{L-1}+1\right)\ldots\left(M_{L-n+1}\Gamma_{L-n+1}+1\right)\left(M_{L-n}\Gamma_{L-n}+1\right)},$$

$$\Gamma_{L-n-1} = \frac{v_{L-n-1}}{\sigma^2\prod_{i=L-n}^{L}(M_i\Gamma_i+1)}$$

$$\Rightarrow \boxed{v_{L-n-1} = \sigma^2\Gamma_{L-n-1}\prod_{i=L-n}^{L}(M_i\Gamma_i+1)}. \tag{A.6}$$

By using the initial assumption, i.e. eq. (A.5):

$$v_{L-(n+1)} = \sigma^2\Gamma_{L-(n+1)}\prod_{i=L-(n+1)+1}^{L}(M_i\Gamma_i+1) \Rightarrow \boxed{v_{L-n-1} = \sigma^2\Gamma_{L-n-1}\prod_{i=L-n}^{L}(M_i\Gamma_i+1)}. \tag{A.7}$$

Hence, since eq. (A.6) and eq. (A.7) are the same, we can write that:

$$\boxed{v_l = \sigma^2\Gamma_l\prod_{i=l+1}^{L}(M_i\Gamma_i+1)}. \tag{A.8}$$

Note that, in case of full-duplex relays which result in self-interference, an additive element I representing the interference is added to the denominator in the Γ equations. Thus, (A.8) can be updated as follows:

$$\boxed{v_l = \left(\sigma^2 + I\right)\Gamma_l\prod_{i=l+1}^{L}(M_i\Gamma_i+1)}. \tag{A.9}$$

Appendix B

In this appendix, we provide a complete mathematical demonstration for eq. (4.25) in order to achieve NOMA through configuring a RIS with S sub-surfaces.

Let $g_{d_k,s} = \mathfrak{g}_{d_k,s} e^{j\theta_{g_{d_k,s}}}, s = \{1, 2, \ldots, S\}$, be the s^{th} element of the channel gain $\mathbf{g}_{d_k}$ between device d_k and the RIS. $\mathfrak{g}_{d_k,s}$ is the amplitude of $g_{d_k,s}$ and $\theta_{g_{d_k,s}}$ its angular phase.
Let $h_s = \mathfrak{h}_s e^{j\theta_{h_s}}, s = \{1, 2, \ldots, S\}$, be the s^{th} element of channel gain $\mathbf{h}_s$ between the RIS and the BS. $\mathfrak{h}_s$ is the amplitude of h_s and θ_{h_s} its angular phase.
Also, let $h_{d_k} = \mathfrak{h}_{d_k} e^{j\theta_{h_{d_k}}}$ be the channel gain between device d_k and the BS. $\mathfrak{h}_{d_k}$ is the amplitude of h_{d_k} and $\theta_{h_{d_k}}$ its angular phase.

In order to have a received power v_{d_k} at the BS, the general constraint to be respected for device d_k, having a transmit power P, is written as follows:

$$v_{d_k} = P \left| \mathbf{g}_{d_k} \mathbf{\Phi} \mathbf{h}_s + h_{d_k} \right|^2 . \tag{B.1}$$

By writing the equation in its trigonometric form, we get:

$$\begin{aligned}
v_{d_k} &= P \left| \sum_{s=1}^{S} \mathfrak{g}_{d_k,s} \mathfrak{h}_s \beta_s e^{j\left(\phi_s + \theta_{g_{d_k,s}} + \theta_{h_s}\right)} + \mathfrak{h}_{d_k} e^{j\theta_{h_{d_k}}} \right|^2 \\
v_{d_k} &= P \left| C + jD \right|^2 , \\
&\text{with: } C = \sum_{s=1}^{S} \mathfrak{g}_{d_k,s} \mathfrak{h}_s \beta_s \cos\left(\phi_s + \theta_{g_{d_k,s}} + \theta_{h_s}\right) + \mathfrak{h}_{d_k} \cos\left(\theta_{h_{d_k}}\right), \\
&\qquad D = \sum_{s=1}^{S} \mathfrak{g}_{d_k,s} \mathfrak{h}_s \beta_s \sin\left(\phi_s + \theta_{g_{d_k,s}} + \theta_{h_s}\right) + \mathfrak{h}_{d_k} \sin\left(\theta_{h_{d_k}}\right).
\end{aligned} \tag{B.2}$$

Knowing that the module of a complex number z is given by $|z| = \sqrt{\mathfrak{Re}(z)^2 + \mathfrak{Im}(z)^2}$, one can

write:

$$\begin{aligned}\frac{v_{d_k}}{P} &= C^2 + D^2 \\ &= \left[\sum_{s=1}^{S} \mathfrak{g}_{d_k,s}\mathfrak{h}_s\beta_s \cos\left(\phi_s + \theta_{g_{d_k,s}} + \theta_{h_s}\right) + \mathfrak{h}_{d_k}\cos\left(\theta_{h_{d_k}}\right)\right]^2 \\ &+ \left[\sum_{s=1}^{S} \mathfrak{g}_{d_k,s}\mathfrak{h}_s\beta_s \sin\left(\phi_s + \theta_{g_{d_k,s}} + \theta_{h_s}\right) + \mathfrak{h}_{d_k}\sin\left(\theta_{h_{d_k}}\right)\right]^2.\end{aligned} \tag{B.3}$$

By expanding eq. (B.3), one obtains:

$$\begin{aligned}\frac{v_{d_k}}{P} &= \sum_{s=1}^{S} \mathfrak{g}_{d_k,s}^2\mathfrak{h}_s^2\beta_s^2 \cos^2\left(\phi_s + \theta_{g_{d_k,s}} + \theta_{h_s}\right) + \mathfrak{h}_{d_k}^2\cos^2\left(\theta_{h_{d_k}}\right) \\ &+ 2\sum_{s=1}^{S-1} \mathfrak{g}_{d_k,s}\mathfrak{h}_s\beta_s \cos\left(\phi_s + \theta_{g_{d_k,s}} + \theta_{h_s}\right) \sum_{s'=s+1}^{S} \mathfrak{g}_{d_k,s'}\mathfrak{h}_{s'}\beta_{s'} \cos\left(\phi_{s'} + \theta_{g_{d_k,s'}} + \theta_{h_{s'}}\right) \\ &+ 2\mathfrak{h}_{d_k}\cos\left(\theta_{h_{d_k}}\right) \sum_{s=1}^{S} \mathfrak{g}_{d_k,s}\mathfrak{h}_s\beta_s \cos\left(\phi_s + \theta_{g_{d_k,s}} + \theta_{h_s}\right) \\ &+ \sum_{s=1}^{S} \mathfrak{g}_{d_k,s}^2\mathfrak{h}_s^2\beta_s^2 \sin^2\left(\phi_s + \theta_{g_{d_k,s}} + \theta_{h_s}\right) + \mathfrak{h}_{d_k}^2\sin^2\left(\theta_{h_{d_k}}\right) \\ &+ 2\sum_{s=1}^{S-1} \mathfrak{g}_{d_k,s}\mathfrak{h}_s\beta_s \sin\left(\phi_s + \theta_{g_{d_k,s}} + \theta_{h_s}\right) \sum_{s'=s+1}^{S} \mathfrak{g}_{d_k,s'}\mathfrak{h}_{s'}\beta_{s'} \sin\left(\phi_{s'} + \theta_{g_{d_k,s'}} + \theta_{h_{s'}}\right) \\ &+ 2\mathfrak{h}_{d_k}\sin\left(\theta_{h_{d_k}}\right) \sum_{s=1}^{S} \mathfrak{g}_{d_k,s}\mathfrak{h}_s\beta_s \sin\left(\phi_s + \theta_{g_{d_k,s}} + \theta_{h_s}\right).\end{aligned} \tag{B.4}$$

$$\begin{aligned}\Rightarrow \frac{v_{d_k}}{P} &= \sum_{s=1}^{S} \mathfrak{g}_{d_k,s}^2\mathfrak{h}_s^2\beta_s^2 \left[\cos^2\left(\phi_s + \theta_{g_{d_k,s}} + \theta_{h_s}\right) + \sin^2\left(\phi_s + \theta_{g_{d_k,s}} + \theta_{h_s}\right)\right] \\ &+ \mathfrak{h}_{d_k}^2\left[\cos^2\left(\theta_{h_{d_k}}\right) + \sin^2\left(\theta_{h_{d_k}}\right)\right] \\ &+ 2\sum_{s=1}^{S-1} \mathfrak{g}_{d_k,s}\mathfrak{h}_s\beta_s \sum_{s'=s+1}^{S} \mathfrak{g}_{d_k,s'}\mathfrak{h}_{s'}\beta_{s'} \cos\left(\phi_s + \theta_{g_{d_k,s}} + \theta_{h_s}\right)\cos\left(\phi_{s'} + \theta_{g_{d_k,s'}} + \theta_{h_{s'}}\right) \\ &+ 2\sum_{s=1}^{S-1} \mathfrak{g}_{d_k,s}\mathfrak{h}_s\beta_s \sum_{s'=s+1}^{S} \mathfrak{g}_{d_k,s'}\mathfrak{h}_{s'}\beta_{s'} \sin\left(\phi_s + \theta_{g_{d_k,s}} + \theta_{h_s}\right)\sin\left(\phi_{s'} + \theta_{g_{d_k,s'}} + \theta_{h_{s'}}\right) \\ &+ 2\mathfrak{h}_{d_k}\sum_{s=1}^{S} \mathfrak{g}_{d_k,s}\mathfrak{h}_s\beta_s \cos\left(\theta_{h_{d_k}}\right)\cos\left(\phi_s + \theta_{g_{d_k,s}} + \theta_{h_s}\right) \\ &+ 2\mathfrak{h}_{d_k}\sum_{s=1}^{S} \mathfrak{g}_{d_k,s}\mathfrak{h}_s\beta_s \sin\left(\theta_{h_{d_k}}\right)\sin\left(\phi_s + \theta_{g_{d_k,s}} + \theta_{h_s}\right).\end{aligned} \tag{B.5}$$

Knowing that $\cos^2(a) + \sin^2(a) = 1$ and $\cos(a)\cos(b) + \sin(a)\sin(b) = \cos(a-b)$, eq. (B.5) can

be re-written as:

$$\begin{aligned}\frac{v_{d_k}}{P} = &\sum_{s=1}^{S} \left(\mathfrak{g}_{d_k,s}\mathfrak{h}_s\beta_s\right)^2 + \mathfrak{h}_{d_k}^2 + 2\mathfrak{h}_{d_k}\sum_{s=1}^{S}\mathfrak{g}_{d_k,s}\mathfrak{h}_s\beta_s\cos\left(\phi_s + \theta_{g_{d_k,s}} + \theta_{h_s} - \theta_{h_{d_k}}\right)\\ &+ 2\sum_{s=1}^{S-1}\mathfrak{g}_{d_k,s}\mathfrak{h}_s\beta_s\sum_{s'=s+1}^{S}\mathfrak{g}_{d_k,s'}\mathfrak{h}_{s'}\beta_{s'}\cos\left(\phi_s + \theta_{g_{d_k,s}} + \theta_{h_s} - \phi_{s'} - \theta_{g_{d_k,s'}} - \theta_{h_{s'}}\right).\end{aligned} \tag{B.6}$$

By using the formulas:

- $\cos(\phi_s + a) = \cos(\phi_s)\cos(a) - \sin(\phi_s)\sin(a)$,
- $\cos(\phi_s - \phi_{s'} + b) = \cos(\phi_s - \phi_{s'})\cos(b) - \sin(\phi_s - \phi_{s'})\sin(b)$,
- $\cos(\phi_s - \phi_{s'}) = \cos(\phi_s)\cos(\phi_{s'}) + \sin(\phi_s)\sin(\phi_{s'})$,

eq. (B.6) can be re-written as:

$$\begin{aligned}\frac{v_{d_k}}{P} = &\sum_{s=1}^{S} \left(\mathfrak{g}_{d_k,s}\mathfrak{h}_s\beta_s\right)^2 + \mathfrak{h}_{d_k}^2 + 2\sum_{s=1}^{S-1}\mathfrak{g}_{d_k,s}\mathfrak{h}_s\beta_s\cos\phi_s\sum_{s'=s+1}^{S}\mathfrak{g}_{d_k,s'}\mathfrak{h}_{s'}\beta_{s'}\cos F_{d_k,s,s'}\cos\phi_{s'}\\ &+ 2\sum_{s=1}^{S-1}\mathfrak{g}_{d_k,s}\mathfrak{h}_s\beta_s\sin\phi_s\sum_{s'=s+1}^{S}\mathfrak{g}_{d_k,s'}\mathfrak{h}_{s'}\beta_{s'}\cos F_{d_k,s,s'}\sin\phi_{s'}\\ &- 2\sum_{s=1}^{S-1}\mathfrak{g}_{d_k,s}\mathfrak{h}_s\beta_s\sin\phi_s\sum_{s'=s+1}^{S}\mathfrak{g}_{d_k,s'}\mathfrak{h}_{s'}\beta_{s'}\sin F_{d_k,s,s'}\cos\phi_{s'}\\ &+ 2\sum_{s=1}^{S-1}\mathfrak{g}_{d_k,s}\mathfrak{h}_s\beta_s\cos\phi_s\sum_{s'=s+1}^{S}\mathfrak{g}_{d_k,s'}\mathfrak{h}_{s'}\beta_{s'}\sin F_{d_k,s,s'}\sin\phi_{s'}\\ &+ 2\mathfrak{h}_{d_k}\sum_{s=1}^{S}\mathfrak{g}_{d_k,s}\mathfrak{h}_s\beta_s\cos G_{d_k,s}\cos\phi_s - 2\mathfrak{h}_{d_k}\sum_{s=1}^{S}\mathfrak{g}_{d_k,s}\mathfrak{h}_s\beta_s\sin G_{d_k,s}\sin\phi_s,\end{aligned} \tag{B.7}$$

with:

$F_{d_k,s,s'} = \theta_{g_{d_k,s}} - \theta_{g_{d_k,s'}} + \theta_{h_s} - \theta_{h_{s'}}$,

$G_{d_k,s} = \theta_{g_{d_k,s}} + \theta_{h_s} - \theta_{h_{d_k}}$.

Appendix C

In this appendix, we show how to find the highest possible received power level that can be attributed to a device d_k and its exact $\tilde{L}_{d_k,exact}$ as shown in eq. (5.24). To do so, we recall that the received power is given by:

$$P^r_{d_k,c} = P\left|\mathbf{g}_{d_k}\Phi\mathbf{h}_s + h_{d_k}\right|^2, \tag{C.1}$$

and should be equal to the highest possible received power level v, given by:

$$v = \sigma^2\Gamma(Q_{\tilde{L}_{d_k,exact}}\Gamma + 1)(\Gamma + 1)^{\tilde{L}_{d_k,exact}-2}. \tag{C.2}$$

Note that we use the notation v instead of v_1 since the notation v_1 will be used for the value of the highest power level after determining the optimal number of power levels L from all $\tilde{L}_{d_k,exact}, k \in \mathcal{K}$.

In order to determine $\tilde{L}_{d_k,exact}$ for a fixed transmit power P, the total channel gain must be maximized in (C.1). Note that the configuration of the RIS plays an essential role in the module of the total channel gain. Let $C(\beta_1, \beta_2, \ldots, \beta_S, \phi_1, \phi_2, \ldots, \phi_S)$ be the function representing the squared module of the total channel gain as a function of the configuration of the RIS elements.

Based on Appendix B, C can be expressed as:

$$
\begin{aligned}
C(\beta_1,\ldots,\beta_S,\phi_1,\ldots,\phi_S) = &\sum_{s=1}^{S}\left(\mathfrak{g}_{d_k,s}\mathfrak{h}_s\beta_s\right)^2 + \mathfrak{h}_{d_k}^2 + 2\sum_{s=1}^{S-1}\mathfrak{g}_{d_k,s}\mathfrak{h}_s\beta_s\cos\phi_s\sum_{s'=s+1}^{S}\mathfrak{g}_{d_k,s'}\mathfrak{h}_{s'}\beta_{s'}\cos F_{d_k,s,s'}\cos\phi_{s'}\\
&+ 2\sum_{s=1}^{S-1}\mathfrak{g}_{d_k,s}\mathfrak{h}_s\beta_s\sin\phi_s\sum_{s'=s+1}^{S}\mathfrak{g}_{d_k,s'}\mathfrak{h}_{s'}\beta_{s'}\cos F_{d_k,s,s'}\sin\phi_{s'}\\
&- 2\sum_{s=1}^{S-1}\mathfrak{g}_{d_k,s}\mathfrak{h}_s\beta_s\sin\phi_s\sum_{s'=s+1}^{S}\mathfrak{g}_{d_k,s'}\mathfrak{h}_{s'}\beta_{s'}\sin F_{d_k,s,s'}\cos\phi_{s'}\\
&+ 2\sum_{s=1}^{S-1}\mathfrak{g}_{d_k,s}\mathfrak{h}_s\beta_s\cos\phi_s\sum_{s'=s+1}^{S}\mathfrak{g}_{d_k,s'}\mathfrak{h}_{s'}\beta_{s'}\sin F_{d_k,s,s'}\sin\phi_{s'}\\
&+ 2\mathfrak{h}_{d_k}\sum_{s=1}^{S}\mathfrak{g}_{d_k,s}\mathfrak{h}_s\beta_s\cos G_{d_k,s}\cos\phi_s - 2\mathfrak{h}_{d_k}\sum_{s=1}^{S}\mathfrak{g}_{d_k,s}\mathfrak{h}_s\beta_s\sin G_{d_k,s}\sin\phi_s,
\end{aligned}
$$

with:

$$
\begin{aligned}
&F_{d_k,s,s'} = \theta_{g_{d_k,s}} - \theta_{g_{d_k,s'}} + \theta_{h_s} - \theta_{h_{s'}},\\
&G_{d_k,s} = \theta_{g_{d_k,s}} + \theta_{h_s} - \theta_{h_{d_k}}.
\end{aligned}
\tag{C.3}
$$

Since β_s is the reflecting amplitude of sub-surface s, one can realize that C is maximum when $\beta_s = 1\forall s$, i.e. there is no absorption of the signal by sub-surface s. Therefore, the maximum value of C depends on the variation of $\phi_s, \forall s$.
For this purpose, let $C = C(\phi_1, ..., \phi_S)$ given by:

$$
\begin{aligned}
C = &\sum_{s=1}^{S}\left(\mathfrak{g}_{d_k,s}\mathfrak{h}_s\right)^2 + \mathfrak{h}_{d_k}^2 + 2\sum_{s=1}^{S-1}\mathfrak{g}_{d_k,s}\mathfrak{h}_s\cos\phi_s\sum_{s'=s+1}^{S}\mathfrak{g}_{d_k,s'}\mathfrak{h}_{s'}\cos F_{d_k,s,s'}\cos\phi_{s'}\\
&+ 2\sum_{s=1}^{S-1}\mathfrak{g}_{d_k,s}\mathfrak{h}_s\sin\phi_s\sum_{s'=s+1}^{S}\mathfrak{g}_{d_k,s'}\mathfrak{h}_{s'}\cos F_{d_k,s,s'}\sin\phi_{s'}\\
&- 2\sum_{s=1}^{S-1}\mathfrak{g}_{d_k,s}\mathfrak{h}_s\sin\phi_s\sum_{s'=s+1}^{S}\mathfrak{g}_{d_k,s'}\mathfrak{h}_{s'}\sin F_{d_k,s,s'}\cos\phi_{s'}\\
&+ 2\sum_{s=1}^{S-1}\mathfrak{g}_{d_k,s}\mathfrak{h}_s\cos\phi_s\sum_{s'=s+1}^{S}\mathfrak{g}_{d_k,s'}\mathfrak{h}_{s'}\sin F_{d_k,s,s'}\sin\phi_{s'}\\
&+ 2\mathfrak{h}_{d_k}\sum_{s=1}^{S}\mathfrak{g}_{d_k,s}\mathfrak{h}_s\cos G_{d_k,s}\cos\phi_s - 2\mathfrak{h}_{d_k}\sum_{s=1}^{S}\mathfrak{g}_{d_k,s}\mathfrak{h}_s\sin G_{d_k,s}\sin\phi_s.
\end{aligned}
\tag{C.4}
$$

C is a multi-variable function. In order to find its critical points/extremums, we start first by deriving the first and second-order partial derivatives.

$$\begin{aligned}\frac{\partial C}{\partial \phi_s} =& -2\mathfrak{g}_{d_k,s}\mathfrak{h}_s \sin\phi_s \sum_{s'=s+1}^{S} \mathfrak{g}_{d_k,s'}\mathfrak{h}_{s'} \cos F_{d_k,s,s'} \cos\phi_{s'} - 2\mathfrak{g}_{d_k,s}\mathfrak{h}_s \sin\phi_s \sum_{s'=1}^{s-1} \mathfrak{g}_{d_k,s'}\mathfrak{h}_{s'} \cos F_{d_k,s,s'} \cos\phi_{s'} \\ &+ 2\mathfrak{g}_{d_k,s}\mathfrak{h}_s \cos\phi_s \sum_{s'=s+1}^{S} \mathfrak{g}_{d_k,s'}\mathfrak{h}_{s'} \cos F_{d_k,s,s'} \sin\phi_{s'} + 2\mathfrak{g}_{d_k,s}\mathfrak{h}_s \cos\phi_s \sum_{s'=1}^{s-1} \mathfrak{g}_{d_k,s'}\mathfrak{h}_{s'} \cos F_{d_k,s,s'} \sin\phi_{s'} \\ &- 2\mathfrak{g}_{d_k,s}\mathfrak{h}_s \cos\phi_s \sum_{s'=s+1}^{S} \mathfrak{g}_{d_k,s'}\mathfrak{h}_{s'} \sin F_{d_k,s,s'} \cos\phi_{s'} + 2\mathfrak{g}_{d_k,s}\mathfrak{h}_s \sin\phi_s \sum_{s'=1}^{s-1} \mathfrak{g}_{d_k,s'}\mathfrak{h}_{s'} \sin F_{d_k,s,s'} \sin\phi_{s'} \\ &- 2\mathfrak{g}_{d_k,s}\mathfrak{h}_s \sin\phi_s \sum_{s'=s+1}^{S} \mathfrak{g}_{d_k,s'}\mathfrak{h}_{s'} \sin F_{d_k,s,s'} \sin\phi_{s'} + 2\mathfrak{g}_{d_k,s}\mathfrak{h}_s \cos\phi_s \sum_{s'=1}^{s-1} \mathfrak{g}_{d_k,s'}\mathfrak{h}_{s'} \sin F_{d_k,s,s'} \cos\phi_{s'} \\ &- 2\mathfrak{h}_{d_k}\mathfrak{g}_{d_k,s}\mathfrak{h}_s \cos G_{d_k,s} \sin\phi_s - 2\mathfrak{h}_{d_k}\mathfrak{g}_{d_k,s}\mathfrak{h}_s \sin G_{d_k,s} \cos\phi_s .\end{aligned} \tag{C.5}$$

$$\Rightarrow \frac{\partial C}{\partial \phi_s} = -2\mathfrak{g}_{d_k,s}\mathfrak{h}_s \sin\phi_s \mathfrak{E} + 2\mathfrak{g}_{d_k,s}\mathfrak{h}_s \cos\phi_s \mathfrak{F}$$

$$\begin{aligned}\mathfrak{E} =& \sum_{s'=s+1}^{S} \mathfrak{g}_{d_k,s'}\mathfrak{h}_{s'} \cos F_{d_k,s,s'} \cos\phi_{s'} + \sum_{s'=1}^{s-1} \mathfrak{g}_{d_k,s'}\mathfrak{h}_{s'} \cos F_{d_k,s,s'} \cos\phi_{s'} \\ &- \sum_{s'=1}^{s-1} \mathfrak{g}_{d_k,s'}\mathfrak{h}_{s'} \sin F_{d_k,s,s'} \sin\phi_{s'} + \sum_{s'=s+1}^{S} \mathfrak{g}_{d_k,s'}\mathfrak{h}_{s'} \sin F_{d_k,s,s'} \sin\phi_{s'} + \mathfrak{h}_{d_k} \cos G_{d_k,s}\end{aligned} \tag{C.6}$$

$$\begin{aligned}\mathfrak{F} =& \sum_{s'=s+1}^{S} \mathfrak{g}_{d_k,s'}\mathfrak{h}_{s'} \cos F_{d_k,s,s'} \sin\phi_{s'} + \sum_{s'=1}^{s-1} \mathfrak{g}_{d_k,s'}\mathfrak{h}_{s'} \cos F_{d_k,s,s'} \sin\phi_{s'} \\ &- \sum_{s'=s+1}^{S} \mathfrak{g}_{d_k,s'}\mathfrak{h}_{s'} \sin F_{d_k,s,s'} \cos\phi_{s'} + \sum_{s'=1}^{s-1} \mathfrak{g}_{d_k,s'}\mathfrak{h}_{s'} \sin F_{d_k,s,s'} \cos\phi_{s'} - \mathfrak{h}_{d_k} \sin G_{d_k,s}\end{aligned} \tag{C.7}$$

$\mathfrak{E}$ can be re-written as:

$$\begin{aligned}\mathfrak{E} =& \sum_{s'=1}^{s-1} \mathfrak{g}_{d_k,s'}\mathfrak{h}_{s'} \left(\cos F_{d_k,s,s'} \cos\phi_{s'} - \sin F_{d_k,s,s'} \sin\phi_{s'}\right) + \mathfrak{h}_{d_k} \cos G_{d_k,s} \\ &+ \sum_{s'=s+1}^{S} \mathfrak{g}_{d_k,s'}\mathfrak{h}_{s'} \left(\cos F_{d_k,s,s'} \cos\phi_{s'} + \sin F_{d_k,s,s'} \sin\phi_{s'}\right)\end{aligned} \tag{C.8}$$

Knowing that $\cos a \cos b - \sin a \sin b = \cos(a+b)$ and $\cos a \cos b + \sin a \sin b = \cos(a-b)$, $\mathfrak{E}$ becomes:

$$\mathfrak{E} = \sum_{s'=1}^{s-1} \mathfrak{g}_{d_k,s'}\mathfrak{h}_{s'} \cos\left(\phi_{s'} + F_{d_k,s,s'}\right) + \mathfrak{h}_{d_k} \cos G_{d_k,s} + \sum_{s'=s+1}^{S} \mathfrak{g}_{d_k,s'}\mathfrak{h}_{s'} \cos\left(\phi_{s'} - F_{d_k,s,s'}\right) \tag{C.9}$$

$\mathfrak{F}$ can be re-written as:

$$\begin{aligned}\mathfrak{F} =& \sum_{s'=1}^{s-1} \mathfrak{g}_{d_k,s'}\mathfrak{h}_{s'} \left(\cos F_{d_k,s,s'} \sin\phi_{s'} + \sin F_{d_k,s,s'} \cos\phi_{s'}\right) - \mathfrak{h}_{d_k} \sin G_{d_k,s} \\ &+ \sum_{s'=s+1}^{S} \mathfrak{g}_{d_k,s'}\mathfrak{h}_{s'} \left(\cos F_{d_k,s,s'} \sin\phi_{s'} + \sin F_{d_k,s,s'} \cos\phi_{s'}\right)\end{aligned} \tag{C.10}$$

Knowing that $\sin a \cos b - \cos a \sin b = \sin(a-b)$ and $\sin a \cos b + \cos a \sin b = \sin(a+b)$, $\mathfrak{F}$ becomes:

$$\mathfrak{F} = \sum_{s'=1}^{s-1} \mathfrak{g}_{d_k,s'} \mathfrak{h}_{s'} \sin\left(\phi_{s'} + F_{d_k,s,s'}\right) - \mathfrak{h}_{d_k} \sin G_{d_k,s} + \sum_{s'=s+1}^{S} \mathfrak{g}_{d_k,s'} \mathfrak{h}_{s'} \sin\left(\phi_{s'} - F_{d_k,s,s'}\right) \tag{C.11}$$

Therefore, $\frac{\partial C}{\partial \phi_s}$ is expressed as:

$$\begin{aligned}\frac{\partial C}{\partial \phi_s} = &- 2\mathfrak{g}_{d_k,s}\mathfrak{h}_s \sin\phi_s \left[\sum_{s'=1}^{s-1} \mathfrak{g}_{d_k,s'}\mathfrak{h}_{s'} \cos\left(\phi_{s'} + F_{d_k,s,s'}\right) + \mathfrak{h}_{d_k} \cos G_{d_k,s} + \sum_{s'=s+1}^{S} \mathfrak{g}_{d_k,s'}\mathfrak{h}_{s'} \cos\left(\phi_{s'} - F_{d_k,s,s'}\right)\right] \\ &+ 2\mathfrak{g}_{d_k,s}\mathfrak{h}_s \cos\phi_s \left[\sum_{s'=1}^{s-1} \mathfrak{g}_{d_k,s'}\mathfrak{h}_{s'} \sin\left(\phi_{s'} + F_{d_k,s,s'}\right) - \mathfrak{h}_{d_k} \sin G_{d_k,s} + \sum_{s'=s+1}^{S} \mathfrak{g}_{d_k,s'}\mathfrak{h}_{s'} \sin\left(\phi_{s'} - F_{d_k,s,s'}\right)\right]\end{aligned} \tag{C.12}$$

In order to find the critical points, we solve $\frac{\partial C}{\partial \phi_s} = 0$. The resulting solution is:

$$\boxed{\tan\phi_s^* = \frac{\sum_{s'=1}^{s-1} \mathfrak{g}_{d_k,s'}\mathfrak{h}_{s'} \sin\left(\phi_{s'} + F_{d_k,s,s'}\right) - \mathfrak{h}_{d_k} \sin G_{d_k,s} + \sum_{s'=s+1}^{S} \mathfrak{g}_{d_k,s'}\mathfrak{h}_{s'} \sin\left(\phi_{s'} - F_{d_k,s,s'}\right)}{\sum_{s'=1}^{s-1} \mathfrak{g}_{d_k,s'}\mathfrak{h}_{s'} \cos\left(\phi_{s'} + F_{d_k,s,s'}\right) + \mathfrak{h}_{d_k} \cos G_{d_k,s} + \sum_{s'=s+1}^{S} \mathfrak{g}_{d_k,s'}\mathfrak{h}_{s'} \cos\left(\phi_{s'} - F_{d_k,s,s'}\right)}} \tag{C.13}$$

Next, we derive the second-order partial derivatives of C in order to find whether the critical points of C found for ϕ_s^* are a local maxima or a local minima.

$$\begin{aligned}\frac{\partial^2 C}{\partial \phi_s^2} = &- 2\mathfrak{g}_{d_k,s}\mathfrak{h}_s \cos\phi_s \left[\sum_{s'=1}^{s-1} \mathfrak{g}_{d_k,s'}\mathfrak{h}_{s'} \cos\left(\phi_{s'} + F_{d_k,s,s'}\right) + \mathfrak{h}_{d_k} \cos G_{d_k,s} + \sum_{s'=s+1}^{S} \mathfrak{g}_{d_k,s'}\mathfrak{h}_{s'} \cos\left(\phi_{s'} - F_{d_k,s,s'}\right)\right] \\ &- 2\mathfrak{g}_{d_k,s}\mathfrak{h}_s \sin\phi_s \left[\sum_{s'=1}^{s-1} \mathfrak{g}_{d_k,s'}\mathfrak{h}_{s'} \sin\left(\phi_{s'} + F_{d_k,s,s'}\right) - \mathfrak{h}_{d_k} \sin G_{d_k,s} + \sum_{s'=s+1}^{S} \mathfrak{g}_{d_k,s'}\mathfrak{h}_{s'} \sin\left(\phi_{s'} - F_{d_k,s,s'}\right)\right].\end{aligned} \tag{C.14}$$

For $s < s'$:

$$\begin{aligned}\frac{\partial^2 C}{\partial \phi_s \partial \phi_{s'}} &= -2\mathfrak{g}_{d_k,s}\mathfrak{h}_s \sin\phi_s \left[-\mathfrak{g}_{d_k,s'}\mathfrak{h}_{s'} \sin\left(\phi_{s'} - F_{d_k,s,s'}\right)\right] + 2\mathfrak{g}_{d_k,s}\mathfrak{h}_s \cos\phi_s \left[\mathfrak{g}_{d_k,s'}\mathfrak{h}_{s'} \cos\left(\phi_{s'} - F_{d_k,s,s'}\right)\right] \\ &= 2\mathfrak{g}_{d_k,s}\mathfrak{h}_s\mathfrak{g}_{d_k,s'}\mathfrak{h}_{s'} \cos\left(\phi_s - \phi_{s'} + F_{d_k,s,s'}\right).\end{aligned} \tag{C.15}$$

For $s > s'$:

$$\begin{aligned}\frac{\partial^2 C}{\partial \phi_s \partial \phi_{s'}} &= -2\mathfrak{g}_{d_k,s}\mathfrak{h}_s \sin\phi_s \left[-\mathfrak{g}_{d_k,s'}\mathfrak{h}_{s'} \sin\left(\phi_{s'} + F_{d_k,s,s'}\right)\right] + 2\mathfrak{g}_{d_k,s}\mathfrak{h}_s \cos\phi_s \left[\mathfrak{g}_{d_k,s'}\mathfrak{h}_{s'} \cos\left(\phi_{s'} + F_{d_k,s,s'}\right)\right] \\ &= 2\mathfrak{g}_{d_k,s}\mathfrak{h}_s\mathfrak{g}_{d_k,s'}\mathfrak{h}_{s'} \cos\left(\phi_s - \phi_{s'} - F_{d_k,s,s'}\right) \\ &= 2\mathfrak{g}_{d_k,s}\mathfrak{h}_s\mathfrak{g}_{d_k,s'}\mathfrak{h}_{s'} \cos\left(\phi_{s'} - \phi_s + F_{d_k,s,s'}\right).\end{aligned} \tag{C.16}$$

As we can see, the second-order partial derivatives of C satisfy Schwarz's theorem since C is continuous, i.e.

$$\frac{\partial^2 C}{\partial \phi_s \partial \phi_{s'}}_{(s<s')} = \frac{\partial^2 C}{\partial \phi_s \partial \phi_{s'}}_{(s>s')} \tag{C.17}$$

The hessian matrix can be written as

$$H = \begin{pmatrix} \frac{\partial^2 C}{\partial \phi_1^2} & \frac{\partial^2 C}{\partial \phi_1 \partial \phi_2} & \cdots & \frac{\partial^2 C}{\partial \phi_1 \partial \phi_S} \\ \frac{\partial^2 C}{\partial \phi_2 \partial \phi_1} & \frac{\partial^2 C}{\partial \phi_2^2} & \cdots & \frac{\partial^2 C}{\partial \phi_1 \partial \phi_S} \\ \vdots & & \ddots & \vdots \\ \frac{\partial^2 C}{\partial \phi_S \partial \phi_1} & & \cdots & \frac{\partial^2 C}{\partial \phi_S^2} \end{pmatrix} \tag{C.18}$$

Then, we determine $\det H$. If $\det H > 0$, the point is an extremum. However, if $\det H < 0$, it is a saddle point (neither a maximum nor a minimum). In order to identify if the extremum is a maximum or a minimum, the trace of H is calculated. We recall that the trace of H is given by the sum of its diagonal elements. If $\mathrm{tr}H < 0$, then the point is a local maximum, otherwise if $\mathrm{tr}H > 0$, it is a local minimum.

Let $|h^*|^2 = C(\phi_1^*, ..., \phi_S^*)$ be the maximum value for the module of the total channel gain for a device d_k. Hence, the maximum received power is given by:

$$P_{d_k}^r = P|h^*|^2. \tag{C.19}$$

Recall that the objective is to find $\tilde{L}_{d_k,exact}$ and $P_{d_k}^r$ should be equal to the discrete power level v. Therefore:

$$\begin{aligned} \sigma^2 \Gamma(Q_L \Gamma + 1)(\Gamma + 1)^{\tilde{L}_{d_k,exact}-2} &= P\,|h^*|^2 \\ \left(\tilde{L}_{d_k,exact} - 2\right) \log(\Gamma + 1) &= \log\left(\frac{P\,|h^*|^2}{\sigma^2 \Gamma(Q_{\tilde{L}_{d_k,exact}} \Gamma + 1)}\right) \end{aligned} \tag{C.20}$$

Hence, the exact value of $\tilde{L}_{d_k,exact}$ is given by:

$$\tilde{L}_{d_k,exact} = \left\lfloor \frac{\log\left(P\,|h^*|^2\right) - \log\left(\sigma^2 \Gamma\left(Q_{\tilde{L}_{d_k,exact}} \Gamma + 1\right)\right)}{\log(\Gamma + 1)} + 2 \right\rfloor. \tag{C.21}$$

Bibliography

[1] S. Al-Sarawi, M. Anbar, R. Abdullah, and A. B. Al Hawari, "Internet of Things Market Analysis Forecasts, 2020–2030," in *2020 Fourth World Conference on Smart Trends in Systems, Security and Sustainability (WorldS4)*, London, UK, Jul. 2020, pp. 449–453.

[2] M. Giordani, M. Polese, M. Mezzavilla, S. Rangan, and M. Zorzi, "Toward 6G Networks: Use Cases and Technologies," *IEEE Commun. Mag.*, vol. 58, no. 3, pp. 55–61, 2020.

[3] C. Bockelmann, N. K. Pratas, G. Wunder, S. Saur, M. Navarro, D. Gregoratti, G. Vivier, E. De Carvalho, Y. Ji, v. Stefanović, P. Popovski, Q. Wang, M. Schellmann, E. Kosmatos, P. Demestichas, M. Raceala-Motoc, P. Jung, S. Stanczak, and A. Dekorsy, "Towards Massive Connectivity Support for Scalable mMTC Communications in 5G Networks," *IEEE Access*, vol. 6, pp. 28 969–28 992, May 2018.

[4] C. Bockelmann, N. Pratas, H. Nikopour, K. Au, T. Svensson, C. Stefanovic, P. Popovski, and A. Dekorsy, "Massive machine-type communications in 5g: physical and MAC-layer solutions," *IEEE Communications Magazine*, vol. 54, no. 9, pp. 59–65, Sept. 2016.

[5] P. Popovski, K. F. Trillingsgaard, O. Simeone, and G. Durisi, "5G Wireless Network Slicing for eMBB, URLLC, and mMTC: A Communication-Theoretic View," *IEEE Access*, vol. 6, pp. 55 765–55 779, Sept. 2018.

[6] S. Vanka, S. Srinivasa, Z. Gong, P. Vizi, K. Stamatiou, and M. Haenggi, "Superposition Coding Strategies: Design and Experimental Evaluation," *IEEE Transactions on Wireless Communications*, vol. 11, no. 7, pp. 2628–2639, 2012.

[7] J. Andrews, "Interference cancellation for cellular systems: a contemporary overview," *IEEE Wireless Communications*, vol. 12, no. 2, pp. 19–29, 2005.

[8] M. Di Renzo, F. H. Danufane, and S. Tretyakov, "Communication Models for Reconfigurable Intelligent Surfaces: From Surface Electromagnetics to Wireless Networks Optimization," *Proceedings of the IEEE*, vol. 110, no. 9, pp. 1164–1209, 2022.

[9] M. A. ElMossallamy, H. Zhang, L. Song, K. G. Seddik, Z. Han, and G. Y. Li, "Reconfigurable Intelligent Surfaces for Wireless Communications: Principles, Challenges, and Opportunities," *IEEE Transactions on Cognitive Communications and Networking*, vol. 6, no. 3, pp. 990–1002, 2020.

[10] N. Varshney and S. De, "AoA-Based Low Complexity Beamforming for Aerial RIS Assisted Communications at mmWaves," *IEEE Commun. Lett.*, vol. 27, no. 6, pp. 1545–1549, Apr. 2023.

[11] A. C. Pogaku, D.-T. Do, B. M. Lee, and N. D. Nguyen, "UAV-Assisted RIS for Future Wireless Communications: A Survey on Optimization and Performance Analysis," *IEEE Access*, vol. 10, pp. 16 320–16 336, 2022.

[12] T. Lattimore and C. Szepesvári, *Bandit Algorithms*. Cambridge University Press, 2020.

[13] A. Garivier and O. Cappé, "The KL-UCB algorithm for bounded stochastic bandits and beyond," in *Proceedings of the 24th annual conference on learning theory*. JMLR Workshop and Conference Proceedings, 2011, pp. 359–376.

[14] S. Agrawal and N. Goyal, "Analysis of thompson sampling for the multi-armed bandit problem," in *Conference on learning theory*. JMLR Workshop and Conference Proceedings, 2012, pp. 39–1.

[15] P. Auer, N. Cesa-Bianchi, and P. Fischer, "Finite-time analysis of the multiarmed bandit problem," *Machine learning*, vol. 47, pp. 235–256, 2002.

[16] A. Anandkumar, N. Michael, A. K. Tang, and A. Swami, "Distributed Algorithms for Learning and Cognitive Medium Access with Logarithmic Regret," *IEEE Journal on Selected Areas in Communications*, vol. 29, no. 4, pp. 731–745, 2011.

[17] D. Kalathil, N. Nayyar, and R. Jain, "Decentralized Learning for Multiplayer Multiarmed Bandits," *IEEE Transactions on Information Theory*, vol. 60, no. 4, pp. 2331–2345, 2014.

[18] K. Liu and Q. Zhao, "Distributed Learning in Multi-Armed Bandit With Multiple Players," *IEEE Transactions on Signal Processing*, vol. 58, no. 11, pp. 5667–5681, 2010.

[19] Z. Tian, J. Wang, J. Wang, and J. Song, "Distributed NOMA-Based Multi-Armed Bandit Approach for Channel Access in Cognitive Radio Networks," *IEEE Wireless Communications Letters*, vol. 8, no. 4, pp. 1112–1115, Aug. 2019.

[20] M.-J. Youssef, V. V. Veeravalli, J. Farah, and C. Abdel Nour, "Stochastic Multi-Player Multi-Armed Bandits with Multiple Plays for Uncoordinated Spectrum Access," in *2020 IEEE 31st Annual International Symposium on Personal, Indoor and Mobile Radio Communications*, London, UK, Sept. 2020, pp. 1–7.

[21] S. Barrachina-Muñoz, A. Chiumento, and B. Bellalta, "Multi-Armed Bandits for Spectrum Allocation in Multi-Agent Channel Bonding WLANs," *IEEE Access*, vol. 9, pp. 133 472–133 490, 2021.

[22] Y. Lin, T. Wang, and S. Wang, "UAV-Assisted Emergency Communications: An Extended Multi-Armed Bandit Perspective," *IEEE Communications Letters*, vol. 23, no. 5, pp. 938–941, 2019.

[23] D. Gale and L. S. Shapley, "College Admissions and the Stability of Marriage," *The American Mathematical Monthly*, vol. 69, no. 1, pp. 9–15, 1962. [Online]. Available: https://doi.org/10.1080/00029890.1962.11989827

[24] B. Zhang, X. Mao, J.-L. Yu, and Z. Han, "Resource allocation for 5G heterogeneous cloud radio access networks with D2D communication: A matching and coalition approach," *IEEE Transactions on Vehicular Technology*, vol. 67, no. 7, pp. 5883–5894, Jul. 2018.

[25] W. Liang, Z. Ding, Y. Li, and L. Song, "User pairing for downlink non-orthogonal multiple access networks using matching algorithm," *IEEE Transactions on communications*, vol. 65, no. 12, pp. 5319–5332, Dec. 2017.

[26] B. Di, S. Bayat, L. Song, and Y. Li, "Radio resource allocation for downlink non-orthogonal multiple access (NOMA) networks using matching theory," in *2015 IEEE global communications conference (GLOBECOM)*. IEEE, Dec. 2015, pp. 1–6.

[27] J. Zhao, Y. Liu, K. K. Chai, Y. Chen, and M. Elkashlan, "Joint Subchannel and Power Allocation for NOMA Enhanced D2D Communications," *IEEE Transactions on Communications*, vol. 65, no. 11, pp. 5081–5094, Nov. 2017.

[28] O. Semiari, W. Saad, S. Valentin, M. Bennis, and B. Maham, "Matching theory for priority-based cell association in the downlink of wireless small cell networks," in *2014 IEEE International Conference on Acoustics, Speech and Signal Processing (ICASSP)*, Florence, Italy, May 2014, pp. 444–448.

[29] I. Bistritz and A. Leshem, "Distributed Multi-Player Bandits - a Game of Thrones Approach," in *Advances in Neural Inf. Process. Syst.*, S. Bengio, H. Wallach, H. Larochelle, K. Grauman, N. Cesa-Bianchi, and R. Garnett, Eds., vol. 31. Curran Associates, Inc., 2018, pp. 7222–7232.

[30] F. Man and W. Lenan, "Extension to Shannon's channel capacity —the theoretical proof," in *2007 6th Int. Conf. on Inf., Commun. Signal Process.*, 2007, pp. 1–4.

[31] D. Gale and H. S. Shapley, "College Admissions and the Stability of Marriage," *American Mathematical Monthly*, vol. 69, no. 1, pp. 9–15, 21962.

[32] D. R. Morrison, S. H. Jacobson, J. J. Sauppe, and E. C. Sewell, "Branch-and-bound algorithms: A survey of recent advances in searching, branching, and pruning," *Discrete Optimization*, vol. 19, pp. 79–102, 2016. [Online]. Available: https://www.sciencedirect.com/science/article/pii/S1572528616000062

[33] J. Doumit, M.-J. Youssef, C. Abdel Nour, J. Farah, and C. Douillard, "Resource Allocation in Full-Duplex Uncoordinated Communication Systems with NOMA," in *2021 IEEE 32nd Annu. Int. Symp. on Pers., Indoor and Mobile Radio Commun. (PIMRC)*, Helsinki, Finland, Sept. 2021, pp. 1104–1110.

[34] M. Zeng, X. Li, G. Li, W. Hao, and O. A. Dobre, "Sum Rate Maximization for IRS-Assisted Uplink NOMA," *IEEE Commun. Lett.*, vol. 25, no. 1, pp. 234–238, 2021.

[35] M. W. Nomeir, Y. Gadallah, and K. G. Seddik, "Uplink Scheduling for Mixed Grant-Based eMBB and Grant-Free URLLC Traffic in 5G Networks," in *2021 17th Int. Conf. on Wireless and Mobile Computing, Networking Commun. (WiMob)*, Bologna, Italy, Oct. 2021, pp. 187–192.

[36] H. Huang and J. Song, "An Uplink Grant-Free Access Solution Based on Sparse Resource Pattern for IoT," in *2020 IEEE International Conference on Electrical Engineering and Photonics (EExPolytech)*, St. Petersburg, Russia, Oct. 2020, pp. 98–101.

[37] C.-W. Pyo, K. Takizawa, M. Moriyama, M. Oodo, H. Tezuka, K. Ishizu, and F. Kojima, "A throughput study of grant-free multiple access for massive wireless communications," in *2017 20th International Symposium on Wireless Personal Multimedia Communications (WPMC)*, Bali, Indonesia, Dec. 2017, pp. 529–534.

[38] H. Zhou, Y. Deng, L. Feltrin, and A. Höglund, "Analyzing Novel Grant-Based and Grant-Free Access Schemes for Small Data Transmission," *IEEE Trans. Commun.*, vol. 70, no. 4, pp. 2805–2819, Feb. 2022.

[39] M. Baghani, S. Parsaeefard, M. Derakhshani, and W. Saad, "Dynamic Non-Orthogonal Multiple Access and Orthogonal Multiple Access in 5G Wireless Networks," *IEEE Transactions on Communications*, vol. 67, no. 9, pp. 6360–6373, 2019.

[40] B. Hidayat and Iskandar, "Capacity Evaluation of Non Orthogonal Multiple Access (NOMA) using 8×8 MIMO in Rayleigh Fading Channel," in *2022 8th International Conference on Wireless and Telematics (ICWT)*, Yogyakarta, Indonesia, Jul. 2022, pp. 1–4.

[41] M. D. Mali and S. S. Chorage, "Spectrally Efficient Multiple Input Multiple Output (MIMO) Non-Orthogonal Multiple Access (NOMA) Technique for Future Wireless Communication," in *2022 2nd Asian Conference on Innovation in Technology (ASIANCON)*, Ravet, India, Aug. 2022, pp. 1–5.

[42] L. Bhardwaj, R. K. Mishra, and R. Shankar, "Examination of Outage probability for Next generation Non Orthogonal Multiple Access Scheme in Uplink and Downlink Scenario," in *2019 IEEE International Symposium on Signal Processing and Information Technology (ISSPIT)*, Ajman, United Arab Emirates, Dec. 2019, pp. 1–5.

[43] F. A. Khales and G. A. Hodtani, "An evaluation of the coverage region for downlink Non-Orthogonal Multiple Access (NOMA) based on Power Allocation Factor," in *2017 Iran Workshop on Communication and Information Theory (IWCIT)*, Tehran, Iran, May 2017, pp. 1–5.

[44] M. Moltafet, N. Mokari, M. R. Javan, H. Saeedi, and H. Pishro-Nik, "A New Multiple Access Technique for 5G: Power Domain Sparse Code Multiple Access (PSMA)," *IEEE Access*, vol. 6, pp. 747–759, 2018.

[45] A. Damnjanovic, J. Montojo, Y. Wei, T. Ji, T. Luo, M. Vajapeyam, T. Yoo, O. Song, and D. Malladi, "A survey on 3GPP heterogeneous networks," *IEEE Wireless Communications*, vol. 18, no. 3, pp. 10–21, 2011.

[46] J. G. Andrews, H. Claussen, M. Dohler, S. Rangan, and M. C. Reed, "Femtocells: Past, Present, and Future," *IEEE Journal on Selected Areas in Communications*, vol. 30, no. 3, pp. 497–508, 2012.

[47] A. Ghosh, N. Mangalvedhe, R. Ratasuk, B. Mondal, M. Cudak, E. Visotsky, T. A. Thomas, J. G. Andrews, P. Xia, H. S. Jo, H. S. Dhillon, and T. D. Novlan, "Heterogeneous cellular networks: From theory to practice," *IEEE Communications Magazine*, vol. 50, no. 6, pp. 54–64, 2012.

[48] C. He, G. Y. Li, F.-C. Zheng, and X. You, "Energy-Efficient Resource Allocation in OFDM Systems With Distributed Antennas," *IEEE Transactions on Vehicular Technology*, vol. 63, no. 3, pp. 1223–1231, 2014.

[49] X. Gu, X. Ji, Z. Ding, W. Wu, and M. Peng, "Outage Probability Analysis of Non-Orthogonal Multiple Access in Cloud Radio Access Networks," *IEEE Commun. Lett.*, vol. 22, no. 1, pp. 149–152, Oct. 2018.

[50] A. Feki, V. Capdevielle, and E. Sorsy, "Self-Organized Resource Allocation for LTE Pico Cells: A Reinforcement Learning Approach," in *2012 IEEE 75th Vehicular Technology Conference (VTC Spring)*, Yokohama, Japan, May 2012, pp. 1–5.

[51] M. N. Esfahani and B. S. Ghahfarokhi, "Improving spectrum efficiency in fractional allocation of radio resources to self-organized femtocells using Learning Automata," in *7'th International Symposium on Telecommunications (IST'2014)*, Tehran, Iran, Sept 2014, pp. 1071–1076.

[52] R. Chen, M. Liu, Y. Hui, N. Cheng, and J. Li, "Reconfigurable Intelligent Surfaces for 6G IoT Wireless Positioning: A Contemporary Survey," *IEEE Internet of Things Journal*, vol. 9, no. 23, pp. 23 570–23 582, 2022.

[53] H. Jiao, H. Liu, and Z. Wang, "Reconfigurable Intelligent Surfaces aided Wireless Communication: Key Technologies and Challenges," in *2022 International Wireless Communications and Mobile Computing (IWCMC)*, Dubrovnik, Croatia, Jun. 2022, pp. 1364–1368.

[54] S. M. R. Islam, N. Avazov, O. A. Dobre, and K.-s. Kwak, "Power-Domain Non-Orthogonal Multiple Access (NOMA) in 5G Systems: Potentials and Challenges," *IEEE Communications Surveys & Tutorials*, vol. 19, no. 2, pp. 721–742, 2017.

[55] K. Lu, Z. Wu, and X. Shao, "A Survey of Non-Orthogonal Multiple Access for 5G," in *2017 IEEE 86th Vehicular Technology Conference (VTC-Fall)*, Toronto, ON, Canada, Sept. 2017, pp. 1–5.

[56] L. Dai, B. Wang, Z. Ding, Z. Wang, S. Chen, and L. Hanzo, "A Survey of Non-Orthogonal Multiple Access for 5G," *IEEE Communications Surveys & Tutorials*, vol. 20, no. 3, pp. 2294–2323, 2018.

[57] M. Hassan, M. Singh, and K. Hamid, "Survey on NOMA and Spectrum Sharing Techniques in 5G," in *2021 IEEE International Conference on Smart Information Systems and Technologies (SIST)*, Nur-Sultan, Kazakhstan, Apr. 2021, pp. 1–4.

[58] H. Nikopour and H. Baligh, "Sparse code multiple access," in *2013 IEEE 24th Annual International Symposium on Personal, Indoor, and Mobile Radio Communications (PIMRC)*, London, UK, Sept. 2013, pp. 332–336.

[59] S. Chen, B. Ren, Q. Gao, S. Kang, S. Sun, and K. Niu, "Pattern Division Multiple Access—A Novel Nonorthogonal Multiple Access for Fifth-Generation Radio Networks," *IEEE Transactions on Vehicular Technology*, vol. 66, no. 4, pp. 3185–3196, 2017.

[60] C. Xu, Y. Hu, C. Liang, J. Ma, and L. Ping, "Massive MIMO, Non-Orthogonal Multiple Access and Interleave Division Multiple Access," *IEEE Access*, vol. 5, pp. 14 728–14 748, 2017.

[61] H. Zuo and X. Tao, "Power allocation optimization for uplink non-orthogonal multiple access systems," in *2017 9th International Conference on Wireless Communications and Signal Processing (WCSP)*, Nanjing, China, Oct. 2017, pp. 1–5.

[62] M. Al-Imari, P. Xiao, M. A. Imran, and R. Tafazolli, "Uplink non-orthogonal multiple access for 5G wireless networks," in *2014 11th International Symposium on Wireless Communications Systems (ISWCS)*, Barcelona, Spain, Aug. 2014, pp. 781–785.

[63] J. Choi, "NOMA-Based Random Access With Multichannel ALOHA," *IEEE Journal on Selected Areas in Communications*, vol. 35, no. 12, pp. 2736–2743, 2017.

[64] J. Zhu, J. Wang, Y. Huang, S. He, X. You, and L. Yang, "On Optimal Power Allocation for Downlink Non-Orthogonal Multiple Access Systems," *IEEE Journal on Selected Areas in Communications*, vol. 35, no. 12, pp. 2744–2757, 2017.

[65] S. Aboagye, A. R. Ndjiongue, T. M. N. Ngatched, O. A. Dobre, and H. V. Poor, "RIS-Assisted Visible Light Communication Systems: A Tutorial," *IEEE Commun. Surveys & Tutorials*, vol. 25, no. 1, pp. 251–288, Dec. 2023.

[66] Y. Liu, X. Liu, X. Mu, T. Hou, J. Xu, M. Di Renzo, and N. Al-Dhahir, "Reconfigurable Intelligent Surfaces: Principles and Opportunities," *IEEE Communications Surveys & Tutorials*, vol. 23, no. 3, pp. 1546–1577, 2021.

[67] R. S. Sutton and A. G. Barto, *Reinforcement Learning: An Introduction*, 2nd ed. The MIT Press, 2018. [Online]. Available: http://incompleteideas.net/book/the-book-2nd.html

[68] M. B. Booth, V. Suresh, N. Michelusi, and D. J. Love, "Multi-Armed Bandit Beam Alignment and Tracking for Mobile Millimeter Wave Communications," *IEEE Communications Letters*, vol. 23, no. 7, pp. 1244–1248, 2019.

[69] Y. Gu, W. Saad, M. Bennis, M. Debbah, and Z. Han, "Matching theory for future wireless networks: fundamentals and applications," *IEEE Communications Magazine*, vol. 53, no. 5, pp. 52–59, May 2015.

[70] E. Balevi, F. T. A. Rabee, and R. D. Gitlin, "ALOHA-NOMA for Massive Machine-to-Machine IoT Communication," in *2018 IEEE Int. Conf. on Commun. (ICC)*, Kansas City, MO, USA, May 2018, pp. 1–5.

[71] A. Mazin, M. Elkourdi, and R. D. Gitlin, "Comparison of Slotted Aloha-NOMA and CSMA/CA for M2M Communications in IoT Networks," in *2018 IEEE 88th Veh. Technol. Conf. (VTC-Fall)*, Chicago, IL, USA, Aug. 2018, pp. 1–5.

[72] M.-R. Hojeij, C. Abdel Nour, J. Farah, and C. Douillard, "Waterfilling-Based Proportional Fairness Scheduler for Downlink Non-Orthogonal Multiple Access," *IEEE Wireless Commun. Lett.*, vol. 6, no. 2, pp. 230–233, Feb. 2017.

[73] J. Farah, E. Sfeir, C. Abdel Nour, and C. Douillard, "New resource allocation techniques for base station power reduction in orthogonal and non-orthogonal multiplexing systems," in *2017 IEEE Intern. Conf. on Commun. Workshops (ICC Workshops)*, Paris, France, May 2017, pp. 618–624.

[74] A. Kilzi, J. Farah, C. Abdel Nour, and C. Douillard, "Mutual Successive Interference Cancellation Strategies in NOMA for Enhancing the Spectral Efficiency of CoMP Systems," *IEEE Trans. on Commun.*, vol. 68, no. 2, pp. 1213–1226, Feb. 2020.

[75] A. Benjebbour, K. Saito, A. Li, Y. Kishiyama, and T. Nakamura, "Non-orthogonal multiple access (NOMA): Concept, performance evaluation and experimental trials," in *2015 Int. Conf. on Wireless Netw. and Mobile Commun. (WINCOM)*, Marrakech, Morocco, Oct. 2015, pp. 1–6.

[76] M. J. Youssef, C. Abdel Nour, J. Farah, and C. Douillard, "Backhaul-Constrained Resource Allocation and 3D Placement for UAV-Enabled Networks," in *2019 IEEE 90th Veh. Technol. Conf. (VTC-Fall)*, Honolulu, HI, USA, USA, Sept. 2019, pp. 1–7.

[77] M. J. Youssef, J. Farah, C. Abdel Nour, and C. Douillard, "Full-Duplex and Backhaul-Constrained UAV-Enabled Networks Using NOMA," *IEEE Trans. on Veh. Technol.*, vol. 69, no. 9, pp. 9667–9681, Sept. 2020.

[78] C. Zhong and Z. Zhang, "Non-Orthogonal Multiple Access With Cooperative Full-Duplex Relaying," *IEEE Commun. Lett.*, vol. 20, no. 12, pp. 2478–2481, Dec. 2016.

[79] J. Doumit, M.-J. Youssef, C. A. Nour, J. Farah, and C. Douillard, "Aoi minimization in mixed traffic full-duplex uncoordinated communication systems with noma," *IEEE Internet of Things J.*, pp. 1–1, Jul. 2023.

[80] N. Zhang, J. Wang, G. Kang, and Y. Liu, "Uplink Non-orthogonal Multiple Access in 5G Systems," *IEEE Commun. Lett.*, vol. 20, no. 3, pp. 458–461, Mar. 2016.

[81] J. Choi, "NOMA-based random access with multichannel aloha," *IEEE J. on Sel. Areas in Commun.*, vol. 35, no. 12, pp. 2736–2743, Oct. 2017.

[82] J. Kim, J. Kim, and S.-H. Park, "Joint Design of Power Control and SIC Decoding Order for Max-Min Fairness optimization in Uplink NOMA Systems," in *2021 Int. Conf. on Inf. Net. (ICOIN)*, Jeju Island, Korea (South), Jan. 2021, pp. 339–342.

[83] I. Baig, N. ul Hasan, M. Zghaibeh, I. U. Khan, and A. S. Saand, "A DST precoding based uplink NOMA scheme for PAPR reduction in 5G wireless network," in *2017 7th Int. Conf. on Modeling, Simul., and Applied Optim. (ICMSAO)*, Sharjah, United Arab Emirates, Apr. 2017, pp. 1–4.

[84] C. Xiao, J. Zeng, W. Ni, X. Su, R. P. Liu, T. Lv, and J. Wang, "Downlink MIMO-NOMA for ultra-reliable low-latency communications," *IEEE J. Sel. Areas Commun.*, vol. 37, no. 4, pp. 780–794, Feb. 2019.

[85] M.-J. Youssef, J. Farah, C. Abdel Nour, and C. Douillard, "Resource Allocation in NOMA Systems for Centralized and Distributed Antennas With Mixed Traffic Using Matching Theory," *IEEE Trans. on Commun.*, vol. 68, no. 1, pp. 414–428, Oct. 2020.

[86] J. Li, Y. Q. Zhao, F. R. Yu, and X. Huang, "Queuing Analysis of Two-Hop Relay Technology in LTE/LTE-A Networks With Unsaturated and Asymmetric Traffic," *IEEE Internet of Things J.*, vol. 3, no. 3, pp. 378–385, June 2016.

[87] H. Chen, Y. Gu, and S.-C. Liew, "Age-of-Information Dependent Random Access for Massive IoT Networks," in *IEEE INFOCOM 2020 - IEEE Conf. on Computer Commun. Workshops (INFOCOM WKSHPS)*, Toronto, ON, Canada, Jul. 2020, pp. 930–935.

[88] J. F. Grybosi, J. L. Rebelatto, and G. L. Moritz, "Age-of-Information of SIC-Aided Massive IoT Networks with Random Access," *IEEE Internet of Things J.*, pp. 1–1, May 2021.

[89] D. C. Atabay, E. Uysal, and O. Kaya, "Improving Age of Information in Random Access Channels," in *IEEE INFOCOM 2020 - IEEE Conf. on Computer Commun. Workshops (INFOCOM WKSHPS)*, Toronto, ON, Canada, Jul. 2020, pp. 912–917.

[90] J.-B. Seo and J. Choi, "On the Outage Probability of Peak Age-of-Information for D/G/1 Queuing Systems," *IEEE Commun. Lett.*, vol. 23, no. 6, pp. 1021–1024, Apr. 2019.

[91] C. Kam, S. Kompella, G. D. Nguyen, J. E. Wieselthier, and A. Ephremides, "Controlling the age of information: Buffer size, deadline, and packet replacement," in *MILCOM 2016 - 2016 IEEE Military Commun. Conf.*, Baltimore, MD, USA, Nov. 2016, pp. 301–306.

[92] R. D. Yates, Y. Sun, D. R. Brown, S. K. Kaul, E. Modiano, and S. Ulukus, "Age of Information: An Introduction and Survey," *IEEE J. on Sel. Areas in Commun.*, vol. 39, no. 5, pp. 1183–1210, Mar. 2021.

[93] S. Kaul, M. Gruteser, V. Rai, and J. Kenney, "Minimizing age of information in vehicular networks," in *2011 8th Annu. IEEE Commun. Soc. Conf. Sensor, Mesh Ad Hoc Commun. Netw.*, Salt Lake City, UT, USA, Jun. 2011, pp. 350–358.

[94] C. Kam, S. Kompella, G. D. Nguyen, J. E. Wieselthier, and A. Ephremides, "Controlling the age of information: Buffer size, deadline, and packet replacement," in *MILCOM 2016 - 2016 IEEE Mil. Commun. Conf.*, Baltimore, MD, USA, Nov. 2016, pp. 301–306.

[95] Y. Inoue, "Analysis of the Age of Information with Packet Deadline and Infinite Buffer Capacity," in *2018 IEEE Int. Symp. Inf. Theory (ISIT)*, Vail, CO, USA, Jun. 2018, pp. 2639–2643.

[96] L. Huang and E. Modiano, "Optimizing age-of-information in a multi-class queueing system," in *2015 IEEE Int. Symp. Inf. Theory (ISIT)*, Hong Kong, China, Jun. 2015, pp. 1681–1685.

[97] A. Soysal and S. Ulukus, "Age of Information in G/G/1/1 Systems: Age Expressions, Bounds, Special Cases, and Optimization," *IEEE Trans. Inf. Theory*, vol. 67, no. 11, pp. 7477–7489, 2021.

[98] C. Kam, S. Kompella, and A. Ephremides, "Age of information under random updates," in *2013 IEEE Int. Symp. Inf. Theory*, Istanbul, Turkey, Jul. 2013, pp. 66–70.

[99] R. D. Yates, "Status Updates through Networks of Parallel Servers," in *2018 IEEE Int. Symp. Inf. Theory (ISIT)*, Vail, CO, USA, Jun. 2018, pp. 2281–2285.

[100] A. M. Bedewy, Y. Sun, and N. B. Shroff, "Minimizing the Age of Information Through Queues," *IEEE Trans. Inf. Theory*, vol. 65, no. 8, pp. 5215–5232, 2019.

[101] X. Li and J. Hwu, "A Frequency Hopping Spread Spectrum Transmission Scheme For Uncoordinated Cognitive Radios," in *2009 IEEE Int. Conf. on Acous., Speech and Signal Proc. (ICASSP)*, Taipei, Taiwan, Apr. 2009, pp. 2345–2348.

[102] M. Bande and V. V. Veeravalli, "Adversarial Multi-user Bandits for Uncoordinated Spectrum Access," in *2019 IEEE Int. Conf. on Acous., Speech and Signal Proc. (ICASSP)*, Brighton, United Kingdom, May 2019, pp. 4514–4518.

[103] Z. Ding, R. Schober, P. Fan, and H. V. Poor, "Simple Semi-Grant-Free Transmission Strategies Assisted by Non-Orthogonal Multiple Access," *IEEE Trans. on Commun.*, vol. 67, no. 6, pp. 4464–4478, Mar. 2019.

[104] H. Jiang, Q. Cui, Y. Gu, X. Qin, X. Zhang, and X. Tao, "Distributed Layered Grant-Free Non-Orthogonal Multiple Access for Massive MTC," in *2018 IEEE 29th Annu. Int. Symp. on Pers., Indoor and Mobile Radio Commun. (PIMRC)*, Bologna, Italy, Sept. 2018, pp. 1–7.

[105] M. J. Youssef, V. V. Veeravalli, J. Farah, and C. Abdel Nour, "Stochastic Multi-Player Multi-Armed Bandits with Multiple Plays for Uncoordinated Spectrum Access," in *2020 IEEE 31st Annu. Int. Symp. on Pers., Indoor and Mobile Radio Commun. (PIMRC)*, London, United Kingdom, United Kingdom, Sept. 2020, pp. 1–7.

[106] M. A. Adjif, O. Habachi, and J. P. Cances, "Joint Channel Selection and Power Control for NOMA: A Multi-Armed Bandit Approach," in *2019 IEEE Wireless Commun. and Netw. Conf. Workshop (WCNC)*, Marrakech, Morocco, Morocco, Apr. 2019, pp. 1–6.

[107] D. P. Zhou and C. J. Tomlin, "Budget-Constrained Multi-Armed Bandits with Multiple Plays," *CoRR*, vol. abs/1711.05928, 2017.

[108] K. Liu and Q. Zhao, "Distributed Learning in Multi-Armed Bandit With Multiple Players," *IEEE Trans. on Signal Process.*, vol. 58, no. 11, pp. 5667–5681, Nov. 2010.

[109] M. Afshang and H. S. Dhillon, "Poisson Cluster Process Based Analysis of HetNets With Correlated User and Base Station Locations," *IEEE Trans. on Wireless Commun.*, vol. 17, no. 4, pp. 2417–2431, Jan. 2018.

[110] S. Gong, X. Lu, D. T. Hoang, D. Niyato, L. Shu, D. I. Kim, and Y.-C. Liang, "Toward Smart Wireless Communications via Intelligent Reflecting Surfaces: A Contemporary Survey," *IEEE Commun. Surveys & Tutorials*, vol. 22, no. 4, pp. 2283–2314, 2020.

[111] J. Zhao, "A Survey of Intelligent Reflecting Surfaces (IRSs): Towards 6G Wireless Communication Networks," 2019. [Online]. Available: https://arxiv.org/abs/1907.04789

[112] J. He, K. Yu, Y. Shi, Y. Zhou, W. Chen, and K. B. Letaief, "Reconfigurable Intelligent Surface Assisted Massive MIMO With Antenna Selection," *IEEE Trans. Wireless Commun.*, vol. 21, no. 7, pp. 4769–4783, Dec. 2022.

[113] Q. Wu and R. Zhang, "Towards Smart and Reconfigurable Environment: Intelligent Reflecting Surface Aided Wireless Network," *IEEE Commun. Mag.*, vol. 58, no. 1, pp. 106–112, 2020.

[114] E. Basar, M. Di Renzo, J. De Rosny, M. Debbah, M.-S. Alouini, and R. Zhang, "Wireless Communications Through Reconfigurable Intelligent Surfaces," *IEEE Access*, vol. 7, pp. 116 753–116 773, 2019.

[115] H. Z. Khan, M. Ali, I. Rashid, A. Ghafoor, and M. Naeem, "Cell Association for Energy Efficient Resource Allocation in Decoupled 5G Heterogeneous Networks," in *2020 IEEE 91st Veh. Techn. Conf. (VTC2020-Spring)*, Antwerp, Belgium, May 2020, pp. 1–5.

[116] H. Zhang, B. Wang, C. Jiang, K. Long, A. Nallanathan, V. C. M. Leung, and H. V. Poor, "Energy Efficient Dynamic Resource Optimization in NOMA System," *IEEE Trans. on Wireless Commun.*, vol. 17, no. 9, pp. 5671–5683, 2018.

[117] M. Ali, S. Qaisar, M. Naeem, and S. Mumtaz, "Energy Efficient Resource Allocation in D2D-Assisted Heterogeneous Networks with Relays," *IEEE Access*, vol. 4, pp. 4902–4911, 2016.

[118] H. Zhang, M. Feng, K. Long, G. K. Karagiannidis, V. C. M. Leung, and H. V. Poor, "Energy Efficient Resource Management in SWIPT Enabled Heterogeneous Networks With NOMA," *IEEE Trans. on Wireless Commun.*, vol. 19, no. 2, pp. 835–845, 2020.

[119] H. Zhang, F. Fang, J. Cheng, K. Long, W. Wang, and V. C. M. Leung, "Energy-Efficient Resource Allocation in NOMA Heterogeneous Networks," *IEEE Wireless Commun.*, vol. 25, no. 2, pp. 48–53, 2018.

[120] M. Zeng, A. Yadav, O. A. Dobre, and H. V. Poor, "Energy-Efficient Joint User-RB Association and Power Allocation for Uplink Hybrid NOMA-OMA," *IEEE Internet of Things J.*, vol. 6, no. 3, pp. 5119–5131, 2019.

[121] J. Farah, J. Akiki, and E. P. Simon, "Energy-Efficient Techniques for Combating the Influence of Reactive Jamming using Non-Orthogonal Multiple Access and Distributed Antenna Systems," in *2019 Wireless Telecommun. Symposium (WTS)*. IEEE, 2019, pp. 1–7.

[122] G. Yang, X. Xu, and Y.-C. Liang, "Intelligent Reflecting Surface Assisted Non-Orthogonal Multiple Access," in *2020 IEEE Wireless Commun. and Net. Conf. (WCNC)*, Seoul, Korea (South), May 2020, pp. 1–6.

[123] Z. Ding and H. Vincent Poor, "A Simple Design of IRS-NOMA Transmission," *IEEE Commun. Lett.*, vol. 24, no. 5, pp. 1119–1123, 2020.

[124] Y. Li, M. Jiang, Q. Zhang, and J. Qin, "Joint Beamforming Design in Multi-Cluster MISO NOMA Reconfigurable Intelligent Surface-Aided Downlink Communication Networks," *IEEE Trans. on Commun.*, vol. 69, no. 1, pp. 664–674, 2021.

[125] J. Zhao, L. Yu, K. Cai, Y. Zhu, and Z. Han, "RIS-Aided Ground-Aerial NOMA Communications: A Distributionally Robust DRL Approach," *IEEE J. on Sel. Areas in Commun.*, vol. 40, no. 4, pp. 1287–1301, 2022.

[126] J. J. Moré, "The Levenberg-Marquardt algorithm: implementation and theory," in *Numerical analysis: proceedings of the biennial Conference held at Dundee, June 28–July 1, 1977*. Springer, 2006, pp. 105–116.

[127] L. Berriche, K. Abed-Meraim, and J.-C. Belfiore, "Investigation of the channel estimation error on MIMO system performance," in *2005 13th European Signal Processing Conf.* IEEE, 2005, pp. 1–4.

[128] Y. Gao, W. Jiang, and T. Kaiser, "Bidirectional branch and bound based antenna selection in massive MIMO systems," in *2015 IEEE 26th Ann. Int. Symp. on Pers., Indoor, and Mobile Radio Commun. (PIMRC)*, Hong Kong, China, Sept. 2015, pp. 563–568.

[129] Y. Li, M. Sheng, X. Wang, Y. Shi, and Y. Zhang, "Globally optimal antenna selection and power allocation for energy efficiency maximization in downlink distributed antenna systems," in *2014 IEEE Global Commun. Conf.*, Austin, TX, USA, Dec. 2014, pp. 3856–3861.

[130] M. Munochiveyi, A. C. Pogaku, D.-T. Do, A.-T. Le, M. Voznak, and N. D. Nguyen, "Reconfigurable Intelligent Surface Aided Multi-User Communications: State-of-the-Art Techniques and Open Issues," *IEEE Access*, vol. 9, pp. 118 584–118 605, 2021.

[131] Y. Zhu and Y. Chen, "Modeling of UAV ground-air communication Channel based on OFDM system," in *2022 IEEE International Conference on Unmanned Systems (ICUS)*, Guangzhou, China, Oct. 2022, pp. 596–599.

[132] S. Zhang, H. Zhang, and L. Song, "Beyond D2D: Full Dimension UAV-to-Everything Communications in 6G," *IEEE Transactions on Vehicular Technology*, vol. 69, no. 6, pp. 6592–6602, Jun. 2020.

[133] L. Ruan, J. Wang, J. Chen, Y. Xu, Y. Yang, H. Jiang, Y. Zhang, and Y. Xu, "Energy-efficient multi-UAV coverage deployment in UAV networks: A game-theoretic framework," *China Communications*, vol. 15, no. 10, pp. 194–209, Oct. 2018.

[134] X. Hu, C. Zhong, M.-S. Alouini, and Z. Zhang, "Robust Design for IRS-Aided Communication Systems With User Location Uncertainty," *IEEE Wireless Communications Letters*, vol. 10, no. 1, pp. 63–67, Jan. 2021.

[135] B. Zheng and R. Zhang, "IRS Meets Relaying: Joint Resource Allocation and Passive Beamforming Optimization," *IEEE Wireless Communications Letters*, vol. 10, no. 9, pp. 2080–2084, Sept. 2021.

[136] X. Mu, Y. Liu, L. Guo, J. Lin, and N. Al-Dhahir, "Capacity and Optimal Resource Allocation for IRS-Assisted Multi-User Communication Systems," *IEEE Transactions on Communications*, vol. 69, no. 6, pp. 3771–3786, Jun. 2021.

[137] M. M. Amri, "Recent Trends in the Reconfigurable Intelligent Surfaces (RIS): Active RIS to Brain-controlled RIS," in *2022 IEEE International Conference on Communication, Networks and Satellite (COMNETSAT)*, Solo, Indonesia, Nov. 2022, pp. 299–304.

[138] H. Lu, Y. Zeng, S. Jin, and R. Zhang, "Aerial Intelligent Reflecting Surface: Joint Placement and Passive Beamforming Design With 3D Beam Flattening," *IEEE Transactions on Wireless Communications*, vol. 20, no. 7, pp. 4128–4143, Jul. 2021.

[139] K. Yu, X. Yu, and J. Cai, "UAVs Assisted Intelligent Reflecting Surfaces SWIPT System With Statistical CSI," *IEEE Journal of Selected Topics in Signal Processing*, vol. 15, no. 5, pp. 1095–1109, Aug. 2021.

[140] C. You, Z. Kang, Y. Zeng, and R. Zhang, "Enabling Smart Reflection in Integrated Air-Ground Wireless Network: IRS Meets UAV," *IEEE Wireless Communications*, vol. 28, no. 6, pp. 138–144, Dec. 2021.

[141] Y. Zeng, R. Zhang, and T. J. Lim, "Throughput Maximization for UAV-Enabled Mobile Relaying Systems," *IEEE Transactions on Communications*, vol. 64, no. 12, pp. 4983–4996, Dec. 2016.

[142] Z. Sheng, H. D. Tuan, T. Q. Duong, and L. Hanzo, "UAV-Aided Two-Way Multi-User Relaying," *IEEE Transactions on Communications*, vol. 69, no. 1, pp. 246–260, Jan. 2021.

[143] T. Shafique, H. Tabassum, and E. Hossain, "Optimization of Wireless Relaying With Flexible UAV-Borne Reflecting Surfaces," *IEEE Transactions on Communications*, vol. 69, no. 1, pp. 309–325, Jan. 2021.

[144] X. Mu, Y. Liu, L. Guo, J. Lin, and N. Al-Dhahir, "Exploiting Intelligent Reflecting Surfaces in NOMA Networks: Joint Beamforming Optimization," *IEEE Transactions on Wireless Communications*, vol. 19, no. 10, pp. 6884–6898, Oct. 2020.

[145] W. Wang, X. Liu, J. Tang, N. Zhao, Y. Chen, Z. Ding, and X. Wang, "Beamforming and Jamming Optimization for IRS-Aided Secure NOMA Networks," *IEEE Transactions on Wireless Communications*, vol. 21, no. 3, pp. 1557–1569, Mar. 2022.

[146] D.-T. Do, T.-T. T. Nguyen, T. N. Nguyen, X. Li, and M. Voznak, "Uplink and Downlink NOMA Transmission Using Full-Duplex UAV," *IEEE Access*, vol. 8, pp. 164 347–164 364, 2020.

[147] D. Zhai, H. Li, X. Tang, R. Zhang, Z. Ding, and F. R. Yu, "Height Optimization and Resource Allocation for NOMA Enhanced UAV-Aided Relay Networks," *IEEE Transactions on Communications*, vol. 69, no. 2, pp. 962–975, Feb. 2021.

[148] S. A. H. Mohsan, N. Q. H. Othman, M. A. Khan, H. Amjad, and J. Żywiołek, "A Comprehensive Review of Micro UAV Charging Techniques," *Micromachines*, vol. 13, no. 6, 2022. [Online]. Available: https://www.mdpi.com/2072-666X/13/6/977

[149] E. Nayebi, A. Ashikhmin, T. L. Marzetta, and H. Yang, "Cell-Free Massive MIMO systems," in *2015 49th Asilomar Conf. on Signals, Systems and Computers*, Pacific Grove, CA, USA, Nov. 2015, pp. 695–699.

COLLEGES SCIENCES
BRETAGNE POUR L'INGENIEUR
LOIRE ET LE NUMERIQUE

IMT Atlantique
Bretagne-Pays de la Loire
École Mines-Télécom

Titre : Optimisation de l'allocation des ressources pour l'internet des objets avec un accès non coordonné au spectre et NOMA

Mots clés : NOMA, RIS, Relais full-duplex, UAV, spectre non coordonné

Résumé : À mesure que l'internet des objets se développe pour inclure des milliards d'appareils connectés, il est appelé à jouer un rôle majeur dans le développement des futurs réseaux de communication sans fil. Cette expansion n'est pas seulement quantitative, elle devrait aussi diversifier les types d'applications que ces réseaux traitent, en allant au-delà des services multimédias traditionnels. Les futurs réseaux sans fil devront fournir des débits de données plus élevés, une fiabilité accrue, une faible latence, une meilleure qualité de service (QoS) et une plus grande capacité d'utilisation. Pour répondre à ces demandes complexes, des approches avancées de l'accès au spectre telles que l'accès multiple non orthogonal (NOMA), la gestion autonome du spectre, les configurations de réseau adaptatives et les communications assistées par des surfaces intelligentes reconfigurables (RIS) sont susceptibles d'être employées. L'objectif de cette thèse est d'optimiser l'allocation des ressources et la configuration du réseau dans les réseaux de la prochaine génération en tirant parti de ces technologies avancées. De multiples configurations de systèmes sont envisagées, comme des types hétérogènes de trafic de données et l'utilisation de communications terrestres et aériennes assistées par RIS. Pour chaque configuration étudiée, nous présentons une solution basée sur NOMA adaptée aux contraintes correspondantes. Les résultats obtenus suggèrent que les solutions proposées surpassent les approches existantes dans la littérature.

Title : Optimizing resource allocation for the Internet of Things with uncoordinated spectrum access and NOMA

Keywords : NOMA, RIS, Full-duplex relays, UAV, Uncoordinated spectrum

Abstract : As the Internet of Things (IoT) expands to include billions of connected devices, it is set to become a major influencer in the development of future wireless communication networks. This expansion is not only about quantity but also it is expected to diversify the kinds of applications these networks handle moving beyond traditional multimedia services. Future wireless networks will be required to deliver higher data rates, increased reliability, low latency, enhanced quality of service (QoS) and greater user capacity. To meet these complex demands, advanced approaches to spectrum access like non-orthogonal multiple access (NOMA), autonomous spectrum management, adaptive network configurations, and reconfigurable intelligent surfaces (RIS)-assisted communications are likely to be employed. The aim of this thesis is to optimize resource allocation and network setup in next-generation networks by leveraging these advanced technologies. Multiple system configurations are considered like heterogeneous types of data traffic and using both terrestrial and aerial RIS-enhanced communications. For every setting studied, we present a NOMA-based solution tailored to its corresponding constraints. Our obtained results suggest that these proposed solutions surpass existing approaches in the literature.